The Penetration of Solar Radiation in Martian Ice Analogues

Thesis

The Penetration of Solar Radiation in Martian Ice Analogues

Thesis submitted for the degree of Doctor of Philosophy

School of Physical Sciences

The Open University

Hannah Elizabeth Chinnery (MSci)

May 2019

Abstract

The penetration depth of broad spectrum solar radiation (300 nm – 1100 nm) in ices relevant to Mars has been measured in the laboratory for the first time. These ices include carbon dioxide and water ices in the form of slab ice, ice of controlled grain sizes, and snow. All of these ice morphologies are observed on the surface of Mars today, and whilst some measurements of water ice have been made for terrestrial applications, many of these cannot be directly compared to carbon dioxide ice because of factors such as impurities in naturally occurring ice, or measurements covering only a narrow spectral range.

The results presented here show that the penetration depth varies with both grain size and ice composition. Grain size (due to light scattering) is the dominant parameter at particle radii applicable to snow, and composition (therefore material-specific optical properties) dominates in larger grains and slab ice. An empirical model is presented, which can be used to predict penetration depth of a specific grain size and composition of ice. This has important applications for modelling surface processes on Mars, many of which have no terrestrial analogue. Relevant features include araneiforms, observed only in association with the seasonal carbon dioxide slab ice, or gullies, which vary in morphology depending on location, indicating varying formation mechanisms. By using more accurate penetration depths for ices on the Martian surface, radiative transfer models describing surface-atmosphere interactions could better simulate these formation processes.

These results can further be applied to modelling icy moons and comets. Future work to expand on this thesis would involve determining the effect of impurities on the e-folding scale of CO_2 ice as Mars's seasonal polar caps contain <0.1% dust. Moreover, measuring the penetration depth in other extra-terrestrial ices would be benefit studies of comets and icy moons.

Acknowledgements

Firstly, I would like to express my gratitude to my supervisors Dr Axel Hagermann, Dr Erika Kaufmann, Prof Stephen Lewis, and Prof Monica Grady, who have guided and supported me all the way through the PhD process. Without their expertise, understanding and patience, this thesis would not exist. Nor would it without the funding from STFC (grant number ST/N50421X/1) and use of the facilities at The Open University.

Next, I would like to thank my husband, for bearing with me throughout the writing of this thesis and for being tirelessly pedantic in his proof reading, and to the rest of my family in backing me through this whole endeavour. Additionally, without the support of my co-postgrad students and good friends Shannon and Hannah, I may have crumbled before getting to the end of this thesis (just like the wonderful cake Shannon often provided). There are undoubtedly many others who deserve my thanks in contributing to my PhD, from friends and family who supported me through the difficult times, to journal reviewers with their helpful critique on the papers which have been published based on this work, but I would use up too much space to list them all here. Thank you all.

Finally, I would like to dedicate this thesis to my mother, Shirley, who inspired me continuously from an age before I can remember. She taught me to pursue my dreams in the face of all the challenges encountered, even when she could no longer be there to hold my hand through to the end.

“There is nothing like looking, if you want to find something.
You certainly usually find something, if you look, but it is not always quite the something you were after.”

– Thorin Oakenshield. The Hobbit, J. R. R. Tolkien

“All shall be done, but it may be harder than you think!”

– Aslan. The Lion, The Witch and the Wardrobe, C. S. Lewis

“It is the questions we can’t answer that teach us the most. They teach us how to think. If you give a man an answer, all he gains is a little fact.
But give him a question and he will look for his own answers.”

– The Wise Man’s Fear, Patrick Rothfuss

Publications

Paper 1 – Data presented in Chapter 4

Chinnery, H.E., Hagermann, A., Kaufmann, E. and Lewis, S.R., 2018. The Penetration of Solar Radiation Into Carbon Dioxide Ice. Journal of Geophysical Research: Planets, 123(4): 864-871.

Paper 2 – Data presented in Chapter 5

Chinnery, H.E., Hagermann, A., Kaufmann, E. and Lewis, S.R., 2019. The Penetration of Solar Radiation Into Water and Carbon Dioxide Snow, With Reference to Mars. Journal of Geophysical Research: Planets, 124(2): 337-348.

Paper 3 – Data presented in Chapter 6

Chinnery, H.E., Hagermann, A., Kaufmann, E. and Lewis, S.R., 2019. The Penetration of Solar Radiation Into Water and Carbon Dioxide Ices of Varying Grain Sizes on Mars. Journal of Geophysical Research: Planets, *In Review*.

Nomenclature

GCM	General Circulation Model
GLF	Glacier-Like Forms
MGCM	Ames Mars General Circulation Model
PAR	Photosynthetically Active Radiation
RSL	Recurring Slope Lineae
SPLD	Southern Polar Layered Deposits
SPRC	Southern Polar Residual Cap
SSGE	Solid-State Greenhouse Effect
THEMIS	Thermal Emission Imaging System, on board Mars Odyssey

Instruments

CRISM	Compact Reconnaissance Imaging Spectrometer for Mars, on board MRO
FREND	Fine Resolution Epithermal Neutron Detector, on board TGO
HiRISE	High Resolution Imaging Science Experiment, on board MRO
MOC	Mars Orbiter Camera, on board MGS
MOLA	Mars Orbiting Laser Altimeter
MONS	Mars Odyssey Neutron Spectrometer

Spacecraft

MGS	Mars Global Surveyor (launched 1996)
MRO	Mars Reconnaissance Orbiter (launched 2005)
TGO	ExoMars Trace Gas Orbiter

Symbols

ζ = E-folding scale/penetration depth (mm)

λ = Wavelength

F = Flux (W m^{-2})

α = Absorption coefficient (m^{-1})

n = Refractive Index

κ = Extinction coefficient

I = Light Intensity

x = Material depth (m)

c = Speed of light in a vacuum

R = Proportion of incident light reflected

T = Proportion of incident light transmitted

ξ = Path length (of light)

Table of Contents

List of Figures

Thesis Overview

Chapter 1. Introduction

Chapter 1 introduces the topic of this thesis, the aims of the research and the rationale behind it. It details different observations and processes which are associated with ice on the surface of Mars, and the way in which solar irradiation interacts with surface ices of different compositions and morphologies. Examples are given as to why it is important to be able to quantify this phenomenon.

Chapter 2. Theoretical & Experimental Background

The theory of light propagation through translucent and particulate media is outlined, along with the mechanisms of ice metamorphism, otherwise known as sintering. The optical constants of water and carbon dioxide ices are given and compared. Previous laboratory based investigations on this topic are also detailed and evaluated.

Chapter 3. Methodology

This chapter includes the methods I employed to create the different types of ices used in the experimental work. It details how I developed my experimental equipment and set up, and outlines the laboratory procedures which were common to all experiments, whilst specific variations on this methodology are given in each corresponding data chapter (chapters 4, 5 and 6).

Chapter 4. The Penetration Depth of Slab ice

Results from light intensity measurements through solid slabs of water and carbon dioxide ice are presented here. The e-folding scale of these ices is calculated from the experimental results and some of the implications discussed. Some of the content in this chapter (specifically, the data relating to the carbon dioxide ice measurements) has been previously published.

Chapter 5. The Penetration Depth of Snow

Results from light intensity measurements through snow made up of both water and carbon dioxide ice are presented in this chapter. The e-folding scale of these snows are calculated and some of the implications discussed. The results from this chapter have been published.

Chapter 6. The Penetration Depth of Granular Ice

Results from light intensity measurements through granular ice of varying grain sizes consisting of both water and carbon dioxide ice are presented. The grain size dependent e-folding scales of these ices are presented and some of the implications discussed.

Chapter 7. Discussion of Results

The e-folding scales calculated from all the experimental work given in the preceding chapters are synthesised and an empirical model is outlined, with supporting theory based on geometrical optics. This is then discussed in context with how the state and composition of surface ice on a planetary body affects the thermal regime of the surface and shallow subsurface, and how this can drive different surface processes, with application to Mars. Further applications to other icy bodies in the solar system are also given.

Chapter 8. Conclusions & Future Work

Some initial experiments which covered the effect of Mars dust contamination in carbon dioxide snow and ice are detailed in the Future Work section, and suggestions how this could be further developed in the future in order to advance the topics covered in this thesis are made. An overview of the final conclusions is given from the investigations detailed in the preceding chapters, concluding this thesis.

Research Questions

I. How does the penetration depth, or e-folding scale, of broad-spectrum solar irradiation in ices vary with ice composition? Is there a difference between water and carbon dioxide ice?

II. How does the penetration depth of broad-spectrum solar irradiation vary with ice morphology, and is this variation consistent across different ice compositions?

III. What are the implications for the differences in solar irradiation penetration depths in the different ice compositions and morphologies, and what does this mean for icy surface processes on Mars, such as the formation of araneiforms in the polar regions?

Chapter 1

Ice on Mars: An Introduction

The presence of ice, in some form, is a common occurrence across the surface and subsurface of Mars, and in this opening chapter the distribution and compositions of Martian ices are detailed, along with associated surface features and their formation mechanisms. In some cases, these formation mechanisms are only inferred or theorised, rather than proven, which highlights the need to understand how icy surfaces behave and evolve when exposed to sunlight. The polar caps on Mars consist of both water and CO_2 ices and exist in a very different atmospheric setting to that of Earth. Recent models and observations show they evolve via complex physical processes which have no terrestrial equivalent (Pilorget et al., 2014). The ability to quantify some of the optical parameters used for modelling and remote sensing is key, with one of the most poorly defined factors being the e-folding scale, otherwise known as the penetration depth, of ice in different morphologies and of different compositions. This provides the main rationale behind this thesis, to investigate the processes and effects of incident solar radiation on surface ices, of different compositions and different morphologies, whether as sheets of ice, large granules or as snow and frost, and how this influences both the evolution of the ice and the surrounding environment.

1.1. Background

Icy surfaces are found to be widespread across the solar system. They range from the water ice deposits of Earth's mountainous glaciers and polar regions, polar craters on airless bodies like Mercury and the Moon (e.g. Ingersoll et al., 1992), comets and objects of the Oort Cloud (e.g. Stern, 2003), through to Pluto, which hosts nitrogen, carbon monoxide and methane ices on its surface (Grundy et al., 2016). Determining the volatile content of a body in space gives an indication of whereabouts in the solar system it originally formed, with an increase in volatile elements with increasing distance from the sun (e.g. Ciesla and Cuzzi, 2006; Lewis, 1972). Of particular interest, and the main focus of this work, is the presence and associated processes of water and carbon dioxide ices on Mars.

Mars hosts a permanent ice cap at each pole: in the north, this is composed primarily of water ice, and is up to 1 km thick, whereas in the south there is a stable layer of carbon dioxide ice overlying water ice. Mars is the only known place in the inner solar system where permanent (under current climatic conditions), naturally occurring, carbon dioxide ice exists on the surface. Each autumn and winter, the atmospheric pressure can drop by up to 25% (e.g. Leighton and Murray, 1966; Snyder, 1979) due to the freezing of CO_2 from the atmosphere to the surface, forming the extensive seasonal polar caps. Carbon dioxide constitutes approximately 95% of the atmosphere of Mars, with water vapour constituting only 0.03% (Gillmann et al., 2009), and so the seasonal deposition of CO_2 ice equates to around 12–16% of the atmosphere by mass (Genova et al., 2016). The seasonal caps are composed almost entirely of carbon dioxide ice, and the southern seasonal cap grows to cover a larger surface area than the northern cap, as, due to the eccentricity of Mars' orbit, the planet is further away from the sun during the southern hemisphere's winter than during the northern winter. Further differences between the seasonal caps include a thicker average depth of the seasonal CO_2 ice in the north, averaging 1.5 m compared to 1.0 m in the south (Matsuo and Heki, 2009; Smith et al., 2001), and a significantly higher proportion of water ice in the northern seasonal cap over the southern cap, although this is only on the scale of millimetres in the form of water ice frost, based on the study by Appéré et al. (2011). The polar caps are the most actively dynamic regions of Mars, and the seasonal exchange of CO_2 from surface to atmosphere and back is the main climatic driver on the planet, creating a strong, planet-wide atmospheric circulation called the condensation flow. The condensation flow transports heat, momentum and mass from the subliming cap to the opposite polar region of cap formation (Forget, 1998), and is also linked to the seasonal dust and water cycles. This demonstrates that the factors influencing the seasonal ice do not only affect the polar regions, but are important for understanding both the present, and past, climate of Mars.

Subsurface ice is abundant, filling the pore space in the upper part of the regolith at mid to high latitudes, possibly even as low as 25° latitude in the southern hemisphere (Vincendon et al., 2010b), and was directly observed by the Phoenix Lander when it dug out a number of trenches around its landing site (68.22° N, 125.7° W), and exposed water ice only a few centimetres below the surface (Smith et al., 2009). Subsurface water ice distribution is being mapped in increasing detail by the Fine Resolution Epithermal Neutron Detector (FREND) on board ExoMars (Mitrofanov et al., 2018), which is currently in the process of detecting hydrogen in the uppermost 1 m of the Martian subsurface. The subsurface hydrogen abundance is then used to determine the water content. Similar measurements have been made previously (e.g. by the Mars Odyssey Neutron Spectrometer, MONS), although on a coarser spatial resolution. The results from MONS, as presented by Feldman et al. (2011), indicate that large areas (outside of the polar regions) could contain water ice abundances greater than what can be held by pore space at <1 m below the surface. Other evidence also indicates large volumes of sequestered water ice in the mid-latitudes. Glacier-like forms (GLFs), viscous flow features and superposed lineated valley fill all describe landforms which are associated with glaciers on Earth, but have also been observed on Mars and are taken to indicate large scale buried ice on Mars. The distribution and volume of GLFs were mapped by Brough et al. (2019), and, based on these observations it is thought that ice thicknesses can be up to ~130 m in some cases, summing to a total volume of ice to be in the range of 523 ± 132 km^3 to 1570 ± 397 km^3 (depending on the exact ice to regolith ratio). This equates to a mean global water layer of 3 – 10 mm in thickness (Brough et al., 2019), demonstrating the vast amount of water likely present as subsurface ice, which is metastable under current climatic conditions.

Both the northern and southern polar caps sit on layered deposits of ice and regolith material. The Southern Polar Layered Deposits (SPLD) consist of bands of dust and water ice, which overlie large buried deposits of CO_2 ice which vary in thickness from tens to thousands of metres (Bierson et al., 2016; Phillips et al., 2011). Mid-latitude subsurface ice deposits are also present, and are thought to have been deposited the past 10 – 20 Ma, during a period of higher obliquity (Brough et al., 2019; Feldman et al., 2011). Obliquity and orbital eccentricity are the main drivers of annual and seasonal climatic variations on Mars. Both of these factors vary over long timescales of 0.1 Ma – 100 Ma (Bills, 1990). The orbital eccentricity causes the southern winter to be colder and longer, as the planet is further from the sun than when the northern winter occurs. The current obliquity of 25.19° is considerably lower than the average over the past 4 Ga of 37.62° (as per the widely accepted model by Laskar et al., 2004), with primary variations occurring on a 0.1 Ma period, and a strong amplitude modulation of 1 Ma, over a range of 10.8° - 38.0° in the last 100 Ma (Bills, 1990). Collectively, these variations are referred to as Milankovitch cycles (as per the theory proposed originally Milutin Milanković in the 1920's to explain long period climatic variations on Earth) and cause periodic fluctuations in the intensity of received insolation. The timing of these are mirrored

in the major and minor laminae of the Polar Layered Deposits (Pollack and Toon, 1982; Toon et al., 1980), in which the interbedding of water, dust and carbon dioxide deposits are observed (Herkenhoff, 2000). The distribution and stability of both surface and subsurface ice is strongly dependent on current obliquity, and orbital eccentricity to a lesser extent. This is due to obliquity being the controlling factor for insolation levels at the poles, as can be seen in Figure 1.1.1. At low obliquities, both poles receive very little insolation due to being near perpendicular to the plane of rotation. However, when the planet has a higher angle of tilt, summertime insolation will be significantly higher, as the polar region is angled towards the sun so much more.

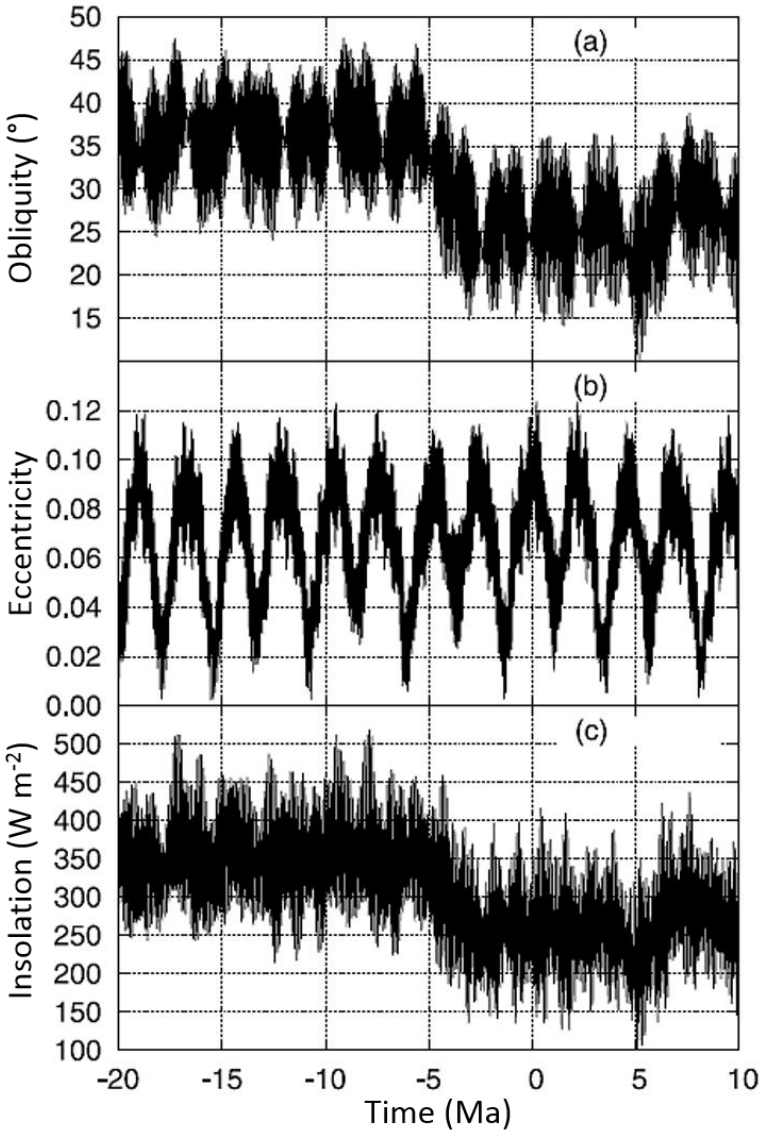

Figure 1.1.1. Obliquity, plotted in panel (a), is the main impactor on insolation levels at the north pole at the summer solstice (L_s = 90°), which shown in panel (c). Orbital eccentricity has a lesser impact (panel b), as can be seen by the strong correlation between (a) and (c), utilising data from the model solution La2004 by Laskar et al. (2004).

The Phoenix Lander also photographed surface water frosts around its location in the northern polar region, and a widespread CO_2 frost cycle has since been discovered, even spanning across the equator at the higher elevations of the Tharsis Volcanic Region (Piqueux et al., 2016). As CO_2 is the main constituent in the atmosphere, surface CO_2 frost formation is not diffusion limited, (unlike water frost) and so if surface temperatures are below the frost point of CO_2, surface frosts will always form. Mars is the only place in our solar system where CO_2 clouds have been directly observed, but it is thought that CO_2 ice is common on the icy satellites in the outer solar system (McCord et al., 1998), and the interstellar medium (Chiar, 1997).

Unique processes have been observed on the Martian surface which have no terrestrial analogue, and therefore novel formation mechanisms must be employed to describe them. Such processes include dry gully formation, which have been observed actively ongoing today (e.g. (Malin and Edgett, 2000). Recognisable gully features, visually similar to those on Earth that are triggered by liquid water mobilising a slope, are generally found on pole facing slopes across the 30° – 50° latitude range in both hemispheres. However, these features are being created in the absence of any detectable liquid water, and under conditions below the triple point of water, which means it can exist only as a solid or as a gas at the present atmospheric conditions on the Martian surface. Figure 1.1.2 compares the phases of water and carbon dioxide over a range of temperature and pressure conditions: at the low pressure and temperature conditions typical to Mars, water usually exists as ice, and in small quantities of water vapour, whereas carbon dioxide is mainly a gas, existing as a solid when temperatures are cold enough.

A completely alien surface feature is that of the 'spiders' observed in the southern polar area, first discovered in the cryptic terrain of the southern polar region. These so called araneiforms tend to occur in the same location each year during ice cap retreat, and are associated with dendritic troughs observed during the summer months, as exampled in Figure 1.1.3 (Kieffer, 2007; Pilorget et al., 2011; Pilorget et al., 2013; Portyankina et al., 2012). Similar surface formations are now being observed throughout the polar regions in both the northern and southern hemispheres (e.g. Bourke and Cranford, 2011; Portyankina et al., 2019; Schwamb et al., 2018). These are discussed further in the following sections.

It has been theorised that it is the presence of carbon dioxide ice on and in the Martian surface which makes these unusual surface features possible. CO_2 constitutes approximately 95% of the Martian atmosphere and, as pointed out previously, each winter 12% - 16% of the atmospheric mass condenses out to form the seasonal polar cap (Genova et al., 2016). The frost point of CO_2 on Mars varies based on the atmospheric pressure at a particular location and time, but is typically 142K – 151K (Mount and Titus, 2015). Ice formation begins at high latitudes in autumn and continues throughout winter, forming the seasonal polar ice cap. This grows with the

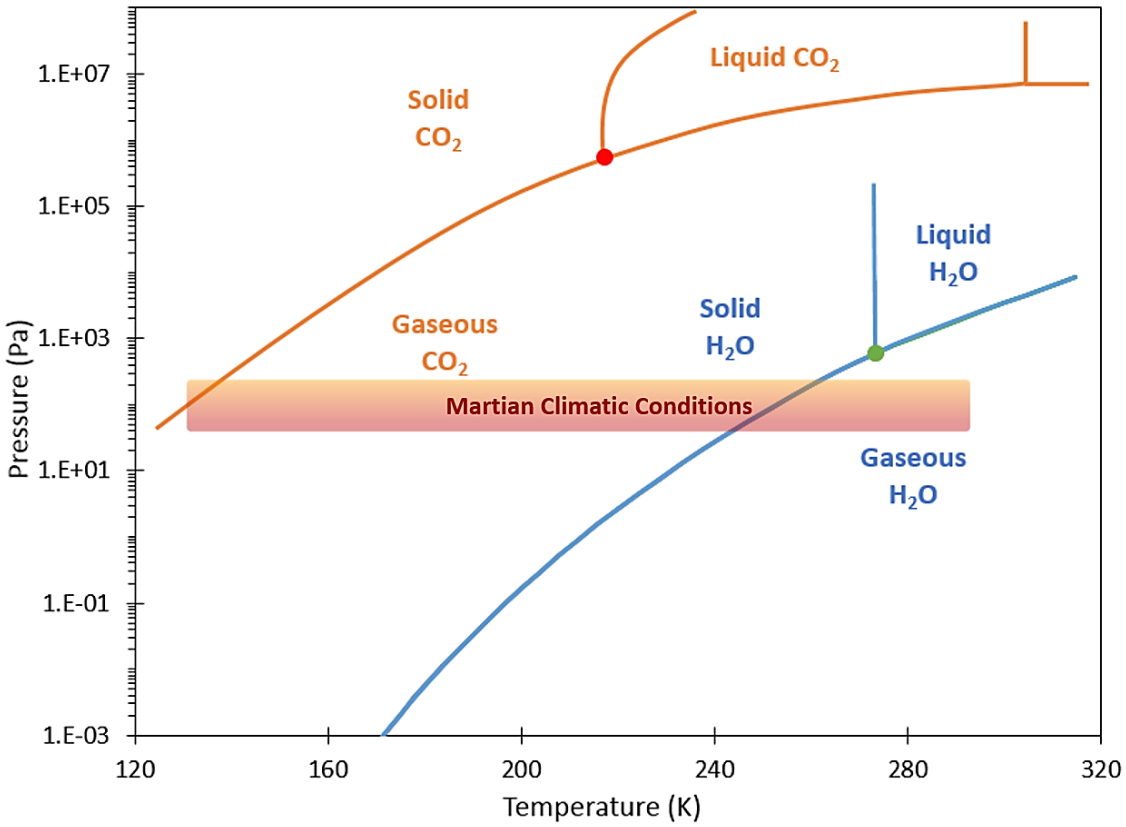

Figure 1.1.2. P-T diagram illustrating the difference between the temperature and pressure conditions required for the different physical states of water and carbon dioxide, overlaid by the range of pressure and temperature conditions experienced on the surface of present day Mars.

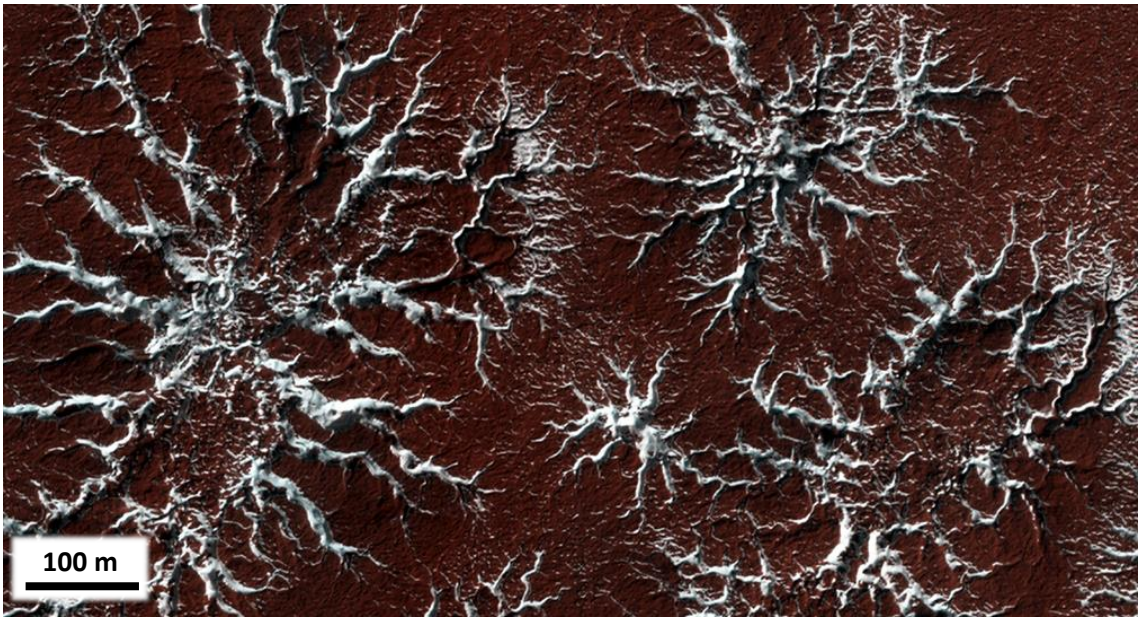

Figure 1.1.3. Characteristic araneiform terrain, which consists of eroded radial channels located in the southern polar region. In this instance, high albedo ice is infilling the channels, making them appear white against the red coloured regolith. Scales typically range from tens of metres to a kilometre in width. Image taken from HiRISE RGB image ESP_020914_0930, image credit NASA/JPL/University of Arizona.

addition of CO_2 ice over and around the permanent polar caps by two methods: direct condensation to the surface in the form of sheets of clear ice, and as carbon dioxide snow. The latter is thought to contribute between 3% - 20% of mass to the seasonal ice cap, based on models by Hayne et al. (2014) which used measurements from the Mars Climate Sounder (MCS). CO_2 snow fall on Mars has been hypothesised for quite some time and is supported by observations of anomalously low brightness temperatures, well below the sublimation temperature of CO_2 and dubbed polar cold spots, in the polar regions (e.g. Forget et al., 1995; Titus et al., 2001). Measurements from the Mars Orbiter Laser Altimeter (MOLA), on board the Mars Global Surveyor (MGS) were used by Smith et al. (2001) to determine the seasonal changes caused by ice/snow deposition, finding that elevation could change up to 2 m at latitudes >80°, with an average icy deposit density of 910 ± 230 kg m^{-3}. The carbon dioxide snow settles and compacts over time, eventually sintering to form a high-density slab through vapour diffusion, partial sublimation and re-condensation across grain boundaries. The process of sintering is described in detail in Chapter 2, Section 3. Slab ice tends to be significantly more translucent than granular ice, and consequently exhibits a lower albedo. The overall surface albedo, when covered by CO_2 slab ice, is dominated by the albedo of the underlying regolith (Piqueux et al., 2003), which has wider implications for the energy budget and surface-atmospheric interactions.

It is likely that an interaction occurs between the deposition of surface CO_2 and other processes, such as the onset of regional dust storms that coincide with the initiation of carbon dioxide condensation, as one example. It is theorised that the increased levels of dust suspended in the atmosphere may act as nuclei for CO_2 ice crystals to form, and so may trigger the precipitation of CO_2 snow (Cull et al., 2010). Alternatively, it may be possible that the onset of CO_2 condensation changes the thermal properties of the surface, changing wind patterns and triggering the dust storms. Kahre et al. (2011) used the NASA Ames Mars General Circulation Model (MGCM) to simulate the effect of atmospheric dust on long term ice cap evolution and atmospheric stability. The results show that, in general, increasing the polar cap albedo increased the rate of atmospheric collapse at all variations of dust loading and orbital obliquities. Atmospheric collapse is defined as the condensation of the CO_2 atmosphere on a global scale (Soto et al., 2014). However, an increase in atmospheric dust when ice cap albedo is 0.5 or lower accelerates atmospheric collapse, whereas if ice albedo is >0.5, increasing atmospheric dust levels reduces the rate of atmospheric collapse. This is because, when cap albedo is low more incident radiation is absorbed by the ice, but by loading the atmosphere with dust the intensity of the incident radiation is reduced, leading the ice to absorb less energy and resulting in more of the CO_2 ice surviving throughout the year. This gradually increases the thickness of the ice and eventually leads to atmospheric collapse. Conversely, if cap albedo is high, increasing atmospheric dust levels provides an insulating layer

which reduces the net radiative heat loss at the top of the atmosphere, therefore leading to reduced rates of CO_2 condensation and subsequent atmospheric collapse (Kahre et al., 2013).

1.2. The Solid-State Greenhouse Effect

The Solid-State Greenhouse Effect (SSGE) describes how solid, translucent media allow for light to penetrate through them and cause a warming effect below the surface, based on a number of different material properties. In nature, this often applies to surface ices. The concept of the SSGE in terrestrial snow and ice has been reported since the early 20th centry (Niederdorfer, 1933), but the application of it to extraterrestrial bodies was first described by Brown and Matson (1987),

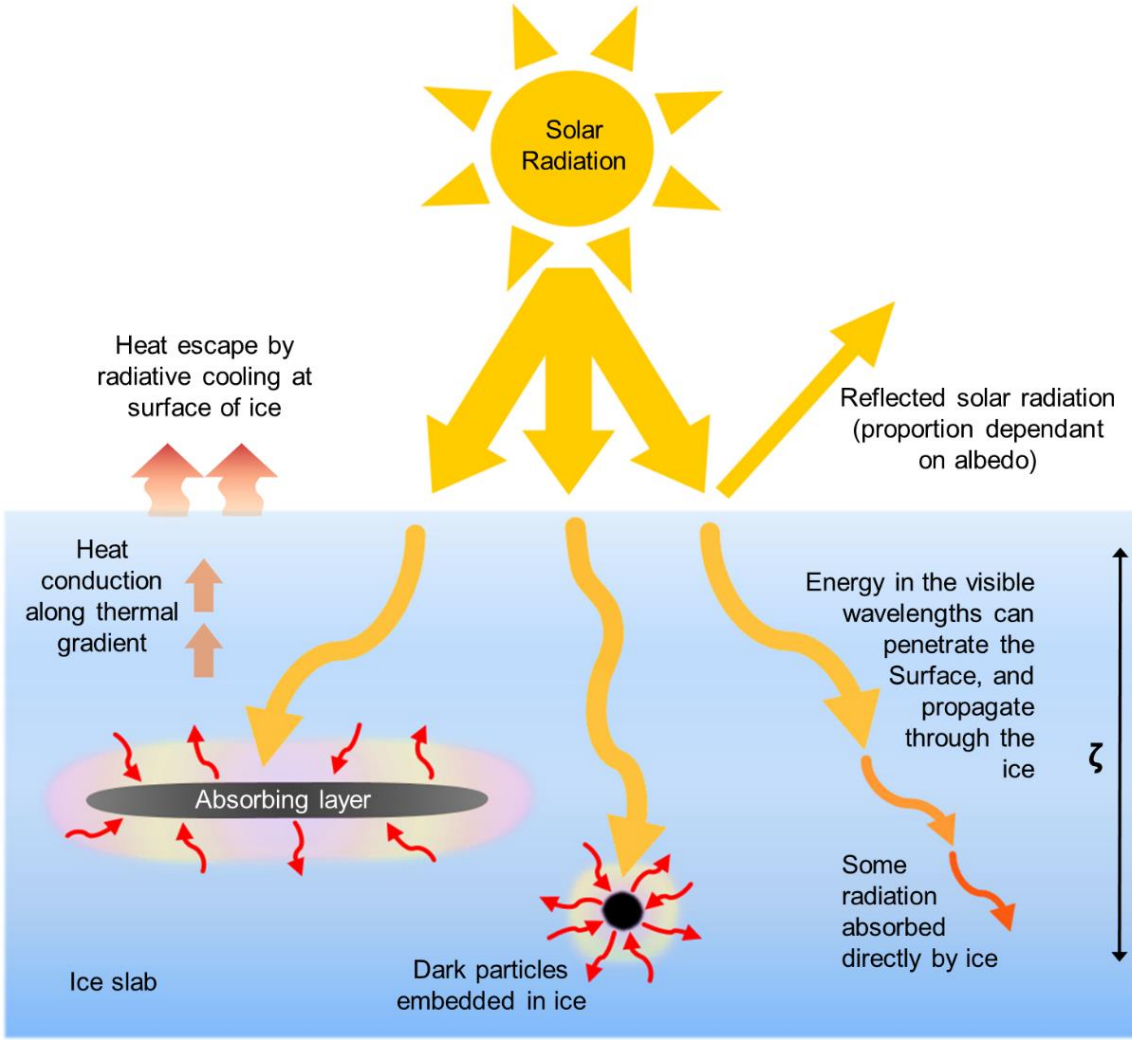

Figure 1.2.1. Diagram visualising the Solid-State Greenhouse Effect (SSGE) in planetary ices. Visible spectrum light can penetrate through the surface and propagate into the body of the ice. Individual, or layers of, dark particles embedded in the ice absorb incoming solar energy at a much faster rate than the ice itself, which re-emit this energy as IR radiation. Ices are opaque in the IR range, and so the energy is unable to efficiently dissipate, leading to localised heating and potentially (but not necessarily) melting/subliming of the ice in the immediate vicinity to the dark particles/absorbing layer.

who coined the term, and the model was developed further in Matson and Brown (1989). Within these studies the authors discussed the importance of broad-spectrum solar radiation propagating into icy surfaces to depths significant in comparison to the diurnal skin depth for thermal diffusion. Due to the transparancy of ice at visible wavelengths, incident irradiation is not just absorbed and reflected (in varying amounts, dependant on albedo) at the surface, but also in the subsurface. This is depicted in Figure 1.2.1.

The subsurface thermal profile of a body is dependent on the physical and thermal properties of the surface material, and incoming energy fluxes, both external (solar radiation) and internal (geothermal gradient). This could occur with almost any composition of regolith, as long as it is optically thin in the visible range, but thick/opaque in the infrared (Brown and Matson, 1987). If the surface material is icy, then the SSGE is an important factor in determining this subsurface thermal profile. The extent of the SSGE is determined by multiple factors, including the optical properties of the icy material, grain size and shape, impurities, depth of ice, etc.

Ices are translucent in the visible wavelength range, whilst being opaque in the infrared. Consequently, irradiation in the visible wavelength range can penetrate through the surface and into the ice. Some of this energy can be absorbed by impurities suspended in the ice, which then re-radiate energy and cause localised heating of the ice. As the ice is opaque in infrared, the reradiated energy cannot escape directly, and energy loss is only possible via conduction along the thermal gradient, leading to melting or sublimation of the ice in the immediate vicinity. Some light may be scattered in different directions within the ice, due to gas bubbles or cracks, attenuating the downwards directed flux. Additionally, a certain proportion of the incident energy will be absorbed by the ice itself (see Figure 1.2.1). The degree to which light is attenuated in this way (purely by the ice) is specific to the material in which it is propagating, and is dependent upon a range of factors, such as the refractive index and absorption coefficient of the material. This is quantified by the penetration depth, otherwise called the absorption scale length, or e-folding scale (ζ). The e-folding scale also happens to be one of the most poorly understood parameters governing heat transfer in ices (Möhlmann, 2010), and has direct implications for the thermal profile of a slab of ice or snow pack, causing the thermal maxima to often be located at some point below the surface of the ice. In some regions of the Antarctic, subsurface melting pools have been discovered, which form due to the absorption of incident solar radiation in the subsurface of the ice (Winther et al., 1996). In the context of Mars, however, the situation is further complicated by the presence of not only water ice and snow but also carbon dioxide ice, and so the need for understanding how light penetrates into both ice compositions, as well as morphologies (snow, large ice granules or sheets of solid ice, known as ‘slab ice’) is required in order to quantify the SSGE.

Whilst some experiments have been conducted to determine the optical, mechanical and thermal properties of solid CO_2, many are non-ideal. Most have used micrometre to millimetre sized samples (e.g. Hudgins et al., 1993; Quirico and Schmitt, 1997), which is insufficient to give bulk parameters suitable for large scale models; others suffered from impure samples (Egan and Spagnolo, 1969), or from highly cracked samples (Ditteon and Kieffer, 1979). In addition, many studies focused on determining the optical properties within discrete wavelength ranges (e.g. Hansen, 1997). Whilst CO_2 ice absorbs in narrow bands in the infrared similar to that of CO_2 gas (Hansen, 1999), and has a strong absorption continuum in the ultraviolet, absorption in the visible range is low (Warren, 1986).

Some similar measurements have been made using water ice. Studies using naturally occurring Antarctic sea ice include those made by Brandt and Warren (1993), Perovich (1996), and Datt et al. (2015), which have focussed on the implications for thermal profiles and subsurface heating on Earth. Perovich (1996) reported that the e-folding scale of naturally occurring sea ice could vary so dramatically, that at 470 nm wavelength the e-folding scale is 24 m, reducing by orders of magnitude to 50 mm at 1000 nm wavelength. Other studies are more applicable to icy bodies in space, ranging from comets to icy moons to the polar regions of Mars, including Kömle et al. (1990) and Kaufmann et al. (2006). However, these all focused on water ice, either pure or with admixtures, and most of these report on the depth of temperature maxima, rather than specifying the e-folding scale (with the exception of Kaufmann et al. (2006) who suggest an e-folding scale of 15 mm for H_2O snow fits their 2D model describing the effect of the SSGE on the thermal evolution on irradiated samples of glass beads and snow). Further measurements have been made for the e-folding scale of water snow, which is discussed further in Chapter 2, along with other relevant laboratory investigations.

Accurately defining the e-folding scale of broad spectrum solar radiation in surface ices is important for two different applications. Firstly, for use in radiative transfer models, which enable improved understanding of the surface and shallow subsurface thermal profile, how this changes over time in response to the presence of surface ice of different morphologies and compositions, and therefore what possible surface processes are occurring in response to this. Second to this is understanding how broad spectrum light penetrates through ice and snow, which is important in the search for extra-terrestrial life. Photosynthetic microbes require light in the wavelength range of 400 nm – 700 nm, dubbed 'Photosynthetically Active Radiation' (PAR), but light in the ultra violet range (10 nm – 400 nm) is damaging to DNA. On Earth, the Ozone Layer filters out almost all UV wavelengths. On Mars, the UV flux is 1000 times that of Earth, due to the lack of ozone in the atmosphere, but the levels of PAR is around 55% less (Cockell and Raven, 2004) due to Mars being farther from the sun than Earth. This means that any potential photosynthetic life would need to

protect itself from damaging UV radiation, likely by being buried under regolith or snow/ice, whilst still being exposed to sufficient PAR levels to enable photosynthesis. There have been a few studies measuring light penetration in snow and ice based on this premise, such as Cockell and Raven (2004) and France et al. (2010), but the research and experiments detailed in this thesis are focussed on the physical effects of light penetration through different ices and the interactions associated with it, rather than any potential astrobiological applications.

Brandt and Warren (1993) argued that the solid state greenhouse effect is insignificant in snow as the visible wavelength range which is able to penetrate into the snow pack is scattered back to the surface without being absorbed, whereas the longer wavelengths of the near-infrared, which are absorbed, are absorbed in just the top couple of millimetres. The SSGE is therefore only significant in materials such as 'blue ice', where the scattering coefficient is small or if the thermal conductivity is low, such as in low-density snow. This statement demonstrates the importance of quantifying the SSGE for the entire range of ice types and morphologies. In addition, the SSGE is likely an important driver of snow metamorphism, or sintering (described in detail in Section 2.3) at low snow densities (Brandt and Warren, 1993), and so deserves to be accurately determined.

1.3. Grain Burrowing

Windblown dust deposited onto the surface of ice is a frequent occurrence on the seasonal ice caps of Mars. Dust grains act as condensation nuclei for clouds and CO_2 snow crystals to form in the atmosphere, and so any snowfall occurring will bring dust with it (Forget et al., 1998). Additionally, dust which has been advected into the polar region will precipitate from the atmosphere over time (Hansen, 1999), and so there will always be a certain amount of dust embedded within the growing seasonal ice. Over winter, when there is little to no irradiation (during the polar night) the dust grains reside in the ice. However, as insolation levels increase during spring, the dust grains will absorb energy from insolation at a much higher rate than the ice, as dust has a much higher absorption in the visible range than either CO_2 or H_2O ice (Hansen, 1999). This leads to heating of the grain, which reradiates infrared energy (to which ice is opaque), causing localised sublimation of the surrounding ice, as demonstrated in Figure 1.3.1.

Each panel in Figure 1.3.1 (labelled 'a' through to 'e') shows the different stages of grain burrowing: a) a grain of regolith is deposited on the surface of the ice and is irradiated by the sun; b) due to lower albedo and higher thermal conductivity, the grain absorbs more energy than the ice, which it then reradiates, causing the ice immediately around the grain to sublimate; c) the grain drops down into the void left by the sublimating CO_2, still absorbing much more energy than the surrounding ice, and reradiating. Due to the saturation of CO_2 in the atmosphere and that the CO_2

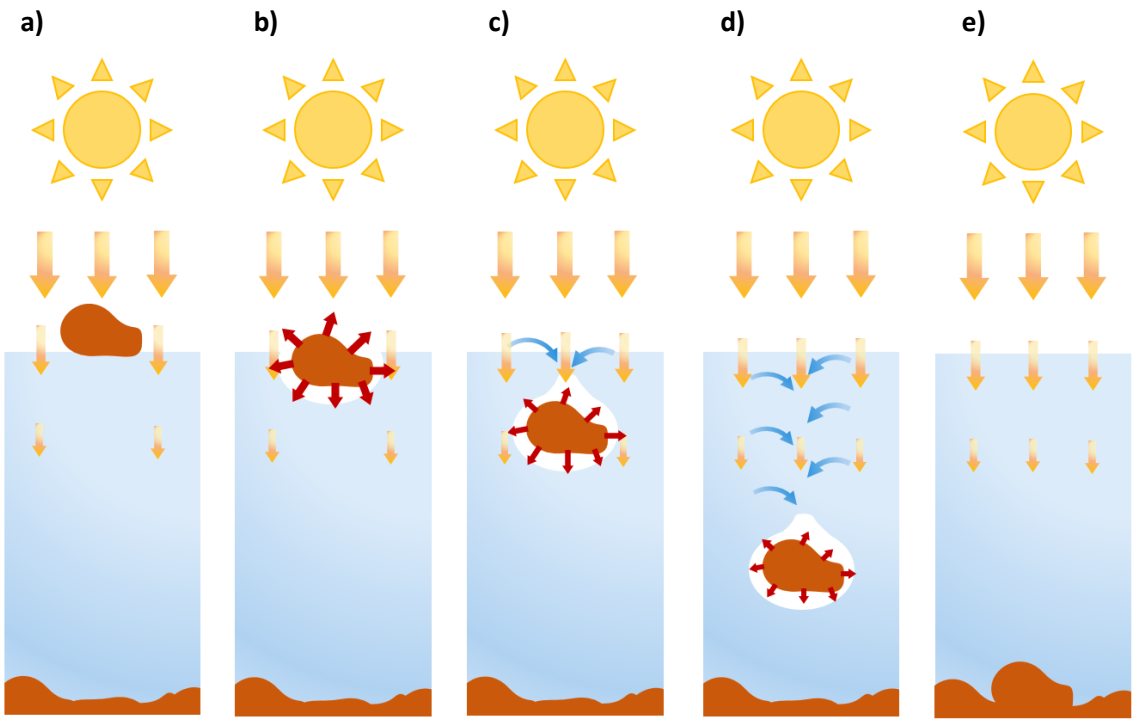

Figure 1.3.1. Diagram showing the process of grain burrowing in CO_2 slab ice when exposed to incident radiation (e.g. Kieffer, 2007; Kieffer et al., 2006)

ice slab is in thermal equilibrium with the atmosphere, ice will recondense over the top of the grain, sealing it in; d) as the grain burrows deeper, it receives less energy from the sun, due to increased attenuation from the thicker layer of ice, and so the rate of descent slows; e) the grain reaches either the bottom of the ice slab, or the depth at which it can no longer receive sufficient insolation to sublimate the surrounding ice, and therefore remains stable. This leads to a self-cleaning process, where any sand or dust deposited onto the surface of the ice will burrow down through the ice deposit, surrounded by a pocket of high pressure gas (Portyankina et al., 2010) and eventually end up at the bottom of the ice or snow pack, or until insufficient insolation is received to continue the process. Therefore, a clear, transparent ice layer is maintained which enables other processes to occur throughout spring through to the crocus date, which is defined as the time when the seasonal polar cap has completely disappeared.

1.4. Araneiforms

Radially branching erosional features in the southern polar region were first defined and mapped by Piqueux et al. (2003). Dubbed ‘spiders’, these low albedo features have been described as ‘spots and radial channels’. Araneiforms are observed during the southern winter and spring, often occurring in the same locations year after year, and are found solely in the South Polar

Layered Deposits (SLPD) in which cover the southern polar region. Previously thought an exception to this, a cluster of spiders were mapped in a nearby area with characteristics similar to that of the SLPD, but the extent of the SLPD has since been redefined by Tanaka et al. (2014) based on improved measurements and imaging of the region to now include these previously outlier spiders.

However, it was in the first mapping effort by Piqueux et al. (2003) that the correlation between these spider formations and CO_2 ice was confirmed, supporting the cold CO_2 jetting model of spider formation. This formation mechanism, proposed by Kieffer (2000), and later expanded upon by Piqueux et al. (2003), Kieffer et al. (2006), Kieffer (2007), Piqueux and Christensen (2008), Thomas et al. (2010), Portyankina et al. (2010), Pilorget et al. (2011), Thomas et al. (2011) and Martínez et al. (2012), is often referred to as the Kieffer model. The Kieffer model requires an indeterminately large-grained, highly transparent CO_2 ice slab overlying poorly consolidated regolith, in the form of the seasonal polar cap. During early spring, increasing levels of solar radiation are incident on the ice slab. Due to the high transparency of the ice to visible wavelengths, but opacity in infrared wavelengths, a solid-state greenhouse is induced. This causes warming of the under-ice substrate, eventually raising the temperature to the sublimation point of CO_2 ice. Subsequent basal sublimation of CO_2 ensues, but as the ice sheet forms a continuous and impermeable barrier, the CO_2 gas is trapped beneath the ice. Eventually, the trapped CO_2 overcomes the cryostatic pressure at the base of the ice, rupturing the overlying slab and causing high-velocity gas venting. This can carry regolith material to the surface, gouging out radial channels in the regolith, depositing the larger and heavier material to form dark fans on top of the ice, and the smallest and lightest grains being ejected into the atmosphere (Portyankina et al., 2019). Fans can be unidirectional, or spread more radially, depending on localised surface winds carrying the material over the top of the ice. This formation process is depicted in Figure 1.4.1.

The correlation between araneiforms and the existence of highly transparent CO_2 slab ice overlying poorly consolidated particulate regolith of the SPLD was confirmed by Kieffer et al. (2006) by using surface temperatures based on THEMIS (Mars Odyssey Thermal Emission Imaging System) data consistent with that of CO_2 ice (~145K), in combination with anomalously low surface albedos. These conditions persist for at least 120 sols following sunrise after the austral polar winter.

Individual araneiforms can span from tens of metres to a kilometre in diameter (Hansen et al., 2010), with multiple interconnected and branching tributaries. A wide range of araneiform morphologies are observed, with some examples shown in Figure 1.4.2, including typical ‘spiders’ with radial branches and a central pit, and ‘lace terrain’, where the dendritic channels are interconnected, but lack a central pit. However, it is not entirely known what governs the different terrain morphologies. They are found across the southern polar region, often in the same locations

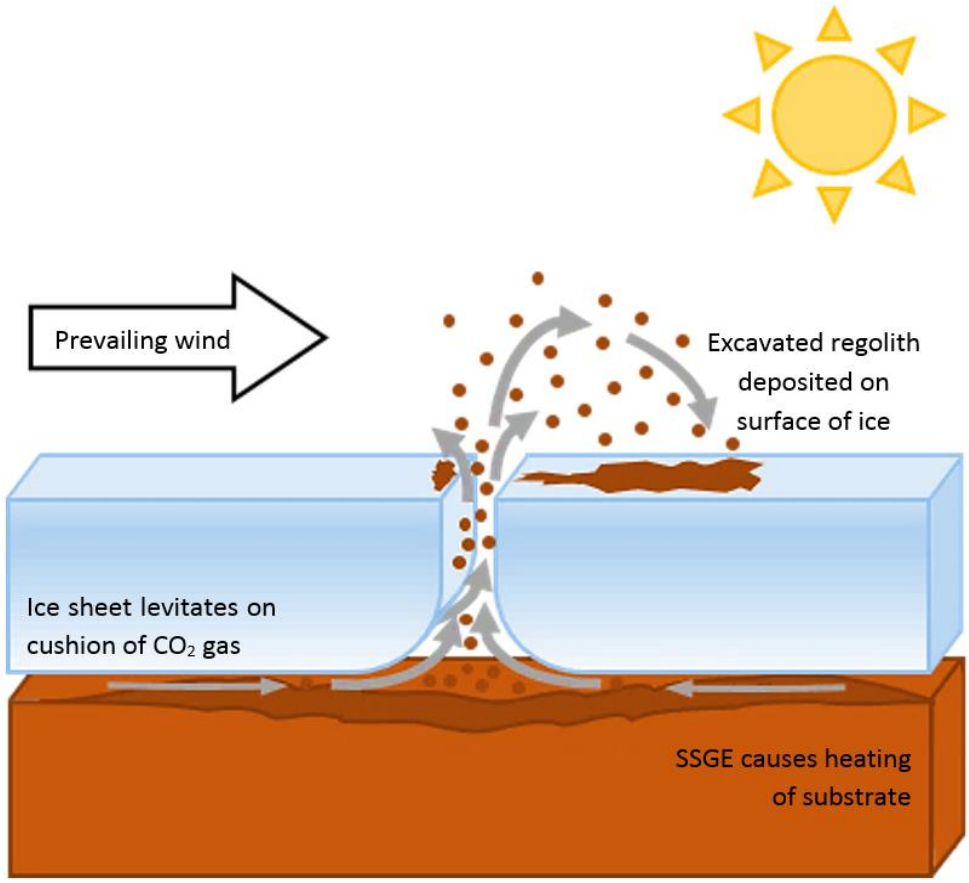

Figure 1.4.1. Schematic of the CO_2 jetting mechanism/Kieffer model which creates features such as spots and fans, and araneiforms (Kieffer et al. 2006).

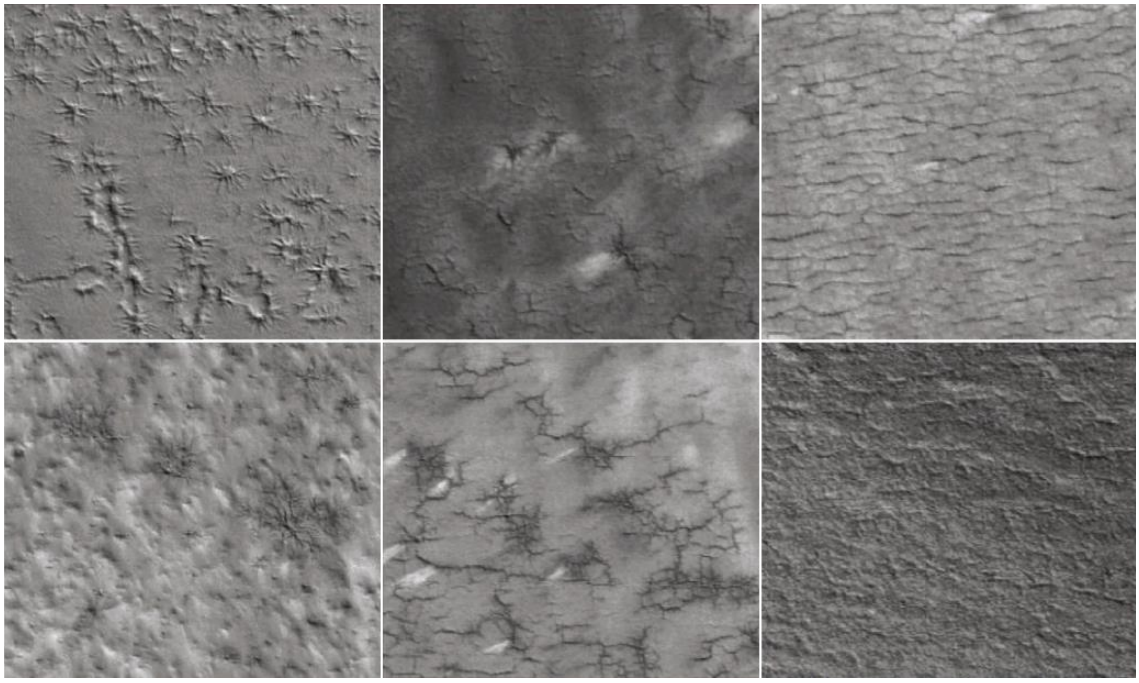

Figure 1.4.2. Araneiforms exhibit a range of morphologies, from individual, well defined central pits with radially arranged troughs branching out (e.g. upper left), to more densely arranged networks with no visible central pits (e.g. lower right), and everything in between (other images). CTX (The Context Camera onboard MRO) images from Schwamb et al. (2018).

each spring, and are thought to gradually carve bigger and deeper channels each consecutive year, whilst also adding new branches, via cold CO_2 jetting. Based on modelling by Piqueux and Christensen (2008), and estimations of current rates of erosion from several years of HiRISE (High Resolution Imaging Science Experiment) observations by Portyankina et al. (2017), it is thought that araneiforms are 1000 – 10000 years old.

Very similar in appearance to the spider formations of the southern hemisphere, northern furrows are theorised to form in much the same way. There are two main differences between these features. Firstly, they differ in scale: northern furrows are typically significantly smaller, typically only ~1.5 m wide (Bourke, 2013), whereas southern spiders can range up to a kilometre across (Portyankina et al., 2017). Secondly, whilst spiders form in the same locations year after year, furrows in the north are ephemeral, occurring in a seemingly random distribution each spring. They are observed as 'curvilinear furrows', which are both shallow and narrow at around 0.25 m deep and 1.5 m wide (Bourke and Cranford, 2011; Bourke, 2013). This is primarily due to the unconsolidated nature of the surface in this location, prone to high winds driving shifting sands during the ice-free summer, which exist as two main latitudinally constrained bands blowing in opposite directions (Bourke and Cranford, 2011; Bourke, 2013; Portyankina et al., 2017). These have now been observed over 95% of the northern polar dunes, in addition to a band across the southern hemisphere running from 40°S to 72°S (Nash and Bourke, 2015). By their ephemeral nature, it is clear that the creation of northern furrows is on-going in the present, but it has now been directly detected that southern spider formation is also active today. Portyankina et al. (2017) showed, by monitoring HiRISE images of the polar areas over several Martian years, and new dendritic troughs have been created during this time period. These are similar in morphology to the northern dendritic furrows, and are described as shallow branching troughs approximately 1.4 m wide. However, consistent with the typical southern spider regime (rather than the northern ephemerality), these persist throughout the year, and grow by extending and developing new tributaries, gradually becoming more spider-like over time. The locations of many of the new dendritic troughs are in the vicinity of dunes, highlighting the requirement for unconsolidated regolith to at least initiate the formation process.

An extensive study by Schwamb et al. (2018) utilised online citizen science (project Planet Four: Terrains/P4T) to identify araneiforms, Swiss Cheese terrain (discussed later in Section 1.6), and craters using images from the Mars Reconnaissance Orbiters' (MRO) Context Camera. This is the most extensive study made to identify these features, and has shown that araneiforms can be found not only in the SPLD (although 75% of them were), but also in the Early Noachian highland unit, and the Amazonian and Hesperian polar units. The distribution of araneiforms and furrows across different geological units show that they are not specific to only one specific geological

setting, but could occur anywhere there is a sufficient supply of unconsolidated regolith, the correct conditions for a CO_2 ice slab to form, and incident energy supplied to cause basal sublimation.

Few experimental investigations have been conducted in order to replicate araneiform type features by induced gas jetting. One such experiment was conducted by de Villiers et al. (2012), during which the authors found that they were able to create similar patterns in unconsolidated granular material using pressure-gradient driven gas flows, with a singular central venting point. This included straight channels, braided channels and quasiperiodic sinuous channels (distinctly different from fluvial meandering channels seen on Earth), which formed converging dendritic patterns similar to those of araneiforms. In different experiments, looking at the potential for insolation driven dust ejection from CO_2 ice, as in the process of depositing the dark fans associated with araneiforms, Kaufmann and Hagermann (2017) used blocks of translucent CO_2 ice with a layer of Mars analogue JSC Mars-1A within the ice to run laboratory simulations in an attempt to recreate this process on a small scale. The experiments were conducted in a Mars simulation chamber under approximately Martian pressure and temperature conditions (5.3 mbar, with the base plate cooled to 150 K). Several different grain size ranges of the simulant were used, and the samples were irradiated with a broad-spectrum solar simulator lamp of intensity 650 Wm^{-2}. They successfully managed to create dust eruptions from the layer within the CO_2 ice, although specific temperature and pressure conditions had to be maintained, namely close to the conditions of phase change. They also found that dust eruptions are likely limited by the grain size of the dust, and by the density and transparency of the overlying ice. The dependency on grain size, and by extension the availability of unconsolidated regolith to begin with, could be one of the underlying reasons to explain why araneiforms seem to be constrained within the SPLD.

However, in order to model this phenomenon with the best approximation to reality, the extent of the SSGE in translucent CO_2 slab ice needs to be quantified, therefore giving clues to the translucency required for this process to occur.

1.5. Gullies

Geologically young (less than a few million years old) gully features were first observed by the Mars Orbiter Camera (MOC) on board the Mars Global Surveyor in 1999 (Malin and Edgett, 2000). These landforms were named gullies due to their resemblance to terrestrial ‘spur and gully’ morphologies which form as a result of liquid water-driven debris flows. They consist of tapered channels which transport material from an upslope alcove to a downslope depositional apron, sometimes accompanied by secondary channels (example in Figure 1.5.1). Classic Martian gullies can span several kilometres in length, and up to 1 km across in the alcove zone, and are found

across the 30° - 50° latitude range in both hemispheres, mainly located on poleward facing slopes (Balme et al., 2006; Dickson et al., 2007; Heldmann, 2005; Heldmann et al., 2007; Heldmann and Mellon, 2004). The southern winter solstice occurs when Mars is almost at aphelion, and so austral winters are longer and colder than boreal winters. Observations show gully activity is greater in the southern hemisphere (Dundas et al., 2015) which implies the formation mechanism is at least linked to seasonal cycles, insolation cycles and/or atmospheric processes.

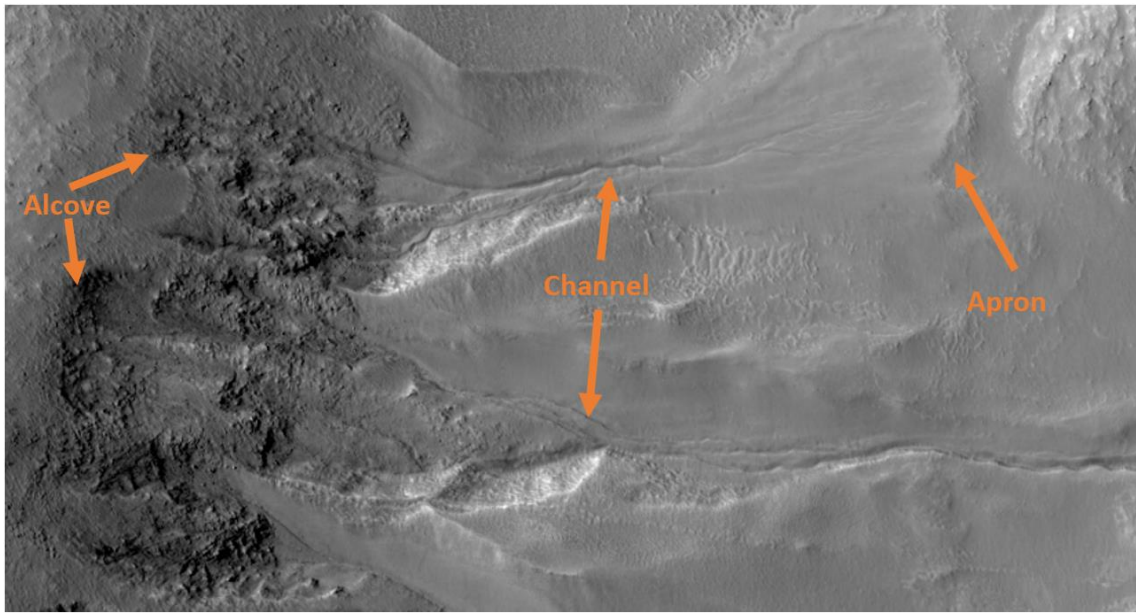

Figure 1.5.1. Example of a 'classic' Martian Gully, with alcoves (left side), channel and apron (best example in upper right), in Copernicus Crater, 48.7° S, 193.7° E. Upper gully approx. 1.5 km long. HiRISE image ESP_039621_1315, Image credit NASA/JPL/University of Arizona.

Consequently, gullies have been attributed to ground water seepage and surface runoff, thus giving indirect evidence of liquid water on the surface of Mars, sourced on subsurface aquifers (Carr, 2006; Malin and Edgett, 2000; Mellon and Phillips, 2001). The temperature and pressure range on the surface of Mars today means conditions are below the triple point of water, and thus it can only exist as ice or vapour at the surface, as explained in section 1.1. To enable liquid water, some studies have invoked geothermal heating of permafrost (Hartmann, 2003; Hartmann, 2001) to generate short-lived, subsurface liquid water flow, whilst others have suggested brines (e.g. Knauth, 2002). However, the presence of gullies on dunes and other high ground means that geothermal-driven melting and aquifers are unlikely to be present (Dundas et al., 2017). It has also been suggested that gullies were formed in the past at higher obliquities, meaning higher atmospheric pressures to allow for insolation-driven melting of snow or subsurface ice (e.g. Costard et al., 2002; Hartmann, 2003; Hecht, 2002; Lee et al., 2001). But these features are active today, with changes and new flows having first been observed by MOC (Malin et al., 2006), which were later found to be occurring seasonally (Dundas et al., 2010; Harrison et al., 2009) and so, even if this

was an explanation of gully formation in the past, it does not explain the observations of activity today.

On the other hand, gullies could be created by an alien process, not requiring water at all. Musselwhite et al. (2001) suggested that liquid carbon dioxide could accumulate to form an 'aquifer' below a CO_2 ice cap/barrier. However, this seems highly unlikely to occur on dune slopes and isolated peaks, due to the very high pressures required to liquefy CO_2, even with the inclusion of clathrates in the system. Initial suggestions of purely dry granular flows with no volatile component (Shinbrot et al., 2004; Treiman, 2003), or with CO_2 ice/frost involvement (Hoffman, 2002; Ishii and Sasaki, 2004), were generally discounted due to the strong resemblance of these Martian gullies with terrestrial counterparts. However, once the timing of gully activity was correlated with the presence of seasonal frosts, these theories began to be expanded upon. Due to such small sources of available water, surface frosts are likely to be only <200 µm in thickness (Vincendon et al., 2010a), and so the involvement of CO_2 frosts in gully formation is more likely, due to the higher prevalence across the surface (Piqueux et al., 2016), especially across the gully forming latitudes (Pilorget and Forget, 2016).

There are several subsets of gullies, including Linear Dune Gullies and Recurrent Slope Lineae (RSL), in addition to the 'classic' gully already described. These vary in terms of scale, morphology and location, and therefore are likely involve a combination of different formation mechanisms. RSL are narrow (0.5 – 5 m in width), dark, linear features on the surfaces of steep (25° – 40°) slopes (McEwen et al., 2011). Activity on RSL is greatest during the warmest seasons, with repeat images from HiRISE showing them to grow in length during late spring and summer and gradually fade over winter, which is contrary to other types of gully activity (McEwen et al., 2011; McEwen et al., 2014). Due to this, it is unlikely that these features are associated with surface ices, and so are not a focus of this study.

One suggested mechanism for gully formation is shown in Figure 1.5.2, which utilises the same concept as the Kieffer model of araneiform creation (the CO_2 jetting model driven by the SSGE). This was proposed by Pilorget and Forget (2016) who generated a model of this scenario, the results of which suggest it capable of triggering mass movements.

In Figure 1.5.2., step a) shows a dune or crater rim in spring, with solid CO_2 slab ice covering the surface. As insolation increases, subsurface heating occurs, triggering basal sublimation leading to cold CO_2 jetting (step b). However, as this is occurring on a slope, the CO_2 ice which has ruptured now slides downhill as a debris flow, carrying regolith material with it. Having reduced the thickness of regolith over the subsurface, the permafrost-like ice-cemented regolith is less insulated and begins to sublimate (step c). This continues until there is enough ice-free regolith to sufficiently

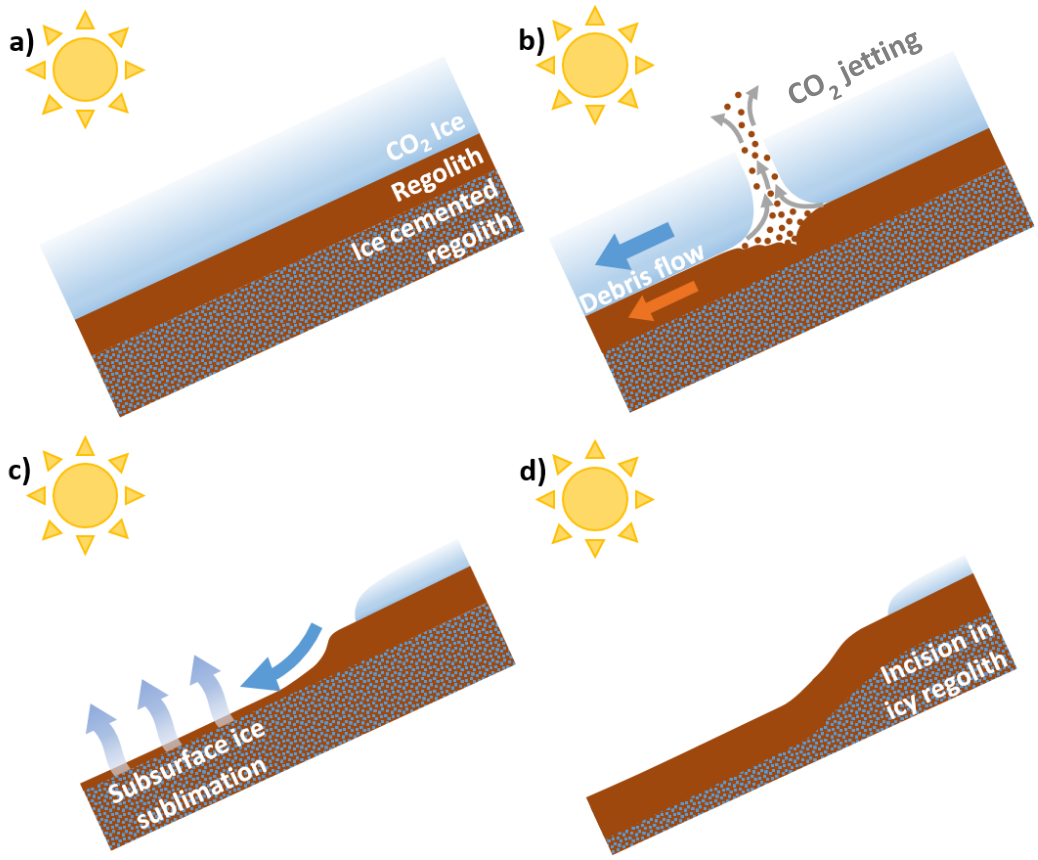

Figure 1.5.2. Formation mechanism of gullies as proposed by Pilorget and Forget (2016), invoking the SSGE in overlying CO_2 slab ice, warming the underlying regolith and triggering debris flows by destabalising the subsurface.

insulate the underlying ground ice, creating a surface 'lag'. The unconsolidated regolith can then be removed by wind and gravity, and as a consequence, the ground level is reduced which eventually forms an incision slope, creating a gully-like feature (step d). This seems to be the most likely cause of gullies at higher latitudes, due to the coverage of the seasonal ice cap and CO_2 slab ice, to around 50° latitude, but less plausible in lower latitudes, as the CO_2 deposits as porous frost on the surface, which is not conducive to sub-ice pressure build up (Dundas et al., 2017).

Gas-suspended fluidised granular flows are also theorised, as first proposed by Hoffman (2002), who modelled a CO_2 gas lubricated flow of clastic debris as the formation mechanism of the channel features observed in Sisyphi Cari, which can be up to 1000 m deep. These features are located at 71°S, which is within the polar region of the seasonal CO_2 ice cap where conditions are too cold for previous theories of water fluidised flows to be plausible. Cedillo-Flores et al. (2011) evidenced the potential of this mechanism, by computing diurnal and seasonal temperatures through a Martian year, including the condensation and sublimation of CO_2 using MARSTHERM, a one-dimensional finite difference thermal model. They ran the model both with no sediment covering CO_2 ground ice, which had been emplaced by CO_2 migrating into the regolith pores and

condensing, and with sand and dust coverages ranging from 0.01 mm to 10 mm in thickness. The results showed that during spring, enough solar energy reached the subsurface ice layer to sublimate the CO_2 and fluidise the overlying sediment.

The first laboratory experiments utilising CO_2 frost condensed onto unconsolidated regolith, which was then allowed to sublimate under Martian atmospheric conditions, were undertaken by Sylvest et al. (2016). These experiments showed that CO_2 frost (which deposits both in-between grains and on top of the regolith) when sublimated, is able to cause mobilisation and trigger mass wasting in dry granular flows. Further laboratory experiments by Sylvest et al. (2018) showed that activity is observed even at very low slope angles, near the angle of repose, and the authors suggest this could occur for even shallower angles when under Martian gravitational conditions. Movement occurred as four discrete types, which were controlled by variations in grain size, regolith type, and slope angle: discrete flows, creep, gas entrainment and grain tumbling. This lends further evidence to CO_2 frost sublimation as a formation mechanism, given the diverse range of gully morphologies observed. However, the point at which this is triggered would be dependent upon, in part, how translucent the CO_2 frost is to solar radiation. When CO_2 ice is present on the surface, it buffers surface temperatures to the frost point, and so the subsurface will warm first due to incident insolation, raising the temperature from beneath the frost. This will be controlled by the penetration depth of that frost, which is specific to both ice composition and grain size.

Linear gullies are quite distinct in appearance, with no terrestrial analogues, and have been located between 36.3° S and 54.3° S on polar and intra-crater dunes (Pasquon et al., 2016). Figure 1.5.3 shows the characteristic morphology of linear dune gullies, with consistent gully width (typically ~10 m, sometimes narrowing downslope) along their length, which can range from a few hundreds of metres to around 2.5 km, and are bounded by raised levees on either side (Diniega et al., 2013). Incisions are shallow, typically 1 m – 2 m (occasionally up to 3 m), getting shallower as the slope levels out near the base of the dune (Jouannic et al., 2012). Their activity is seasonal, constrained to the end of winter and beginning of spring, in direct correlation with the final stages of CO_2 ice sublimation across the region (Pasquon et al., 2016).

Unlike ‘classic’ Martian gullies, linear gullies do not have associated debris aprons at the bottom on the slope, but instead a ‘terminal pit’ (or multiple pits) is often observed (note the speckled terrain just visible in the lower left of Figure 1.5.3. The main hypotheses of formation for linear gullies was proposed by Diniega et al. (2013), who suggest that blocks of defrosting seasonal CO_2 slab ice break off at the apex of dunes, and slide downslope, buffered by basal sublimation from the block of CO_2 ice (shown in Figure 1.5.4). This is similar to the Leidenfrost Effect (Leidenfrost, 1966), which describes the process which occurs when a colder liquid or solid comes

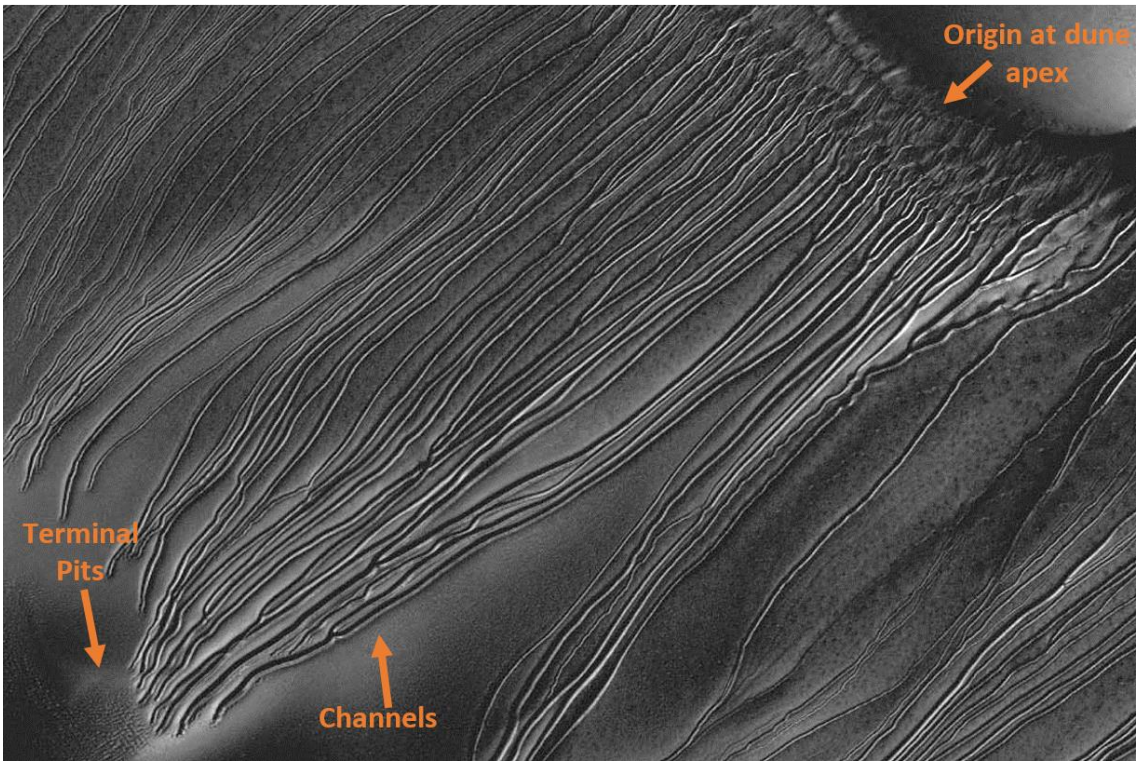

Figure 1.5.3. HiRISE image (PSP_001440_1255) of linear dune gullies at 54.25° S, 12.92° E, on the slope of a large dune in Russel Crater. Image credit: NASA/JPL-Caltech/Univ. of Arizona.

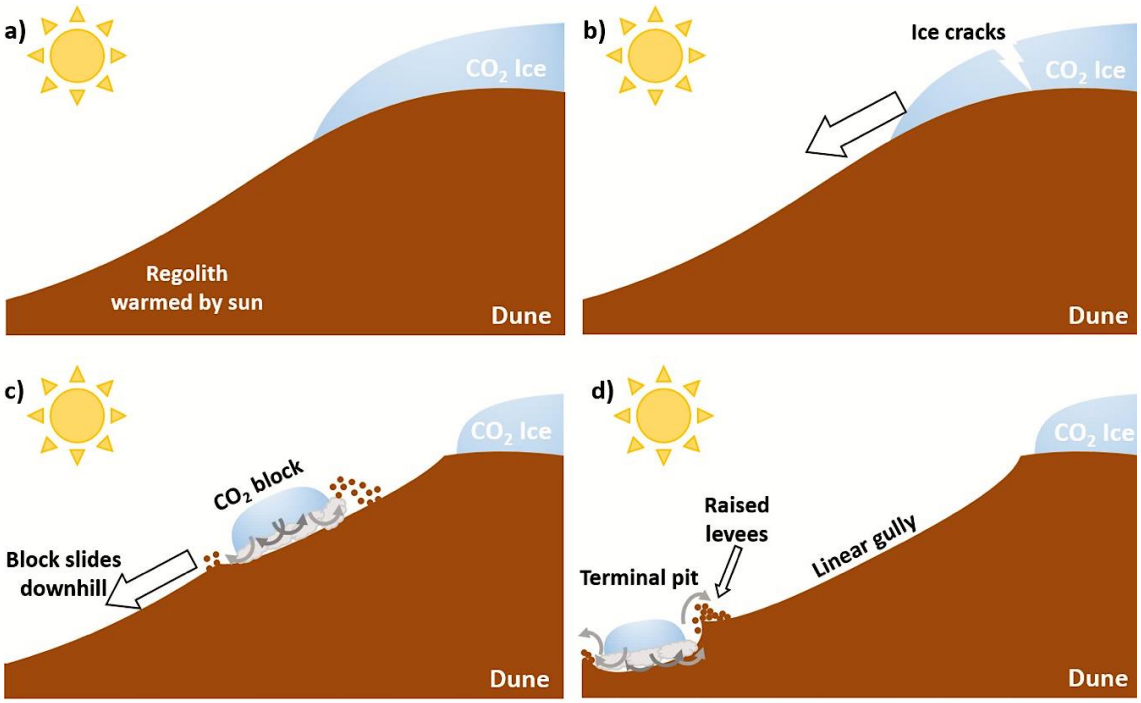

Figure 1.5.4. Proposed formation mechanism of linear gullies with associated terminal pits, as per the theory in Diniega et al. (2013).

into contact with a much warmer substrate (significantly above the sublimation or boiling point), causing the cold object to levitate on a cushion of gas when the pressure exerted by the released gas is greater than the weight of the object. The gas cushion significantly reduces, or entirely removes, friction from the block moving over the regolith, enabling it to slide down shallow slopes of even only a few degrees (Mc Keown et al., 2017). The diagram in Figure 1.5.4 depicts this process, where surface regolith is warmed by the sun (a), then, during defrosting, blocks of ice can break off and slide onto the warmed regolith (b). The rapid basal sublimation caused by contact with the warm surface results in the CO_2 ice blocks to carving out channels as they move downslope (c). When the block eventually come to a halt at the bottom of the slope it will continue sublimating, gradually burrowing down in one spot, until completely sublimated (d). This final sublimation phase forms the terminal pit, and it is suggested that multiple pits could be formed simply by the CO_2 block breaking up, which is entirely plausible by the block hitting a rock, or if it shatters due to thermal expansion, as demonstrated during field tests of sliding CO_2 blocks down dune slopes in Utah by Bourke et al. (2016).

Mc Keown et al. (2017) conducted laboratory experiments in an attempt to simulate this process. Using solid blocks of CO_2 ice placed on warm, unconsolidated regolith simulant, they recreated terminal pits, where the sublimating CO_2 block excavated a depression, depositing the material to form raised levees around it. Whilst this linear gully formation is ultimately caused by basal sublimation of a mobile block of CO_2 ice moving over warmer, ice free regolith, in order to understand initiation of this process, the timing and causation of the block break off in the first place, it is vital to know about the thermal and optical properties of CO_2 slab ice, coupled with atmospheric conditions and insolation levels during this time.

1.6. Swiss Cheese Terrain

Unusual looking surface terrain observed in the southern polar region, colloquially called ‘Swiss Cheese’, is composed of a combination of troughs, mesas, quasi-circular flat bottomed pits and other lobate depressions, as seen in Figure 1.6.1. Features can range in size from a few hundred metres to more than a kilometre in diameter, although they appear to have a relatively consistent depth of approximately 8 m, based on shadow analyses (Thomas et al., 2000). The depression walls tend to show light and dark striations 1 m – 2 m in thickness, and a general trend of less circular shapes occurring with latitude, indicating a connection with insolation and their formation (Byrne and Ingersoll, 2003).

Swiss Cheese terrain features are observed solely on the SPRC, which is the only place where CO_2 ice is exposed year round, covering an area greater than 80,000 km^2 (Thomas et al.,

2013; Thomas et al., 2009; Thomas et al., 2005). They are characterised by higher albedo CO_2 ice which has been highly eroded over time, ranging from 2 m to 10 m in thickness (Byrne and Ingersoll, 2003; Thomas et al., 2000), but with the total ice coverage of the residual cap fluctuating year on year. Malin et al. (2001) reported that the walls of the depressions can expand at rates of 1 m to 3 m per year, indicating this is a process involving CO_2 rather than H_2O due to its higher volatility. The model developed by Byrne and Ingersoll (2003) which successfully reproduced some of the typical features and topography of the Swiss Cheese terrain, and matched it with temperature measurements made by THEMIS, which showed that during summer, the floors of the depressions covered by their data could not be CO_2 ice due to temperatures being too high, and so support a structure of H_2O ice underlying an approximately 10 m thick CO_2 ice layer which is gradually being eroded.

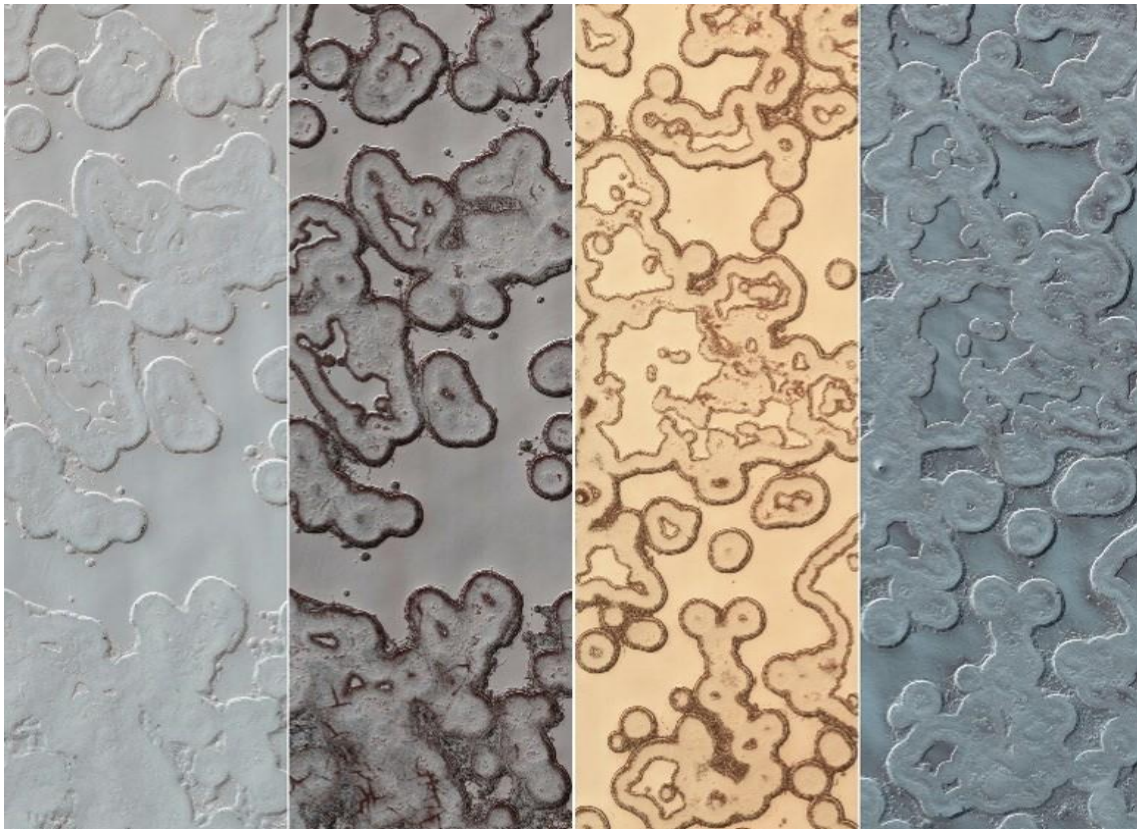

Figure 1.6.1. An example of 'Swiss Cheese' terrain, which consists of shallow pits where carbon dioxide ice has sublimated away. Images taken by MRO, from left to right, on: 03/2013, 05/2013, 09/2007, and 12/2012 over approximately the same area. Image credit: NASA / JPL / UA.

The 'citizen science' powered study by Schwamb et al. (2018) mapped the distribution of different surface features at high latitudes on Mars, and found that there was no location where araneiforms and Swiss Cheese terrain occurred together, and almost all identification of Swiss Cheese terrain was within the SPRC, confirming their previously mapped distribution. This is indicative of Swiss Cheese features and araneiforms occurring due to differing physical

compositions and settings – likely that araneiforms only occur where there is no H_2O ice present, and Swiss Cheese requiring CO_2 ice to be layered on top of H_2O. Especially important for CO_2 ice which survives throughout summer is accurate knowledge of how the CO_2 ice deposits interact with incident sunlight over time. This includes how the ice changes in response to the high insolation levels of the summertime, and other erosional processes which cause the ice to weather and break up or be contaminated by water ice and dust. All these individual factors would help piece together how this terrain evolves over time. Also, determining the difference in penetration depths between water ice and carbon dioxide ice, in both slab form and granular/highly cracked and eroded ice is vital for providing well-informed formation models. Thomas et al. (2009) concluded that there is currently no good explanation for the formation of these features seen in what they called the 'Escher terrain', due to the apparent counter-intuitive nature of the stratigraphy based on their interpretation. It is now mainly referred to as Swiss Cheese Terrain. Brown and Matson (1987) observed an increase of the water ice signature on the SPRC using data from the Compact Reconnaissance Imaging Spectrometer for Mars (CRISM) on board MRO. Based on their model, Brown et al. favoured the hypothesis that this is due to direct deposition of water ice onto the SPRC due to cold trapping (conditions for which are likely based on GCM models), but cannot rule out the possibility of this either being due to sublimation of CO_2 and subsequent exposure of underlying water ice, or being due to the deposition of water ice particles condensing within a CO_2 sublimation stream.

1.7. Beyond Mars

Volatile ices are found in abundance throughout the solar system. Whilst Mars is the only body on which CO_2 clouds have been observed (Herr and Pimentel, 1969; Montmessin et al., 2007), CO_2 ice is thought to occur on icy satellites throughout the outer solar system (e.g. McCord et al., 1998) and the interstellar medium (Chiar, 1997). CO_2 ice is one of the major constituents of cometary nuclei but is not usually observed at the surface due to its volatility on exposure to irradiation (Filacchione et al., 2016). The SSGE is a major influencer in the structure and composition of a comet's nucleus, causing highly volatile materials, such as CO_2 and CO, to migrate deeper towards the centre of the nucleus, leaving less volatile ices, such as water, near or at the surface (De Sanctis et al., 2006). However, Filacchione et al. (2016) observed surface CO_2 ice deposits on the surface of comet 67P/Curyumov-Gerasimenko using the infrared spectrometer on board the Rosetta spacecraft, as the comet was coming out of its 'winter' period, which disappeared over the course of around 3 weeks of increased insolation levels. Around 6 weeks after the initial detection of surface CO_2 ice, H_2O ice was detected in the same location, suggesting that the presence of

surface CO_2 is an ephemeral occurrence. The fact that the region was particularly well shadowed suggests that, when no longer exposed to irradiation, the area cools quickly which enables condensation of CO_2 ice whilst the nucleus is still warm, due to low thermal inertia of the material (Choukroun et al., 2015), and so CO_2 continues to sublimate at depth and is redeposited at cold traps on the surface. With an accurate understanding of the penetration depth of solar radiation in ices present in comets, the thermal regime of exposed ices at the surface, and the underlying stratified layers of different ices could be better modelled and understood. Knowledge of solid or slab ice might be insufficient, as comets are highly porous, and so treating the ice as a granular material may be more applicable. Comets contain high proportions of carbon, in addition to many other substances, and so being able to understand the effect of each individual component is important to be able to build up the big picture of what is happening inside a comet.

Geyser-like eruptions that reached an altitude of 8 km above the surface of Triton, Neptune's largest satellite, were observed by Voyager 2 in 1990. With an ambient surface temperature of 38 ±3 K, it was suggested that the geysers were the result of subsurface heating caused by the SSGE in nitrogen ice on the surface (Soderblom et al., 1990). In their study, Soderblom et al. suggest that it would only require an increase of 4 K in order to generate geyser–like activity. Other ices detected on Triton's surface include methane, carbon monoxide, and carbon dioxide (Brown et al., 1995). Whilst the experimental measurements presented in later chapters of this thesis only focus on water and carbon dioxide ices, this is an example of how important it is to obtain measurements of the penetration depth of the full range of different ices which naturally occur in the solar system.

Chapter 2

Theoretical & Experimental Background

This chapter details the laws governing light propagation in translucent media, both as solid slabs and as granular materials which are scattering and absorbing. The process of snow metamorphism, specifically 'sintering', is described in Section 2.1. This is an important factor to consider, firstly, for minimising sintering rates during experimental work involving snow and granular ice (especially for carbon dioxide ice), and secondly, as a formation mechanism for larger granular carbon dioxide ice deposits on Mars. The key points of the underlying optical theory applicable to this work are given in Section 2.2, and other associated phenomena, such as the optical properties of water and carbon dioxide ices (discussed in Section 2.3), are described and the implications for the measurements in this and any other work with ices are discussed. This is followed by an account of previous light penetration measurements in ices and snow in Section 2.4, with a discussion of the conclusions drawn from them, weighing the pros and cons of their methods and their applicability to this body of work.

2.1. Ice Sintering

Ice is a crystalline solid phase of a volatile species. Ices are distinguished from rocky material on a planetary surface by their comparatively low density, low melting point and their optical properties, particularly their transparency in the visible range (Eluszkiewicz et al., 1995). When discussing ice, we typically think of water ice as this is what occurs naturally on Earth. Water ice has as many as 13 known crystal structures, but almost all naturally occurring ice has a hexagonal crystal structure – I_h (Blackford, 2007). The exception to this is found in the upper atmosphere, where I_c ice (a metastable cubic structure) forms, but only at temperatures below -80°C. Warmer than this, it reverts back to I_h. However, due to the low temperature and pressure conditions on Mars, water ice freezes as a metastable stacking disordered form, I_{sd} (Malkin et al., 2015; Murray et al., 2015a), which is made up of cubic and hexagonal sequences, creating crystals with 3-fold symmetry, as opposed to the typical terrestrial six-fold symmetry of hexagonal ice (Murray et al., 2015b). Crystal shape is important because it influences crystal fall speeds, growth rates and optical properties (Mangan et al., 2017). Foster et al. (1998) showed that the extinction, adsorption and scattering efficiencies in the IR are sensitive to crystal shape. It is thought to be unlikely that CO_2 forms dendritic structures under Martian conditions as this only happens when crystal growth becomes diffusion limited (Mangan et al., 2017). Whilst the crystal lattice formed is cubic, it is possible for a range of crystal shapes to form, depending on the relative growth rate of the groups of crystal faces. This means that the crystal structure can range from cubic to octahedral.

Sintering is the process of grain growth and densification in order to achieve a thermodynamic state of minimum surface energy. It can occur in almost any granular material under the right conditions, and is vital in different processes, ranging from firing pottery, the fabrication of powder metallurgical parts (Kang, 2005), and volcanic ash deposits to form tuff lithologies. Sintering processes can be split into four types: liquid phase sintering, solid state sintering, transient liquid phase sintering and viscous flow sintering. Transient liquid phase sintering could be an important factor when considering sintering of snow on Earth, but due to the pressure and temperature conditions on Mars, it is unlikely to be relevant. Therefore, for the purposes of this work, only solid state sintering is considered, as I am specifically focussed on the processes occurring in ices on Mars. Terrestrial water ice occurs naturally in many different morphologies which vary in density. This ranges from fresh snow, which varies in density from 80 kg m^{-3} to 200 kg m^{-3}, and porosity of 80% – 90% (Blackford, 2007; Heki, 2004), to first year sea ice densities typically range from 840 – 910 kg m^{-3} for ice above the waterline (Timco and Frederking, 1996). The process of sintering can cause the transition from a low density state (snow) to high (glacial ice).

Swinkels and Ashby (1981) divide the sintering process into four stages, and whilst their work was focussed on the sintering process for metallurgy, the concepts are very similar, and their model has been used as a starting point for the modelling of water ice sintering (Molaro et al., 2019). Sintering starts at Stage 0: at the point of grain contact, adhesion occurs via interatomic forces, creating an initial neck. Stage 1 sees neck growth via surface and volume diffusion (see Figure 2.2.1) until the necks reach around 0.5 – 0.8 times the grain radius. The rate of neck growth decreases as mass is redistributed to form spherical pores between grains, and whilst some densification occurs at this stage, it is not yet a dominant effect. Stage 2 is the transition from a geometry of individual grains to the point at which it is difficult to distinguish the individual geometries, and can no longer be deemed an aggregate. Stage 3 is dominated by densification of the now solid but porous slab of ice, causing pore shrinkage and therefore volume reduction. This final stage occurs over a much longer timescale compared to neck growth time frames. These stages occur via six microscopic mechanisms: surface diffusion from a surface source, lattice diffusion from a surface source, vapour transport from a surface source, grain boundary diffusion from a boundary source, lattice diffusion from a boundary source, and lattice diffusion from dislocation sources (Eluszkiewicz et al., 1995); all of which can be seen in Figure 2.2.1.

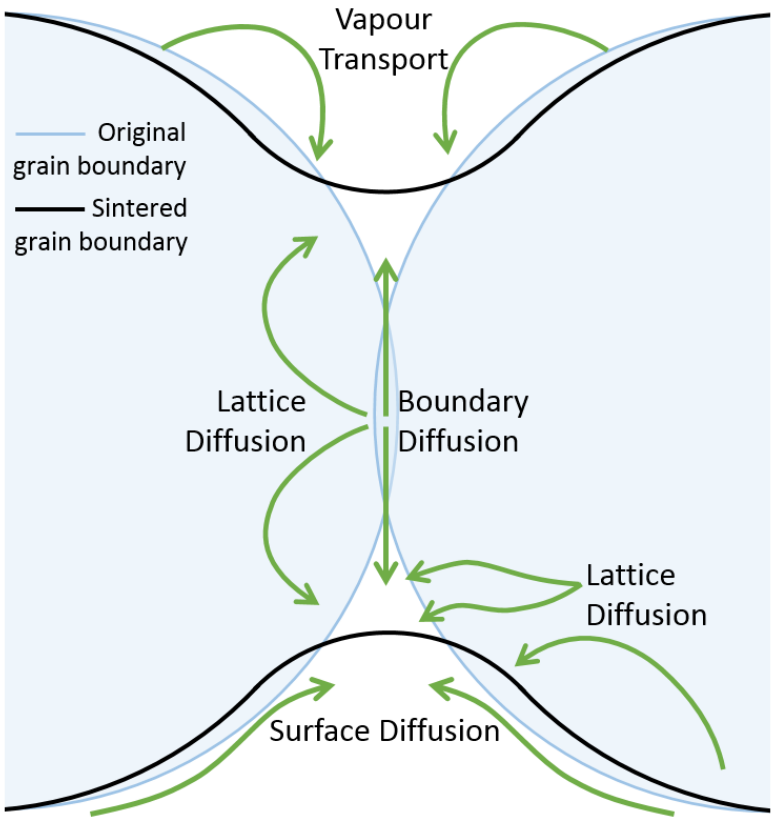

Figure 2.1.1. A range of different mechanisms contribute to the process of sintering, and one or more may be occurring at the same time, with others being dominant at different stages of the process.

The Swinkels and Ashby (1981) model has been adapted and modified to be applied specifically to ice. Explicitly important for snow metamorphism is grain growth due to vapour diffusion driven by a temperature gradient (Gubler, 1985), but the Swinkels and Ashby (1981) model has formed the basis for many models used to predict the effects of sintering on other planetary bodies, such as Mars, Triton, Pluto, comets, etc. (e.g. Eluszkiewicz, 1991; Eluszkiewicz, 1993; Eluszkiewicz et al., 2005; Kossacki, 2015; Kossacki et al., 2015; Schaible et al., 2017). Most recently, Molaro et al. (2019) analyse the application of this model for water ice sintering and find it accurate to within an order of magnitude for predicting neck growth rates. They also stress that sintering rates are extremely sensitive to both temperature and grain size, with sintering rates fastest at temperatures close to the frost point and with the smallest grains.

There are many other ices which undergo sintering and are found throughout the solar system. Metamorphism is likely to occur slightly differently under different environments: on Earth, air is present between the ice grains which can enable heat transfer via convection (which cannot occur in a vacuum, and there is often a liquid water phase present, which is simply not the case on many airless bodies or those with much less dense atmospheres (Eluszkiewicz et al., 1995). This highlights the need for further experimental work studying sintering under low atmospheric pressures with good thermal control, in order to understand more about how these processes occur elsewhere in the solar system. As the work of this thesis focusses specifically on the icy processes occurring on Mars, the emphasis is primarily on the sintering of carbon dioxide ice.

The Kieffer model for CO_2 jetting (Kieffer et al., 2000; etc. see Section 1.4 for details) requires the presence of a solid impermeable layer of CO_2 slab ice. If CO_2 snow fall makes a considerable contribution to the seasonal ice sheet, sintering must be occurring for this to form the continuous, low albedo ice slab, as observed in the spring. On Earth, freshly fallen snow has a density ranging from 80 kg m^{-3}- 200 kg m^{-3}, which gradually increases in density to around 500 kg m^{-3} (e.g. Blackford, 2007; Heki, 2004) through compaction and sintering. Smith et al. (2001) utilised topography data from MOLA collected over a Martian year correlated with changes in gravity measurements derived from MGS Doppler tracking residuals to estimate CO_2 snow density to be 901 ± 230 kg m^{-3}. However, Feldman (2003) modelled CO_2 deposit thicknesses based on neutron spectroscopy gamma ray spectrometer instruments aboard Mars Odyssey, which suggested that the density of the CO_2 snow deposits are significantly lower than initially thought. This was a realistic claim, as a density of 901 kg m^{-3} equated to porosity of approximately 58%, which is significantly lower than freshly fallen snow or newly condensed frost. Feldman (2003) goes on to suggest that a CO_2 deposit with a density which increases with time is much more consistent with their observations. Further work by Matsuo and Heki (2009), again comparing surface elevation with gravity data, shows that a fresh CO_2 snow deposit of density ~100 kg m^{-3}, which gradually

becomes denser, reaching ~1000 kg m^{-3} immediately prior to thawing, via gravity driven densification and sintering of CO_2 crystals, best explains the data. In the same study, the authors go on to say how, over their observation period of three winters, maximum CO_2 densities varied between years and between hemispheres. The highest CO_2 densities occurred in the southern winter after a global dust storm, which they hypothesised was the direct cause of the highest densities due to higher levels of dust being incorporated into the snow (simply as a result of incorporating the high density silicate particles) or by increasing the rate of sintering via increased heat flow.

All the evidence seems to suggest that sintering of CO_2 ice grains is an important process in the formation of the seasonal ice caps on Mars, and so needs to be considered when addressing light penetration into surficial deposits, including the effect on grain size and density of the ice/snow. In fact, Eluszkiewicz (1993) says that sintering and densification is most likely to occur in the seasonal ice caps of Mars, given that initial frost grain size is sufficiently small (<10 µm). This is based on analysis of the microphysical processes governing sintering at constant frost temperature under Martian conditions, with fixed low levels of contaminants. In reality, all of these factors could vary, increasing or decreasing the likelihood/extent of sintering, and perhaps influencing the grain size range over which sintering could occur. It is therefore important to have accurate measurements of the penetration depth of CO_2 ice deposits for all grain sizes, from the very finest snow/frost deposit, which is likely to undergo sintering, growing in grain size and density (therefore forming larger granular ices) until a continuous slab of CO_2 ice has formed. By knowing the penetration depth of broad spectrum solar radiation in the surface ice deposit at each step of this process, for a broad range of grain sizes, much more precise models can be developed to study the seasonal ice cap development and associated processes, such as CO_2 jetting and the formation of araneiforms.

2.2. Light Transmission and Scattering

Any attempt to determine a relationship between how far light penetrates into a medium, and how that penetration depth is affected by exact composition and grain morphology needs to take into account the underlying theory of light propagation in solid materials. In this section, the theory of light transmission and scattering is outlined, mainly using geometrical optics. The reasons for the use of geometrical optics over other optical theories (e.g. Mie theory) is explained. This theory is considered later in this thesis when attempting to derive a model which explains the experimental results of light penetration in slabs of ice, snow and granular ices of two different compositions, as presented in chapters 4, 5 and 6.

Electromagnetic waves propagating in a medium may be attenuated by both scattering and absorption in varying proportions. The extent of this attenuation is governed by the optical properties of that medium, which are described by the complex refractive index, m:

$$m = n + ik \tag{1}$$

Where n is the real part of the complex index of refraction, often just referred to as the refractive index, and ik is the imaginary part of the complex index of refraction, commonly known as the extinction coefficient. This equation defines what are often referred to as the 'optical constants', although this term is slightly misleading as both the refractive index (to a lesser extent) and the extinction coefficient (to a much greater extent) are often highly dependent on wavelength (Bohren and Huffman, 1983). The refractive index can be determined by the phase velocity v of a wave travelling through a medium relative to the speed of light in a vacuum, c:

$$n = c/v \tag{2}$$

and, therefore, governs the change in angle between the angle of incidence and the angle of refraction, as given by Snell's Law:

$$\frac{sin\theta_2}{sin\theta_1} = \frac{v_2}{v_1} = \frac{n_2}{n_1} \tag{3}$$

The imaginary part of the complex index of refraction, k, defines the attenuation experienced as a wave propagates through a medium. Beer's Law, sometimes known as the Bouguer-Lambert Law, states that the reduction in irradiance, I, with wavelength, λ (in energy per unit area and time) is exponential with distance travelled, z, through the medium which has an attenuation coefficient, α, as long as the material is homogenous and isotropic:

$$I(z, \lambda) = I(0, \lambda)\, e^{-\alpha z} \tag{4}$$

In materials which are linear, isotropic and homogenous, the attenuation coefficient is related to the extinction coefficient, κ, and as a function of wavelength λ, by:

$$\alpha = {}^{4\pi\kappa}/_{\lambda}. \tag{5}$$

In order to understand the principles behind light propagation in translucent media, the bulk optical properties of that material must first be determined. These are specific to the composition of that material and include the refractive index, and the reflection, transmission and absorption coefficients which describe the way in which light travels through a volume of a given material. However, light propagation is also affected by the nature of the interface between external and internal materials, and so grain size and shape will also have an effect. In materials which are birefringent, the angle between the plane wave polarisation and the crystal axis is also

required to fully define their optical constants (Hansen, 1997). Hexagonal water ice exhibits uniaxial birefringence, but, due to its cubic crystal structure CO_2 ice is optically isotropic.

Attenuation (or extinction) is comprised of both absorption and scattering (Bohren and Huffman, 1983). Generally, at visible wavelengths, extinction/attenuation is dominated by scattering in highly transparent materials as absorption is low. Therefore, attenuation by particles of said transparent material is quite different from that of the bulk solid. As long as particle size is larger than wavelength, then extinction dominated by scattering is virtually independent of photon energy, and therefore wavelength (Bohren and Huffman, 1983), as is the case in the study of snow and ice granules on a macro scale and therefore applicable to this thesis.

Scattering is a product of heterogeneity in a system, either at the molecular scale or accumulations of molecules (Bohren and Huffman, 1983). Regardless of scale, the underlying physics remains the same. Scattering occurs when an object is subject to incident electromagnetic radiation, which causes the electrical charges in the object to be set into an oscillatory motion due to the electric field of the incoming wave. Some of the energy is transformed into (for example) thermal energy, resulting in 'absorption', with the rest of the energy being radiated in all directions as electromagnetic waves, or 'dipole radiation', which is commonly called 'scattered' energy (Bohren and Huffman, 1983).

Everything except a perfect vacuum is heterogeneous. Materials which appear homogenous can be examined at the molecular scale and shown to in fact be heterogenous; therefore, all matter scatters light. Many phenomena associated with light are actually caused by scattering, even those not normally attributed to it, such as diffuse reflections by rough surfaces, diffraction caused by slits, gratings and edges, and specular reflection and refraction at optically smooth interfaces (Bohren and Huffman, 1983). Many materials, including solids, liquids and many gases, are optically dense, meaning that the molecular separation is much less than the wavelength of incident light. As a consequence, each molecule within a medium is acted upon by both the incident and the resultant re-radiated energy from other molecules around it. The net outcome of this is for secondary waves to superpose on both each other and on the incident wave, resulting in a refracted wave. The incident wave is completely attenuated inside the medium, and the refracted waves outside the medium superpose to give a specularly reflected (i.e. at a single angle, as opposed to 'diffuse' reflection over a range of angles) wave. This collective process is called Ewald-Oseen extinction theory. As per Eq. 2, the propagation velocity of the refracted wave is dependent on the speed of light in a vacuum and the refractive index. The refractive index is determined by the polarisability of each molecule and the number of molecules per unit volume. It is therefore variations in molecular density, concentration fluctuations (such as stirring sugar into water), or

orientation fluctuations (in materials with non-spherical molecules), which cause observable scattering, rather than just purely refraction.

When discussing scattering phenomena, it is important to note the type of scattering being discussed, whether it is scattering by molecular fluctuations or by particles on a macro scale. The former involves thermodynamic principles, tends to be on a much lesser scale than the latter, and is not the focus of this work. There are further sub-categories of scattering, such as elastic scattering, which occurs when light is scattered with no change in wavelength, as opposed to inelastic, where wavelength is altered, such as in Raman scattering (e.g. Long, 2002).

Optical constants for a bulk material are not directly measurable, and so must be calculated from measurable quantities. This often involves experiments measuring light transmission through the material. Figure 2.2.1 demonstrates how a beam of light I_i is incident on an optically smooth slab of translucent material (meaning that surface roughness must be sufficiently small compared to the wavelength of the incident light). A proportion of the light is reflected, (reflectance R) at the first interface and the rest of the light enters the slab and is attenuated by a factor of $e^{(-\alpha h)}$ (where h is slab thickness, and α is the absorption coefficient). At the second interface the light is exiting the slab, at which point some of the light is again reflected, with the rest transmitted out of the slab. The process continues indefinitely, yielding an infinite series which can be summed to give the transmission through the slab, T_{slab}, to give Eq. 6:

$$T_{slab} = (1 - R)^2 \, e^{-\alpha h} \tag{6}$$

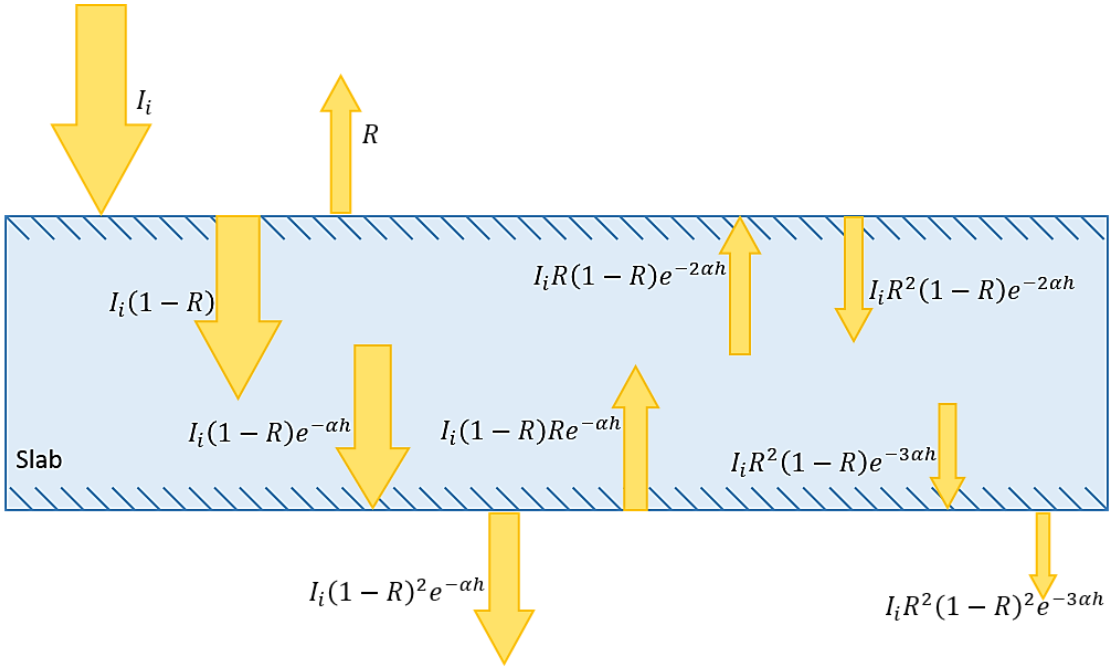

Figure 2.2.1. The transmission of incident light in a slab which is translucent, homogeneous and isotropic, where $\boldsymbol{I}$= irradiance, $\boldsymbol{R}$= reflectance, $\boldsymbol{h}$ = slab thickness, and $\boldsymbol{\alpha}$ = absorption coefficient The series continues until all the energy from the incident beam has been attenuated, although only the first two components are shown here.

When light is instead shone on a collection of particles, the complexity of the light's propagation through that medium is greatly increased. The way in which light propagates is dependent upon the shape, size, and composition of the particle, in addition to its proximity to surrounding particles. There are different theories of light scattering by particles, depending upon the ratio of particle size to wavelength. Mie theory describes the behaviour of light scattered by a homogenous, isotropic spherical particle embedded in a non-absorbing medium (Mie, 1908). Mie theory is only applicable when grain size is similar to the wavelength of the incident light, and is used in many different fields of applications where the particle size can be approximated to meet this criteria, including studying interstellar dust, near-field optics, plasmonics and optical particle characterisation (Wriedt, 2012). Adaptations have been made to Mie's original theory in order to account for the particles to be within an absorbing medium, and there are now a large range of algorithms and programs which utilise Mie Theory to run the large and complicated calculations required in order to solve this problem. However, the smallest particle sizes of interest for this study are those I categorise as snow (smallest defined grain size range measured 0.355 – 0.500 mm), which are sufficiently large compared to the wavelength range (300 – 1100 nm) used that the complexity of Mie Theory is not required, and that any measurements taken of snow are on a macro scale and so lack sufficient detail for the application of Mie theory (Bohren and Barkstrom, 1974). For the study of scattering processes when particle size is much smaller than wavelength, Rayleigh scattering is used, which states that scattered irradiance is proportional to $1/\lambda^4$ (e.g. Bohren and Huffman, 1983). Rayleigh scattering is also not appropriate for this work, due to its applicability only to particle radii << λ. Therefore, some simpler approximations can be implemented using geometrical optics, which are sufficient for describing systems with larger particles which are not accurately defined.

In geometrical optics, the way in which light behaves at an interface is modelled as a ray which is governed by Snell's Law (Eq. 2) and Fresnel equations (Bohren and Huffman, 1983). Fresnel equations describe how incident electromagnetic waves behave at interfaces of optically different media, explaining wave polarisations and determining both the electric (and by extension magnetic) fields and phase shifts involved. Using these, the reflection and transmission coefficients can be calculated, but use of Fresnel equations are not considered within the scope of this current work.

Assuming a perfectly spherical particle of a homogenous, isotropic and non-absorbing medium, the fraction of transmitted energy absorbed between each interface, W_{abs} (e.g. between points 1 and 2 in Figure 2.2.2), of a particle is $1 - e^{\alpha\xi}$ (where α is the absorption coefficient and ξ path length). The path length ξ is calculated using the particle's radius a and the refractive index, n:

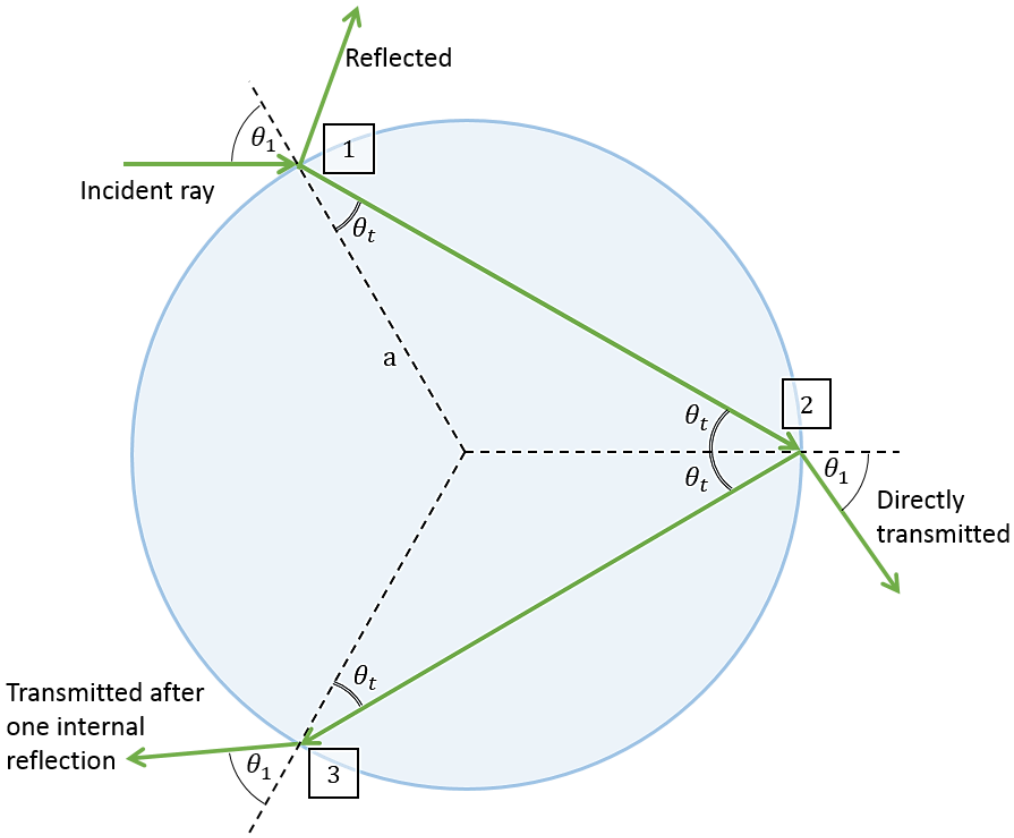

Figure 2.2.2. Example of a ray tracing diagram in a homogenous, isotropic non-absorbing sphere.

$$\xi = 2\mathrm{a}\frac{\sqrt{n^2 - sin^2\theta_i}}{n} \tag{7}$$

As long as the particle is sufficiently weakly absorbing, so that $2\mathrm{a}\alpha \ll 1$, further approximations can be made:

$$1 - e^{\alpha\xi} \cong \alpha\xi \ , \ \frac{1}{1 - R\, e^{-\alpha\xi}} \cong \frac{1}{T} \tag{8}$$

Where T is transmittance , R is reflectance and ξ is path length. Eq. 8 can be summed for all internal rays to give the total absorbed energy W_{abs}, which is used to determine the absorption cross section, $C_{abs} = W_{abs}/I_i$:

$$C_{abs} = \frac{4}{3}\pi\mathrm{a}^3\frac{\alpha}{n}\left(n^3 - (n^2 - 1)^{3/2}\right) \tag{9}$$

When a weakly absorbing particle is small compared to wavelength, within the limits of geometrical optics, the cross sectional area is proportional to the particles' volume, as can be seen in Eq. 9. Eq. 9 has been widely applied to radiative transfer models for snow, such as in Bohren and Barkstrom (1974), and clouds (e.g. Twomey and Bohren, 1980). However, for the experimental work in this thesis, the ice particle size range is considered large compared to wavelength, and so this equation cannot be directly applied.

It is therefore clear that, whilst proper constraints on the bulk optical properties of a material are essential, it is not simply a matter of scaling these to apply to granular or particulate material. Many other factors are required to be able to describe light propagation and scattering in granular ices and snow, including a good determination of both grain size and shape. The theory of geometrical optics, and the different optical properties which have been discussed are considered further in application to describing how the penetration depth, ζ, or e-folding scale, of water and carbon dioxide ices of different morphologies behaves in Chapter 7.

The penetration depth of a material is defined as the depth of material x required to reduce the downward directed energy flux, F, to $1/e$, or 37%, of its initial intensity:

$$F(x) = e^{-x/\zeta} \tag{10}$$

Equation 10 is used to calculate the penetration depth from light intensity measurements (as detailed in Section 3.6). In addition, the theoretical penetration depth of a material can be found simply by taking the inverse of the absorption coefficient α. However, all naturally occurring materials contain imperfections, a factor which is not accounted for, and neither are particle size and shape. As a consequence, simply using the theoretical penetration depth is not adequate for characterising scattering media, such as snow. Due to the direct relationship of the penetration depth of a bulk material with its absorption coefficient, which is highly wavelength dependent, practical measurements are also highly sensitive to the wavelength of light being used, and therefore the wavelength range must always be considered. Shorter wavelengths in the ultraviolet are generally attenuated much more rapidly than the longer wavelengths of the infrared. Consequently, these longer wavelengths will penetrate much deeper into a material. This is discussed further in Section 2.4. However, ices are opaque to infrared radiation, and so the scenario is not quite so simple. The transparency of visible wavelengths, but opacity in the infrared, forms the basic principle behind the Solid State Greenhouse Effect (introduced in Section 1.2). In order to understand the absorption and scattering behaviour of small particles, first the optical properties of the bulk material must be known. Details of the specific optical properties of water and carbon dioxide ices are given in Section 2.3.

2.3. Optical Properties of Water and Carbon Dioxide Ices

Much is known about how water ice responds to incident radiation of different wavelengths. Water ice absorbs strongly throughout the ultraviolet at wavelengths < 170 nm, with minimum absorption at 400 nm, absorption occurs throughout the infrared but is only weakly absorbing in the microwave range >1 cm (Warren et al., 2006). On the other hand, CO_2 ice absorbs

strongly only in three narrow bands in the mid-infrared (λ < 25 μm), and two lattice absorptions in the far infrared (λ > 25 μm), with only very weak absorption in between these bands (Hansen, 1997). Solid CO_2 also exhibits a strong absorption continuum in the ultra violet (wavelengths of 50 – 130 nm) due to electronic transitions (Warren, 1986). CO_2 ice is relatively transparent in the visible region, but absorption is not as weak as it is in H_2O ice, where α (the absorption coefficient) is a factor of ~400 times smaller. In the infrared, absorption maxima in solid CO_2 are approximately the same as in the gas: near 1.4, 2.0, 2.7, 4.3 and 15.0 μm wavelengths, corresponding to vibrational transitions of the CO_2 molecule (Warren, 1986). The spectrum is characterised by strong, narrow absorption lines, of which the intensity, width and location are all temperature dependent, generally broadening with increasing temperature. Between these absorption lines, α is very small, but not negligible. It is important to be able to accurately define this as it affects the reflectance and emittance of planetary surfaces. Even when α is 5-6 orders of magnitude smaller than in the strong bands, absorption of solar radiation by CO_2 snow can be quite significant, in the region of ~30% (Warren, 1986). For measurements made by Warren (1986), they assumed that the $^{13}C/^{12}C$ isotopic ratio for other planetary surfaces is the same as on Earth, and due to the temperature dependence of the absorption coefficient, the authors made measurements at several different temperatures to give a comprehensive description of the optical properties of CO_2 ice.

The absorption coefficient, α, of a substance can be determined from experimental measurements (where absorption follows Beer's law), by taking the natural logarithm of the transmission, T, and dividing by the path length, d (Hansen, 1997):

$$\alpha = \frac{\ln T}{d} \tag{11}$$

Egan and Spagnolo (1969) measured the complex index of refraction for commercial CO_2 ice in the wavelength range of 0.35 – 1.0 μm. Their techniques involved determining the Brewster angle on bulk solid CO_2, and absorption was found from direct transmission measurements on thin sections of CO_2 ice. Narrow band interference filters were used in conjunction with a monochromator to eliminate errors caused by scattered light at wavelengths outside the field of this study. Measurements were made at 0.35, 0.46, 0.56, 0.70, 0.97 and 1.0 μm. The commercial dry ice used had additives of 50 ppm water and 50 ppm Kadol extra heavy white mineral oil. The optical absorption of water was known (at the time by Irvine and Pollack, 1967), and that of the mineral oil was measured by Egan and Spagnolo to be negligibly small over the 0.35 – 1.0 μm wavelength range (the refractive index of the oil was known to be 1.4819 at wavelength 0.5893 μm). The assumption was made that the optical contribution of these impurities would be roughly proportional to their concentrations provided they do not enter the lattice structure of the CO_2 molecule (Egan and Spagnolo, 1969), and therefore the effect of these impurities deemed to be

negligibly small. The effect of the water absorption band at 0.97 μm was below the resolution on the measurements made.

In the Egan and Spagnolo (1969) study the CO_2 ice sample was held in a Pyrex cylinder, and polished by rubbing an aluminium plate on it. If this was not done, then the irregular surface would scatter ice and make determining the Brewster angle difficult (Egan and Spagnolo, 1969). Light transmission experiments were undertaken using an optically clear polished sample of CO_2 ice approximately 1 cm thick. If the sample was not optically clear, then the imaginary portion of the complex index could be a factor of 10 higher due to increased light scatter. Transmission was measured as a function of thickness whilst the CO_2 ice sublimated, and the ice block polished between each measurement. The Warren (1986) optical constants for CO_2 ice appear to be the most comprehensive to date, replacing the Egan and Spagnolo (1969) in terms of both purity of the samples and accuracy of measurements. They used samples of 40 nm - 420 nm thick to measure transmission in the strong IR band at a wavelength of 4.3 nm, and in the UV, some were only 20 nm thick. In the spectral regions where absorption is weak, samples on a scale of at least a few millimetres thick were needed, but they struggled to create these whilst maintaining transparency, and a smooth surface to minimise scattering. Some more recent studies have built on these, making further improvements and filling in gaps left by Warren (1986), such as studies by Sandford and Allamandola (1990), Calvin (1990) and Foster et al. (1998), but these were not made over the visible wavelength range and so are not applicable to this study. A compilation of the optical properties (refractive index and absorption coefficient) are collated in Table 2.3.1. These are given, wherever possible, at or as close to the same wavelength for comparison purposes.

Wavelength	**H_2O Ice**		**Wavelength**	**CO_2 Ice**	
λ (nm)	n	$\alpha\ (\mathrm{m}^{-1})$	**λ (nm)**	n **(±0.05)**	$\alpha\ (\mathrm{m}^{-1})$
350	1.3249	2.00×10^{-11}	**363**	1.432	6.78×10^{-7}
400	1.3194	2.365×10^{-11}	**401**	1.426	6.83×10^{-7}
550	1.3110	2.289×10^{-9}	**553**	1.413	8.27×10^{-7}
620	1.3088	8.580×10^{-9}	**616**	1.411	9.92×10^{-7}
800	1.3049	1.340×10^{-7}	**805**	1.406	1.55×10^{-6}
1000	1.3015	1.620×10^{-6}	**1000**	1.404	2.13×10^{-6}
1100	1.2998	1.700×10^{-6}	**1100**	1.403	2.50×10^{-6}

Table 2.3.1. The optical constants of the refractive index n and absorption coefficient α, for water ice at 266 K (Warren and Brandt, 2008) and carbon dioxide ice at approximately 82 K (Warren, 1986), across the optical range covered by the experiments in this thesis (300 – 1100 nm), at (as close as possible to) comparable wavelengths.

Measurements of the optical properties of CO_2 ice are difficult to perform due to the difficulties inherent on creating and maintaining perfectly smooth, uncracked and uncontaminated CO_2 ice samples throughout the length of the experiments, in part due to its high thermal expansion coefficient, and the low temperatures required to maintain solid CO_2.

Light transmission through snow is dominated by scattering (rather than absorption, which is the major controlling factor in solid ices) and is independent of wavelength through the 350 – 600 nm range for water snow (Warren et al., 2006). Emissivity is the measure of the amount of radiation a material emits compared to that of a black body under the same viewing conditions. The emissivity of water snow is almost 100% across the thermal infrared, independent of particle size, whereas CO_2 snow or frost emissivity varies with particle size (Warren et al., 1990). This is an important difference to note for use in radiative modelling of the Martian polar regions (Hansen, 1997). The optical properties of snow have been mainly measured on naturally occurring samples from across the Arctic and the Antarctic. A study by Beaglehole et al. (1998) was made at several different locations near Scott Base in the Antarctic, across the wavelength range of 350 – 900 nm, and showed how scattering dominated the transmittance at the shorter wavelengths, but that the extent of this varied from one site to another. Their suggested explanation for this was the presence of varying levels of volcanic dust contaminating the samples. This effect is repeated time and again throughout the literature: only very small amounts of an absorbing contaminant within a snow pack can dramatically influence its albedo and other optical properties (e.g. France et al., 2010; Kaufmann and Hagermann, 2015; Warren, 1984). Other important parameters for light transmittance through snow include snowpack density and grain size.

Some other physical properties are of interest when studying CO_2 ice covered surfaces. Examples include measurements of the thermal properties of porous CO_2 ice under vacuum conditions made by Seiferlin et al. (1996), which gave particularly low values, as expected, and the rheological properties of CO_2 ice, measured by Durham et al. (2010), which proved to have the lowest viscosity of all planetary ice analogues.

2.4. Previous Experimental Studies of the Penetration Depth of Ices

A number of light penetration measurements, with a focus on determining the penetration depth of light and quantifying the SSGE, have been made using water ice. Studies using naturally occurring Antarctic sea ice include those made by Brandt and Warren (1993), Perovich (1996) and Datt et al. (2015), focusing on the implications for thermal profiles and subsurface heating on Earth. Brandt and Warren (1993) criticized previous studies, such as Rusin (1961) and Schlatter (1972), who used an average value for the penetration depth across all wavelengths (Schlatter gives this as

50 cm, but it is unclear where this value originates from). As the absorption coefficient of water ice varies by five orders of magnitude across the solar spectrum depending on wavelength, this will also impact the penetration depth based on wavelength. The study by Brandt and Warren (1993) modelled the SSGE in ice and snow by subdividing the solar spectrum into 118 bands, giving penetration depths that ranged from 240 mm at a wavelength of 470 nm, to 0.4 mm at 2000 nm wavelength for snow of 100 µm grain radius and density of 400 kg m^{-3}. They compared their results to those made using a wavelength averaged penetration depth and showed that the studies using the wavelength averaged value overestimated subsurface heating, in both the extent of the temperature rise and the depth at which the temperature maxima occurred. In this thesis I have attempted to avoid these pitfalls by making measurements of the penetration depth over a broad spectral range. The broad spectral range simulates sunlight, with the correct relative intensities for each wavelength, over the range of 300 nm to 1100 nm.

Other studies have more of a focus on icy bodies in space, ranging from comets (e.g. Kömle et al., 1990) and icy moons to the polar regions of Mars (e.g. France et al., 2010; Kaufmann and Hagermann, 2015). Kömle et al. (1990) focussed on the thermal response of both pure and dusty ices to solar irradiation mainly in a cometary setting. Kaufmann et al. (2006) performed laboratory experiments irradiating a range of translucent samples, including glass beads, blocks of pure water ice and blocks of layered water ice with absorbing layers, under cryo-vacuum conditions using a solar simulator lamp. These measurements also focused on determining the depth of the temperature maxima, however, the authors did suggest that an e-folding scale of 15 mm for water ice fits their model of how the SSGE effects the evolution of the thermal profile over time. Further measurements have been made for the e-folding scale of water snow.

Kaufmann and Hagermann (2015) and France et al. (2010) conducted experiments to determine the e-folding scale of water snow, and the effect of adding Mars simulant dust to the snow, using different methodologies, resulting in e-folding scales for pure water snow an order of magnitude different. The snow samples used by Kaufmann and Hagermann (2015) were made by an industrial snow cannon and were later found to contain some contaminants. This is acceptable for determining the effect of dust contamination, as it was the only variable in the system, but not so accurate for determining the e-folding scale of pure water snow. Therefore, their value of 5.4 ± 1 mm for the e-folding scale of pure water snow over the wavelength range of 300 nm – 1100nm (the same range used for the experiments in this thesis) is likely to be too low because the effect of even small amounts of contaminants decreases the e-folding scale. France et al. (2010) also conducted light intensity measurements through pure and dust contaminated snow packs. Conversely, they generated their water snow by spraying pure water into a bath of liquid nitrogen, similar to the method detailed in Section 3.1, meaning the snow was free of contaminants.

However, the samples were then left to sinter for 24 hours at 253 K, which would result in a not insignificant degree of sintering. This goes some way to explaining why their e-folding scale is an order of magnitude greater than that measured by Kaufmann and Hagermann (2015). In addition to this, France et al. (2010) used discrete wavelengths from 400 nm to 700 nm, whereas the measurements presented by Kaufmann and Hagermann are across the broader wavelength range, which could also explain some discrepancy in the results. This is demonstrated by the vast range of e-folding scales of sea ice reported by Perovich (1996) and discrete wavelength ranges, from 24 m at λ = 470 nm, decreasing dramatically 2m at λ = 700 nm, to 5 cm at λ = 1000 nm.

Another variable which has been researched to some extent is snow pack density. Whilst there are clear relationships with grain size and various optical properties (e.g. Warren, 1982; Wiscombe and Warren, 1980), the correlation between light transmission and density is less well constrained. Bohren and Beschta (1979) conducted measurements through compacted and uncompacted naturally formed snow, to find no correlation between density and albedo. Perovich (2007) made measurements of the extinction coefficient of snow at different densities across the wavelength range 450 nm to 750 nm, to find no significant link within a highly scattered dataset. They conclude that other factors, such as grain size, are much more important in controlling light penetration through a snowpack. Building on this, Libois et al. (2013) argue that not only grain size but grain shape is important when studying light penetration in snow, and construct a model and undertake practical experiments which show that modelling snow grains as a collection of perfect spheres generally causes the e-folding scale to be overestimated. Further measurements are made in Libois et al. (2014), and the authors determine that grain shape can be defined by two parameters, the geometric asymmetry factor, and particularly the absorption enhancement parameter. If these parameters can be accurately determined, modelling of optical radiative transfer models involving snow processes can be much improved.

What none of these studies addressed, however, is how the presence of CO_2 snow, rather than water snow, effects the light penetration depth within Martian snow packs.

In a recent experimental study by Portyankina et al. (2018), carbon dioxide ice samples were grown under different pressure and temperature conditions in order to explore the effect of this on texture and ice transparency. This included creating CO_2 ice under Martian conditions for the first time. They found a wide range of CO_2 ice textures formed depending on the exact P-T conditions, including (but not limited to) CO_2 crystals resembling snowflakes (generated at a pressure of 24 mbar and temperature of 160 K), a continuous translucent layer akin to slab ice (at 55 mbar pressure, temperature of 140 K), and multicrystal CO_2 ice which formed small hollow triangular prisms (at 7 mbar pressure, temperature of 125 K). Of particular interest was the formation of slab ice, which occurred most often at pressures and temperatures close to the

thermodynamic equilibrium between solid and gas phases, but developed in three different ways: firstly, by filling the voids between pre-existing crystals whilst CO_2 gas pressures increased and the temperature decreased; secondly by growing outwards from multiple 'seed' locations (seeds similar to the 'snowflakes' in appearance) until eventually merging to form a continuous layer; or finally by spreading from a single condensation seed point. The authors summarise that, under typical polar conditions for Mars, CO_2 ice deposits in slab ice form, but that this can occur in a range of ways, and can form slab ice of varying quality, depending of the level of cracking, water ice contamination, or just general variations in the translucency of the ice. This indicates that whilst it is expected to find slab ice, during both growth of the ice sheet and break up during spring from higher insolation levels, discontinuous or granular ice could be present on the surface, of varying grain sizes, or with a range of 'effective grain sizes' between cracks in the slab. For this reason, measurements have been conducted of the penetration depth of broad spectrum solar radiation in slab ice, snow, and granular ices of specified grain size ranges, composed of water and carbon dioxide ices.

Chapter 3

Experimental Methodology

Various techniques were used to generate different ice and snow samples, of both water and carbon dioxide in composition. These methods are detailed in the following sections, along with the typical characterisation of that type of sample (i.e. grain size ranges, grain shape or ice clarity). This is followed by a description of the equipment and development of the laboratory set up, which was based initially on the experimental procedures of the dusty snow experiments by Kaufmann and Hagermann (2015) and adapted iteratively problems were encountered. The aim of each iteration was to improve sample fidelity and control of variables, such as greater thermal control of the ice sample, or a reduction in contamination. The final experimental procedures are laid out, along with a description of how the data was processed and the broad spectrum e-folding scales of the different ice and snow samples are calculated.

3.1. Snow Preparation

CO_2 snow was made by rapid decompression from a cylinder of liquid CO_2, using an Air Liquide Snowpack maker (see Figure 3.3.1), which is simply a cylindrical container wrapped in porous material secured by Velcro and connected directly to a CO_2 cylinder, to collect the ice particles as they exit the nozzle. Once the snowmaker was full and felt compact, the material was unwrapped, and the cylindrical snowpack removed. The snow was then immersed in liquid nitrogen, which caused immediate disintegration of the snow pack, and ensured homogenous, fine grained snow, similar to the method of Kossacki et al. (1997). The suspension was then poured through a sieve to remove the snow from liquid nitrogen. At this point, the snow was around the temperature of liquid nitrogen, and was stored in sealed bags and kept in an insulated polystyrene container in a freezer at 187 K for the duration of the experiments (around 2 – 3 hours in total), extracting only the quantity required for each experimental run. Due to the presence of some remaining liquid nitrogen in the container, the snow remained cold enough to prevent sintering within the timescales required (see Kossacki, 1997), which would have caused the snow to clump and make it difficult to work with, invalidating the results.

Water snow was made by spraying deionised water into a dewar of liquid nitrogen. Once a sufficient amount of snow had formed in the bottom of the dewar the liquid nitrogen was then

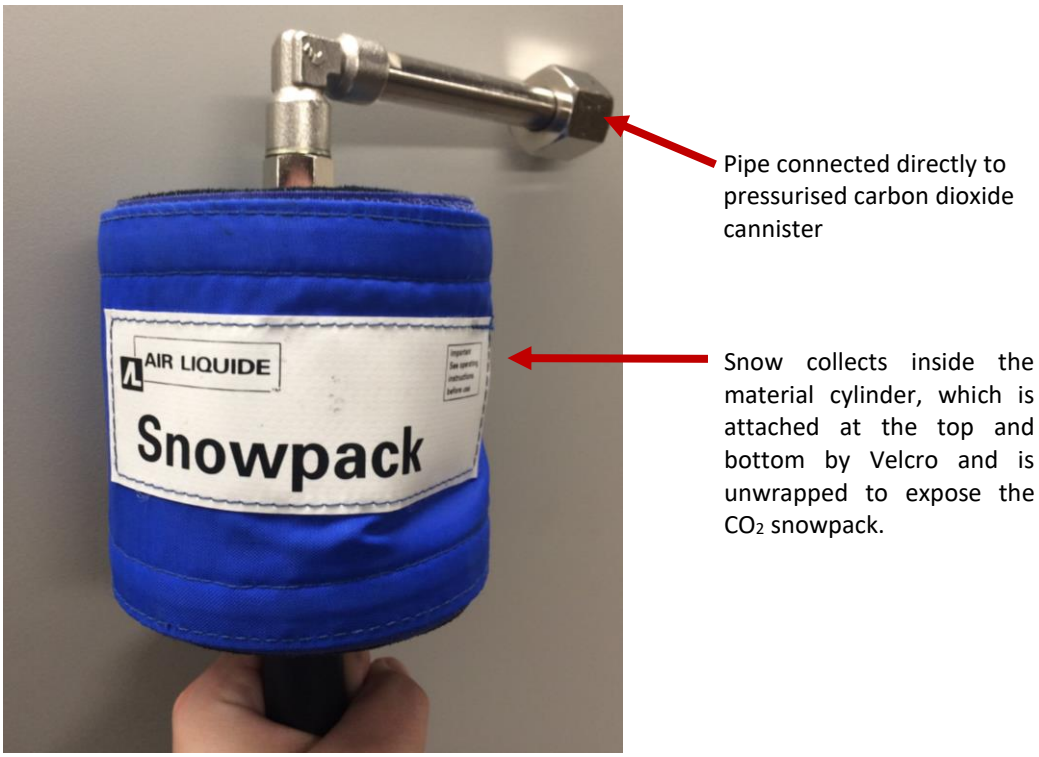

Figure 3.1.1. Air Liquid Snowpack maker, as used to make all carbon dioxide snow used in these experiments.

poured through a sieve (1.18 mm mesh size) to remove any larger ice chunks from the snow. As with the CO_2 snow, this was kept in sealed bags within an insulated box in the deep freezer, and used on the day of production, in order to avoid sintering. The resulting snow samples, both CO_2 and H_2O, can be seen in Figure 3.1.2.

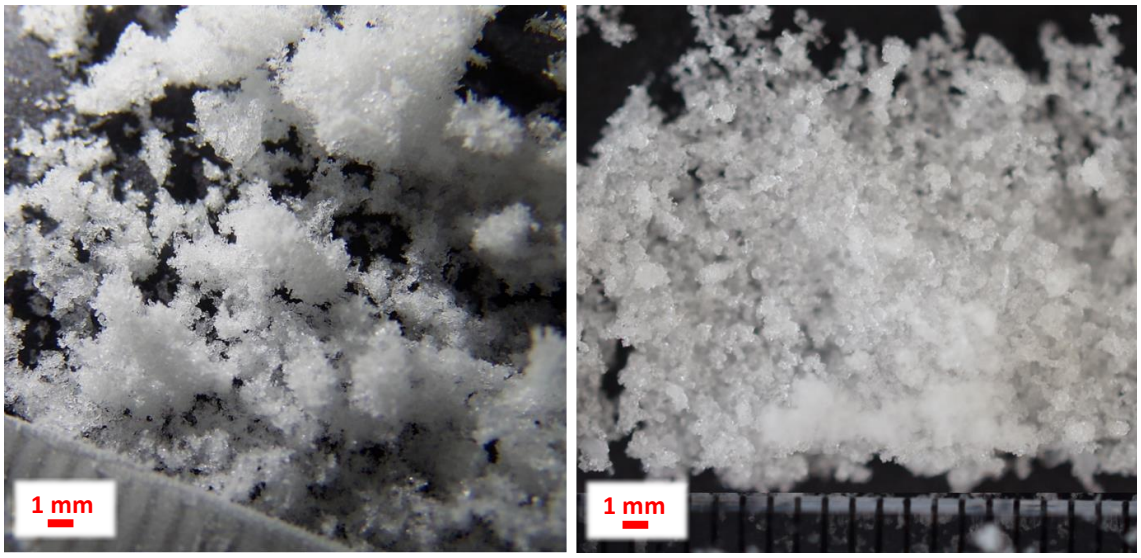

Figure 3.1.2. Examples of freshly made carbon dioxide snow (left) and water snow (right). Each notch on the ruler shown at the bottom on both photographs is 1 mm.

Once made, the water snow was sieved using a range of standard sample sieve sizes (mesh sizes, and therefore upper grain size range: 1.18 mm, 1.00 mmm 0.85 mm, 0.60 mm, 0.50 mm, 0.212 mm, and 0.053 mm) in order to determine if there was any grain size effect on the e-folding scale. Note that, in this context, 'grain size' refers to conglomerates of small ice granules rather than grains of compact ice. Figure 3.1.2 shows the typical structure of the snow formed for these experiments: both CO_2 and H_2O snow is fine-grained and fluffy in appearance. Whilst water ice crystals on Earth exhibit hexagonal symmetry, carbon dioxide ice has cubic symmetry (Mangan et al., 2017), as shown in Figure 3.1.3. However, this does not necessarily mean that solid CO_2 forms crystals that are cubic in shape. Foster et al. (1998) formed CO_2 ice crystals at 1 mbar pressure and a temperature of 77 K and, using a low temperature SEM, found that they commonly formed bipyramid crystals. This is distinctly different from the variety of crystals formed by water ice, such as the typical snow flake shape. Much more extensive laboratory experiments have been conducted by Portyankina et al. (2018) to freeze CO_2 under a variety of pressures and temperatures, but most importantly including typical Martian conditions. Their experiments formed a much wider array of CO_2 ice morphologies, including some crystals which resembled snowflakes (formed under 24 mbar pressure at 160 K), but only at their coldest temperatures (125 K) did they observe a similar crystal shape to Foster et al. The range of ices formed by Portyankina et al., and the implications for light penetration and the associated processes on the Martian surface, are discussed in later chapters.

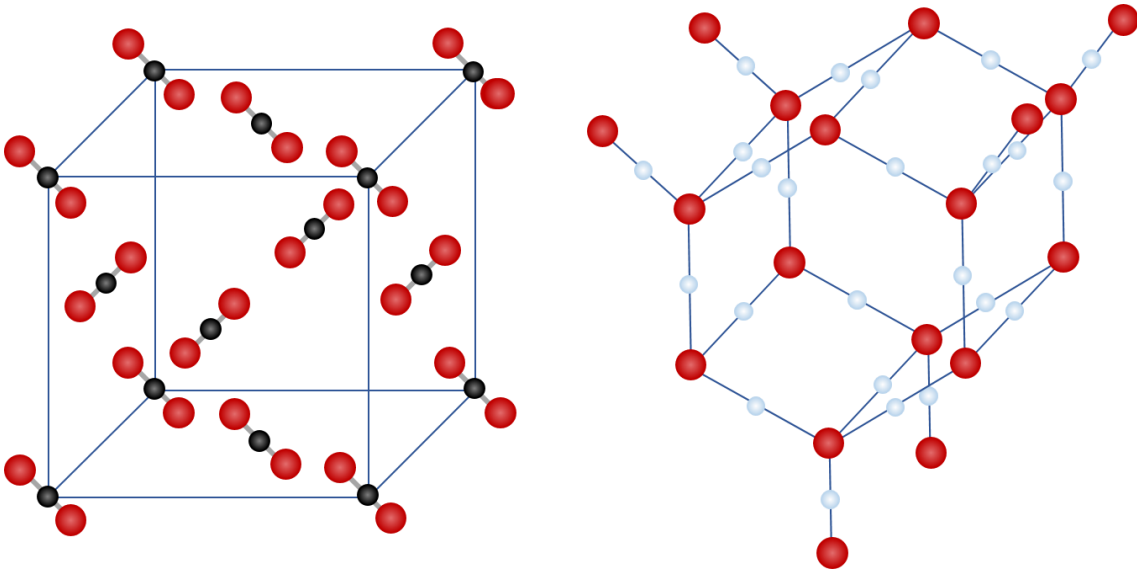

Figure 3.1.3. Basic structure of solid carbon dioxide (left) with cubic symmetry, and water (right) exhibiting hexagonal symmetry. Oxygen atoms shown as red, carbon as black, and hydrogen white.

Most importantly for this study, as both carbon dioxide snow and water snow were formed by droplets freezing instantly (CO_2 by immediate decompression when exiting the pressurised cylinder, and H_2O on instant contact when droplets sprayed onto the surface of liquid nitrogen), there was insufficient time for any sort of dendritic crystal, or snowflakes, to form. Therefore, even though the crystal structure forms a different shape for CO_2 and H_2O, I am confident that both snows formed by the methods outlined here create small, semi-spherical grains which are similar in morphology for both ice types. This is supported by images taken of samples of both CO_2 and H_2O, such as that shown in Figure 3.1.2. More detailed grain shape analysis was not possible due to the extremely cold temperatures required to maintain CO_2 ice without sublimation and sintering occurring.

The sieves were pre-cooled in the freezer, for use with water snow, and in a dewar with some liquid nitrogen poured through them, for use with carbon dioxide snow. Sieving was performed in a freezer, with the different snow samples immediately bagged and stored back in the freezer. The intention had been to repeat this process with CO_2 snow. However, due to the rapid sintering rates, and requirement for the sieves to be kept below the freezing point of CO_2, the process rendered the sample unusable for these experiments. Therefore, I conducted a grain size analysis on 3 additional samples of CO_2 snow prepared using the same method to that used in the experiments and used the proportional grain sizes from these extra samples to be representative of each batch of snow made. The proportional grain size distribution within each CO_2 snow pack sieved and weighed can be seen in Figure 3.1.4.

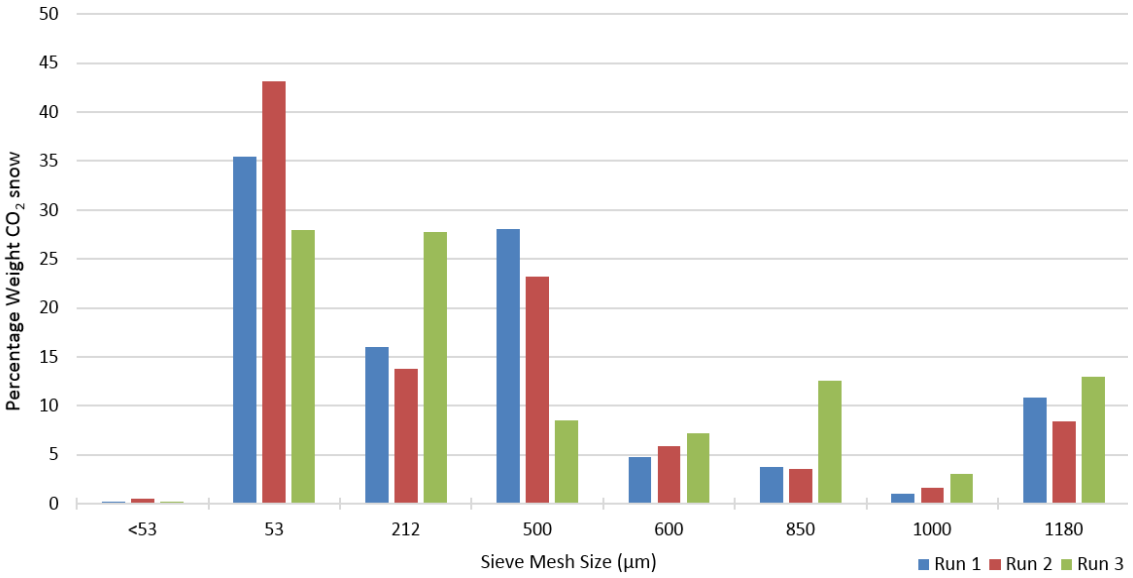

Figure 3.1.4. Representative grain size distribution in CO_2 snowpacks using my methodology.

Throughout these experiments, all samples are freshly prepared and stored for as short a time as possible, under conditions which minimise the possibility of sintering. Ice samples were therefore kept in sealed bags, within insulated boxes kept in the freezer at 187 K for short periods of time. CO_2 snow, due to its rapid sintering rate was kept suspended in small amounts of liquid nitrogen.

3.2. Slab Ice Formation

CO_2 slab ice was made using a direct condensation device cooled by liquid nitrogen, with a continuous supply of CO_2 gas. A heating coil was placed on the top of the device to maintain a thermal profile for preferential condensation to occur from the base of the container upwards, to avoid ice forming over the gas inflow which would prevent further deposition. This resulted in a large cylinder of CO_2 ice, with a set diameter based on the internal dimensions of the equipment, which was then cut to size using a standard hand saw and polished smooth. If a large reduction in ice thickness was required, then the ice would be sawn and then polished; if only a small change then the ice was rubbed against a rough metal surface to encourage more rapid sublimation (like using coarse sandpaper) before being polished smooth again using a smooth, flat metal surface. The thickness was measured and then the sample placed back into the chamber for the next set of light intensity measurements.

The quality of initial samples was not ideal: the ice was cloudy and highly cracked. This was due to the inherent difficulties of creating CO_2 ice. Examples of these can be seen in Figure 3.2.1, where poor thermal control during ice formation, and subsequently in the removal of the ice block

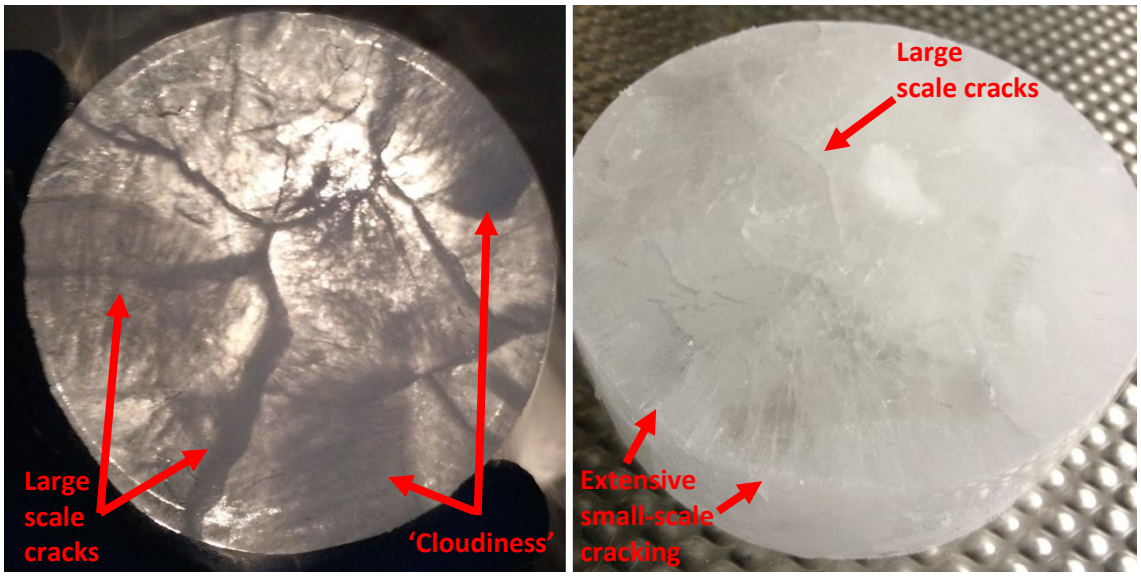

Figure 3.2.1. CO_2 ice samples 1 *left* and 2 *right* were of lower quality than the subsequent samples. Both samples approximately 128 mm in diameter.

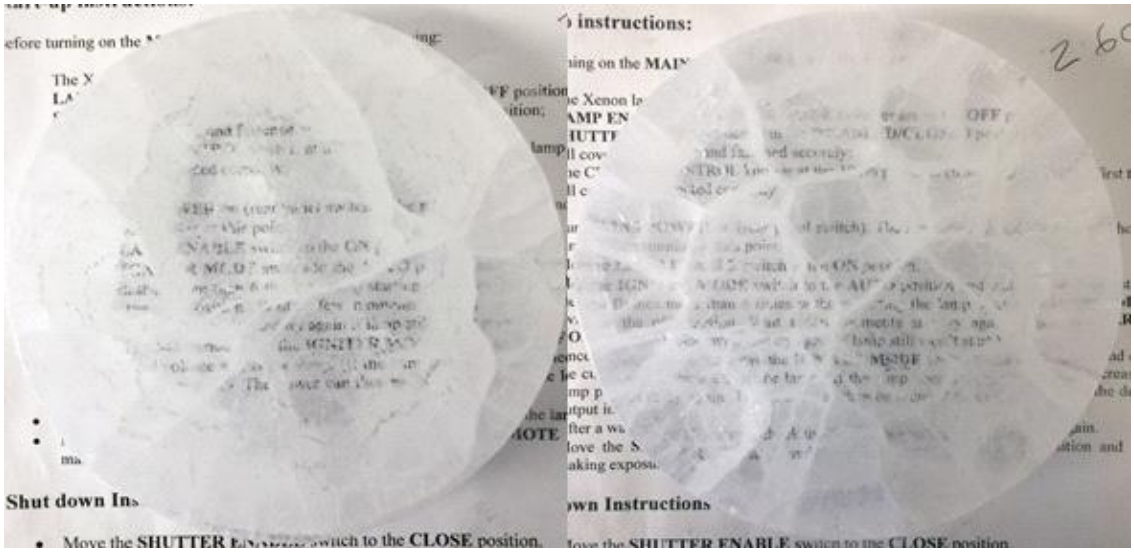

Figure 3.2.2**.** Samples 3 and 4 of the CO_2 slab ice, both at a thickness of 26 mm. These were of better quality than the previous sample attempts due to better thermal constraints during the formation and extraction process. Samples 128 mm in diameter.

from the condensing chamber lead to cloudy ice from too rapid ice growth rates, and thermal cracking. Henceforth, when referring to samples as 'poor quality' , 'cloudy' or 'highly cracked', it is in order to compare the visual state of the sample to those shown in Figure 3.2.1, where large areas of 'cloudiness' can be seen in sample 1 (left), whilst only exhibiting minor cracking (few, large scale cracks with uncracked ice visible in between), or major cracking in Sample 2, which exhibits both large scale cracks and extensive small scale cracking, also giving the appearance of 'cloudiness' to the sample.

Figure 3.2.2 shows that the later samples of CO_2 slab ice produced were visually highly translucent in between the large scale cracks, generally separated by several centimetres, with minimal 'cloudiness'. The main problem being the thermal cracking which occurred repeatedly throughout the experiment. If the temperature of the sample was changed too rapidly, then the whole sample shattered (as demonstrated in Figure 3.2.3, *right*). Shattering of the ice sample was experienced in carbon dioxide ice but not water ice because the thermal expansion coefficient is significantly greater for CO_2 than water ice, as shown on the left panel of Figure 3.2.3 (Mangan et al., 2017; Manzhelii et al., 1971; Röttger et al., 2012).

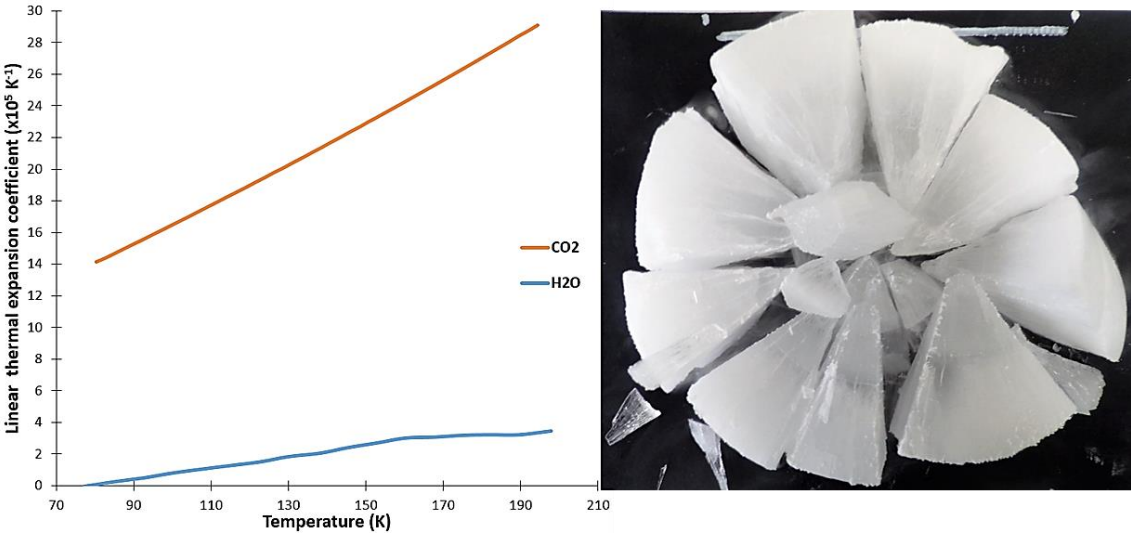

Figure 3.2.3. *Left:* Linear thermal expansion coefficients (x10^5) for CO_2 (orange line, data from Mangan et al., 2017)) and H_2O data (blue line, data from Röttger et al., 2012). *Right:* CO_2 ice sample (originally 128 mm diameter) shattered due to rapid thermal expansion when placed on metal work surface directly from condensing chamber, which had been submerged in liquid nitrogen immediately prior to extraction.

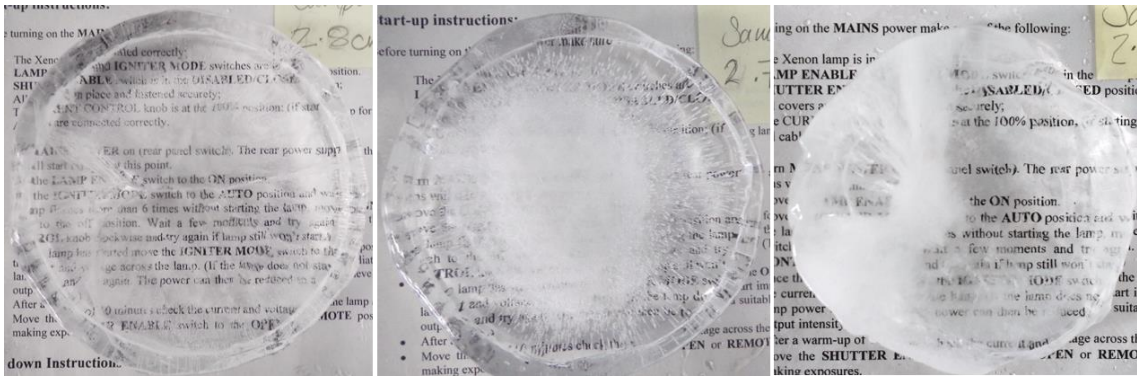

Figure 3.2.4. Examples of water ice slabs, ranging from the best quality produced (left, thickness of 28 mm), to ones with air bubbles (centre, 27 mm thickness), and a sample which froze too rapidly (right, 23mm thickness). Each sample is approximately 110 mm in diameter.

Equivalent water ice samples were made by boiling deionised water, and cooling slowly until frozen in plastic containers, which could be easily cut away from the sample. The slower the cooling/freezing rate, the better (fewer air bubbles, fewer cracks) the resulting ice sample. Therefore, the deionised water was first refrigerated and then allowed to freeze at -5°C in the freezer. Once solid, the ice was removed from the containers and cut to the desired thickness. The top and bottom of each sample was melted on a metal plate and polished smooth, then stored in the freezer at around -20°C. The colder temperature ensured minimal ice melting during experiments. Examples of the water ice samples can be seen in Figure 3.2.4, which exhibit a range of ice qualities, the analyses of which is detailed in chapter 4.

3.3. Making Granular Ice

Both water and carbon dioxide granular ices were made from solid ice as detailed in section 3.2. These were then broken up by smashing the ice blocks with a hammer (see Figure 3.3.1), and separated into discrete grain size ranges using an assortment of precooled sieve sizes: for water ice these were simply cooled in the freezer, but for CO_2 ice they were cooled using liquid nitrogen. Work with the CO_2 ice had to be completed as rapidly as possibly to reduce both sublimation of the CO_2 and minimise contamination from water frost deposition on the grains. The whole process took place inside a chest freezer, in order to keep temperatures low and frost to a minimum. The sieve sizes used for both the H_2O and CO_2 granular ice experiments were: 0.355 mm, 0.50 mm, 0.60 mm, 0.71 mm, 0.85 mm, 1.00 mm, 1.18 mm, 2.00 mm, 3.35 mm, 4.00 mm, 5.60 mm and 8.00 mm. Once sieved, the grain samples were stored in a sealed and labelled insulated container in the freezer at 187 K.

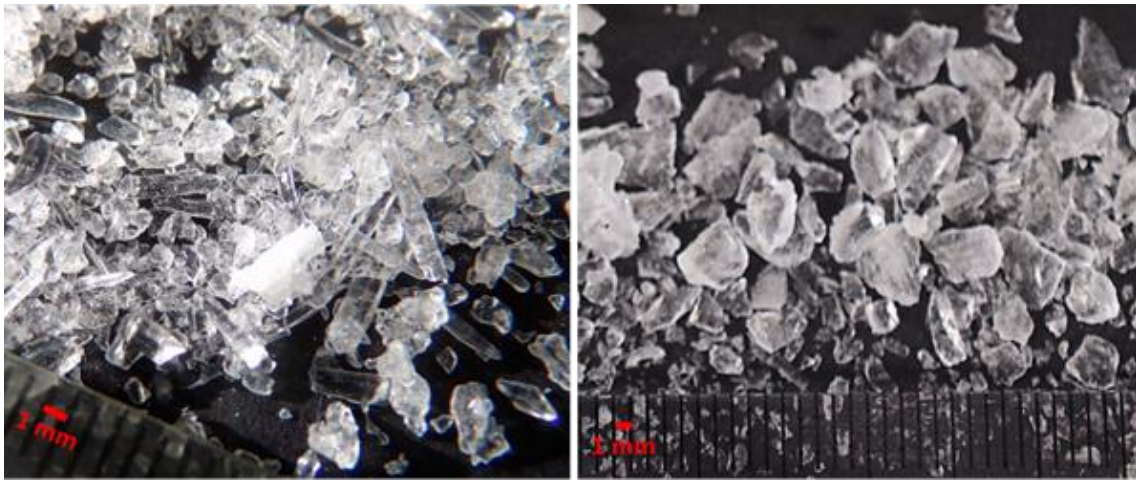

Figure 3.3.1. Grains of carbon dioxide ice (left) and water ice (right) prior to sieving.

3.4. Development of the Experimental Set-Up

All experiments conducted to determine the e-folding scale of an ice sample followed the same basic methodology. The development of the experimental method used here started by analysing those employed in other studies on similar topics. The aim of the study by France et al. (2010) was to determine the depth of a photohabitable zone within a dusty snowpack on Mars. They produced water snow by spraying water into a liquid nitrogen bath, much like the method used in the snow experiments in this thesis. The snow was then sieved and placed in the freezer for 24 hours at 253 K. Light intensity measurements were made in a different way than those used to obtain the data detailed in this thesis: the snow was illuminated with diffuse radiation from domestic light fittings, and measurements were made with a fibre optic probe encased in a solid steel tube attached to a spectrometer and inserted vertically into the snow at 1.5 cm intervals. By using fibre optic detectors inserted into the snow pack vertically, a number of problems are introduced. Firstly, the steel probe would have made a hole in the snowpack, and even if very small, this would still allow light to penetrate down to a greater depth in the snow pack than it would otherwise be able to. Secondly, the steel tube would also introduce a material with high thermal conductivity, increasing heat flow to depth within the snow, which could result in localised melting or sintering. Either sintering or melting would increase the amount of light able to propagate down to depth. Both of these effects would result in a larger e-folding scale. Finally, there is a chance of the detectors being positioned in their own shadow, therefore reducing the detected light intensity, and reducing the e-folding scale.

Kaufmann et al. (2006) conducted a series of laboratory experiments to determine the effect of the SSGE in glass beads and water ice samples, but made thermal measurements to determine the depth of the temperature maxima within the sample. For this, the authors used a similar set up to France et al. (2010), but inserted the thermocouples at intervals horizontally into the sample as opposed to vertically, and then illuminated with a solar simulator lamp. For temperature measurements, the thermocouples need to be in contact with the snow, and so whilst this method did not introduce a vertical hole into the sample, unlike the methods used by France et al, for optical measurements it was still less than ideal due to the introduction of horizontal holes in the sample.

Some of these factors are mitigated by the experimental procedure used by Kaufmann and Hagermann (2015): no measuring device is inserted into the sample, and light intensity through the sample is measured using a pyranometer placed underneath a sample suspended on a glass sheet. The methods followed to generate the measurements within this thesis were adapted from that used by Kaufmann and Hagermann (2015) to determine the effect of Mars-dust contamination on

the e-folding scale of water snow. The exact methods have been optimised for each type of ice sample used, tailored to overcome, or at least minimise, the effect of the specific challenges presented. This was an iterative process, often through trial and error, but eventually led to an experimental set-up capable of producing repeatable and reliable results with each sample type. Figure 3.4.1 shows the starting point of this process.

All samples were irradiated with a full spectrum solar simulator lamp (LS1000R3, Solar Light Company). This lamp simulates the spectrum of solar radiation without the influence of the Earth's atmosphere, and so is a good approximation to the irradiation received on Mars, but does not account for the effects of atmospheric composition, clouds or suspended dust. These are, however, very minor effects when compared to Earth's atmosphere, and only significant if the atmosphere is

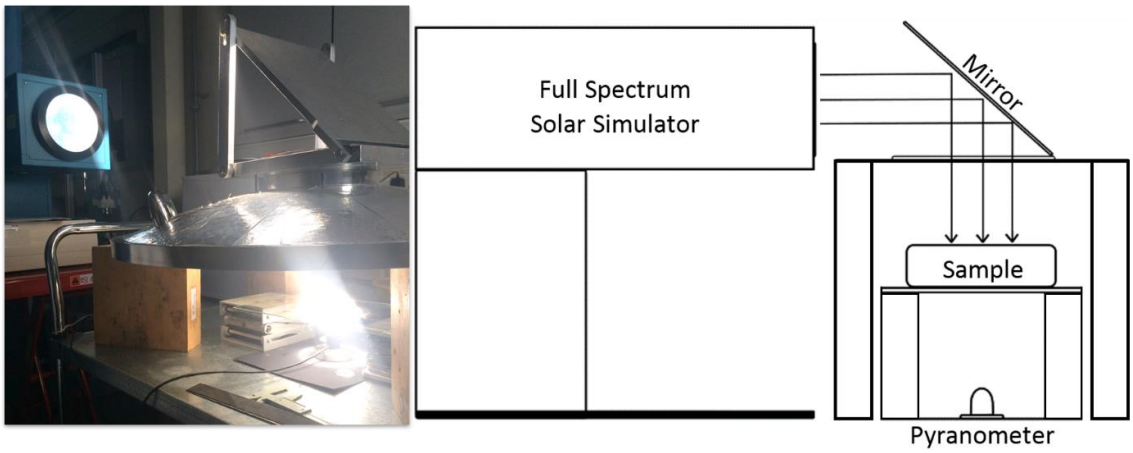

Figure 3.4.1. Initial laboratory set up included the sample being held above the pyranometer on a glass plate, with the whole system exposed to ambient air conditions.

Figure 3.4.**2.** *Left:* water frost accumulating on a CO_2 ice grain. *Right:* a rim of water ice around a thin slice of carbon dioxide snow.

unusually dusty, such as during and immediately after regional dust storms (Haberle et al., 2017; Read and Lewis, 2004). A number of problems arose whilst utilising the initial equipment arrangement (Figure 3.4.1). Figure 3.4.2 shows how water frost accumulates on exposed carbon dioxide ice, and Figure 3.4.3 shows how CO_2 snow evolves when stored at 187 K in the freezer for a long period of time. This demonstrates the process of sintering, which occurs most rapidly when the ice is near its condensation temperature (this process is explained in Section 2.3). Therefore, when CO_2 ice is exposed to ambient temperatures, not only does it begin to immediately sublimate, sintering occurs rapidly (seconds to minutes, rather than days to weeks). This is problematic for measurements of light penetration, as the sintering process causes both grain growth and densification, therefore increasing the distance light can travel within the grains prior to encountering a scattering surface. This means that the results would be inaccurate for the stated

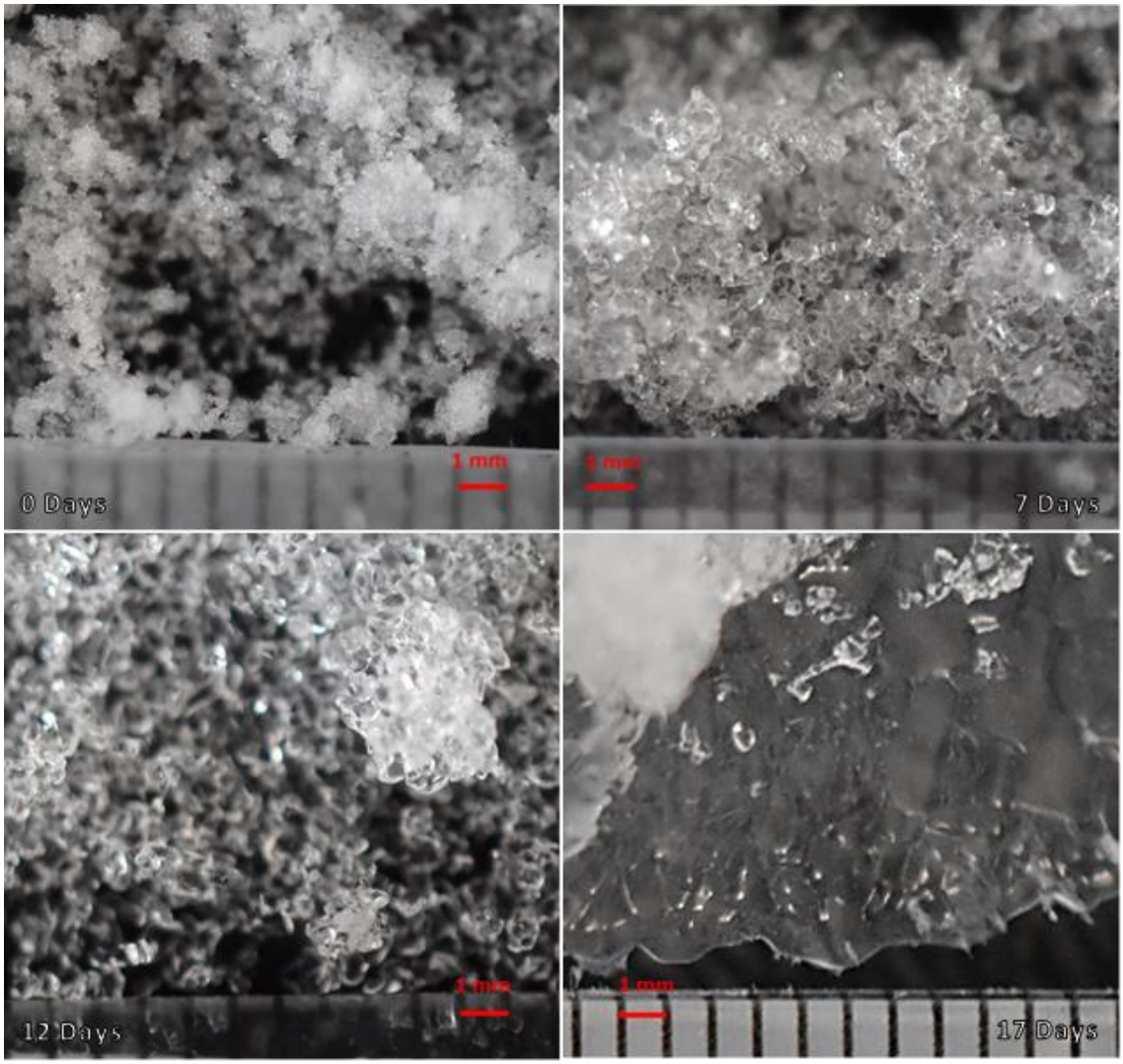

Figure 3.4.3. From top left to bottom right: Freshly made CO_2 snow; CO_2 snow left in the freezer at 187 K for 7 days; CO_2 snow left in freezer for 12 days; CO_2 snow left in freezer for 17 days. Over time the very fine grains of snow in the first image gradually grow in size and join up until forming solid sheets of ice several centimetres in length, in the 17 day image (bottom right).

initial ice morphology, and sintering needs to be suppressed. Additional problems observed included the ability for external light to be detected by the pyranometer, high rates of CO_2 sublimation and water ice melting.

A range of modifications were undertaken in order to mitigate these factors: the sample was now placed inside a chamber which was completely black, which eliminated stray light being accidentally detected and allowed for the sample to be (partially) isolated from ambient atmospheric conditions; a gas line was added which provided a steady stream of argon into the chamber, displacing the air and therefore removing the moisture from inside the chamber; samples were inserted into the chamber via a hatch (see Figure 3.4.4). However, a number of issues persisted. The sublimation and sintering rates were still too high, and whilst much less water frost

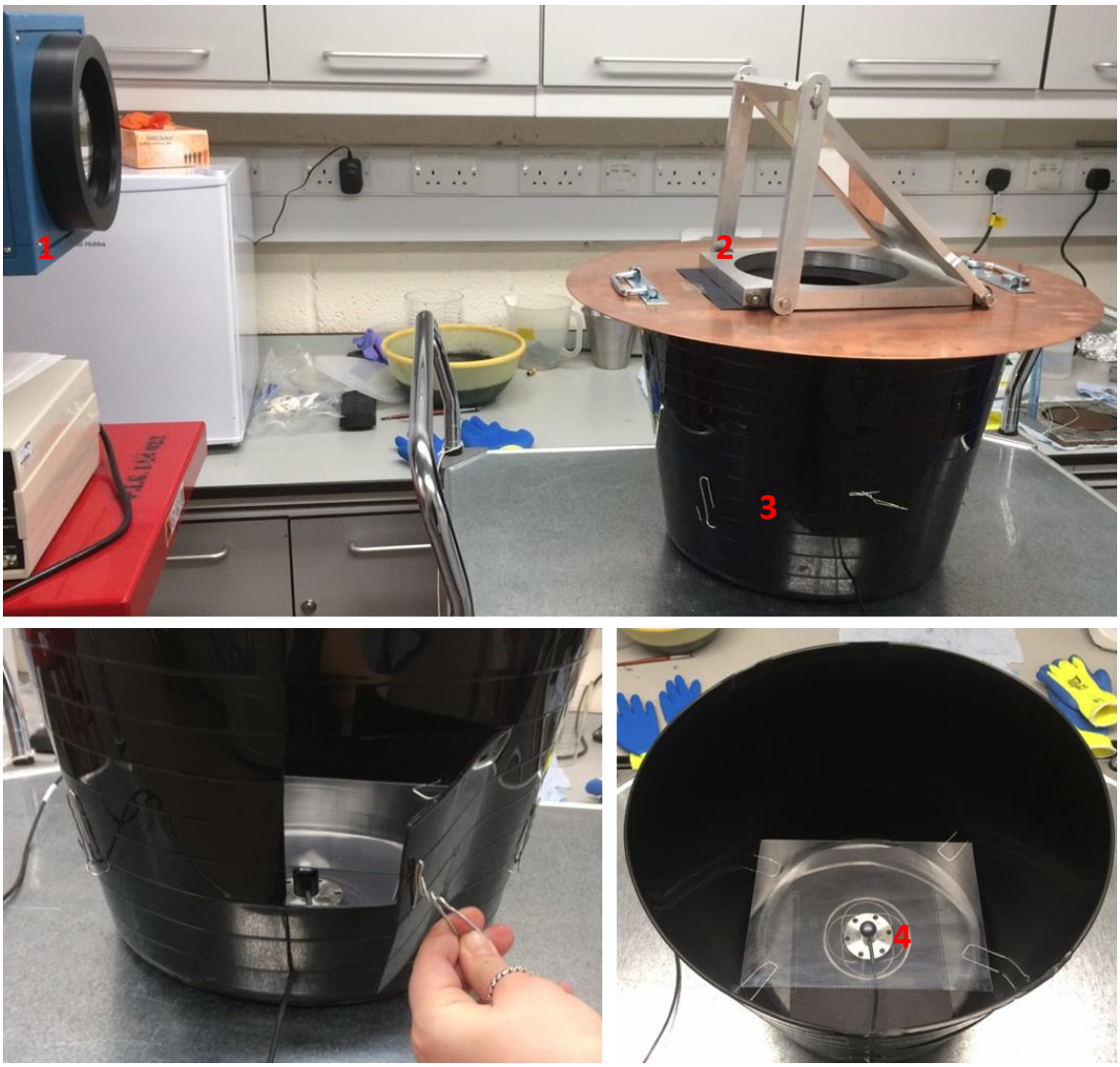

Figure 3.4.4. Improved equipment for experimental measurements, including placing samples and pyranometer within a black chamber to reduce ambient light levels, and flooding it with argon gas to remove water vapour from the vicinity, reducing frost contamination. In upper image, the Solar simulator lamp [1], shines a beam onto the mirror [2], which reflects it into the experimental chamber [3], through the sample, where, in the lower right image. the light intensity is recorded by the pyranometer [4].

was contaminating CO_2 samples, H_2O ice was still forming on the base of the glass plate on which the CO_2 ice was placed.

Further adjustments were made, including running the argon line through a liquid nitrogen bath to cool it, and the addition of insulation to both the chamber and the gas line in. The glass plate was then placed on top of a Perspex cylinder and sealed to the underside of the glass. The argon line in was split to supply the Perspex cylinder directly as well as the rest of the chamber. This ensured the underside of the glass plate would remain as cold as possible, reducing sintering and sublimation/melting rates, as well as keeping it completely frost free. Samples could now only be inserted and removed via the hole in the top of the chamber through which the light was reflected

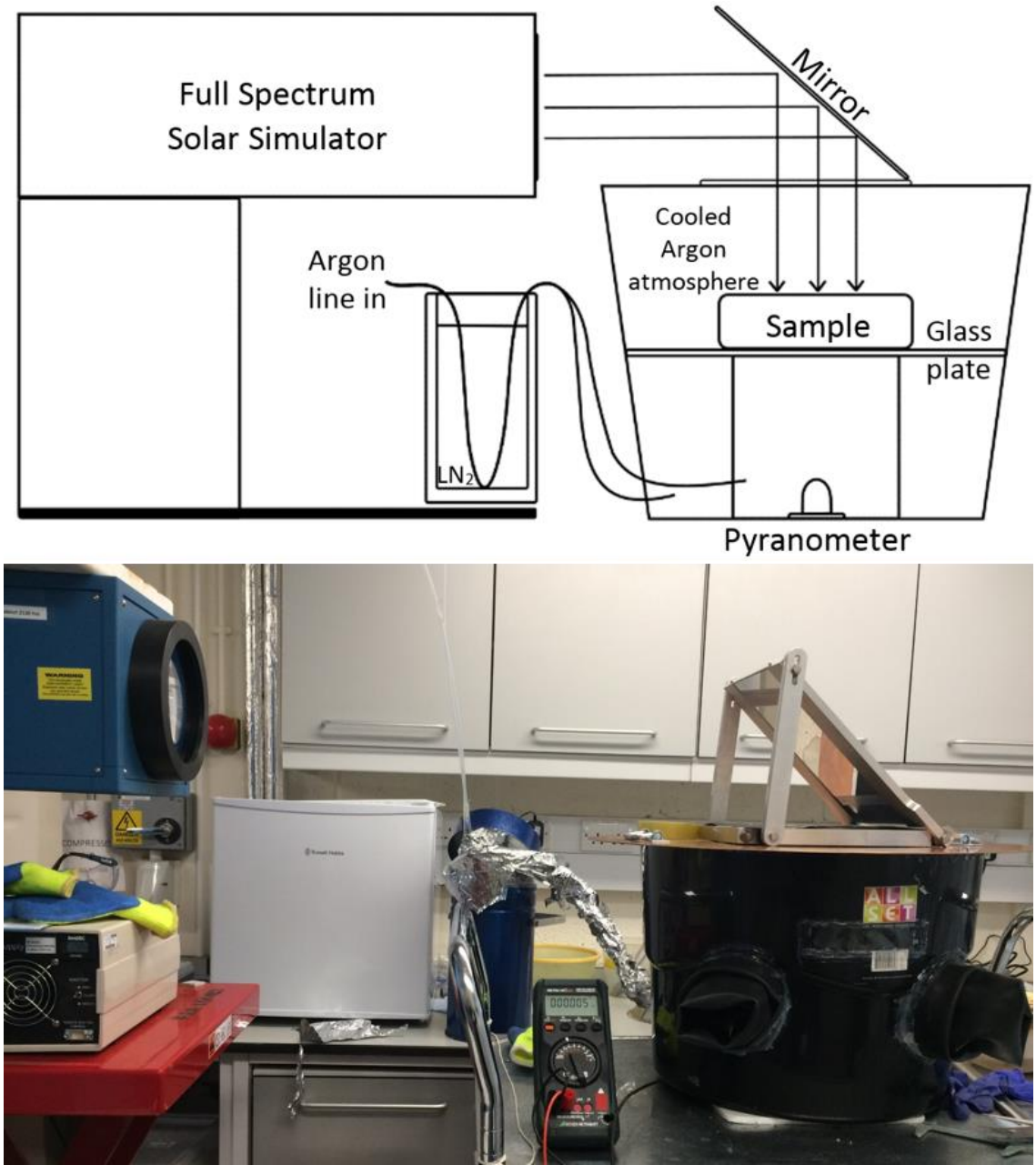

Figure 3.4.5. Schematic and photograph of final experimental set up which enabled temperatures to be reduced and moisture content within the chamber kept to a minimum.

and manipulated using the rubber gloves sealed into the sides of the chamber walls. The final laboratory set up is shown in Figure 3.4.5.

Slab ice samples, of both kinds, were placed directly into the chamber and on the glass plate. Snow and granular ice samples were held within a series of copper rings of known thickness, which could be removed, and the sample smoothed flat again to get consistent range of sample thicknesses for measurements to be taken. The samples were irradiated using a full spectrum solar simulator (LS1000R3, Solar Light Company), with the beam directed via a mirror to penetrate the sample perpendicular to its surface. The transmitted irradiation was then measured using a pyranometer (CS300, Campbell Scientific Ltd., with a voltaic detector diameter of 12 mm). Prior to the experiment commencement, the beam intensity was measured with the pyranometer to monitor consistency, although it is important to note that our e-folding scale results are independent of total irradiance.

The experiment chamber and contents (including glass plate which the sample was placed on and the scraper), were pre-cooled prior to experiment commencement by use of the cooled argon. If these were cooled in the freezer separately, whilst they may have been colder, they would immediately frost up when removed from the freezer and placed in the chamber. Some lumps of CO_2 snow were also placed in the bottom of the chamber, away from the pyranometer, in order to facilitate more efficient cooling at this initial stage. These had completely sublimated by the time experiments were under way. There was no specific temperature control other than to cool the system as much as possible.

The solar simulator lamp was then turned on, and the measurement (in mV) from the pyranometer recorded. For most samples, the measurements were repeated four times for each sample thickness: once in the centre of the sample and three additional measurements at approximately 120° offset from centre. This was to average out any small inhomogeneities encountered in the sample, which was moved around via a small hatch in the side of the chamber.

Sample dimensions were dictated by both the equipment available and the need to ensure the diameter of any sample was at least twice the sample thickness. This is based on calculations by Bohren and Barkstrom (1974), who used Two Flux Theory to calculate sample dimensions required for use in light intensity measurements through snow samples in order to determine the absorption and scattering coefficients, whilst ensuring the walls of the sample holder did not interfere with the results. This rule was also implemented in the study by Beaglehole, et al. (1998) of solar radiation transmittance in Antarctic snow. As a consequence, samples of all ice types follow this rule. For the snow and granular ice samples, the thickness was reduced in increments of 5 mm, by removing the top-most copper ring and smoothing the top of the sample so that it is flat and

level. For slab ice, the sample would be removed from the chamber, the ice thickness decreased and measured, and then returned to the chamber for the next set of measurements. Specifics of the methods for each ice type can be found in the corresponding chapters (4, 5 and 6).

3.5. Data Collection

The data collected for each sample included: dimensions, mass at beginning of each sample run (and for solid ice samples, at each thickness), and light intensity measurements. To gain accurate mass measurements, any pieces of equipment included with the sample, such as the 'sample base holder' and the various copper rings, were weighed prior to being filled with ice or snow, so that their weight could then be deducted from the overall full weight to obtain the mass of just the ice/snow sample. These measurements are recorded in Table 3.5.1. The sample volume (m^3) was calculated from the equipment dimensions, and subsequently the density (kg m^{-3}).

All light intensity measurements were made using pyranometer sensitive to wavelengths from 300 nm to 1100 nm (absolute accuracy ±5% for daily total radiation).

Equipment	Mass (g)
2 cm copper ring	83.40
1 cm copper ring	41.73
0.5 cm copper ring	20.70
Sample base holder	8.28

Table 3.5.1. Mass measurements of relevant equipment used.

3.6. Calculating the E-folding Scale

The e-folding scale ζ of broad spectrum solar radiation penetration in a translucent medium can be calculated from light intensity measurements, or downward directed flux, F, as a function of ice thickness, x, using the following equation:

$$F(x) = e^{-x/\zeta} \tag{12}$$

The e-folding scale is calculated from the raw light intensity measurements by first adjusting the data to a zero depth x_0 to remove the effect of albedo. This depth will vary

depending on the type of ice: the more translucent the ice is, the larger x_0 should be. For snow data, this was set to 5 mm, and for slab ice this was at least 8 mm (water ice slab measurements were only made to a minimum depth of 10 mm, and so this is the depth used). This is discussed further in the subsequent data chapters (4, 5 and 6). All data are then normalized accordingly, and by rearranging Equation 12, the e-folding scale (ζ) can be calculated. The full datasets of raw light intensity measurements for both CO_2 and H_2O snows are available in Appendix B.

Chapter 4

The Penetration Depth of Slab Ice

This chapter describes experiments which investigated the penetration depth of solar radiation into slab ices. Section 4.1 gives some background and rationale behind these experiments. Section 4.2 covers the methods specific to these experiments, building on the general experimental procedures detailed in Chapter 3. Experimental data and results based on carbon dioxide ice light intensity measurements are given in Section 4.3, and the corresponding water ice results are given in Section 4.4. These are compared and discussed in Section 4.5. The raw data relating to the experiments discussed in this chapter can be found in Appendix A.

The carbon dioxide slab ice results detailed in Section 4.3 have been previously published:

Chinnery, H.E., Hagermann, A., Kaufmann, E. and Lewis, S.R., 2018. The Penetration of Solar Radiation Into Carbon Dioxide Ice. Journal of Geophysical Research: Planets, 123(4): 864-871.

4.1. Introduction

As discussed in Chapter 1, CO_2 ice forms on Mars as the seasonal polar ice sheet, which begins to grow during the autumn, and occurs in both hemispheres. During late winter and early spring, when the polar night has ended and the ice sheet is exposed to solar radiation (even if only for brief periods of time initially), araneiform features begin to be observed. The details of the formation mechanism of these is given in Section 1.4, and evidence of CO_2 jetting has been observed in both hemispheres: first in the south where they were named 'spiders' by Piqueux et al. (2003), and then more recently in the north by Bourke and Cranford (2011) and Bourke (2013). Comparisons between these features observed between the two hemispheres suggest that they are formed by the same mechanism, with the main difference being that the southern 'spiders' form in the same locations each year, where the CO_2 jets carve furrows into the bedrock, which is thought to create a weakness in the overlying ice during the following year, predisposing it to rupture at the same locations each year. In contrast to this, those observed in the northern hemisphere seem to be ephemeral, occurring in different locations each spring, although they have been associated with polygonal ground morphology (Bourke, 2013), and at the peaks and bases of dunes (Hansen et al., 2013). This lack of permanence is thought to be due to the much thicker layer of dusty regolith and the presence of dunes, meaning that in between each phase of ice sheet growth, regional winds shift the regolith covering, and so the bed rock furrows are unable to form and carve deep into the surface of the rock.

One of the overriding questions is why these features form where CO_2 sheet ice is observed but not water ice? This links directly to my research questions, looking to understand the difference between light penetration through water and carbon dioxide ices, and what this means for the unique surface processes occurring on Mars. The following experiments were designed to probe this question.

The prevailing consensus is that, as per the CO_2 jetting model proposed by Kieffer (2000), translucent CO_2 slab ice allows solar irradiation to penetrate through sufficiently to transfer energy into the underlying regolith. The regolith is therefore heated, causing the base of the ice sheet to sublimate. This process continues until the pressure from the CO_2 gas exceeds the strength of the ice sheet which ruptures, forming a gas jet which carries regolith material with it to the surface, carving out channels in the regolith below. However, nowhere in the literature has it sufficiently been explained as to why this process does not occur on Earth in glacial or ice covered environments, or why this is not seen in association with water ice on Mars. Being able to directly compare the e-folding scale of carbon dioxide and water ices, measured under the same conditions, should give some indication of the underlying explanation behind this phenomenon.

4.2. Methods

CO_2 ice samples were prepared by condensing CO_2 directly from the gas phase within a pressure vessel immersed in liquid nitrogen, following the methodology detailed in Kaufmann and Hagermann (2017). This forms large CO_2 ice blocks, which were then cut to size and polished smooth prior to experiment commencement, as per the methods detailed in Section 3.2. This polishing minimises surface scattering of light due to an uneven interface between air and ice. Resizing and polishing of the ice was repeated for each thickness measured. The average densities of the prepared samples were ~1500 kg m^{-3}. This process had to be conducted carefully, and in as cold an environment as possible, in order to reduce the chance of cracking or the whole sample shattering due to rapid thermal expansion. CO_2 ice samples had to be removed immediately from the condensing container once no longer immersed in liquid nitrogen, as if allowed to warm, the thermal expansion of the ice rendered it almost impossible to remove from the metal cylinder, unless left for so long that the CO_2 would begin to sublimate, allowing it to slide free. Once removed from the cylinder, the ice block was sealed in a plastic zip-lock bag to isolate it from the air in order to prevent water frost contamination. The sample was then immediately placed in the freezer at 187 K and left to warm up slowly from the temperature of liquid nitrogen (77 K), in order to prevent any further ice cracking or shattering.

Water ice samples were made by boiling deionised water, and cooling slowly until frozen in plastic containers, which could be easily cut away from the sample (as explained in Section 3.2). Experiments for both the water and carbon dioxide ices were undertaken in an argon-filled chamber, which was first cooled with liquid nitrogen. This both reduced the sublimation rate of the CO_2 ice, and minimised water frost deposition on both the sample and the glass plate which the sample was placed on, in addition to preventing melting of the water ice.

Samples were irradiated using a full spectrum solar simulator, with the beam directed via a mirror to penetrate the sample perpendicular to the polished surface of the sample. The transmitted irradiation was then measured using a pyranometer (CS300, Campbell Scientific Ltd.) able to detect wavelengths from 300 nm to 1100 nm. It is important to note that e-folding scales derived are independent of total irradiance, although this was found to be quite consistent when measured with the pyranometer prior to the experiment commencement for each sample, varying from 119.7 mV to 123.5 mV.

Four measurements were made at a range of ice thicknesses in order to determine how light transmission varies as a function of thickness: one reading was made in the centre of the sample, and three further measurements radially spaced approximately 120° offset from centre. This ensured the measurements were made over a range of cracked and clear ice, which should

therefore be representative of the ice conditions which occur naturally. This is consistent with the findings of Hansen (1999), who reported how some areas of the seasonal CO_2 caps evolve with time (and increasing insolation through early spring) from low albedo and high emissivity to brighter, fractured, and lower emissivity regions. Sample 1 was measured at the greatest thickness I could obtain from a sample, in order to gauge the rate of change with thickness and the range of measurements required. As the few measurements at 73 mm, 70 mm and 67 mm showed very little difference in light intensity through the sample (this can be seen in Figure 4.3.1), I determined that subsequent measurements could begin from a significantly thinner ice slab. Therefore, measurements ranged at ice thickness from around 50 mm to 5 mm, in varying increments.

Reliable albedo measurements are difficult to obtain, and so, to avoid these additional uncertainties, only measurements made using a minimum thickness of ice are considered in the calculations. Measurements are then adjusted to use this minimum thickness as the zero point for calculation of the e-folding scale. This is consistent with the methods of Kaufmann and Hagermann (2015).

4.3. CO_2 Ice Results

Four measurements of light intensity through the ice sample were made for each ice thickness, for which the mean light intensity at each thickness has been calculated and plotted in Figure 4.3.1. Errors are estimated to be ± 1 mm in ice thickness, based on a small error allowance in measuring exact thicknesses, and minor deviations on the surface of the ice across the sample. Errors in light intensity readings are deemed to be negligible in comparison. Whilst there is some scatter, the data can be approximated to the exponential curve fitted to each sample dataset.

As each sample was prepared and used, the technique was refined and higher quality, more transparent ice was produced. This accounts for the general increase in intensity of light propagating through the samples. Figure 4.3.1 shows samples 3 and 4 at the same thickness. It is important to note that, whilst sample 4 appears to have a greater number of cracks through it, in between the cracks the ice is more transparent than in sample 3, which has a more clouded appearance, especially outwards of the centre. This is reflected in the data, with overall better light propagation through the sample and significantly higher light intensities at smaller ice thicknesses.

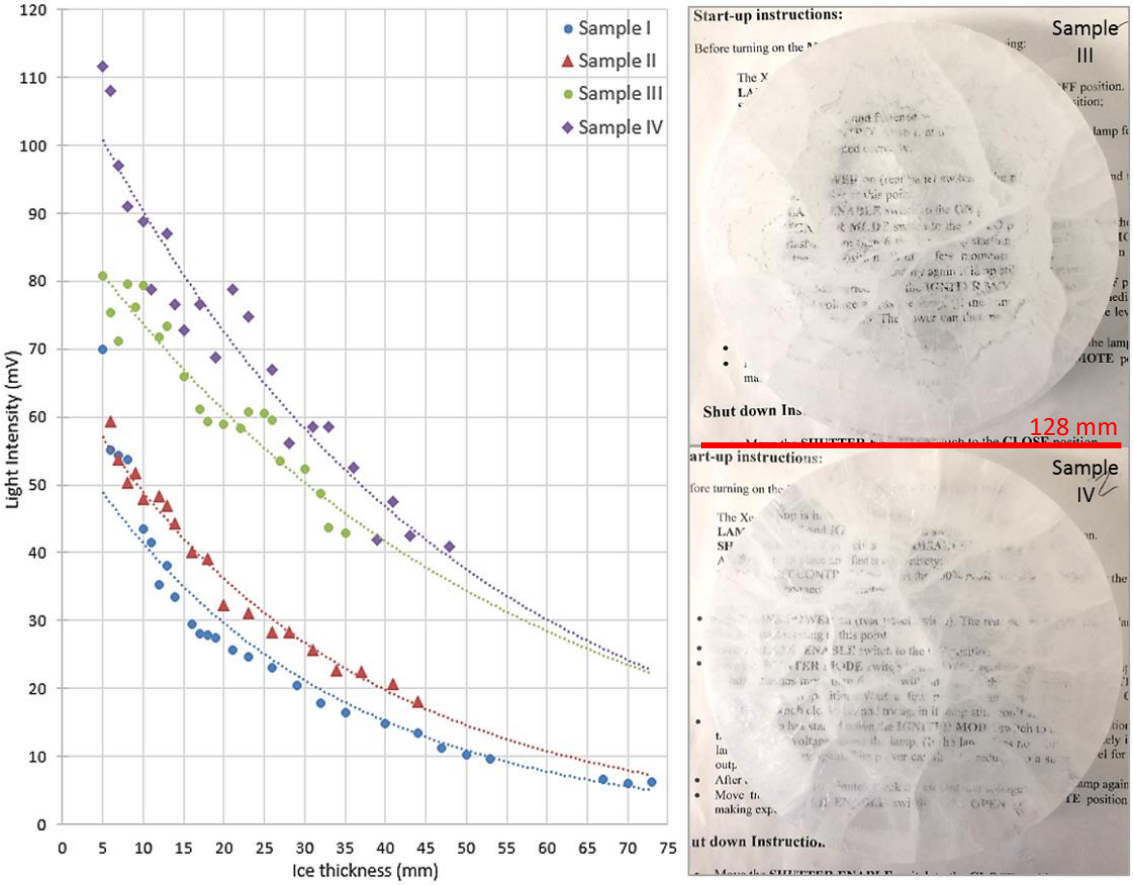

Figure 4.3.1. *Left* Mean light intensity data plotted against ice thickness, with exponential curves plotted in dotted lines. These are an approximate fit to demonstrate these data can be modelled by an exponential function. *Upper right* Sample 3 at a thickness of 26 mm, overlying text to demonstrate transparency. This is a standard method of visually judging transparency of ice samples, first reported by Behn (1900). *Lower Right* Sample 4 at a thickness of 26 mm, overlying the same example text.

In order to calculate the e-folding scale from light intensity measurements, Kaufmann and Hagermann (2015) used 5 mm of snow thickness for their measurements. However, as ice is more transparent than snow, a greater thickness will be required for these e-folding scale measurements. After studying the data, an example using the average data points for each sample thickness can be seen in Figure 4.3.2. The data should approximate to a straight line when plotted against the log of light intensity, and it can be seen that the measurements made using the thinnest of samples deviate from this linear trend consistently. The point at which this deviation begins was identified as 8 mm and therefore it was decided 8 mm should be sufficient to reliably eliminate albedo variations. The inclusion of the light intensity measurements from samples <8mm thick can alter the e-folding scale results from 3% to 20%, based on my results. Subsequently, 8 mm is taken as the zero point x=0, with all other measurements normalised accordingly. Further to this, all tests were made within a black chamber, which shielded the sample from ambient radiation and minimised reflections that could interfere with the results.

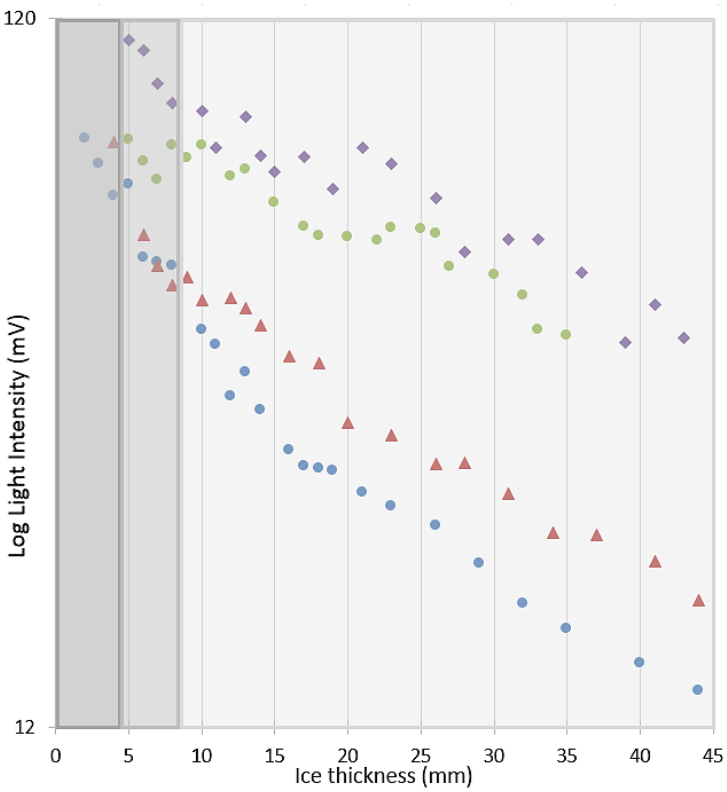

Figure 4.3.2. The average light intensity passing through the sample at each ice thickness is plotted, including all data points (darkest shading), implementing a 5 mm thickness cut off (mid-shading), as used for the e-folding scale measurements of water snow by Kaufmann and Hagermann (2015), and a 8 mm cut off (rest of data).

On closer inspection of these data, it can be seen that there are some sudden drops in light intensity at certain thicknesses through individual samples. This trend is even more pronounced when studying the raw data – especially the minimum and maximum values. Consequently, these have been plotted in Figure 4.3.3. By analysing the data in this way, we can identify when the large cracking events occurred in the samples (example of the effect of cracking on light intensity measurements shown red). Cracks due to thermal expansion were a problem throughout the duration of these experiments, and seems to be a common problem reported in the literature when making measurements with CO_2 ice (e. g. Portyankina et al. (2016). This is because CO_2 ice has a large thermal expansion coefficient (Manzhelii et al., 1971) which is an at least order of magnitude greater than that of water ice (please refer to Figure 3.2.3). This results in cracking which temporarily negates the increase in transparency with decreasing ice thickness, and so complicates the data analysis. The more transparent and better quality the sample at the start, the more cracking episodes occur, and the greater the effect on the light penetration measurements. This is why samples 3 and 4 allow for better light penetration overall, but the data are more scattered.

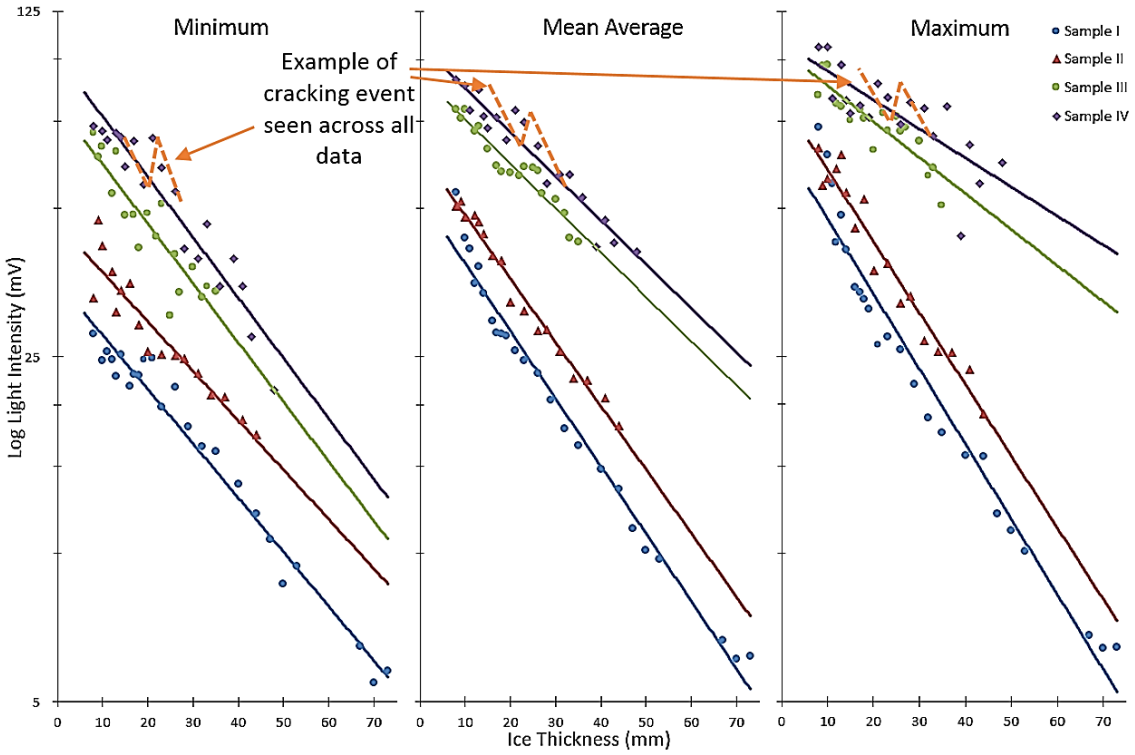

Figure 4.3.3. The minimum (*left*), maximum (*centre*) and mean (*right*) measurements of light intensity through CO_2 ice samples are plotted at varying ice thicknesses. A line of best fit is plotted, and the exponential function of this line is then used to calculate the e-folding scale. Much of the scatter around these lines are due to cracking events within the ice sample (e.g. if all four measurements happen to have been made over cracks rather than perfect ice, the maximum light intensity which is possible to pass through the sample may not have been recorded).

As a consequence, the e-folding scale calculations have been conducted on an exponential curve fitted to the data, repeated for the minimum light intensity measurements – representative of highly cracked ice or cloudy ice states, maximum light intensity measurements – representative of the most ideal and transparent samples, and then the average light intensity measurements. This range of different states for the ice samples has value, as it is representative of the different states of a natural ice slab as it would occur in the Martian polar regions. Here, the ice caps are thought to evolve over time from low albedo smooth slab ice through to bright, highly fractured ice in the Martian spring (Hansen, 1999).

The e-folding scale calculated using minimum light intensity measurements for samples 1 and 2 is higher than that calculated using the maximum data (see Table 4.3.1). This can be explained by the fact that these samples started out more opaque or ‘cloudy’, and so light penetration was lower than in the other samples. As measurements commenced, the minimum amount of light able to penetrate through the sample increased steadily. However, additional cracks would reduce the maximum light intensity, and so the rate of increase in light penetration was slower than that for the minimum results. In contrast, samples 3 and 4 were much more transparent at the beginning,

and so any cracks forming would affect the minimum and maximum readings more equally than in samples 1 and 2. Consequently, we have more confidence in the results obtained from samples 3 and 4. The quality of the exponential fit can be demonstrated by assessing the coefficient of determination, which is a measure of the goodness of fit, R^2 (Devore, 2004), of the exponential trend line to the data. If the exponential trend line perfectly explained the observed data, then R^2 would equal 1, whereas if some variation is unexplained R^2 <1; the closer R^2 is to unity the better the trend line explains the data. For sample 3: R^2 Min = 0.853, R^2 Mean = 0.921 and R^2 Max = 0.772. For sample 4: R^2 Min = 0.902, R^2 Mean = 0.929 and R^2 Max = 0.622. The trend line fit to the maximum data is the worst for both samples, but this is due to the erratic measurements from the cracking events. The fits of the trend lines to the minimum data, but most importantly to the mean data, are both good, and therefore shows that this method of fitting an exponential curve to light intensity measurements, which is then used to calculate the e-folding scale, is a viable approach.

Sample No.	E-folding Scale, ζ (mm) CO_2		
	Min Intensity	Mean Intensity	Max Intensity
1	40.00	32.58	28.57
2	43.48	33.33	30.30
3	35.71	47.62	58.82
4	35.71	47.62	71.43

Table 4.3.1. E-folding scale of CO_2 slab ice results based on the minimum, mean and maximum light intensity measurements for each sample.

4.4. H_2O Ice Results

11 samples of solid water ice were prepared, following the methodology previously detailed in Section 3.2. Measurements were taken at five locations, one in the centre, and 4 locations at approximately 90° to each other, roughly 40 mm from the centre of the sample, whilst ensuring the area around the pyranometer was completely within the shadow of the ice. As with the CO_2 ice, the errors in ice thickness are estimated to be ± 2 mm, with errors in light intensity readings to be negligible in comparison. Figure 4.4.1 shows photographs of all the samples, ranging in thickness from 15 mm to 35 mm. From these it can be clearly seen that some samples are of better quality than others, and that almost all have some 'cloudiness' or 'milkiness' in the middle of the samples. This is simply an effect of the freezing process and is a combination of small air

bubbles and some internal fracturing. However, in some samples this extended outwards from the centre in streaks or segments, making the whole ice slab inhomogeneous. This is likely to be due to the water cooling and freezing too rapidly.

Measurements were made on all samples. However, the data from samples which were the most inhomogeneous are extremely inconsistent and have been excluded from further analyses. The samples exhibiting the most extreme inhomogeneities are sample numbers 4, 9 and 11, and have been denoted by red crosses in Figure 4.4.2. It should be noted that Sample 3 exhibits a similar distribution of cloudy and clear ice sections, but not to the same extent, with smaller proportion of cloudy ice, and so has not been excluded. Additionally, the cloudiness in samples 5 and 7 radiates out further than in some of the other samples, which is not ideal, but as it appears to be radially quite consistent the data from these samples are also retained for analysis.

Due to the comparative stability of water ice, as opposed to the CO_2 ice, a second set of measurements was made at each ice thickness for all samples. The intention of this was to increase the sample size in order to increase the reliability of results. Upon data analysis it became clear that that the light intensity measurements made in the centre of the sample were of significantly lower intensity than those made in the surrounding area, and, when the data were averaged, this caused a skew in the result which was not representative of the whole (see example of raw data in Table 4.2). This effect can be seen quite consistently throughout the data, and so the 'centre' data measurement has also been excluded from all further analysis. Upon visual examination of the samples, it can be clearly seen that there is a region of air bubbles concentrated in the centre of each sample, and so it would be inaccurate to include measurements made at these locations due to the vastly increased scattering centres though which the light passes.

Whilst removing this central measurement reduces the data spread, some variation remains due to a combination of the naturally occurring imperfections in the ice, slight variation in the output intensity of the solar simulator and human error in accuracy of recording the measurements. The large cracking events which were noted during the CO_2 ice measurements, and which are observed in the resulting data, are not seen to the same extent in the water ice measurements. Not only does water ice have a much lower thermal expansion coefficient than CO_2 ice, but the temperature range which the water ice samples were exposed to were not as extreme, as they were stored at >-20°C between measurements, rather than -86°C which CO_2 ice was stored at.

Ice thickness (mm)	Light Intensity (mV)				
	Centre	90°	180°	270°	360°
30	17.761	53.215	51.438	48.427	37.618
25	36.244	51.855	73.924	47.289	66.432
16	36.397	99.116	97.698	79.273	91.071

Table 4.4.1. Example of raw light intensity measurements made on water ice Sample 1. The first measurement was made in the middle of the sample – 'Centre', with the others spaced radially about the centre. The angles denote approximate locations of measurements, when 360° was orientated towards the viewing direction. Whilst there is quite a large scatter in the data as a whole, the biggest difference is seen between the measurements made at the centre of the sample compared to all the others (often the centre intensity measurement is approximately only 50% of the other measurements). This disproportionately effects the mean value calculated from the data, which is then used to determine the e-folding scale.

The e-folding scale results, calculated from light intensity measurements of water ice slabs, are shown in Table 4.4.1. Following the same methodology used to calculate the e-folding scale of CO_2 ice, the data were separated out into the minimum, maximum and mean values for each sample. The average (mean) of all samples is given, and then the average calculated by excluding the identified poor quality samples (Samples 4, 9 and 11). It is the use of these final results which is recommended. Both the full and edited data are displayed in the graphs shown in Figure 4.4.2, where, whilst there is still variation within the data, it is more consistent when the poor quality samples and central data points are excluded. R^2 has also been determined for the water samples. Sample 2 is excluded from this analysis, as there are only two data points so R^2 will always equal 1. By averaging across all samples and data subsets (minimum, mean, and maximum light intensities) the R^2 value can be compared for the full dataset and the data excluding the central measurement points. By removing the centre measurements, the mean R^2 value has improved from $R^2 = 0.819$ to $R^2 = 0.825$.

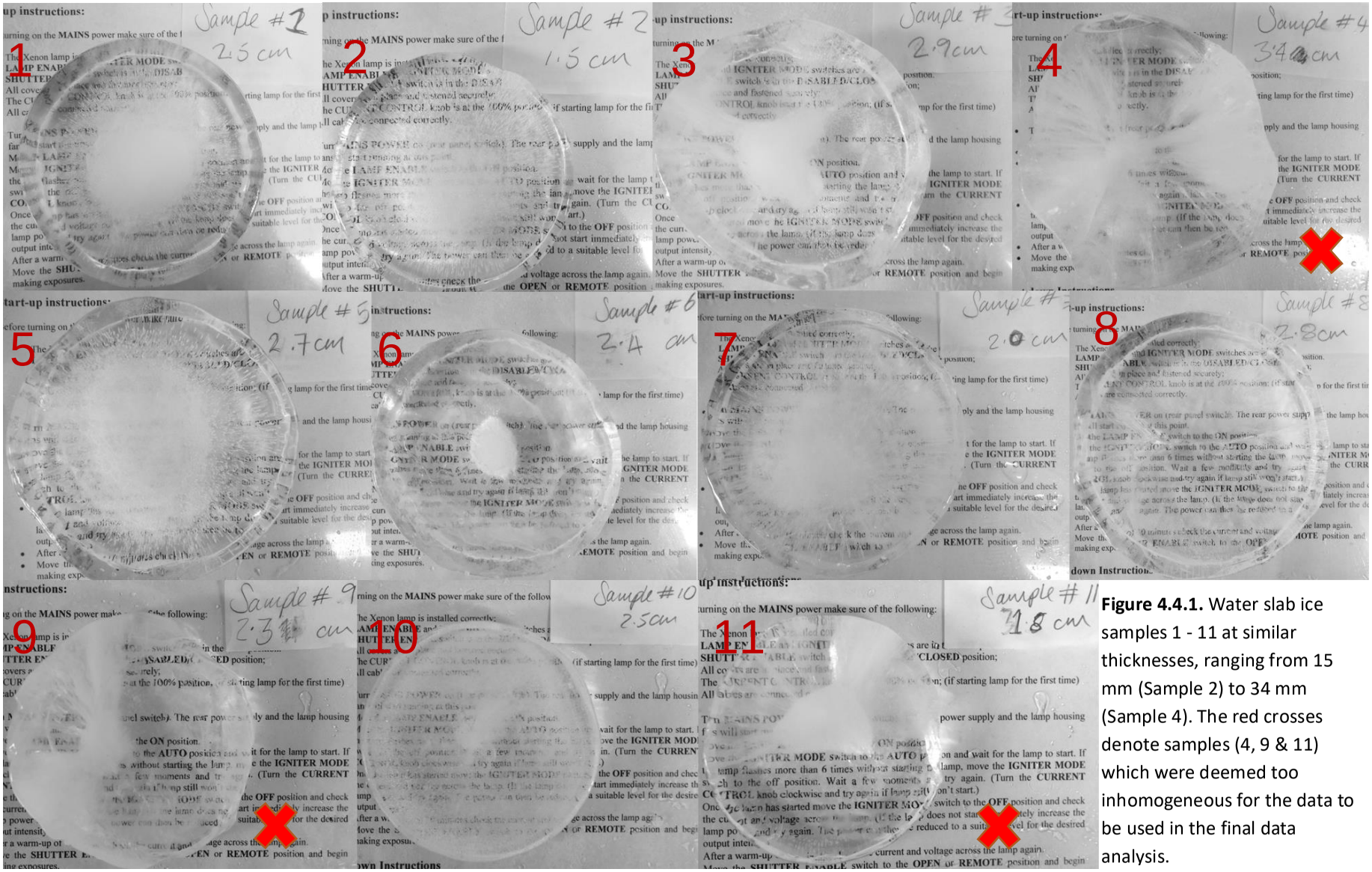

Figure 4.4.1. Water slab ice samples 1 - 11 at similar thicknesses, ranging from 15 mm (Sample 2) to 34 mm (Sample 4). The red crosses denote samples (4, 9 & 11) which were deemed too inhomogeneous for the data to be used in the final data analysis.

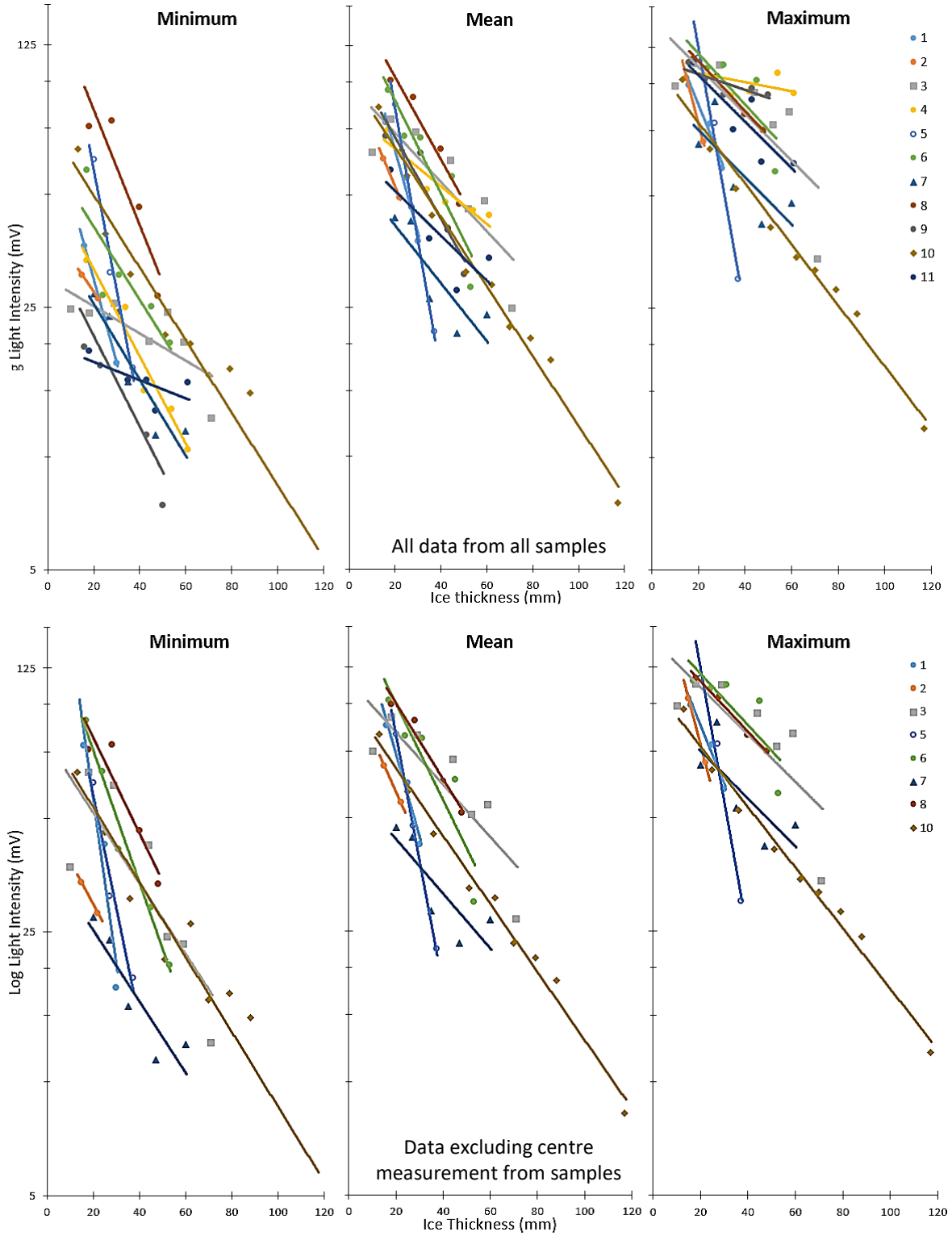

Figure 4.4.2. *Top*: graphs displaying the minimum, mean, and maximum values from all locations on all samples. *Bottom*: graphs showing the edited data set. This excludes measurements made at the centre of each sample, and all of the data from samples 4, 9 and 11. All graphs are plotted with a logarithmic scale on the y-axis. By removing the central data points, averaged across all the data, this improved the quality of the exponential fit (R^2) from mean R^2=0.8184 to R^2=0.8250 (excluding sample 2 in both instances because, with only two data points R^2=1).

Sample No.	E-folding Scale, ζ (mm) H_2O		
	Min Intensity	Mean Intensity	Max Intensity
1	9.90	20.00	28.57
2	38.46	31.25	17.86
3	45.45	62.50	71.43
✖ *4*	*31.25*	*83.33*	*333.33*
5	14.49	12.99	12.35
6	25.00	34.48	62.50
7	45.45	58.82	66.67
8	34.48	43.48	66.67
✖ *9*	*25.00*	*37.04*	*200.00*
10	43.48	47.62	55.56
✖ *11*	*100.00*	*66.67*	*71.43*
Mean (all)	37.54	45.29	89.67
Mean (edited)	**32.09**	**38.89**	**47.70**

Table 4.4.2. E-folding scales calculated using outer measurements only (central data excluded). Samples 4, 9 and 11, which are denoted by red crosses, are excluded from the mean (edited) value given at the bottom of the table. These correspond to the samples marked in Figure 4.4.1.

4.5. Discussion

By comparing the final results for carbon dioxide and water slab ice we can see that, the e-folding scale of CO_2 ice is consistently higher than that of H_2O ice (see Table 4.5.1). This is true for each subset of results: whether the e-folding scale was calculated using the minimum light intensity data, the average, or the maximum, each consistently gives a lower e-folding scale for water ice than for carbon dioxide ice.

When comparing the results from both the water and carbon dioxide ices, it should be reiterated that these ices were formed in the laboratory under terrestrial conditions. This means that, whilst every effort was made to reduce the content of air bubbles which formed in water ice, they are obviously very much present in the samples, albeit concentrated in the central regions of the slab, measurements from which have been excluded. However, water ice forming on Mars is unlikely to have anywhere near as much trapped atmospheric gas, due to the much lower atmospheric pressure. It would therefore be reasonable to assume that the general e-folding scale

used for H_2O slab ice is ζ = 38.9 mm, unless in pristine condition (no cracks, bubbles or impurities) when ζ = 47.7 mm would be appropriate.

Ice composition	Average E-folding Scale, ζ (mm)		
	Min	Mean	Max
CO_2	35.71	47.62	65.13
H_2O	32.09	38.89	47.70

Table 4.5.1. Summary table of the calculated e-folding scales for water and carbon dioxide slab ice based on broad spectrum (300 - 1100 nm) light intensity measurements.

As for CO_2 ice, during the course of the measurements, both the temperature was kept as cold as possible, and the atmosphere within the chamber as dry as possible, by flooding with cooled argon. However, this method was not perfect as the processes of replacing the samples introduced some ambient air into the chamber, and so some small amount of water frost did form on the glass on which the samples were placed. This was cleaned off completely between samples, and so was only a very minor factor. However, fluctuations in temperature did occur, and in some cases led to cracking of the ice. The effect of this was reduced by the way in which the data was processed: by taking the minimum values for each ice thickness measurement, the maximum and then the mean separately to calculate the range of penetration depths depending on the state of the ice slab.

It is therefore reasonable to give an e-folding scale value of ζ = 35.7 mm ± 7.7 mm for cracked, higher albedo CO_2 ice, but for perfectly smooth, unblemished slab ice ζ = 65.1 mm ± 6.3 mm would be more applicable. Similarly, I would recommend the use of ζ = 32.1 mm for cracked, cloudy water ice, ζ = 47.7 mm for pristine, highly translucent ice, and ζ = 38.9 mm for an 'average' water ice slab. However, I would urge caution with using the highest estimations of the e-folding scale, for in reality, any thermal variations, such as the diurnal insolation cycle, are likely to cause thermal cracking of the CO_2 slab ice. Although to counter this, a slab of CO_2 ice on Mars is able to self-heal: in the same way that sintering occurs (by diffusion and re-condensation), so, as long as conditions are favourable CO_2 ice will form within the cracks, sealing them and once again reducing the albedo and increasing the penetration depth.

The range of penetration depths calculated for CO_2 ice has applications in late winter at the end of the polar night, when a thick, clean CO_2 ice slab is present on the surface, as described by Pilorget et al. (2011). As insolation levels increase dark spots, or spiders, rapidly begin to form, which then contaminates the ice with dust from the underlying regolith. For other scenarios where

the slab would be illuminated diurnally with solar radiation, the use of ζ = 47.6 mm for an average CO_2 ice slab is recommended.

Chapter 5

The Penetration Depth of Snow

In this chapter, the specific methods used for making light intensity measurements in snow are detailed, with samples composed of both water and carbon dioxide ices. This builds on the general experimental methodology given in Chapter 3. The penetration depth of broad spectrum solar radiation has been calculated for each sample, with the results presented here. The advantages and limitations of these experiments are discussed, along with some applications for the results.

The data presented in Section 5.3 of this chapter have been previously published in:

Chinnery, H. E., Hagermann, A., Kaufmann, E. and Lewis, S. R., 2019. The Penetration of Solar Radiation into Water and Carbon Dioxide Snow, with reference to Mars. Journal of Geophysical Research: Planets, 124(2): 337-348.

5.1. Introduction

Whilst there have been numerous measurements of the penetration depth of light in water snow, these have tended to be on naturally occurring samples, with no grain size constraints, no contaminant control and at discreet light wavelength ranges. The snow used for the e-folding scale experiments by Kaufmann and Hagermann (2015) was made by an industrial snow cannon, and was later found to contain some contaminants. This is acceptable for determining the effect of dust contamination, which was their goal, as it was the only variable in the system, but not ideal for determining the e-folding scale of pure water snow. Therefore, Kaufmann & Hagermann's value of 5.4 ± 1 mm for the e-folding scale of pure water snow is likely to be too small because the effect of contaminants generally decreases the e-folding scale.

France et al. (2010) also conducted light intensity measurements through pure and dust contaminated snow packs. They generated their water snow by spraying pure water into a bath of liquid nitrogen, similar to the method used in the study presented here, meaning the snow was free of contaminants. However, the samples were then left to sinter for 24 hours at 253 K. Based on hardness measurements of snow sintered to different degrees by Grabowski (personal communication, 2018), this would result in the snow being substantially sintered, equivalent to a 10 – 15 % increase in hardness. This results in grains both growing and partially fusing together, thus removing scattering surfaces and increasing the path length over which light propagates through the snow grains. In contrast, there is no current literature on the topic of light penetration on carbon dioxide snow, despite this being a naturally occurring phenomenon on Mars (e.g. Hayne et al., 2012; Kuroda et al., 2013; Titus et al., 2001).

Here the experimental results for the broad spectrum (wavelength range of 300 nm – 1100 nm) e-folding scale of snow, composed of both H_2O and CO_2 ices are given, in order to determine how the presence of CO_2 snow affects surface processes which are driven by the interaction of solar irradiation with a surface. It is also important to have accurate and consistent water snow measurements, made under the same conditions, in order for direct comparisons to be made. The full dataset can be found in Appendix B.

For the purposes of this investigation, 'snow' is used to describe fine-grained or porous ice deposits, of either H_2O or CO_2 ice. This could therefore be representative of both snowfall and surface frosts. Kaufmann and Hagermann (2015) and France et al. (2010) conducted experiments to determine the effect of adding Mars simulant dust to the e-folding scale of light in water snow, using different methodologies. These experiments resulted in e-folding scales for pure water snow an order of magnitude different. What neither of these studies addressed, however, is how the presence of CO_2 snow, rather than water snow, affects the light penetration depth within Martian

snow packs. CO_2 snow is a likely occurrence on Mars due to the climatic conditions prevalent today. However, the extent of snowfall is currently not agreed upon: simulations by Kuroda et al. (2013) suggest around 50% of the seasonal cap originates as snow, whereas models by Hayne et al. (2014) give a 3% - 20% mass contribution by snowfall to the seasonal ice deposits. On the other hand, water snow or surface frosts, the latter having been observed by the Phoenix Lander (Smith et al., 2009), are likely to contribute a much smaller amount to surface ices due to the very small proportion of water vapour in the atmosphere, approximately 0.03% (Gillmann et al., 2009).

The combination of all these factors shows the importance of broad wavelength range light penetration measurements, using both pure CO_2 and H_2O snow, in order to accurately determine the penetration depth of solar light. These experiments were specifically designed to tackle the second of my research questions: how does the penetration depth of broad-spectrum solar irradiation vary with ice morphology? In addition to this, these results allow the penetration depths for water and carbon dioxide snow to be directly compared. On a broader scale, these measurements could lead to more accurate models of radiative transfer at the Martian surface, which could improve estimates of CO_2 snow deposition (such as those by Forget et al. (1998)), sub-snow surface temperatures and snow-covered shallow subsurface heat flow gradients, all of which could contribute to a better understanding of the dynamic Martian surface.

5.2. Method

A series of copper rings 86 mm in diameter (painted black on the inside to prevent internal reflections), and of 5 mm, 10 mm and 20 mm in thickness, were used to contain the snow samples at set thicknesses inside the chamber. This ensured consistent volumes of snow and made reducing the thickness of the snow pack for consecutive measurements quick and accurate. The sample was placed on the glass plate inside the chamber, the solar simulator lamp turned on and first light intensity measurement taken. The shutter was closed on the solar lamp between measurements in order to minimise sublimation and sintering. For water snow, four measurements were made per snow thickness, one in the centre and three further measurements at different locations in the sample offset from the centre. This is in order to reduce the effect of any slight inhomogeneities present within the sample. However, due to the rapid sintering rate of CO_2 snow just one measurement per snow thickness could be made. To compensate, many more CO_2 snow samples were measured, so that a similar volume of data for both snow compositions was achieved. The experimental set up and equipment used is described in detail in Section 3.4, with a schematic shown in Figure 3.4.5.

The top copper ring was then removed, and the snow sample gently scraped smooth along the level of the underlying copper ring with the flat edge of a plastic spatula to the next required thickness. This was conducted whilst inside the chamber and flooded with cooled argon. The lamp shutter was then opened in order to take the next measurement, and the process repeated as swiftly as possible. Bohren and Barkstrom (1974) suggested that light transmission experiments in snow should be made using a sample container whose diameter is at least twice the maximum sample thickness, in order for any interference from the walls on the sample to be negligible. Therefore, the maximum snow thickness used for any measurements was 35 mm (to ensure this effect is minimised completely). In addition, like Kaufmann and Hagermann (2015), I found that the larger the snow sample, the greater the errors induced from a number of sources. Consequently, to minimise the error of sample thickness measurement, maximise the amount of energy analysed by the pyranometer, and minimise errors introduced by secondary reflections from and diffuse scattering within the sample, measurements were mainly taken over a range of 15 mm, and the results exclusively calculated over this range. Measurements were taken through samples at 15 mm, 10 mm and 5 mm for both water and carbon dioxide snows.

Each sample was weighed prior to irradiation commencement, and so the initial density of each snow pack has been calculated for both H_2O and CO_2 snow. It was not possible to weigh the samples in between irradiation events at each thickness, as this would have exposed the samples to warmer temperatures and humidity, accelerating sintering rates and increasing the amount of water frost contamination in CO_2 snow samples, and melting in the water snow samples. It was particularly important to prevent melting of the water snow, as not only does liquid water have a slightly different refractive index to ice, water pooling in-between snow grains would essentially decrease the number of scattering surfaces within the solid by joining up grains with an optically similar material (ice/air boundary compared to ice/water boundary), and so will cause much less scattering, and therefore less attenuation, than without the liquid phase. Large differences between the optical properties of two adjacent media cause a greater amount of refraction and therefore scattering to occur, and as liquid water has a much more similar refractive index to ice than air does. This will have the effect of reducing attenuation within the snow pack, increasing the e-folding scale. Efforts were made at each reduction of snow thickness to only scrape the surface level without compacting the snow pack, although it is acknowledged that some small amount of compaction may have occurred.

Cooled argon continuously flowed into the chamber in an attempt to mitigate the formation of water frost on both the samples of CO_2 snow, and on the glass plate suspending the samples above the pyranometer. This also aided in maintaining cold temperatures within the chamber in order to minimise melting, sublimation and sintering.

5.3. Results

Light intensity measurements made through CO_2 and H_2O snow samples of different thicknesses were conducted using the same experimental set up, and the results used to calculate the e-folding scale, or penetration depth, of each material. These were made using a broad wavelength range across the visible spectrum (300 – 1100 nm). Figure 5.3.1 shows how the e-folding scale varies with density. A practice run was made to test the initial experimental setup and, for the sake of completeness, is also plotted and denoted by an orange cross. Several alterations to the setup were made based on this measurement, which included improvements to reduce air leakage into the chamber and flooding the chamber with cooled argon to prevent the formation of water frost.

The e-folding scale is calculated from the raw light intensity measurements by first adjusting the data for the 5 mm measurement to be taken as the zero depth to remove the effect of albedo (as discussed in section 3.6). All data are then normalized accordingly, and the e-folding scale ζ is calculated as per the methods described in Section 3.6. The full datasets of raw light

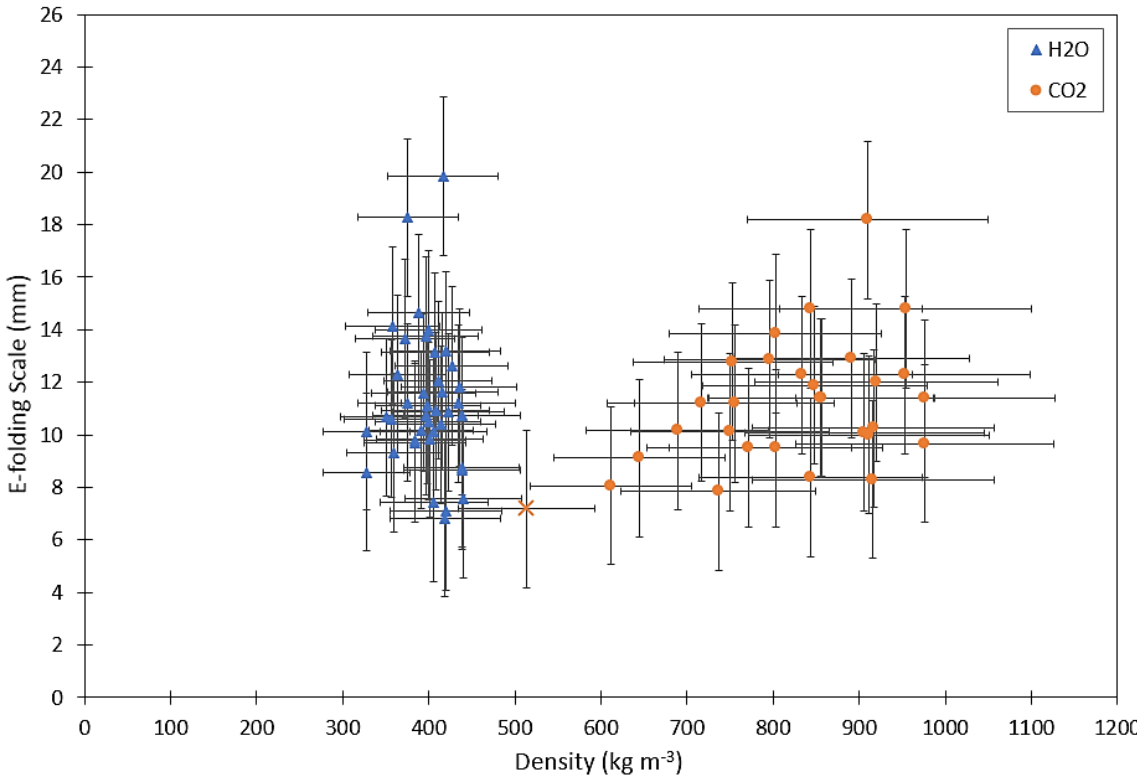

Figure 5.3.1. E-folding scale results plotted with snow pack starting density. The data point denoted by the orange cross was an initial run with CO_2 snow, which enabled the experimental setup to be refined. This practice run was excluded from further analyses of the data. Errors in the density measurements (horizontal error bars) are calculated based on measuring equipment tolerances, and the vertical errors for the e-folding scale account for both equipment tolerances and potential compaction introduced when scraping each snow thickness flat.

intensity measurements for both CO_2 and H_2O snows can be found in Appendix B. As water snow measurements have 4 data points for each sample thickness, the raw light intensity readings were averaged for each snow depth prior to calculating the e-folding scale. The results are plotted in Figure 5.3.1, where it can be seen that there is a weak correlation of higher e-folding scale with increased density, although this is less evident in the H_2O snow data than in CO_2 snow.

The density of CO_2 snow on Mars has been constrained to 910 ± 230 kgm^{-3} based on calculations by Smith et al. (2001), a range which is covered by our measurements, but could be significantly less dense upon initial deposition (Matsuo & Heki, 2009). To determine ice deposit density, the authors used changes in topography recorded by the Mars Orbiter Laser Altimeter (MOLA) on board the Mars Global Surveyor (MGS), and combined them with gravity information from MGS tracking data over the same time period. They then compared this information with the modelled changes in atmospheric pressure and the condensed/sublimated mass of CO_2 predicted by the general circulation models used, in order to calculate the density of the surface deposits. As the authors were conservative in their estimates of the dynamic range of elevation change, the value of 910 ± 230 kg m^{-3} is suggested to be at the upper end of the CO_2 snow density range on Mars. My results suggest that the e-folding scale does not vary significantly over the range of densities measured at the start of each experimental sample run. This observation is consistent with previous studies measuring other optical properties of water snow; Bohren and Beschta (1979) found that, if grain size were kept constant, then there was no significant change in albedo with compaction (an average 1 percentage point decrease in albedo for compacted snow, not significant at the 90% confidence level).

The mean e-folding scale of water snow was found to be 11.24 mm, and 11.25 mm for CO_2 snow (excluding the practice run). This result was unexpected given that the optical properties of these two materials are quite different. Additionally, the reported e-folding scale for H_2O and CO_2 slab ice has quite a large variation: the measurements reported in Chapter 4 show the e-folding scale of CO_2 slab ice varied from 35 mm to 65 mm depending upon the state of the ice sample, such as the extent of cracking or 'cloudiness' of the ice. The same method for water ice yielded e-folding scales ranging from 32 mm to 48 mm, smaller than for CO_2 ice. However, we propose that for small grain sizes such as snow, such a small amount of light transmission occurs through the ice grains that the material properties have a negligible effect and light transmission is dominated by scattering/multiple reflections between grains. This suggests that at these smallest scales, grain morphology and the number of scattering surfaces is more important than snow composition.

Water snow was prepared and sieved as outlined in the methodology (Section 5.2), and light transmission was measured on discreet grain size ranges. Artificial water snow can be kept pure and stable much more easily than CO_2 snow, and so grain size dependence was tested using only the former. If this had been attempted with CO_2 snow then sintering and H_2O frost accumulation would have occurred during the multiple sieving steps required, rendering the samples unusable. Figure 5.3.2 displays the results from the grain size analysis, where there is no discernible trend linking e-folding scale with grain sizes at this small scale, although it should be noted that scatter in the data increased with decreasing snow grain size. This is likely due to a number of factors, including the ability to accurately sieve such small ice grains to the prescribed size range, and the increase in the rate of sintering with decreasing grain size. It is therefore likely that the experimental error is highest at the smallest grain sizes and reduces with increasing grain size. However, I suspect the main contributing factor to this is sintering, and as the rate of CO_2 ice sintering is, as far as I am aware, unconstrained, I cannot determine the extent of the impact on these measurements. For simplicity, an experimental error of ±3 mm is applied to this data, with a caution that this value is likely higher at the very smallest grain sizes, and possibly lower with the larger grains.

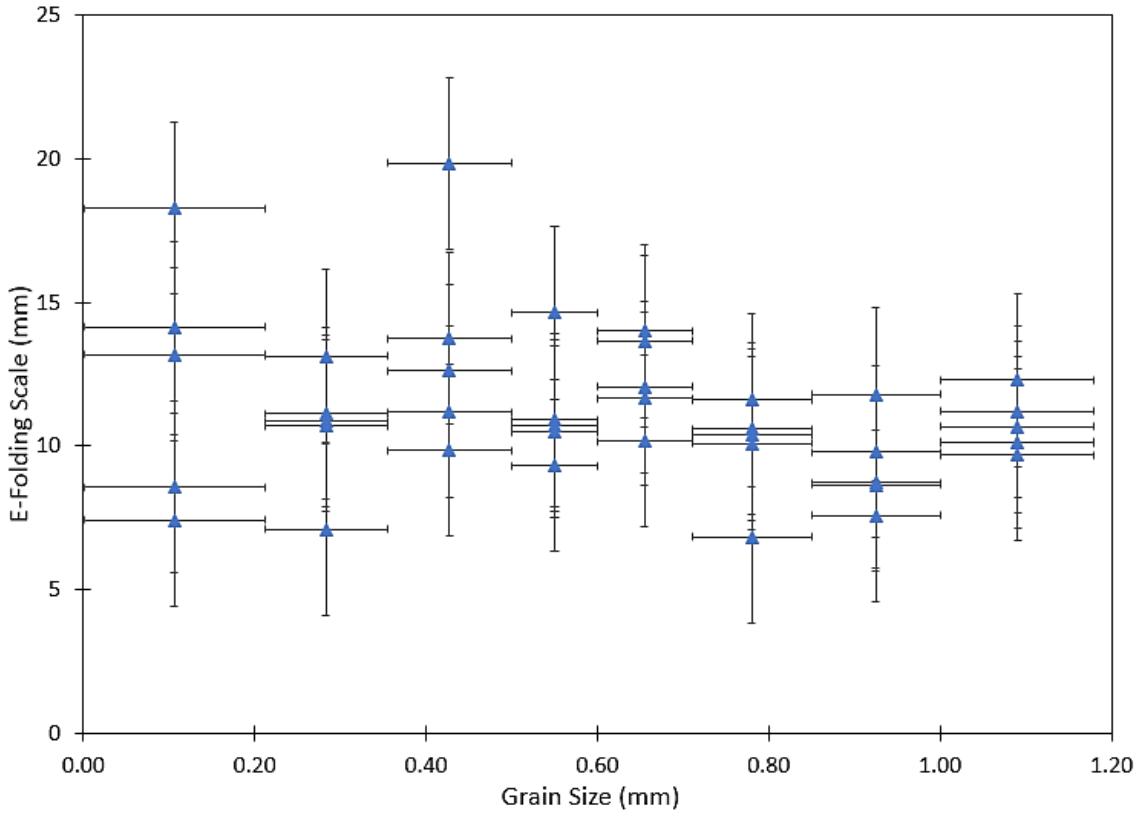

Figure 5.3.2. The e-folding scale results for water snow, dependent on snow grain size. Snow grains larger than 1.18 mm were deemed too big to be defined as 'snow', and so are not used for these analyses. Horizontal error bars simply denote the range of grain sizes contained within that sample. Vertical errors here are based on the experimental error, including device tolerance and potential slight deviations from snowpack thickness or surface smoothness.

An additional contributor to errors can be seen upon close scrutiny of the water snow. The snow grains had been sieved to discrete grain sizes, but when observed closely, or digitally magnified, it can be seen that the 'grains' actually appeared to consist of clumps of even smaller granules, as shown in Figure 5.3.3 for the grain size range 0.71 – 0.85 mm. It is therefore perhaps more accurate to describe the grain size ranges by using only the upper boundary. Whilst a finer meshed sieve was also used to define the lower limit of the grain size range, it cannot be conclusively said that that smallest individual grains are larger than this, only that the smallest clumps of grains are at least this size.

Figure 5.3.3. Water snow sieved to grain sizes between 0.71 mm - 0.85 mm. On initial inspection the grain size range appears consistent (left). However, when inspected at closer range (right), noting the scale shown on both images is in millimetres, clusters of grains much smaller than 0.71 mm can be seen clustered together forming conglomerates which appear to fall within the desired grain size range.

Based on these observations, it is impossible to tell with certainty whether these granular conglomerates behave optically as one unit, or as the individual constituents, scattering light at each internal interface. It would be reasonable to assume a range of behaviour with regard to this, depending on the extent to which the conglomerate grain has fused together. It should, however, be noted that the snow used for the actual measurements was kept at consistently lower temperatures than the sample shown here, which would have warmed, and therefore likely sintered, to a greater extent during the process of photographing it. This suggests one contributing factor as to why, in the data presented here (Figure 5.3.2), we observe no significant trend between the penetration depth and grain size, despite theoretically being expected. In addition to this, as presented in Chapter 4, I found the e-folding scale of CO_2 slab ice to vary from around 35 mm to 65 mm, the upper limit being for near-pristine slabs, and the lower for highly cracked imperfect ice, reducing the effective 'grain size' or path length between cracks. It seems most likely that the large

range of actual grain sizes, due to the difficulties in constraining the grain sizes by sieving, make it difficult to discern a trend in the data.

Beaglehole et al. (1998), conducted light transmission experiments in naturally formed Antarctic snow, and modelled their results using spherical snow particles and two flux theory, which showed that whilst the absorption coefficient should scale with relative density, the scattering coefficient should scale inversely with grain size. This helps explain my observation of little density dependence in the e-folding scale results from these measurements of snow grains <1.18 mm, and why it is the same regardless of composition, as little absorption is occurring. However, it also implies that there should be strong grain size dependence. I suggest that this trend is obscured by uncertainties in determining the minimum grain size range for each snow sample, as discussed above. Combined with the relatively small range of grain sizes analysed, this results in inherent errors which are larger than the amplitude of any trend which could have been recorded. A more extensive range of measurements covering a much larger range of ice grain sizes, formed using compact ice, would be required to determine the underlying cause of these observations.

5.4. Discussion

The snow used for the e-folding scale experiments by Kaufmann and Hagermann (2015) was made by an industrial snow cannon and contained some contaminants. and so the e-folding scale value of 5.4 ± 1 mm is likely to be too low an estimate for pure snow. France et al. (2010) also conducted light intensity measurements through pure and dust contaminated snow packs. Their snow was made using deionised water in a method similar to that presented in this thesis, but their samples were left to sinter for 24 hours at 253 K. As sintering changes the structure and effective grain size of the snow, I think this results in their reported e-folding scales to be too large, at an order of magnitude greater than that measured by Kaufmann and Hagermann (2015). By contrast, the samples for our measurements were always freshly prepared – and contained minimal impurities. It should also be noted that France et al. (2010) used a narrower wavelength range, from 400 nm to 700 nm, whereas the measurements presented here utilise the broader wavelength range of the pyranometer (300 nm – 1100 nm), which could also explain some discrepancy in the results. This is demonstrated by the vast range of e-folding scales of sea ice reported by Perovich (1996) and discrete wavelength ranges, from 24 m at λ = 470 nm, decreasing dramatically to 5 cm at λ = 1000 nm and 6 mm at λ = 1400 nm.

A sophisticated model of solar radiation penetration in CO_2 ice was created by Pilorget et al. (2011) which combined both radiative and conductive heat transfer methods with the optical

properties of carbon dioxide ice. The findings presented in this chapter are consistent in principle with these model results, in that small grains of CO_2 ice, of a size classed as 'snow' throughout this study, do now allow enough light to penetrate through a layer to allow for any significant heating of the underlying regolith. What this study did not provide, however, were the resultant penetration depths for CO_2 ice in the different scenarios modelled.

An implication of such a small e-folding scale for fine-grained ices is that if there is even a small amount of snow cover on top of the seasonal ice slab, which could remain suitably cold so as to not cause rapid sintering of the snow, then light penetration into the ice sheet could be dramatically dampened. This would hamper the formation of araneiforms, for example, which only occur when adequate energy can be transmitted through the ice to the underlying regolith. This is in order to heat the regolith sufficiently to cause basal sublimation which leads to CO_2 jetting, as per the CO_2 jetting model (Kieffer, 2007; Kieffer et al., 2006; Kieffer et al., 2000; etc.).

Perovich (1996) states that, on Earth, a 25 cm covering of snow on top of an ice sheet would reduce light transmittance to less than 1%, implying an e-folding scale of less than 5 cm. Whilst this would be a large amount of CO_2 snow to accumulate on Mars, the simulations run by Colaprete (2002) indicate that 0.75 g of CO_2 snow could be deposited per cm^2 during one hour of snowfall beneath the CO_2 clouds forming the polar hood. If using a snow density of 910 kg m^{-3} (Smith et al., 2001), this equates to 8.2 mm thick deposit of snow, and given the e-folding depth of 11.2 mm ±3 mm, even at these lesser snow depths a significant reduction in radiation intensity will occur, potentially halting the CO_2 jetting process whilst the snow remains in situ. Smith et al. (2001) monitored elevation changes using MOLA over a Martian year and found not only the expected increase in elevation due to seasonal ice deposition during winter, but they also observed transient accumulations of snow during the summer in both the northern and southern hemispheres. They attribute this to CO_2 snowfall, which in the northern hemisphere only occurred over the residual ice cap at 85°N, with an approximate 40 cm accumulation near the end of summer. In the south, however, localised elevation changes were recorded both on and off the residual cap, of 30 cm and 50 cm depths at the latitude of 65°S during late spring-early summer. The authors speculate that these summer snowfalls could be caused by shadowing of the surface by regional topography (which seems unlikely given the relatively low topographic profile of the polar regions), redistribution of surface frosts by winds, or transient local storms of greater intensity than predicted by the models of that time. The authors did not comment on the time period over which these deposits were recorded in the elevation data, but it is likely they would not have remained at their initial thickness long, for if temperatures were close to, but remained below, the sublimation point of CO_2 ice, sintering would occur rapidly. The rate of this is currently unknown. However, in Section 3.4 it is shown that, if CO_2 snow is kept close to the sublimation point under terrestrial

conditions (in this case at 187 K in the laboratory freezer), grain growth and densification is already well underway within seven days, and forms thin sheets of ice by 17 days (see Figure 3.4.3). In order to maintain consistent temperatures, the samples were not checked daily and so these processes could have occurred in less time than was recorded. This could be comparable to sintering rates on Mars, as long as the temperature is close to the sublimation point for the pressure conditions, although more work on this is required. However, at temperatures much lower than the sublimation point, sintering rates will be lower, and so snow deposits would be longer lived.

That being said, it would not necessarily require snowfall to emplace fine-grained ice deposits. One of the issues raised by Pilorget et al. (2011) was that CO_2 jetting was observed on dune slopes but not on the flat areas between dunes. They suggested that venting was still occurring in these areas, but the underlying regolith on the flat areas has a higher albedo than that of the dune material, and so made it harder to observe. In addition to the issue of detection, it could also be speculated that, if fine-grained icy debris ejected from the vents on the dune slopes were carried downslope (either simply by gravity, or wind-blown) and deposited around the foot of the dune, that the presence of even a thin layer of granular ice on top of the slab ice, combined with the higher albedo regolith (therefore less absorbing) could be enough to suppress jetting activity.

CO_2 sublimation processes have also been linked to the formation of gullies in the absence of liquid water (e.g. Cedillo-Flores et al., 2011; Hoffman, 2002; Pilorget and Forget, 2016; Vincendon, 2015). These are mainly found in the 30°- 60° latitude range in both hemispheres, and activity has been linked to the time when seasonal CO_2 frost is present on the surface and beginning to defrost (Pilorget and Forget, 2016). In a series of laboratory experiments, Sylvest et al. (2018) condensed CO_2 frost onto JSC Mars-1 simulant regolith, held at angles ranging from 10° through to the angle of repose, in order to investigate gully formation when exposed to incident radiation. They found that the CO_2 formed as fine grained deposits on the surface, which they estimated to range in size from a maximum of 1 mm down to the size of the pore space (Sylvest, 2018, personal communication), and between the regolith grains beneath the surface. Significant thicknesses of CO_2 frost (up to several centimetres) can accumulate on pole-facing slopes even at mid-latitudes, despite being illuminated by the sun (Schorghofer and Edgett, 2006).

The combined results from light intensity measurements in snow of both compositions suggest that at smallest scales, grain morphology and the number of scattering surfaces is more important than snow composition. This means that, regardless of whether carbon dioxide or water snow of frost is forming, if that deposit has an e-folding scale of only 1.1 cm the underlying material, be it regolith or ice, is largely unaffected by insolation - and thus might remain colder than anticipated. Lower subsurface temperatures reduce gas movement through the pores in a sediment, affecting both the subsurface-atmosphere exchange of CO_2 and the likelihood of

sediment movement to be triggered by CO_2 sublimation. Lower subsurface temperatures also affect the sublimation of other volatiles present in the subsurface, such as water, increasing the survival time of any subsurface water ice deposits. Consequently, when the surface frosts have sublimed, the shallow subsurface will warm rapidly, causing subsurface volatiles to also sublimate. This could lead to slope destabilisation due to the high volume of outwards gas flow through pore spaces, and the removal of ice concreting regolith grains together. The combines impact of these two effects could trigger a gas-fluidised granular flow downslope, thus initiating the formation of a 'classic' gully, as per the model by Pilorget and Forget (2016) (and demonstrated in Figure 1.5.2).

Chapter 6

The Penetration Depth of Granular Ices

In this chapter the results from the light intensity measurements made through granular ices of both water and carbon dioxide compositions are presented. These range from grains as small as 0.355 mm in diameter, through to 8.00 mm in diameter. The specific methods implemented for sample preparation and measurements are detailed, building on those outlined in Chapter 3, and the e-folding scale for each grain size range calculated and presented here.

6.1. Introduction

Chapter 4 detailed the results for the penetration depth of broad spectrum solar irradiation in water and carbon dioxide ice in its most massive form, followed by its finest – snow, the results of which can be seen in Chapter 5. However, how the two end-member measurements relate to each other, and the behaviour exhibited in between is not defined. In addition, it is also unknown whether the same behaviour is seen for both carbon dioxide and water ice. My second research question is directly concerned with how the e-folding scale changes with grain size and composition, and so the experiments presented in this chapter were designed to specifically target the question of how the e-folding scale is dependent on grain size.

Some past experimental work of light penetration measurements in water ices and snow are detailed in the literature, but these have either been on naturally occurring Antarctic snow and sea ice (with all associated contaminants) such as Beaglehole et al. (1998), Brandt and Warren (1993), Datt et al. (2015) and Perovich (1996); impure snow (Kaufmann and Hagermann, 2015), or using narrower wavelength ranges, such as France et al. (2010), whose snow samples were stored for 24 hours in the freezer at 253 K, which may have resulted in a small but significant degree of sintering. Fewer previous works have focussed on carbon dioxide ice, but these also suffered from problems such as impurities in the ice (Egan and Spagnolo, 1969) and the use of samples only micrometres to a couple of millimetres in thickness (Hudgins et al., 1993; Quirico and Schmitt, 1997). What appears to have not been addressed is the relationship between the broad-spectrum penetration depth of solar radiation and the grain size of the ice.

Seasonal ice cap growth on Mars begins in autumn and is thought to occur via a combination of direct condensation of CO_2 from the atmosphere to the surface, and by precipitation as CO_2 snow (Kuroda et al., 2013). Surface water frosts were observed in situ by NASA's Phoenix Lander in 2008 (Smith et al., 2009), at its location in the Northern polar region, a photograph of which can be seen in Figure 6.1.1. A widespread, low-latitude diurnal CO_2 frost cycle was discovered in 2016 (Piqueux et al., 2016), showing the importance of understanding the behaviour of both ice compositions on Mars. Ice which forms as snow and frost gradually sinters and anneals to form slab ice, with high transparency and low albedo (Forget et al., 1995; Forget et al., 1998; Forget and Pollack, 1996). The process of sintering causes grain growth and densification over time, effectively changing the size and shape of the grains and increasing the optical path length through the ice. Therefore the penetration depth of that ice deposit will increase as the ice becomes more sintered (Eluszkiewicz, 1993).

In addition to frost and snow formation, ice grains of varying sizes are likely to be present on the surface of Mars due to a number of different processes. During spring, increased solar

irradiation initiates CO_2 jetting and araneiform formation. It is also likely that increased daytime insolation causes cracking due to thermal expansion/contraction cycles. Both of these processes can result in localised break-up of the ice slab into smaller pieces. CO_2 jetting can cause underlying regolith material to be brought to the surface, which has been observed as fans of debris orientated with the prevailing wind direction, and so contaminating the ice with dust. Wind-blown dust can also be deposited on the surface of the ice, although a dusty ice surface is likely to be short-lived. Solar radiation is absorbed by the dust grains much more rapidly than the ice due to the much lower albedo of dust. The dust grains then radiate heat to the ice in the immediate vicinity, causing it to sublimate. This process continues as the grain burrows down through the ice pack in its own microscopic sublimating gas bubble, until it is ejected from the bottom of the ice or can no longer receive enough insolation to cause localised sublimation, at which point isolated lenses of dust may accumulate at a particular depth in the ice sheet, depending on the penetration depth of sunlight. The linear burrow left behind is likely to rapidly reseal due to the overlying gas and ice receiving little heat from the grain, and so it refreezes, thus maintaining low slab porosity (Kieffer, 2007; Kieffer et al., 2000; Portyankina et al., 2010). This behaviour of dust layers in CO_2 ice has been recreated in the laboratory by Kaufmann and Hagermann (2017) demonstrating the CO_2 jetting mechanism.

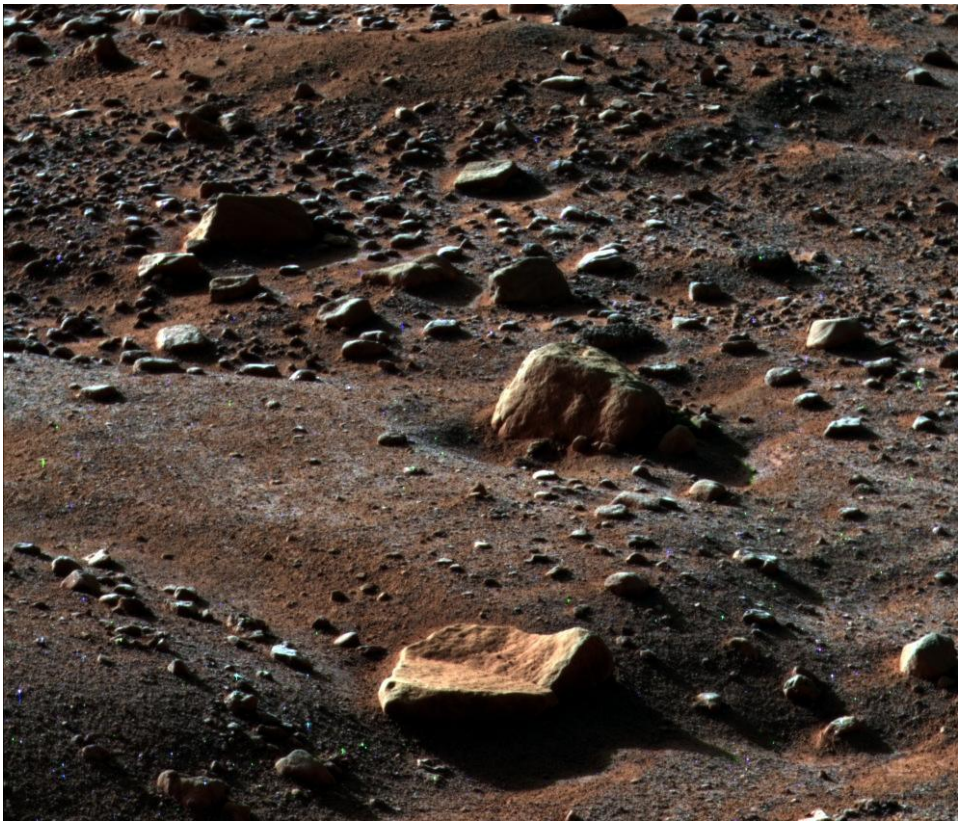

Figure 6.1.1. Photograph taken by NASA's Phoenix Lander at 6 am on its 79th Sol after landing, showing water frost visible on the surface. Image Credit: NASA/JPL-Caltech/University of Arizona/Texas A&M University.

Whilst accumulations of granular ice may not be particularly long-lived if the ice particles are small - microphysical models suggest surface sintering could occur rapidly, removing particles less than 1 mm in a matter of days (Clark et al., 1983; Eluszkiewicz, 1993; Eluszkiewicz et al., 2005) - particles larger in size or below the immediate surface could remain stable for much longer. Some small-grained deposits have indeed been observed to be much longer-lived, although these are thought to be in locations of frequent snowfall (Hayne et al., 2012). Therefore, in order to determine an accurate view of an icy subsurface, we need to understand how the penetration depth varies with grain size.

In this chapter I present my findings on how the e-folding scale varies with grain size, for both water and carbon dioxide ices. This has significant implications for understanding the evolution of the Martian seasonal and permanent polar caps, which incorporate both ice compositions in varying proportions, as well as the full range of grain sizes, which can change over time. It is important to understand how light penetrates into ice in all its different forms, as this leads to unique surface processes, such as CO_2 jetting (Kieffer et al., 2006), which by having constraints for the e-folding scale for the full range of ice grains sizes and compositions, will lead to improved models and a greater understanding of the Martian surface.

6.2. Method

Preparation of granular ice was conducted as per the methods described in Section 3.3. Measurements were then made on samples of each grain size range, and each discrete range contained at least 3 samples (but up to 6 in some cases). The light intensity measurements were made in exactly the same way as used for snow samples (detailed in Section 5.2). Similar problems to those which were encountered with snow measurements, such as sintering/melting, small amounts of the ice sticking to the glass plate, etc., were also encountered with finer grain size ranges. The larger grains were generally easier to work with as both sublimation and sintering rates were lower (than with smaller grains) due to the smaller surface area to volume ratio. However, at the largest particle sizes, the grains became large when compared to the dimensions of the sample containers. This made it more difficult to accurately scrape the sample flat along the top of the copper rings, and so presented an upper limit on the grain size ranges which could be measured with the equipment available. The sieve mesh sizes used to separate out the ice grains were: 0.355 mm, 0.50 mm, 0.60 mm, 0.71 mm, 0.85 mm, 1.00 mm, 1.18 mm, 2.00 mm, 3.50 mm, 4.00 mm, 5.60 mm and 8.00 mm.

6.3. Results and Analysis

Light intensity measurements were made at four locations at each sample thickness. Measurements were recorded and then averaged to give a mean light intensity per granular ice sample, per ice depth. In accordance with the methodology implemented in chapters 4 and 5, and that used by Kaufmann and Hagermann (2015), measurements taken at 5 mm snow/granular ice depth were taken as the reference point, and subsequent values normalised accordingly. This is because reliable albedo measurements are difficult to obtain, and so to avoid these additional uncertainties, only measurements taken at depths greater than that required to eliminate albedo variations were used. For the small ice grains, this snow scenario is adequate.

However, in Chapter 4 I found that for slab ice measurements a minimum ice depth of 8 mm was needed to remove the effects of albedo from the results, and a greater range of ice thickness measurements was required due to the increased transparency of compact ice. The granular ice samples were measured in increments of 5 mm, which reflects the copper ring sizes used to adjust sample height. With increasing grain size, the reference depth to which all measurements are adjusted to was increased to 10 mm, from 5 mm (as used for snow), and the depth range was also increased (see Table 6.3.1.). An additional advantage of increasing the minimum ice depth was to ensure that even with the largest grain sizes, there would be a full coverage of ice across the sample at more than one grain thick, which ensures consistency in measurements. If the sample were to be reduced to the thickness of just one grain,

Grain size range (mm)	Depth range of measurements used to calculate e-folding scale (mm)	
	CO_2	H_2O
0.355 – 0.50	5 – 10	5 – 10
0.50 – 0.60	5 – 10	5 – 10
0.60 – 0.71	5 – 10	5 – 10
0.71 – 0.85	5 – 10	5 – 10
0.85 – 1.00	5 – 10	5 – 10
1.00 – 1.18	5 – 10	5 – 10
1.18 – 2.00	5 – 15	5 – 15
2.00 – 3.35	5 – 20	5 – 20
3.35 – 4.00	10 – 25	10 – 25
4.00 – 5.60	10 – 30	10 – 30
5.60 – 8.00	10 – 30	10 – 30

Table 6.3.1. Granular ice depth ranges over which the e-folding scale was derived. Both the starting depth or 'zero point' and the range of depth required increased with larger grain sizes due to lower albedo and greater transparency of the sample.

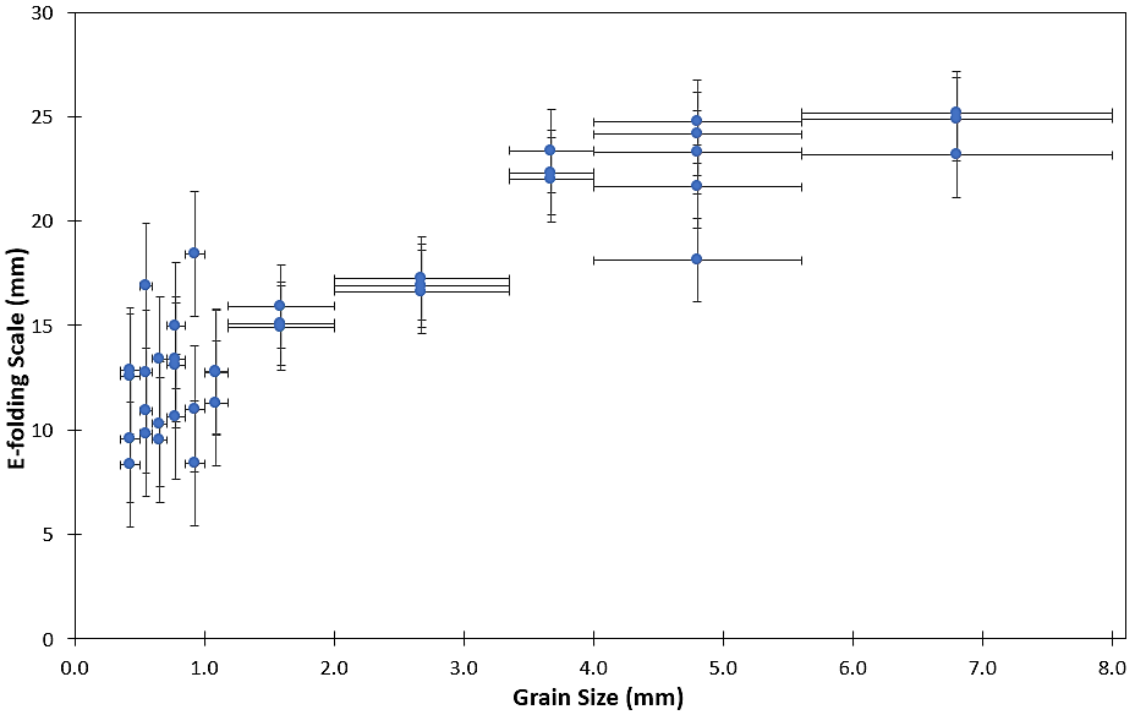

Figure 6.3.1. Results from light intensity measurements were used to calculate the e-folding scale of granular CO_2 ice, plotted here, showing an increase with larger grain size. Horizontal error bars denote the grain size range, vertical error bars are the estimated experimental error of ±2 mm for grain sizes >1.18 mm, and ±3 mm for grain sizes <1.18 mm.

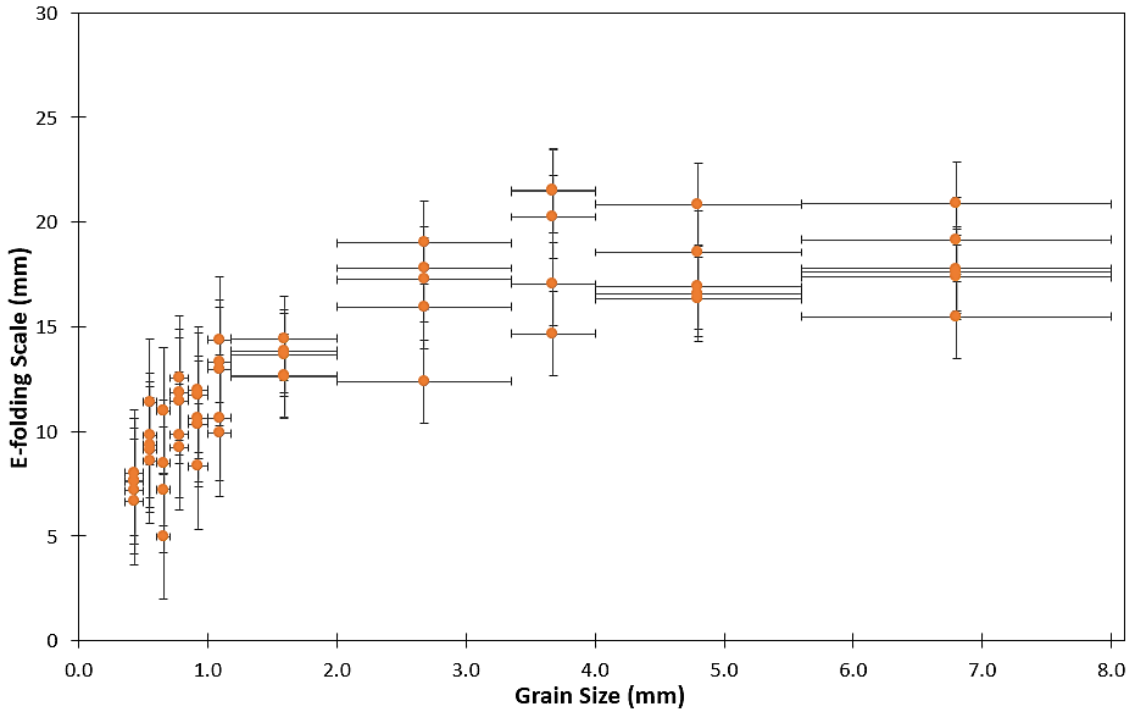

Figure 6.3.2. Results from light intensity measurements were used to calculate the e-folding scale of granular H_2O ice, plotted here, showing an increase with larger grain size. Horizontal error bars denote the grain size range, vertical error bars are the estimated experimental error of ±2 mm for grain sizes >1.18 mm, and ±3 mm for grain sizes <1.18 mm.

then there is a chance of accidentally making a measurement between the grains, rather than ensuring light is always penetrating through at least one layer of ice grains before being recorded by the pyranometer.

The normalised measurement values were then used to calculate the e-folding scale for those grain sizes. The resulting e-folding scales for granular CO_2 and H_2O ice have been plotted in Figure 6.3.1 and Figure 6.3.2 respectively. For both plots the horizontal error bars denote the range of grain sizes used in each experimental sample, and the vertical errors for the e-folding scale are an estimate based on experimental error, including device tolerance and human error. Generally, the penetration depth increases with increasing grain size, as would be expected, although not linearly.

In both types of ice, but more pronounced with CO_2 ice, there is greater data scatter at the smallest grain sizes. This is due to several factors. In CO_2 ice, the smallest grains experience the most rapid sintering, Whilst efforts were made to minimise this (e.g. using samples as quickly as possible after preparation, storing for the short periods required using liquid nitrogen to cool the samples, flooding the experimental chamber with cooled argon gas), it is likely that some sintering occurred when the grains were exposed to the solar simulator irradiation.

Similarly, with the smallest grains of water ice, a small amount of melting occurred when the solar simulator lamp was in operation. The chamber was still cooled, but not to such cold temperatures as was used for CO_2 ice measurements. This is because, during testing, cooling the chamber too much caused the grains in contact with the glass to stick, and made collecting multiple measurements difficult. All of these issues were dramatically reduced in the larger ice grain sizes. Due to this, I estimate the data errors on grain sizes <1.18 mm to be ±3 mm, as used for the snow e-folding scale measurements in Chapter 4, but for the larger grains >1.18 mm ±2 mm, akin to the slab ice measurements presented in Chapter 3.

It can be seen from the data presented in Figure 6.3.1 and Figure 6.3.2 that the e-folding scale increases with increasing grain size. However, granules of carbon dioxide ice appear to get more translucent with increasing grain size than water ice does, and the relationship between penetration depth and grain size is neither a linear function nor a simple power law. The trend for the carbon dioxide results appears to still be increasing with grain size, whereas, the water results appear to have plateaued, not significantly increasing at grain sizes greater than ~4.00 mm. Consequently, further analysis is required to fit a trend to adequately describe this data, and is discussed further in Chapter 7.

Chapter 7

Discussion of Results

All results from the broad spectrum solar radiation penetration depth experiments in water and carbon dioxide ices are brought together and presented here, in Section 7.1. These are then discussed, analysed, and used to determine an empirical model which enables the penetration depth to be predicted based on grain size and ice composition. The implications and different applications of the results and subsequent model for Mars and beyond are discussed in section 7.2.

7.1. Grain Size Dependence Model

The penetration depth in ices is highly wavelength dependent, primarily because the absorption coefficient can vary by many orders of magnitude across the visible wavelength range (as detailed in Chapter 2). If grain size remains constant, then the penetration depth decreases with increasing wavelength. This is evidenced by the results put forward by Perovich (1996) for the penetration depth of light in sea ice at different wavelengths, which ranged from 24 m at λ = 470 nm, 2 m at λ = 700 nm, to 0.05 m at λ = 1000 nm. The decrease in penetration depth with increasing wavelength is because the absorption coefficient α of water ice varies by several orders of magnitude across the wavelength range, with the minimum absorption (and therefore maximum transmission) occurring at 470 nm. Transmitted irradiation, I, of a given wavelength, through a thickness of ice, z, can be calculated using Beer's (or the Bouguer-Lambert) Law:

$$I(z,\lambda) = I(0,\lambda)\, e^{-\alpha z} \tag{14}$$

thus, the reduction in irradiance intensity is exponentially greater than the change in the absorption coefficient. Since the penetration depth is dependent on grain size, it therefore follows that if wavelength is held constant, the penetration depth will increase with grain size because the ratio between wavelength and grain size increases. Li et al. (2001) used this principle to model the penetration depths of different wavelengths in a 1 m thick snow pack as detected by the AVIRIS (Airborne Visible/Infrared Imaging Spectrometer) instrument. The penetration depths calculated from their model which are applicable to my wavelength range (300 nm – 1100 nm) are shown in Table 7.1.1.

Grain Size (mm)	Penetration Depth (mm)	
	λ = 860 nm	λ = 1050 nm
0.05	33	12
0.10	48	18
0.20	69	26
0.50	110	41
1.00	160	58
2.00	220	81

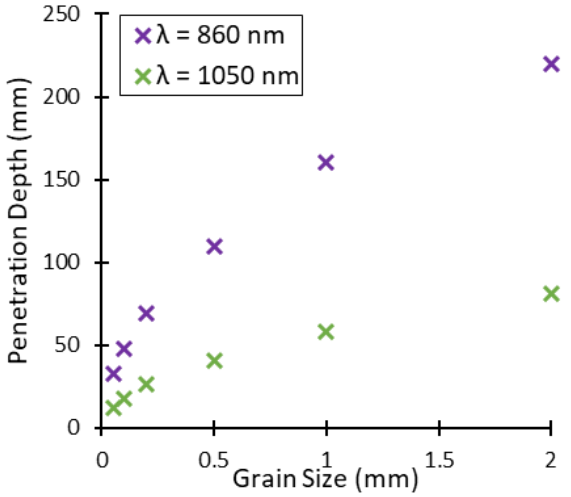

Table 7.1.1. Selection of data based on applicable wavelength range from Li et al. (2001): Penetration depths in snow of specified grain size at specific wavelengths.

When plotted, the relationship between these data (from Li et al, 2001) follows the trend line: $y = k\,x^{0.5}$, with a being wavelength dependent. This forms the basis of the model derived here for water and carbon dioxide ice granules of different sizes. Generally, at visible wavelengths in materials that are highly transparent, extinction is dominated by scattering. Therefore, attenuation of light by particles of said transparent material is quite different from that of the bulk solid. As long as particle size is larger than wavelength, extinction dominated by scattering is virtually independent of photon energy (Bohren and Huffman, 1983). Consequently, the scattering coefficient of water snow is independent of wavelength across the visible and near ultraviolet (Warren and Brandt, 2008). The expectation is that the scattering coefficient of CO_2 snow exhibits the same behaviour, but no direct measurements have been made. The absorption coefficient α is proportional to the scattering coefficient, which is inversely proportional to grain size, as smaller grains in a fixed volume result in a greater number of scattering interfaces. However, this does not mean that the absorption coefficient of the bulk material, or the refractive index, should be disregarded, as absorption should be fundamentally related to the mass of the material, whilst scattering is morphology dependent (Schwerdtfeger and Weller, 1977). Therefore, a comprehensive model describing the penetration depth in translucent granular material would require both factors to be taken into account.

The dependence of the e-folding scale on grain size can be approximated by using the following equation, which can be seen plotted alongside the e-folding scale results of the granular ice measurements in Figure 7.1.1 and Figure 7.1.2:

$$\zeta = k + \left(\frac{d}{b}\right)^{0.5} \tag{15}$$

where $k = 5.370, b_{H2O} = 0.030, b_{CO2} = 0.0144,$ and $d =$ diameter of ice grain.

I have adapted the square root dependency from the empirical equation of Li et al (2001), but expanded it to take into account the known parameters and thereby fully explain the broad spectrum measurements presented in this study. Schwerdtfeger and Weller (1977) made measurements of downwards-directed flux in naturally occurring snows at Plateau Station in Antarctica, and they determined from their data that the asymptotic flux extinction coefficient is equal to 0.030 scaled by grain diameter. According to Domine et al. (2008), the inverse of the asymptotic flux extinction coefficient is equal to the e-folding scale., However, I found that this does not fit my data, and so needs to be scaled by a constant which varies between water and carbon dioxide. This is because d should equal the effective diameter of non-spherical snow grains, which would be significantly smaller than the actual ice grain radius due to scattering from small features within the grain (Domine et al., 2008). Because of this, d needs to be scaled by a factor related, in theory, to the scattering and absorption coefficients, and would therefore be material specific.

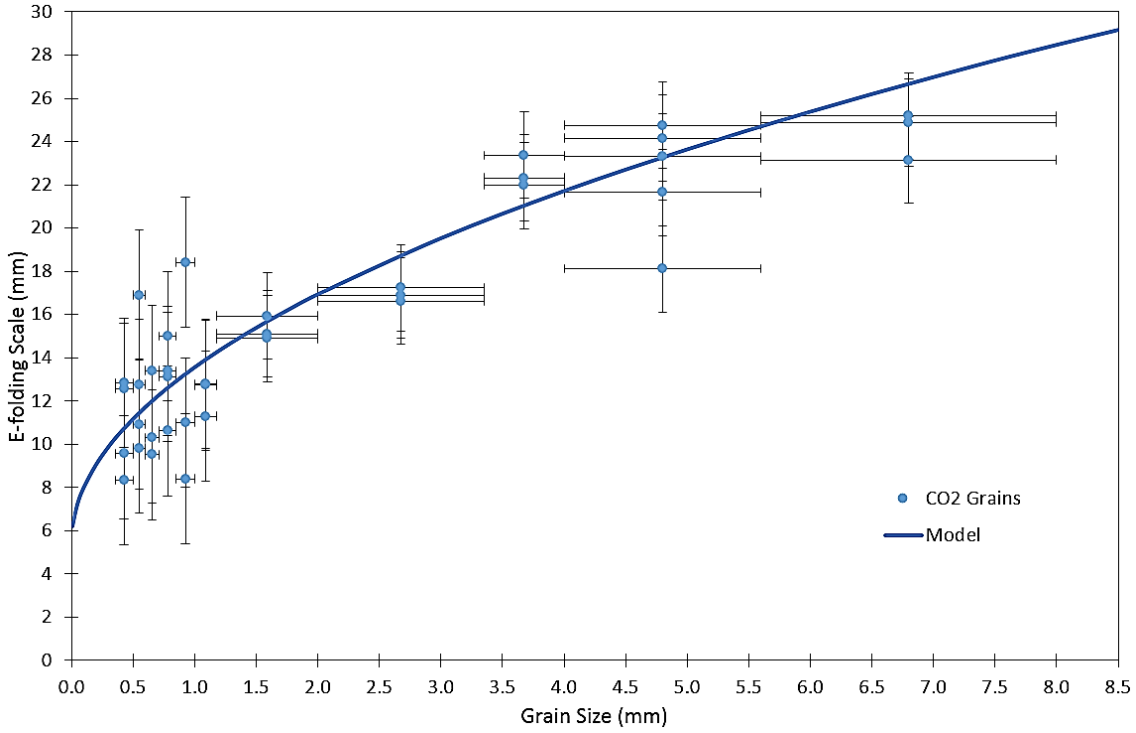

Figure 7.1.1. The e-folding scale of granular CO_2 ice with varying grain size, plotted with the model results for comparison.

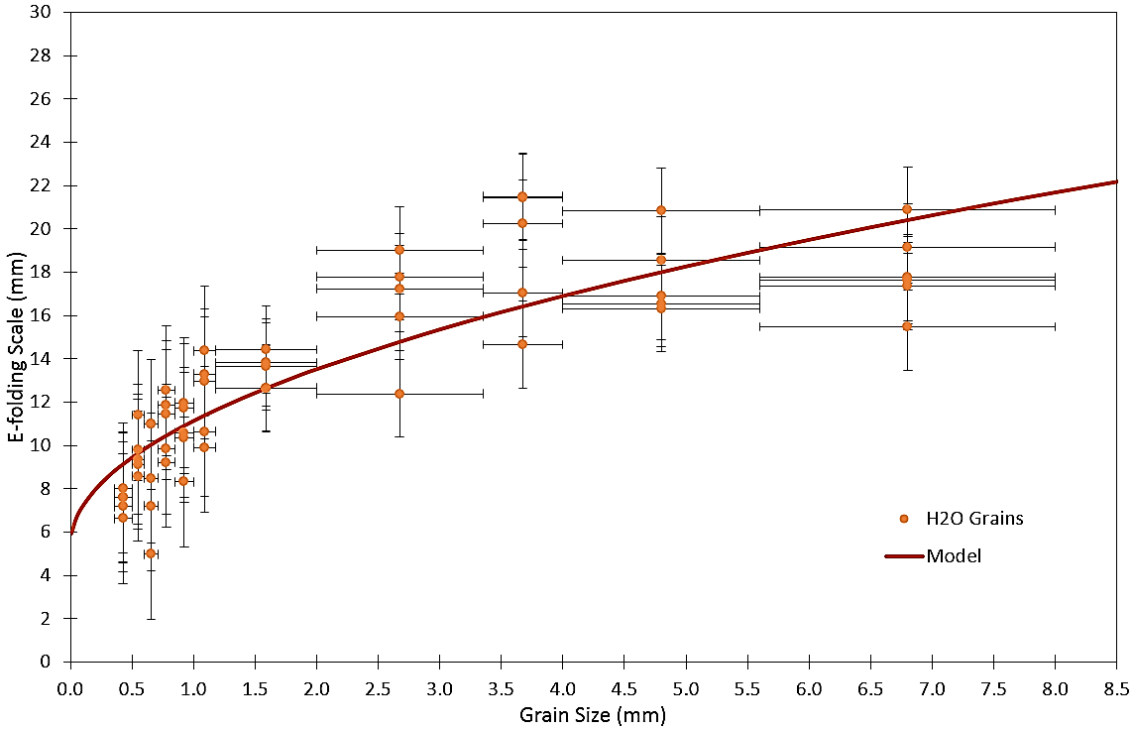

Figure 7.1.2. The e-folding scale of granular water ice with varying grain size, plotted with the model results for comparison.

However, as the measurements presented here are made over the broad spectral range of 300 nm – 1100 nm, and the absorption coefficient for both water and carbon dioxide ice increases by several orders of magnitude over this range, it would require both integrating values over the wavelength ranges, possibly weighted to account for the wavelengths with higher intensity in the solar spectrum than others, and much more detailed measurements in order to derive this scaling factor theoretically from first principles. Therefore, for the purposes of this study and the ability to predict the penetration depth of broad spectrum solar irradiation in either water or carbon dioxide ice, I use the value of 0.030 as the scaling factor for water ice, as determined by Schwerdtfeger and Weller (1977), and use a least-squares method to determine an empirical fit for the scaling factor of carbon dioxide ice, denoted by b_{H2O}, and b_{CO2} respectively. This same method was used to determine a, which is constant for both ice compositions.

This model is applicable for use across the visible spectrum where my measurements were made (300 – 1100 nm), and up to a limited grain size, above which the material could be deemed to be slab ice. Of itself, it does not take wavelength into account, although as both the refractive index *n* and the absorption coefficient α are wavelength dependent, the ideal would be for these to be substituted into this equation. However, with the current limited data I am unable to do this. Moreover, the motivation of this work was to quantify the full-spectrum integrated amount of solar energy that can penetrate ices on the surface of Mars and not light transmission at isolated wavelengths. The measured e-folding scales for all morphologies of CO_2 ice are plotted in Figure 7.1.3, and the same for water ice morphologies in Figure 7.1.4. The model gives a good prediction of the e-folding scale up to the point at which slab ice is plotted. The 'effective grain size' was chosen for slab ice via the analysis of photographs of the sample using the software package ImageJ (Schneider et al., 2012), with the smallest distance between cracks measured to be approximately 10 mm, and the largest 40 mm for carbon dioxide ice, and 15 mm to 45 mm for water ice, as this had fewer cracks and larger areas of unblemished ice in the samples (see sample images in Chapter 4). The average e-folding scale values for all measurements made, of both ice compositions, are plotted on Figure 7.1.5, where the resultant model for CO_2 and H_2O ices can be directly compared.

This model is a first approximation for quantifying the relationship between the penetration depths of broad spectrum solar radiation in granular ice of different compositions. More extensive measurements are required in order to refine this further, allowing for the optical properties of the ices to be fully integrated into the equation, as would be ideal. This would also allow for an upper boundary to be defined, where the e-folding scale would plateau and remain constant beyond a constant grain size.

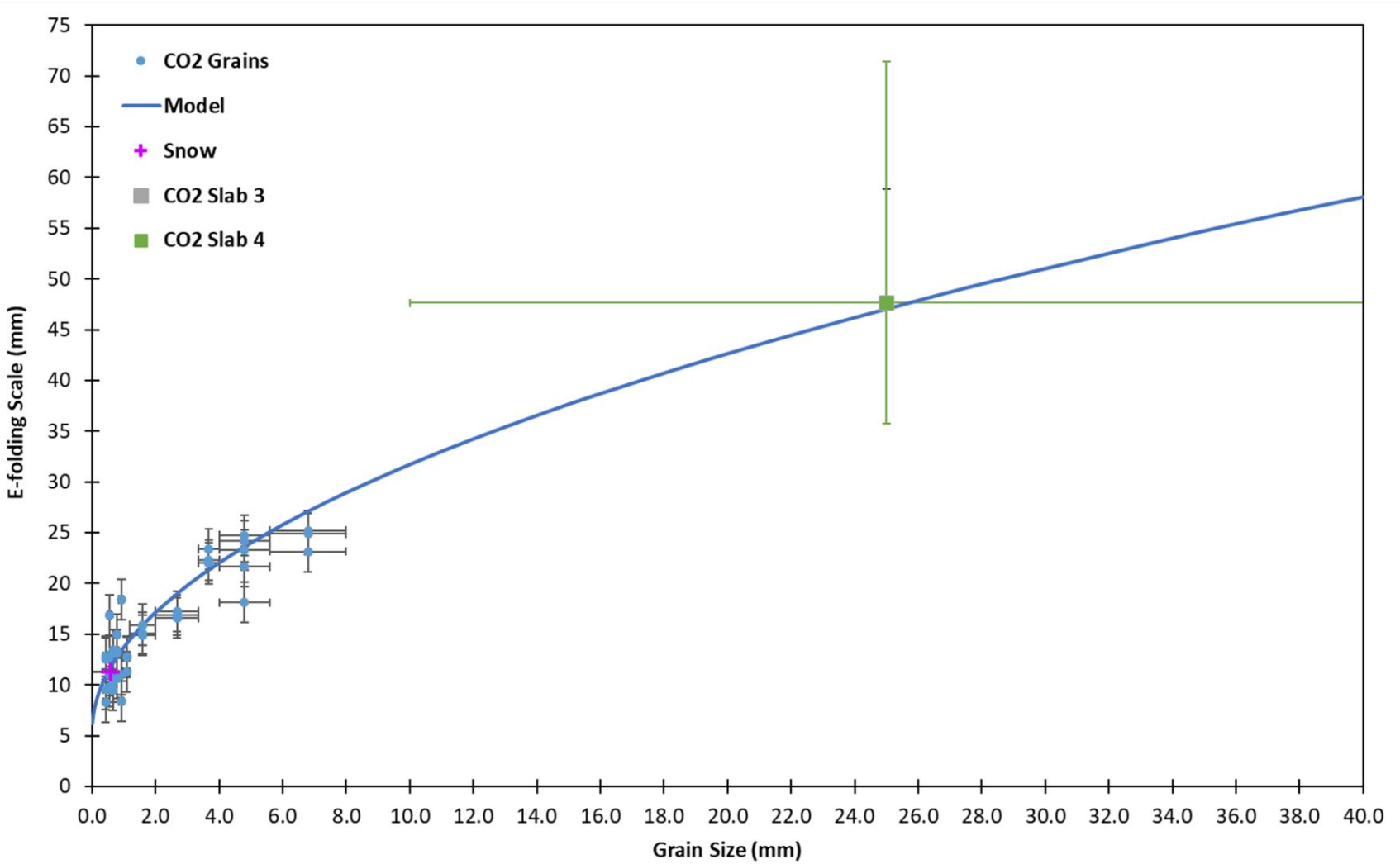

Figure 7.1.3. All calculated e-folding scale results for CO_2 ice, including all slab ice samples, all granular ices and the mean snow e-folding scale, compared with the modelled trend line. Please note that slab ice samples 3 and 4 plot in the same location on the graph, although the 'min' and 'max' values differed (denoted here by the vertical error bars).

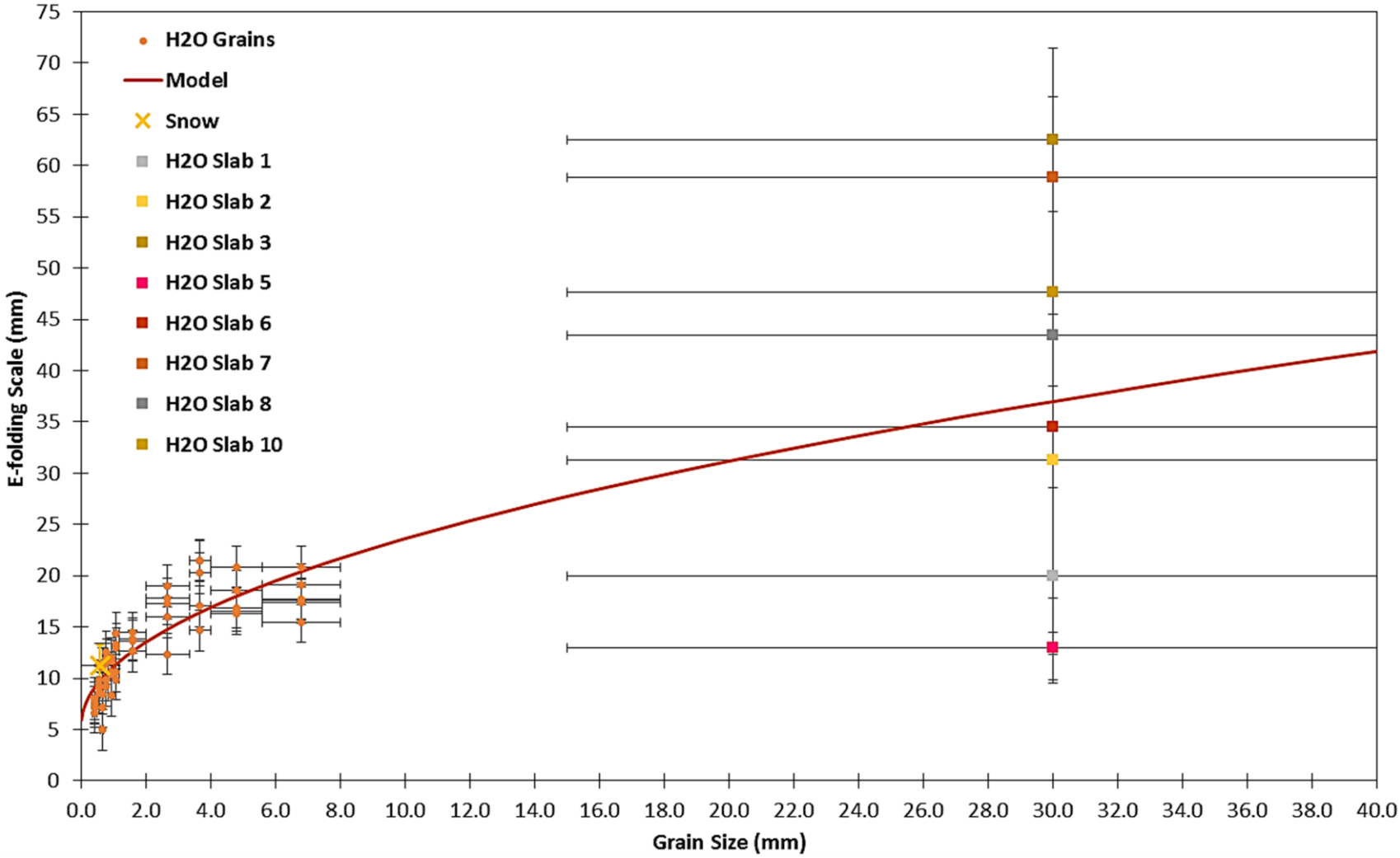

Figure 7.1.4. All calculated e-folding scale results for H_2O ice, including all slab ice samples, all granular ices and the mean snow e-folding scale, compared with the modelled trend line.

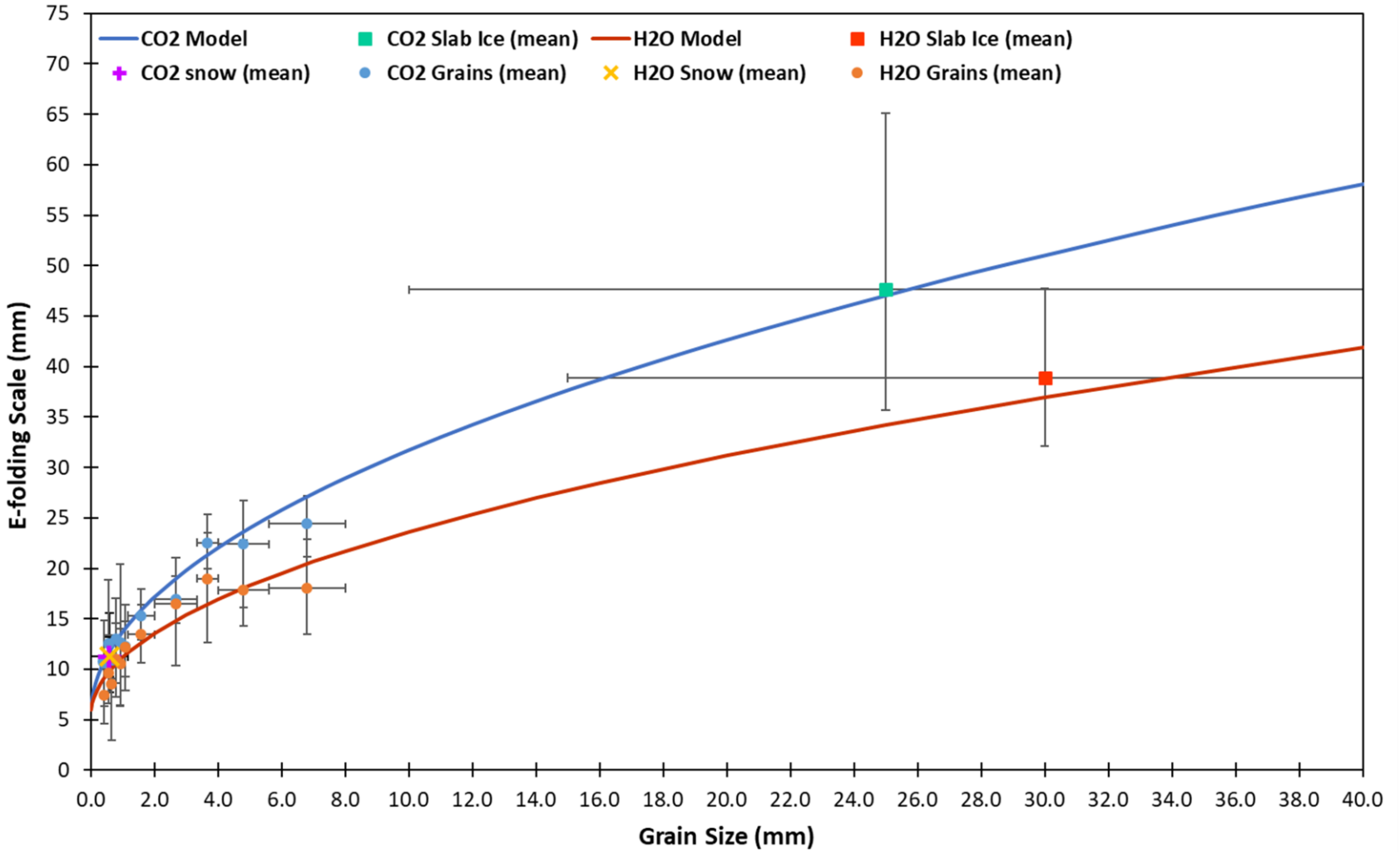

Figure 7.1.5. The calculated mean e-folding scale results for both CO_2 and H_2O ices, including slab ice samples, granular ices and snow, compared with the modelled trend lines. Please note, the vertical errors for the e-folding scale of snow for both compositions is ± 3 mm, as this is not obvious from the graph due to the concentration of data points.

Further work in order to confirm and/or refine this model would be beneficial, conducted by measuring the penetration depth in a range of different ices which occur on other planetary bodies in the solar system. Furthermore, this would be improved by a greater range of grain size measurements and having improved thermal control over the samples of slab ice, which would enable light intensity measurements in more pristine ice slabs, allowing for the maximum e-folding scale to be determined and placing the upper boundary on the model. Another aspect which could be integrated into the model is the effect of contaminants, such as the measurements performed by Kaufmann and Hagermann (2015) who used Mars simulant JSC-1A to contaminate water snow samples and determine the effect on the penetration depth of broad spectrum solar irradiation. If this were to be conducted using CO_2 snow and ice, this would greatly improve our understanding of how the Martian polar regions behave, and further improve modelling the formation of araneiforms and gullies, for example.

Results for the e-folding scale of ice grains of different sizes fit well with the snow results of ζ_{snow}= 11.2 mm ± 3.0 mm (Chapter 5) at one end of the spectrum, and on average $\zeta_{CO2\ slab}$= 47.6 mm ± 2.0 mm, up to 65.1 ± 2 mm for the best quality ice samples (Chapter 4) at the other. In a study

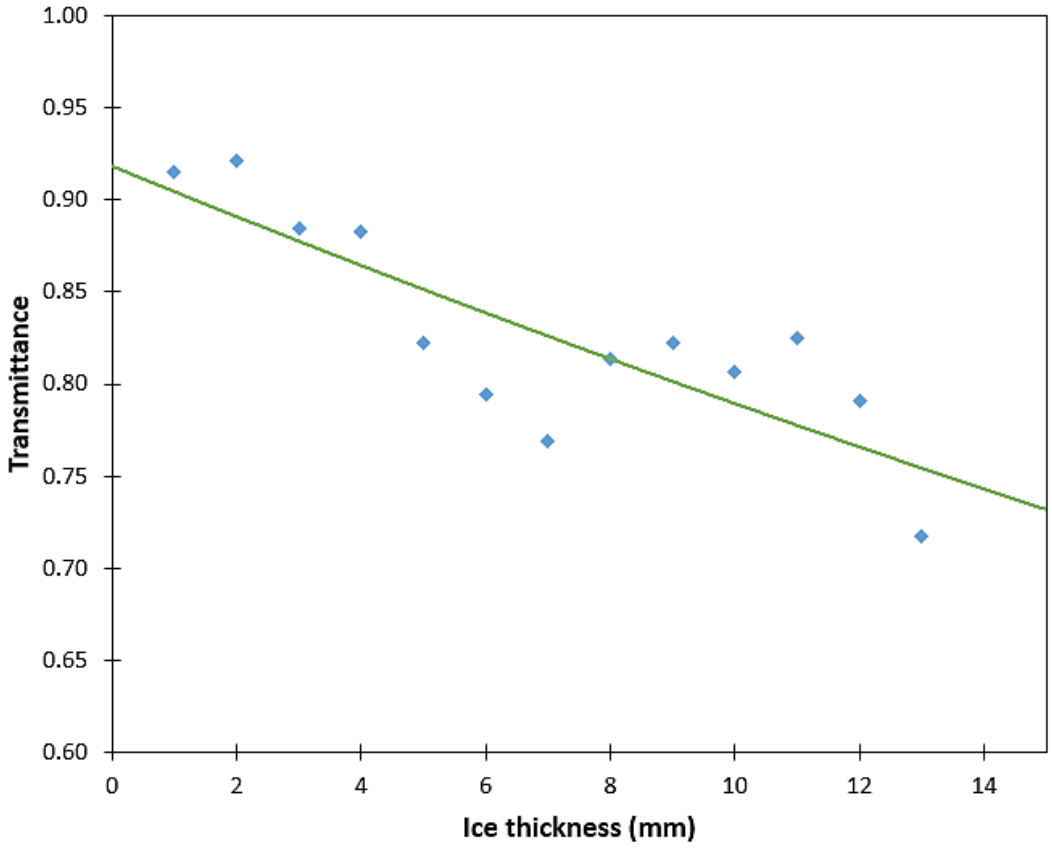

Figure 7.1.6. Light transmittance measurements (450 nm - 900 nm) through CO_2 slab ice samples formed under Martian temperature and pressure conditions by Portyankina et al. (2018), with an exponential trend line fitted to the data, which is used to calculate the e-folding scale.

by Portyankina et al. (2018), light transmittance was measured through one of the CO_2 ice samples they formed under Martian conditions in a thermally controlled Martian simulation chamber, over the wavelength range 450 – 900 nm (data shown in Figure 7.1.6). By fitting an exponential trend (Figure 7.1.6) and calculating the e-folding scale in exactly the same way as used in Chapter 4, $\zeta_{CO2\ slab}$= 66.7 mm based on the measurements of Portyankina et al. (2018). This value plots at the upper range for the penetration depth of carbon dioxide slab ice, based on my measurements (maximum slab ice ζ_{CO2} = 65.1 ± 6.3 mm), due to Portyankina et al.'s superior temperature and pressure control, but is nonetheless consistent within the error margins of my work.

7.2. Implications and Applications of Results

For both water and carbon dioxide ice, there is a clear trend from a regime of light propagation in granular ice of the smallest grain sizes (snow, grain size ≤1 mm) to slab ice (grain size →∞), although the point at which it would be appropriate to switch from the 'grain size' model to slab ice regime is difficult to define, depending on how unblemished the slab ice is. However, these measurements and my model have applications for all instances of granular and sheet ices on planetary bodies, including Earth, comets, and icy moons, in addition to Mars.

Specifically for Mars, accurate knowledge of light transmission through ice is needed for heat transfer models which can reliably predict surface-atmosphere interactions when involving surface ice, such as frosts, snow falls, sintered snow and snow sintering rates as it metamorphoses into solid ice. This last point is particularly interesting, as the more sintered a snow pack becomes, the larger the effective grain size, and so the penetration depth increases. This results in less energy being absorbed by the ice itself, and so the sintering rate would potentially decrease. However, this would have to be balanced against the effect of the greater potential for heating of the underlying regolith with a larger penetration depth, which would re-radiate energy back to the ice and potentially increasing sintering rates (if not causing sublimation). The upper limit of the model is the slab ice of the seasonal ice sheets, where the penetration depth of incident sunlight is one of the main controls on CO_2 jetting and the formation of araneiforms.

Depending on the extent of heating required to heat the regolith sufficiently to cause basal sublimation of the CO_2 ice (which depends on starting temperature, timescales, regolith properties, etc.), the e-folding scale of the ice sets the maximum thickness of the ice sheet for CO_2 jetting to initiate, and consequently create araneiforms. The mechanical properties of the ice sheet set the minimum ice thickness required, as the ice would need to be thick enough to be sufficiently strong for adequate sub-ice gas pressure to accumulate in order for sediment transport to occur upon ice

rupture and gas pressure release. The results of the e-folding scale of CO_2 slab ice range from an average maximum of 65.13 mm ± 6.3 mm to an average minimum of 35.71 mm ± 7.7 mm (see Section 4.3 for full details). Rather than this range of results suggesting uncertainty over the quality of the measurements or samples, it actually provides a valuable insight over the range of e-folding scales which are applicable to CO_2 (or H_2O) slab ice, depending on its physical state. For high quality, unblemished CO_2 ice, it would be advisable to apply an e-folding scale of the average maximum value ~65 mm, for slightly cloudy with minor cracking the mean value of ~46 mm would be appropriate, and for highly cracked and poor quality ice, the lower value of ~36 mm should be used. An example of where this full range of results are applicable can be seen in Figure 7.2.1

The images in Figure 7.2.1 were taken by the HiRISE camera on board MRO spacecraft and are of a region in the Northern Polar Erg, dubbed 'Arrakis' (incidentally named after the fictional desert planet in the series Dune, by Franks Herbert), and shows the progression of the surface over the course of spring, after the polar night has ended (first light occurs approximately at L_s= 316°, based on insolation data from the Mars Climate Database (Forget et al., 1999; Millour et al., 2018). The first image was taken at L_s= 0.6°, immediately after the northern spring equinox, and shows the seasonal polar ice cap covering the topography in the form of a thick, clean CO_2 ice. The albedo and colouration of the surface is dominated by the underlying regolith due to the translucency of the CO_2 slab. As spring progresses, and therefore insolation increases, activity first begins on the inter-dune material, in the form of dark fans deposited on the surface from CO_2 jets (Hansen et al., 2013), initiated via the SSGE and through the mechanisms described in the Kieffer model, and then continues as jetting and fan formation on the tops and slopes of the dunes. Material is both blown by local winds and falls downslope on the dunes.

The surface continues to brighten as the originally pristine CO_2 ice slab is broken up by the gas jetting process, which ruptures the slab ice and deposits dark regolith material on the surface. In some cases also depositing granular CO_2 ice which freezes from CO_2 gas jets which cool adiabatically upon release from the subsurface is also deposited, creating bright streaks on the slab ice surface (Titus et al., 2007). In addition to this, ice break up could also be occurring by thermal expansion; CO_2 ice has a significantly larger thermal expansion coefficient than water ice, as explained in Section 3.2, and will expand and contract significantly with day-night insolation cycles. Polygonal cracks generally occur on the flat stoss side of dunes, and are widespread (Hansen et al, 2013). Additionally, crestline cracks are observed and likely occur via brittle failure at the apex of the dunes, exposing dark dune material which can then be blown downslope.

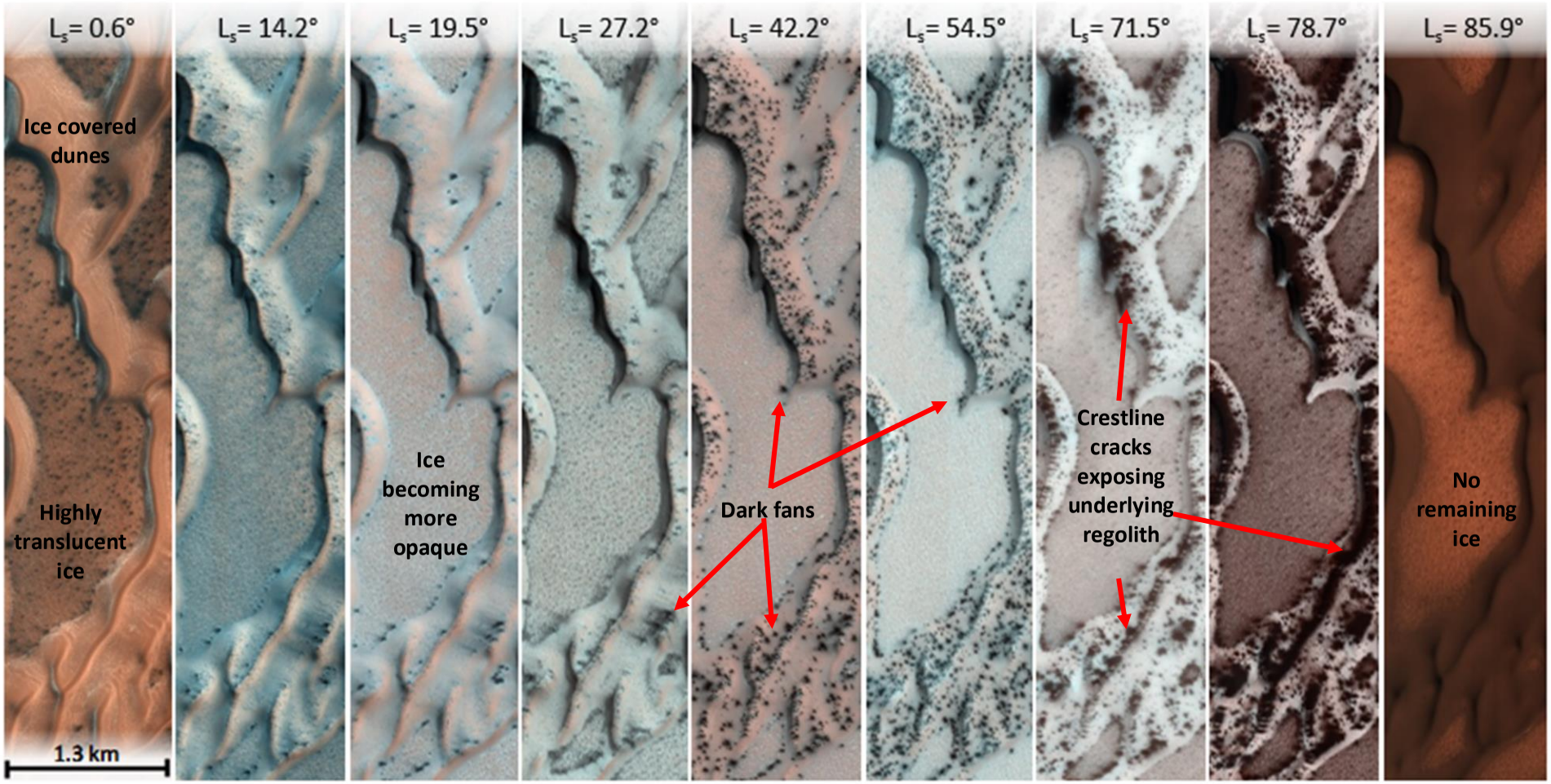

Figure 7.2.1. A series of images taken by HiRISE of the Arrakis region, at 80° N, 122.5° E, beginning in early spring (First panel taken at L_s=0.6° around the spring equinox) through to almost the summer equinox, which is at L_s=90°. The first panel was acquired in August 2013, with the others following sequentially through to February 2014. All images are RGB colour and non-map projected. From left to right: ESP_032884_2600, ESP_033240_2600, ESP_033385_2600, ESP_033596_2600, ESP_034018_2600, ESP_034374_2600, ESP_034875_2600, ESP_035086_2600, ESP_035297_2600.

Evidence for crestline cracks can be seen particularly well at L_s= 71.5° and L_s= 78.7° (in both Figure 7.2.1 and magnified in Figure 7.2.2), with material exposed along the ridge of the dune and flowing down the leeward slope ((Hansen et al., 2013). Further to this, smaller scale polygonal cracks appear to be present covering the inter-dune flats, and whilst at this level of zoom the images are slightly pixelated, this texture is not seen earlier on in the image sequence, nor can it be seen to the same extent in the L_s= 85.9° panel of Figure 7.2.1 when almost all of the ice has sublimated. This feature has been previously identified by Portyankina et al. (2012) in the southern hemisphere but at the same latitude (see Figure 2, panel C in the paper by Portyankina et al. (2012) for an example). There is still some surface roughness and a similar texture in the inter-dune material, which could be indicative of thermal contraction cracks in ice-rich permafrost, as observed elsewhere on Mars and in terrestrial permafrost (e.g. Levy et al., 2009; Levy et al., 2010; Mellon, 1997).

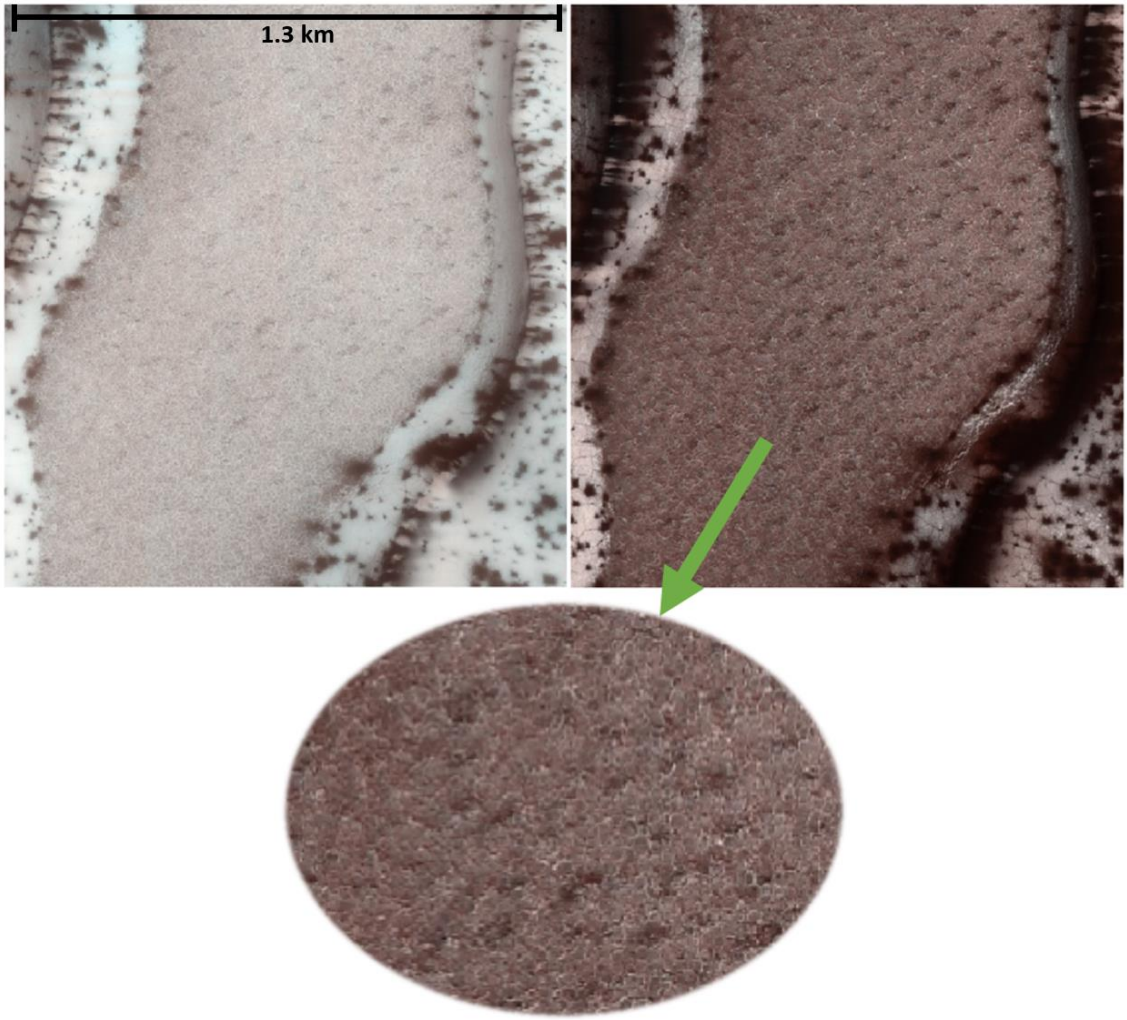

Figure 7.2.2. A magnified look at the inter-dune region at (left) L_s= 71.5° and (right) L_s= 78.7°, which appears to show both large cracks with fans emanating from them at the peak of the dunes, as shown previously in Hansen et al. (2013), but also a finer scale polygonal crack network covering the entirety of the flat space between dunes, as suggested by Portyankina et al. (2012).

In the context of modelling the processes observed throughout the springtime activity, determining the thickness of the CO_2 ice and the penetration depth of that ice is of high importance. For each image shown in Figure 7.2.1, I have extracted surface temperature (K), the surface CO_2 ice (kg m^{-3}) and maximum solar flux at the surface from the Mars Climate Database (Forget et al., 1999; Lewis et al., 1999; Millour et al., 2018). The average of daily surface temperature and surface ice was taken and used to indicate whether ice would be stable on the surface at that time. The value of 1600 kg m^{-3} is used for CO_2 ice density (Maass and Barnes, 1926). Although the density of CO_2 ice is highly temperature dependent, this standard value is a good enough approximation at temperatures around the reference temperature of 168K (Mangan et al., 2017). An appropriate e-folding scale, based on all the measurements and results presented in this thesis, is assigned to each scenario, and then the maximum daily solar flux for each day sampled was used to calculate the maximum solar flux able to reach through the ice to the underlying regolith, given these parameters (shown in Table 7.2.1).

The largest e-folding scale calculated from my results was based on measurements from Sample 4 (please refer to Table 4.3.1) of 71.4 mm, and this was applied to L_s= 0.6°, as this is the most pristine ice condition. Some ice brightening had started to occur by L_s= 14.2°, and so the average 'maximum intensity' e-folding scale was assigned (shortened to 'mean max' in Table 7.2.1).

Solar Longitude (L_s)	Mean Surface Temp	Mean Surface CO_2 ice	Calculated CO_2 slab thickness	Max Daily Solar Flux	E-folding Scale		Max Solar Flux to regolith
	K	kg m^{-2}	m	W m^{-2}	mm	Reason	W m^{-2}
0.6	150.11	400.29	0.2502	48.43	71.4	max slab	1.46
14.2	150.10	396.82	0.2480	74.24	65.1	mean max	1.64
19.5	150.45	364.76	0.2280	82.30	47.6	mean slab	0.68
27.2	151.05	310.26	0.1939	93.52	47.6	mean slab	1.59
42.2	152.22	204.07	0.1275	115.36	35.7	min slab	3.24
54.5	169.04	126.75	0.0792	125.71	31.72	10 mm	10.35
71.5	198.75	-	-	-	-	-	-
78.7	207.24	-	-	-	-	-	-

Table 7.2.1 Assignment of e-folding scales to different times through spring based on images shown in Figure 7.2.1, and the resultant solar flux able to penetrate through the ice to the underlying regolith, based on climatic information extracted from the Mars Climate Database for the corresponding times and locations. The final panel, L_s= 85.9° is excluded due to the lack of ice present on the surface. At L_s= 71.5° and L_s= 78.7°, the average daily temperature is above the sublimation point of CO_2, and so the calculation has not been completed.

The average e-folding scale of slab ice based on my measurements was 47.6 mm, appropriate for where the ice slab ice is still translucent, but there is some minor cracking and imperfections present. This was therefore applied to L_s= 19.5° and L_s= 27.2° (shortened to 'mean slab' in table). The e-folding scale is calculated from the minimum light intensity measurements from the slab ice experiments, so those which likely penetrated through cracks and cloudy sections of ice, gave a result of 35.7 mm, which was applied to L_s= 42.2°. From this point on, the ice is so cracked, with potentially quite large amounts of the ice being granular rather than continuous, that I have used Equation 14 to calculate the e-folding scale given a reasonable grain size estimate: at L_s= 54.5°, this is 10 mm grains or 'effective grain size' as the size of solid ice sections between cracks; at L_s= 71.5° and L_s= 78.7°, the average daily temperature is above the sublimation point of CO_2, and so the calculation has not been completed. However, quite clearly from the images shown in Figure 7.2.1, there is ice still present on this surface. This is likely due to temperature only rising above the frost point for a portion of the day, and so sublimation would occur during that time, but not all the ice would disappear before temperature dipped back down again. Finally, at L_s= 85.9° no surface ice is visible, and the average surface temperature is 207 K which is well above the sublimation temperature of CO_2 ice, and so has not been considered in this analysis.

Interestingly, these results show that after the onset of ice activity, which reduces the penetration depth of the ice, the flux able to penetrate through to the underlying regolith initially decreases before increasing again, even though incident solar flux is increasing steadily. Whether this could be observed in the timing of jetting activity remains to be seen, and this simple indication of the solar flux able to be absorbed by the underlying regolith requires combining with a model of the subsurface thermal and physical composition in a comprehensive radiative transfer model, in order to determine whether the whole sequence of events over the course of spring can be modelled.

CO_2 sublimation processes have been linked to the formation of gullies in the absence of liquid water (e.g. Cedillo-Flores et al., 2011; Hoffman, 2002; Pilorget and Forget, 2016; Vincendon, 2015). These are mainly found in the 30–60° latitude range in both hemispheres, and activity has been linked to the time when seasonal CO_2 frost is present on the surface and beginning to defrost (Pilorget and Forget, 2016). In a series of laboratory experiments, Sylvest et al. (2018) condensed CO_2 frost onto JSC Mars-1 simulant regolith, held at angles ranging from 10° through to the angle of repose, in order to investigate gully formation when exposed to incident radiation. They found that the CO_2 formed as fine-grained deposits on the surface, and between the regolith grains. Significant thicknesses of CO_2 frost (up to several centimetres) can accumulate on pole-facing slopes even at mid-latitudes and so are illuminated by the sun (Schorghofer and Edgett, 2006). Being able to quantify how much incident energy is absorbed by the CO_2 ice grains and how much is

transmitted to the underlying regolith by knowing the e-folding scale of the granular CO_2 ice observed on slopes means that calculations can be made to determine if these same scenarios as created in the laboratory by Sylvest et al. (2018) are energetically feasible under Martian gravitational and atmospheric conditions.

Further to this, on the South Polar Residual Cap (SPRC), lobate features form a combination of troughs, mesas, quasi-circular flat bottomed pits and other depressions, which are collectively referred to as 'Swiss-cheese terrain' (Thomas et al., 2013; Thomas et al., 2009; Thomas et al., 2005). This Swiss Cheese terrain is associated with a thin layer of carbon dioxide ice overlying the permanent polar cap at the south pole, and is described as sublimation features. The 'citizen science' powered study by Schwamb et al. (2018) mapped the distribution of different surface features at high latitudes on Mars, and found that there was no location where araneiforms and Swiss Cheese terrain occurred together, and almost all identification of Swiss Cheese Terrain was within the SPRC. The SPRC is the only place where there is residual CO_2 ice exposed all year round covering an area greater than 80000 km^2 (Thomas et al., 2013) and is characterised by higher albedo CO_2 ice which has been highly eroded over time, ranging from 2 m to 10 m in thickness (Byrne and Ingersoll, 2003; Thomas et al., 2000).

Knowledge of how long-term CO_2 ice deposits interact with incident sunlight over time, especially those which survive throughout the summer (with the associated high insolation levels) and how this changes when the ice has undergone varying levels of erosion (broken down into fractured and/or granular material), with the potential of water ice inclusions (or CO_2 overlaying the water ice) would improve models and our understanding of how this terrain evolves. Thomas et al. (2009) concluded that there is currently no good explanation for the formation of these features seen in the 'Escher terrain', so-called due to the apparent counterintuitive nature of the stratigraphy based on their interpretation (now called Swiss Cheese Terrain). Brown et al. (2014) observed an increase of the water ice signature on the SPRC using data from the Compact Reconnaissance Imaging Spectrometer for Mars (CRISM) on board MRO. Based on their model, Brown et al. favour the hypothesis that this is due to direct deposition of water ice onto the SPRC due to cold trapping (conditions for which are likely based on GCM models), but cannot rule out the possibility of this either being due to sublimation of CO_2 and subsequent exposure of underlying water ice, or being due to the deposition of water ice particles condensing within a sublimation flow above CO_2 ice. If models could incorporate the different penetration depths of granular ice of the corresponding composition on the surface of the SPRC, it could give additional insights as to which of these theories are more likely, based on the predicted landforms from these models.

France et al. (2010) inferred from their light penetration experiments into Mars dust contaminated water snow that there is at least a 2 cm deep region within a dusty Martian water

snowpack located at the northern polar cap, located at around 11 cm depth, which could support life, photosynthetic or otherwise, as this would provide enough protection from harmful UV radiation. However, the likelihood that there is long term water snow in sufficient quantities to enable there to be at least 11 cm of snow cover is questionable. There is simply not enough water vapour in the atmosphere to be depositing that much snow, only a few precipitable micrometres (1 pr-µm 1 gm^{-2}) are present at any time (Spiga et al., 2017). It is known that the permanent northern polar cap consists entirely of water ice, which is present all year round. This, however, does not have a 'snow' morphology, but is solid ice. Thin coverings of surface water frosts were observed by Phoenix Lander to occur on a daily basis (Smith et al., 2009), but these were only µm scale frost coverings (as shown in Figure 6.1.1 in previous chapter). Phoenix also observed clouds 4 - 6 km above the surface, from which fell streaks of water ice crystals (very fine grained snow), which sublimated before reaching the surface (Whiteway et al., 2008). This phenomenon is referred to as Virga streaks on Earth, and do not contribute to any accumulation of snow on the ground. Terrestrial snow falls typically from nimbostratus clouds (e.g. Braithwaite et al., 2008), thick cloud cover at mid to low altitudes, and such water clouds are not observed in the Martian atmosphere – which are mainly cirrus-type cloud with just a few isolated occurrences of high altitude trails and thin cumulus in the aphelion cloud belt (Clancy et al., 2017), making heavy snow fall and accumulation on the scales of centimetres highly unlikely.

In fact, it is much more likely for large volumes of CO_2 snow and granular ice deposits to accumulate, rather than water ice (e.g. Forget et al., 1995; Hayne et al., 2014; Hayne et al., 2012; Kuroda et al., 2013; Titus et al., 2001). Given that the atmosphere is primarily composed of CO_2 gas, the growth of CO_2 ice crystals is not limited by the very low partial pressure of water vapour in the atmosphere as water ice crystals are, and so CO_2 snow is much more abundant than H_2O snow on Mars. Hayne et al. (2014) developed a model based on observations of CO_2 clouds in the south polar region by the Mars Climate Sounder (MCS) which suggests that CO_2 snowfall contributes 3% – 20% by mass to the seasonal ice deposits over the latitude range 70° - 90° S, and, because the atmosphere in this region remains close to CO_2 saturation levels, unlike the water snowfall observed by Phoenix, the falling CO_2 snow is unlikely to sublimate before reaching the surface (Hayne et al., 2014). This means that snow will accumulate and remain on the ground, and snowfall was found to be an inevitable consequence of the polar energy budget in the Hayne et al. (2014) model.

A model of solar radiation penetration in CO_2 ice was created by Pilorget et al. (2011), who combined both radiative and conductive heat transfer methods with the optical properties of carbon dioxide ice. The findings presented in this thesis are consistent in principle with their model results, in that small grains of CO_2 ice, of a size classed as snow throughout this study, do now allow enough light to penetrate through a layer to allow for any significant heating of the underlying

regolith. What the Pilorget et al. (2011) study did not provide, however, were the resultant penetration depths for CO_2 ice in the different scenarios modelled.

An e-folding scale of only 11.2 mm in snow would mean that the underlying material, be it regolith or ice, is largely unaffected by insolation—and thus might remain colder than anticipated. Lower subsurface temperatures reduce gas movement through the pores in a sediment, affecting both the subsurface-atmosphere exchange of CO_2 and the likelihood of sediment movement to be triggered by CO_2 sublimation. Lower subsurface temperatures also affect the sublimation of other volatiles potentially present in the subsurface, such as water, increasing the survival time of any subsurface water ice deposits.

Such a small e-folding scale for fine-grained ices means that, even with a thin snow (on the scale of mm) covering the seasonal ice cap, light penetration into the ice sheet could be significantly dampened. Due to the low temperatures during winter and through spring, it is reasonable to think that these fine grained deposits could remain emplaced for long enough to have a noticeable effect, reducing light penetration into the slab, which would keep the temperature of the slab low and therefore help maintain the snow cover on top of it. This feedback loop would bolster slab and snow cover longevity, keeping snow sintering rates low due to the maintained low temperatures. It would also hamper the formation of araneiforms, for example, which only occur when adequate energy can be transmitted through the ice to the underlying regolith. This is in order to heat the regolith sufficiently to cause basal sublimation which leads to CO_2 jetting, as per the CO_2 jetting model (Kieffer, 2000; Kieffer, 2007; Kieffer et al., 2006). Perovich (1996) states that, on Earth, a 25-cm covering of snow on top of an ice sheet would reduce light transmittance to less than 1%, implying an e-folding scale of less than 6 cm. While this would be a large amount of CO_2 snow to accumulate on Mars, the simulations run by Colaprete (2002) indicate that 0.75 g of CO_2 snow could be deposited per square centimetre during 1 hr of snowfall beneath the CO_2 clouds forming the polar hood. If using a snow density of 910 kg m^{-3} (Smith et al., 2001), this equates to 8.2 mm thick deposit of snow, and given the e-folding depth of 11.2 ± 3 mm, even at these lesser snow depths a significant reduction in radiation intensity will occur, potentially halting the CO_2 jetting process while the snow remains in situ.

Snow fall would not necessarily be required to emplace fine-grained ice deposits. One of the issues raised by Pilorget et al. (2011) was that CO_2 jetting was observed on dune slopes but not on the flat areas between dunes. They suggested that venting was still occurring in these areas, but the underlying regolith on the flat areas has a higher albedo than that of the dune material and so made it harder to observe. A higher albedo would also imply less subsurface heating within the regolith itself. In addition to the issue of detection, it could also be speculated that, if fine-grained icy debris ejected from the vents on the dune slopes were carried downslope (either simply by

gravity or windblown) and deposited around the foot of the dune, this could cause the observed increase in albedo. Even if this only formed a very thin layer of granular ice on top of the slab ice, the decrease of the penetration depth of the ice combined with the higher albedo regolith (therefore less absorbing), could be enough to suppress jetting activity.

The measurements presented in Chapter 5 give the same e-folding scale for water snow as CO_2 snow. This suggests, in terms of light penetration, that it does not matter what the composition of the snow is. However, it is currently unknown how the presence of dust within the snowpack affects light penetration in CO_2 snow. Some measurements have been made of water snow with contaminants such as black carbon (for simulating cometary ices) or Mars simulant regolith (e.g. Clow, 1987; France et al., 2010; Kaufmann and Hagermann, 2015; Kömle et al., 1990), but no such measurements of dust-contaminated CO_2 snow packs have been made to date. This is a topic which should be investigated further and is an important factor for heat transfer at the Martian surface, and a particular contaminant will not necessarily have the same effect as it does in water snow.

Having well-defined grain size dependent penetration depths for both water and carbon dioxide ices also has applications for elsewhere in the solar system. This includes icy moons such as Triton, which has a diverse icy surface, composed of at least nitrogen, methane, carbon monoxide and carbon dioxide ices (Brown et al., 1995); many of the Jovian satellites have icy surfaces, as they are out beyond the frost point in the solar system. Water ice is a major component of the surfaces of Europa, Ganymede and Callisto (Dalton et al., 2010), and the dark terrain observed on both Ganymede and Callisto correlated with CO_2 ice distribution based on absorption data (Hibbitts, 2003), although it is not expected that pure CO_2 ice exists in large amounts due to its high vapour pressure, but most likely as mixtures in water ice or adsorbed on minerals.

Comets also host both water ice (usually near the surface), and carbon dioxide ice (a major component of the nucleus, usually buried at depth) (e.g. De Sanctis et al., 2006; Filacchione et al., 2016). However, as observed on the comet 67P/ Curyumov-Gerasimenko, sometimes CO_2 ice is exposed (Filacchione et al., 2016), and so, to determine the thermal structure it is important to understand how irradiation penetrates into all components of a comet. This could lead to improved structural and chemical models of the cometary subsurface, and help predict at what depth different chemical species of ices occur when the penetration depths are coupled with the complex models of heat transport through a cometary nucleus, including porosity, phase transfers and ice structure, sintering, etc. Further improvements on this could be made by making measurements using other common ices in the solar system, such as methane and carbon monoxide, as well as being able to quantify the effect of contaminants such as black carbon powder (often used in cometary simulation experiments), or other regolith simulants, within these ices.

Chapter 8

Future Work and Conclusions

Building on the lessons learned, as documented in the preceding chapters, this final chapter proposes the potential direction and outlines the scientific scope of potential future work within this topic. This is presented in Section 8.1, which details some initial experimental work, undertaken during the course of the experiments presented in Chapters 4, 5 and 6, to investigate the effect of Mars simulant dust within a carbon dioxide snow pack on its e-folding scale. Section 8.2 summarises the findings of this work, both the experimental results and their potential applications, which concludes this thesis.

8.1. Future Work: Dusty Snow

Presented here are the results from some initial experiments which have been conducted to investigate how the presence of Mars dust contaminating carbon dioxide snow affects the e-folding scale. This early stage experimental work was used as proof of concept, but the results show that much more work is required to develop an experimental set-up sufficiently equipped to deal with the additional challenges the presence of regolith simulant within the snowpack provides. It is for this reason that, whilst some experiments have already been conducted, that this topic is included as 'Future Work'. The regolith simulant utilised was JSC Mars-1A, which was sieved to <20 µm in grain size, to approximate is the likely particle size which could be deposited onto or within a snowpack from the atmosphere (please see explanation on grain size range given in Section 8.1.2). Whilst the results from these experiments are given, the laboratory work proved to be extremely difficult with the equipment and experimental procedures developed for the work presented in Chapters 4, 5 and 6 of this thesis. Further development is required, and some suggestions for improvements and future work on this topic are given.

8.1.1 Background

It is rare to encounter naturally occurring, completely pure snow or ice on a planetary surface. Even small amounts of terrestrial soil dust or soot contaminating an ice deposit, on the order of parts per million, can reduce surface albedo and affect the surface energy budget, as shown by Warren (1984) in Antarctic snow packs. Several authors have investigated, either by experimentation or by modelling, the effect of impurities within the snowpack or ice slab on light propagation and subsequent thermal profiles, including Clow (1987), France et al (2010), and Kaufmann and Hagermann (2016). Other studies, such as that by Beaglehole et al. (1998), have stressed the importance of such work, as the optical behaviour of snow is highly sensitive to even the smallest changes in dust content. Whether the contaminant is mixed with the snow grains as an 'external mixture', or whether it is included within the grain of ice itself as an 'internal mixture' can make an important difference, with internal mixtures being more opaque than external mixtures with the same dust concentrations (Ackerman and Toon, 1981).

The methods used in these measurements are based on those detailed in Chapter 3 and how the data presented in the rest of this thesis was collected. Some modifications are made to this, based on lessons from the Kaufmann and Hagermann (2016) experiments, which studied how the penetration depth of broad spectrum solar radiation in water snow samples was affected by contamination by varying proportions of Mars regolith simulant.

8.1.2 Experiments

A series of experiments were conducted as part of the laboratory-based research for this thesis, in order to determine the e-folding scale of a dusty CO_2 snow pack containing varying quantities of dust. This utilised JSC MARS-1A regolith simulant sieved to <20 µm. The upper grain size limit was chosen in order to focus on mainly windblown material on Mars - dust suspended in the atmosphere has an estimated grain size radii range of 1.0 – 10.0 µm (Toon et al., 1977), although, given high enough wind speeds larger grains can be saltated (grains temporarily blown from the surface and then redeposited, but not suspended within the atmosphere) – up to 210 µm diameter particles can be moved by wind speeds of 2.2 ms^{-1} under Martian atmospheric conditions (Greeley et al., 1980). Dust is also likely delivered to ice accumulations via deposition within a snow particle, the dust grains having acted as the nucleation points for CO_2 clouds to form (Colaprete, 2002), and so would originate from dust suspended in the atmosphere. However, there are a number of difficulties in sieving a material to ≤10 µm, including the small quantity of that grain size range contained within the simulant sample, the ease of which this particle size becomes suspended in the air, and grains becoming electrostatically charged and therefore sticking to the sieves and other equipment. As a consequence, I chose to sieve using a 20 µm mesh size, so that I could obtain sufficient dust quantities whilst isolating grains with diameters which can either be suspended in the atmosphere or be easily saltated at low wind speeds. A lower grain size limit was not imposed as a different study by Clancy et al. (1995) suggests that the grain size distribution of atmospheric dust could be significantly smaller than the Toon et al. (1977) results, reporting particle sizes down to a sub-micrometre scale. The uncertainty is predominantly due to uncertainties in dust composition, and so determining the optical properties sufficiently to discern an exact grain size range from spectrometer data is challenging, however, these smaller grain radii estimates are based on dust of a palagonite composition.

The CO_2 snow was made using the method outlined in Section 3.1 and weighed prior to submersion in liquid nitrogen. The snow was sieved to <1 mm. The correct proportion of dust was calculated and weighed out, and then mixed with the CO_2 snow and liquid nitrogen suspension to create a homogenous mixture. Just enough liquid nitrogen was used to cover the snow pack. This enabled good mixing of dust and snow to produce a homogenous sample, whilst maintaining temperatures too cold for either sublimation or sintering of the CO_2 snow to occur and immersed to prevent water frost contamination. By using this methodology, an external mixture of dust and snow is formed (internal and external mixtures are defined in Section 8.1.1), and so any results would be an estimate of the upper range of penetration depths for dusty snow on Mars, which probably forms as an internal mixture, with dust particles forming the condensation nuclei for growing ice grains within clouds (Forget et al., 1998).

Hansen (1999) used surface emissivity models to determine a dust content of <0.1% by weight in the polar CO_2 ice deposits, which is also consistent with previous estimates based on Mariners 7 and 9 IRS and IRIS measurements, respectively. In order to determine a trend of change in penetration depth with dust content, measurements were acquired at higher and lower mixing ratios. Therefore, a mixture of 1% dust by weight was chosen as a starting point for these experiments. Figure 8.1.1 shows an initial attempt at making this sample. This gave a surprisingly dark colouring to the snow, and even when just removed from liquid nitrogen, began to clump and sinter, with a consistency more like mud than snow. As a consequence, it was impossible to retrieve light intensity measurements through this sample batch, as sintering occurred so rapidly that firstly the ice grains could no longer be considered <1mm in grain size. The rapid sintering also made it impossible to reduce the snow thickness for subsequent measurements. Figure 8.1.2 demonstrates the extent of the sintering which occurred, causing a layer approximately 4 mm thick to become welded so cohesively it could be picked up whilst retaining structural integrity.

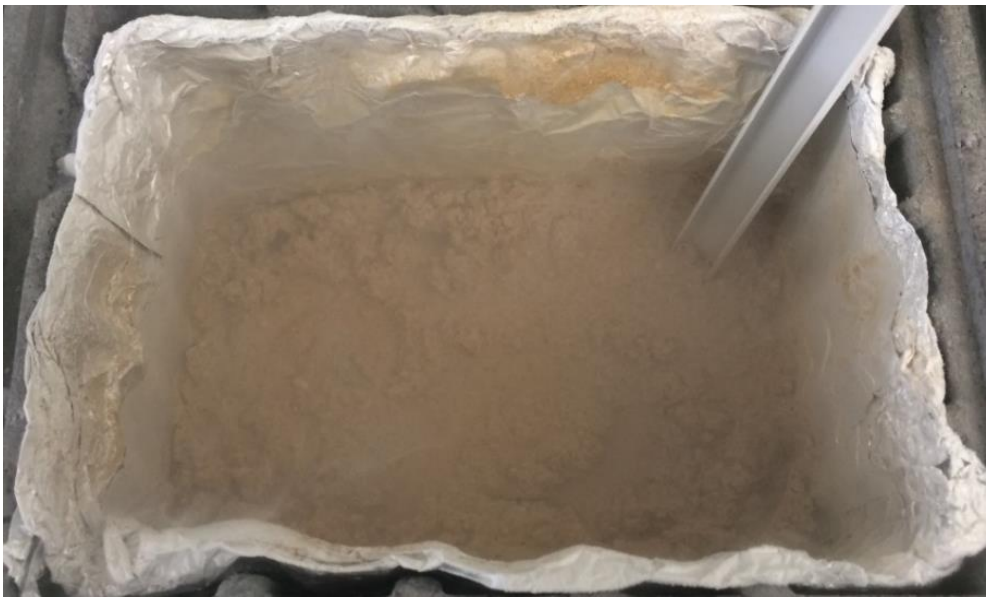

Figure 8.1.1. The mixture of 1% Mars simulant (<20 µm grain size) with CO_2 snow rapidly sintered, taking on a lumpy consistency if not fully submerged in liquid nitrogen. Note the dark colouring of the snow, despite just 1% dust content.

The next sample was made with 0.5% dust content, but with much the same result. Consequently, the dust content was reduced to 0.1% dust by weight. This still gave a strong colouration to the snow mixture (see Figure 8.1.3), but not as dark in colour as the 1% and 0.5% concentrations. The resulting sample was a much more manageable snow mixture, and whilst rapid sintering remained a problem, some results were obtained. For subsequent measurements, the dust content was gradually decreased further, and results were acquired for 0.06% and 0.02% dust content. Results can be seen in Table 8.1.1. Errors have not been estimated due to the poor control

Figure 8.1.2. Once devoid of liquid nitrogen, the dusty snow mixture sintered rapidly, so that it became unusable for experimentation. This solid slab formed in less than a minute when left at ambient conditions.

Figure 8.1.3. 0.1% Mars simulant dust mixed with CO_2 snow and suspended in liquid nitrogen.

of variables and unquantified effect of sintering on the optical transmittance within the snow, but errors are assumed to be large.

The series of photographs in Figure 8.1.4 are of a sample of dusty CO_2 snow exposed to ambient temperature and light levels over time. The effect is subtle but, upon close examination of the images, it can be seen that there are several changes to the surface over a short amount of time

Sample Number	E-folding Scale of dusty CO_2 snowpacks (mm)		
	0.02%	**0.06%**	**0.10%**
1	10.101	9.461	7.435
2	14.815	7.496	9.785
3	12.407	13.831	11.249
4	12.887	8.718	11.834
5	17.452	16.000	10.246
6	13.316	8.666	7.911
7	15.748	-	-
8	15.848	-	-
Mean	14.072	10.695	9.743

Table 8.1.1. The calculated e-folding scales from light intensity measurements through dusty CO_2 snow samples with different dust contents. Percentage dust given by weight.

(total 4 minutes). The surface appears to firstly become rougher in texture, paler in colour, and in the final picture (240 seconds) there is a cracked, platy texture, not dissimilar to desiccation cracks observed in dried out mud. This is likely due to different processes occurring simultaneously: CO_2 at, and immediately below, the surface begins to sublimate, with the gas release disturbing the uppermost layer of dust, increasing surface roughness; dust grains absorb radiation energy and heat more rapidly than the CO_2 ice, which could lead to the initiation of grain burrowing (see section 1.3); CO_2 which is not immediately sublimating is sintering at an increased rate due to the additional heat input provided by the dust grains, providing a thin cohesive crust on the surface, which is then broken up by thermal expansion, sublimation and gas escape around the edge of the sample; dusty snow has potentially sintered to the copper ring initially and then sublimates preferentially around the edge (see the gaps around the inside rim of the sample at 240 seconds) due to higher heat flux from the copper ring. The white rim at 45 seconds is likely to be water frost deposited from the air onto the sample, as can be seen around the outside edge of the copper sample holder.

When a sample was exposed to irradiation from the solar simulator, this whole process occurred in a matter of seconds, making accurate measurements virtually impossible. Understanding the presence of dust on or within the ice is important, not just due to how this affects the penetration depth of sunlight through the ice pack, but also for other controlling factors.

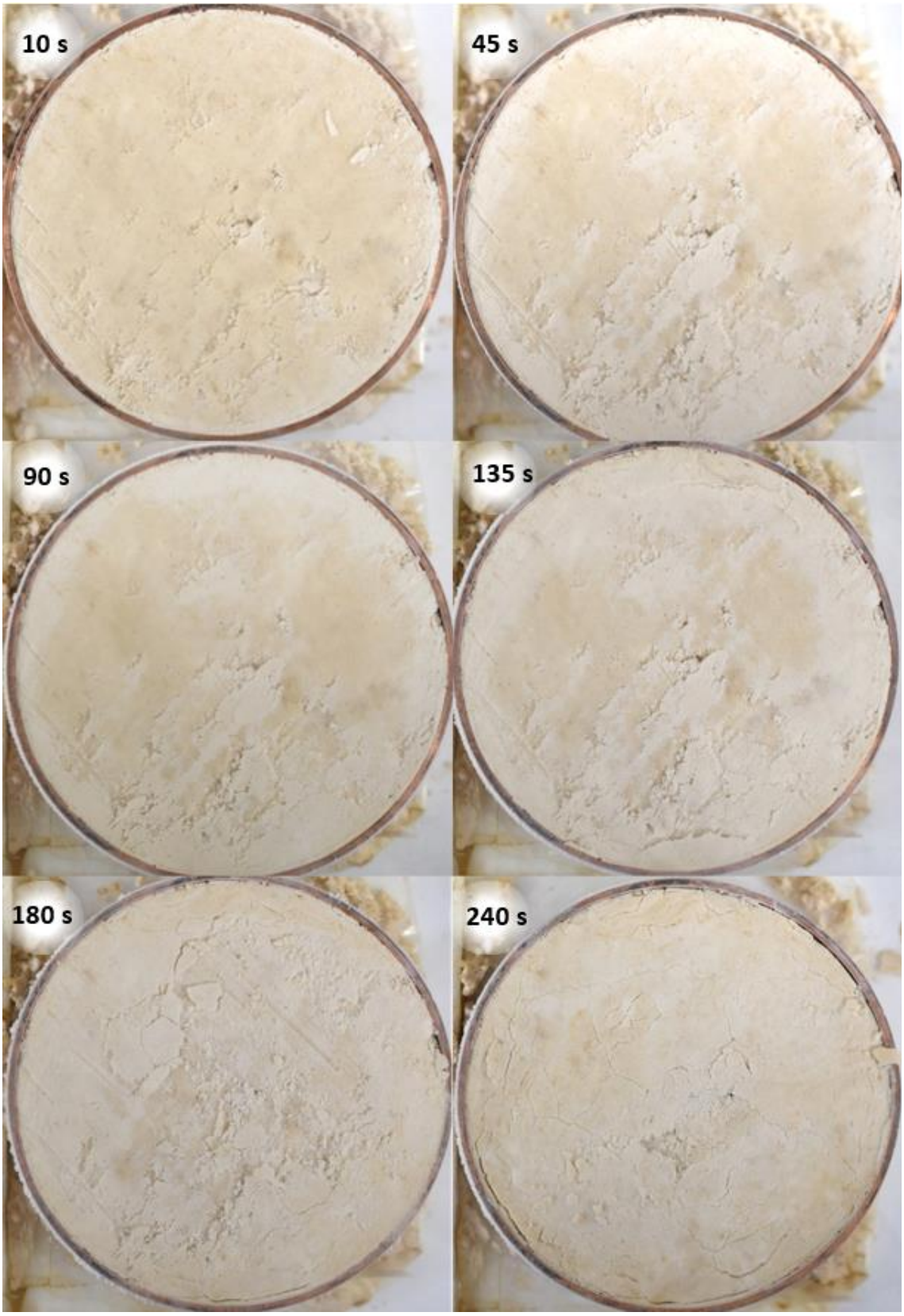

Figure 8.1.4. A sample of CO_2 snow mixed with 0.06% Mars analogue dust (by weight) was left at ambient conditions for a total of four minutes. From top left to bottom right: Exposure time (in seconds) 10 s, 45 s, 90 s, 135 s, 180 s, 240 s.

The results from the dusty CO_2 snow measurements are plotted in Figure 8.1.5, including the e-folding scales from the individual samples, and then the average of these for each dust concentration. Kaufmann and Hagermann (2015)'s dusty water snow results showed a trend of the e-folding scale of water snow ζ, with percentage dust content d (in weight percentage), given by

$$\zeta(d) = 5.1\ exp^{(-d/2.6131)} \quad (16)$$

This is plotted alongside the dusty CO_2 results for comparison, and it is clear that this trend does not fit the results given here.

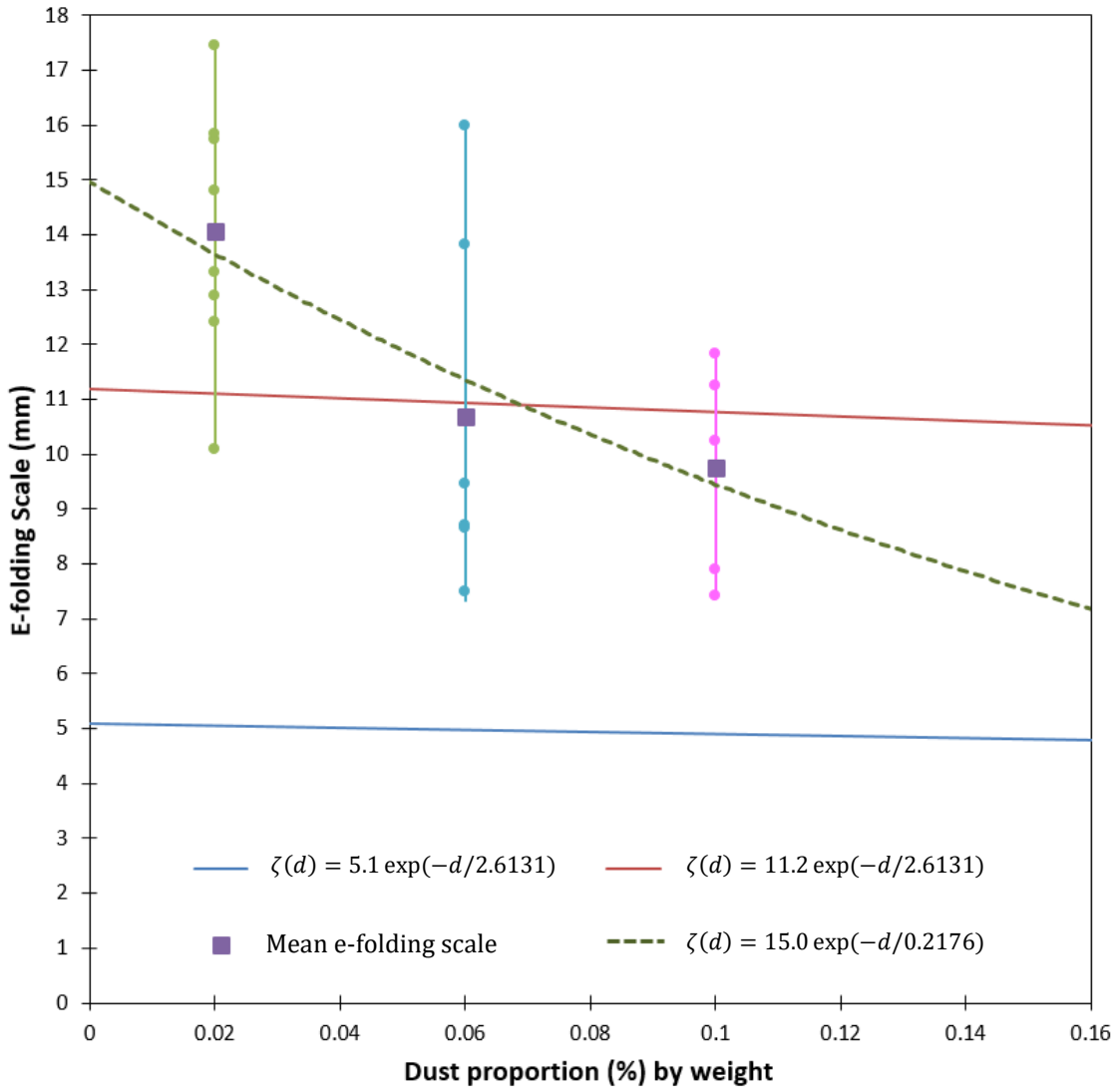

Figure 8.1.5. Calculated e-folding scale results from light intensity measurements through dusty CO_2 snow packs containing different percentages of dust. Due to the large uncertainties inherent in these measurements, error bars are not included. All samples are plotted on the graph (circles) and the arithmetic mean e-folding scale of each dust concentration is plotted as purple squares. The blue line denotes the predicted results using the equation from Kaufmann and Hagermann (2015). The red line shows a suggested adjustment to this equation for CO_2 snow instead of water. The dotted green line is a simple exponential fit to the mean e-folding scale results using a least squares method to indicate an equation to describe the data presented.

However, as discussed in Section 2.2, Kaufmann and Hagermann (2015) report the e-folding scale of water snow to be 5.4 ±1 mm, which is within the error margin of 5.1, the value which multiplies the exponent in their equation. Hence, I replaced this with the value given in Chapter 5 for the e-folding scale of both water and carbon dioxide snow: 11.2 mm ±3 mm, which is plotted along with the dusty CO_2 snow results in Figure 8.1.5.

Given the spread of the e-folding scale results, it is entirely possible that this trend could also explain these carbon dioxide results, although when compared to the average e-folding scale for each dust proportion, it is not a particularly good fit. There are several other factors which could be causing discrepancies: the water snow was mixed with standard grain size distribution Martian regolith analogue, whereas for the CO_2 experiments the JSC Mars-1A was sieved to only use grain sizes less than 20 µm; there could be some water frost contamination on the CO_2 samples; sintering of the CO_2 was a major effect, which was not reported as an issue for the water experiments; and the experimental set up was slightly different, although the methods employed were very similar. The dotted green line gives an empirical fit to the average results for each dust concentration as an indication to what the trend could look like. However, without a much larger data set, and improved laboratory setup optimised for making these measurements (improved thermal control is the main requirement), it is impossible to formulate any relationship between dust contamination in carbon dioxide snow and broad spectrum light penetration, and whether this relationship differs significantly from the effect of dust mixed with water snow.

8.2. Conclusions

For the first time a complete suite of light intensity measurements to calculate the penetration depth of broad spectrum (300 nm – 1100 nm) solar radiation has been made in both water and carbon dioxide ices, across a range of ice morphologies (snow, granular ice and slab ice), using consistent equipment and methodology. Through this experimental work I have found that, at the smallest grain sizes (<1 mm), ice composition seems to make little difference within the error ranges of the measurements; the e-folding scale of water or carbon dioxide snow is 11.2 mm ±3 mm. This is due to the high proportion of scattering surfaces to ice volume, which results in the dominant light propagation method being scattering in-between grains, rather than transmission through the grains. As grain size increases, so does the penetration depth, which begins to differ with composition, with carbon dioxide ice exhibiting a larger penetration depth than water ice. This difference is at its maximum with the largest 'grain size', slab ice. This relationship between the e-folding scale ζ, ice composition and grain size d can be approximated by

$$\zeta = 5.370 + \left(\frac{d}{b}\right)^{0.5} \quad (17)$$

where $b_{H2O} = 0.030 \; and \; b_{CO2} = 0.0144$, valid from the near-UV through the visible and into the near-IR wavelength range of 300 nm – 1100 nm. The e-folding scale of slab ice can be modelled by using an 'effective grain size' – the size of unblemished ice sections between cracks. Further work, with improved thermal control, would be required to determine the upper boundary for the absolute maximum effective grain size which equates to the e-folding scale of slab ice.

The implications of these results play an important role in models of the near surface energy balance on Mars, in that reliable, experimentally verified values for the penetration depth of solar radiation in specific ices can be used in those numerical models, with the aim to improve our understanding of various surface phenomena observed on the surface of Mars, in association with surface ice composed of either water or carbon dioxide. This could help explain the formation conditions of such features as araneiforms, for which there is no terrestrial analogue, or dry gullies, active today and being formed in the absence of liquid water, but displaying many fluvial-like landforms.

Further work which would expand and refine the results given in this thesis would include conducting the same broad spectrum irradiation experiments with other types of ices which are common in the solar system, such as methane, carbon monoxide or nitrogen ice, as found on bodies in the outer solar system. This would help refine the model given here, to find out if the same relationship holds true for all translucent ices. Additionally, determining the effect of contaminants such as regolith simulant or black carbon in ices and snows is an important aspect for determining the thermal state of an icy surface, as only a tiny proportion of dark contaminant can considerably decrease the penetration depth and the albedo of surface ice or snow. This final aspect is especially important for the surface of Mars, which has an active dust cycle, and in the study of comets, which contain large amounts of dark, carbon-rich material.

8.3. Responses to Research Questions

I. How does the penetration depth, or e-folding scale, of broad-spectrum solar irradiation in ices vary with ice composition? Is there a difference between water and carbon dioxide ice?

Based on my experimental results, the e-folding scale, or penetration depth, of broad spectrum (300 nm – 1100 nm) solar irradiation in ice is dependent upon composition. In its simplest form, the penetration depth of water slab ice is, on average ζ_{H2O} = 38.9 ±2 mm, ranging from 47.7 ±2 mm to

32.1 ±2 mm, depending on the quality (presence of cracks, air bubbles, etc.) of the ice. Whereas, the penetration depth in carbon dioxide slab ice is, on average ζ_{CO2} = 47.6 mm, ranging from 65.1 ±2 mm to 35.7 ±2 mm, again, dependent on ice quality. The largest penetration depths for each ice composition is for samples of the highest quality, meaning that they contained little to no cracks or air bubbles. Conversely, the lower measurement range is applicable for highly cracked, hazed or milky samples potentially containing air bubbles. This means that solid CO_2 ice is significantly more translucent to this wavelength range of light than H_2O ice is, given a similar level of cracking or ice bubbles present, with the largest difference being observed in ices with the highest level of homogeneity. These results have implications for the energy budget of any surface on which ice is emplaced and is subject to solar radiation. Moreover, the range of results is important. Given knowledge of the state of the ice (i.e. extent of cracking, or bubble content), which could be inferred from other data, such as albedo and/or ice density, a different value for the e-folding scale could be applied for different scenarios.

II. How does the penetration depth of broad-spectrum solar irradiation vary with ice morphology, and is this variation consistent across different ice compositions?

Data obtained from the slab ice experiments (Chapter 4) showed that the e-folding scale of the ice depended not only on ice composition, but also on the quality of the ice sample. Highly cracked, milky, or imperfect ice samples resulted in a smaller e-folding scale. This gave a range of calculated penetration depths, depending on the subset of data utilised: for water ice, the results obtained from light intensity measurements through the most cracked or bubbly areas gave an e-folding scale of ζ = 32.1 ±2 mm, whereas those measurements made through the clearest parts of the ice gave an e-folding scale of ζ = 47.7 ±2 mm. In contrast, the same measurements in carbon dioxide ice ranged from ζ = 35.7 ±2 mm to ζ = 65.1 ±2 mm respectively. At the opposite end of the grain size spectrum, the light intensity measurements through snow (classed here as particles <1 mm) to determine the penetration depth was found to be ζ_{snow} =11 ±3 mm, for both water and carbon dioxide ice compositions. To further investigate this apparent conundrum, experiments to determine the penetration depth were made through granular ice, of controlled grain size ranges for both ice compositions. The results from the granular ice experiments gave a trend of an increasing difference in penetration depth with increasing grain size. Equation 3 quantifies the relationship between the penetration depth of broad-spectrum irradiation, and the grain size of ice composed of either water or carbon dioxide.

III. What are the implications for the differences in solar irradiation penetration depths in the different ice compositions and morphologies, and what does this mean for icy surface processes on Mars, such as the formation of araneiforms in the polar regions?

Features such as araneiforms, which are observed in the polar regions of Mars today, but (as yet) nowhere else in the solar system, form because of a unique set of circumstances. The results detailed earlier in this section imply that one of the controlling factors may be the presence of carbon dioxide slab ice, rather than water ice, because of the larger e-folding scale of CO_2 ice. This means that more energy from incident sunlight is able to penetrate down through the ice sheet and be absorbed by the regolith below. The absorbed energy is then reradiated, warming the base of the ice sheet. However, as ice is opaque to infrared wavelengths, heating is constrained to the base of the ice slab, causing sublimation and resulting in CO_2 gas production. This continues until the gas pressure overcomes the strength of the ice, and ruptures, forming a CO_2 gas jet and carrying with it unconsolidated regolith material, as described in the Kieffer model (Kieffer, 2000). There are clearly many other factors controlling the formation of araneiforms, including the physical state of the regolith, such as the extent of consolidation, grain size, and thermal conductivity, as well as insolation levels, local topography, etc. However, as stated by Möhlmann (2010) and by Kaufmann and Hagermann (2015), the penetration depth of extra-terrestrial ices is the most uncertain parameter governing heat transfer into snow or ice-packs on Mars because of its dependence on other, equally poorly known parameters. By having a better understanding of how solar irradiation penetrates into these ices, models intending to simulate environments such as the Swiss cheese terrain, or gully formation invoking a similar mechanism to CO_2 jetting, could be updated and improved. Having a better constraint on the thickness of the carbon dioxide slab ice cover in areas such as the Cryptic Region, where araneiforms occur each year, would enable some verification of these measured penetration depths. This is because, when combined with accurate parameters for the underlying regolith (such as grain size, thermal conductivity, density) calculations could then be made to determine if enough solar energy can be transported to the regolith through the ice to generate basal sublimation and initiate the CO_2 jetting process, as observed.

References

Ackerman, T.P. and Toon, O.B., 1981. Absorption of visible radiation in atmosphere containing mixtures of absorbing and nonabsorbing particles. Applied Optics, 20(20): 3661-3668.

Appéré, T., Schmitt, B., Langevin, Y., Douté, S., Pommerol, A., Forget, F., Spiga, A., Gondet, B. and Bibring, J.P., 2011. Winter and spring evolution of northern seasonal deposits on Mars from OMEGA on Mars Express. Journal of Geophysical Research, 116(E5).

Balme, M., Mangold, N., Baratoux, D., Costard, F., Gosselin, M., Masson, P., Pinet, P. and Neukum, G., 2006. Orientation and distribution of recent gullies in the southern hemisphere of Mars: Observations from High Resolution Stereo Camera/Mars Express (HRSC/MEX) and Mars Orbiter Camera/Mars Global Surveyor (MOC/MGS) data. Journal of Geophysical Research, 111(E5).

Beaglehole, D., Ramanathan, B. and Rumberg, J., 1998. The UV to IR transmittance of Antarctic snow. Journal of Geophysical Research: Atmospheres, 103(D8): 8849-8857.

Behn, U., 1900. Ueber die Dichte der Kohlensäure im festen und flüssigem Zustande. Annalen der Physik, 308(12).

Bierson, C.J., Phillips, R.J., Smith, I.B., Wood, S.E., Putzig, N.E., Nunes, D. and Byrne, S., 2016. Stratigraphy and evolution of the buried CO_2 deposit in the Martian south polar cap. Geophysical Research Letters, 43(9): 4172-4179.

Bills, B.G., 1990. The rigid body obliquity history of Mars. Journal of Geophysical Research, 95(B9): 14137.

Blackford, J.R., 2007. Sintering and microstructure of ice: a review. Journal of Physics D: Applied Physics, 40(21): R355-R385.

Bohren, C.F. and Barkstrom, B.R., 1974. Theory of the optical properties of snow. Journal of Geophysical Research, 79(30): 4527-4535.

Bohren, C.F. and Beschta, R.L., 1979. Snowpack Albedo and Snow Density. Cold Regions Science and Technology, 1: 47-50.

Bohren, C.F. and Huffman, D.R., 1983. Absorption and Scattering of Light by Small Particles. Wiley-Interscience, New York.

Bourke, M. and Cranford, A., 2011. Seasonal formation of furrows on polar dunes, Fifth Mars Polar Science Conference.

Bourke, M., Nield, J., Diniega, S., Hansen, C.J. and McElwaine, J., 2016. A field study of the geomorphic effects of sublimating CO_2 blocks on dune slopes at Coral Pink Dunes, Utah., EGU General Assembly, Vienna, Austria.

Bourke, M.C., 2013. The formation of sand furrows by cryo-venting on Martian dunes, 44th Lunar and Planetary Science Conference.

Braithwaite, N., Lewis, S.R. and Ross, S.M., 2008. Understanding the Weather. The Open University S189 course text, in partnership with the Royal Meteorological Society, Milton Keynes: Open University.

Brandt, R., E. and Warren, S., G., 1993. Solar-heating rates and temperature profiles in antarctic snow and ice. Journal of Glaciology, 39(131): 99-110.

Brough, S., Hubbard, B. and Hubbard, A., 2019. Area and volume of mid-latitude glacier-like forms on Mars. Earth and Planetary Science Letters, 507: 10-20.

Brown, A.J., Piqueux, S. and Titus, T.N., 2014. Interannual observations and quantification of summertime H_2O ice deposition on the Martian CO_2 ice south polar cap. Earth and Planetary Science Letters, 406: 102-109.

Brown, B.H. and Matson, D.L., 1987. Thermal Effects of Insolation Propagation into the Regoliths of Airless Bodies. Icarus, 72: 84-94.

Brown, R.H., Cruikshank, D.P., Veverka, J., Helfenstein, P. and Eluszkiewicz, J., 1995. Surface composition and photometric properties of Triton., Neptune and Triton. University Arizona Press, Tucson, USA.

Byrne, S. and Ingersoll, A.P., 2003. A Sublimation Model for Martian South Polar Ice Features. Science, 299(5609): 1051-1053.

Calvin, W.M., 1990. Additions and corrections to the absorption coefficients of CO_2 Ice: Applications to the Martian south polar cap. Journal of Geophysical Research, 95(B9): 14743.

Carr, M.H., 2006. The Surface of Mars. Cambridge University Press, Cambridge.

Cedillo-Flores, Y., Treiman, A., H., Lasue, J. and Clifford, S., M., 2011. CO_2 gas fluidization in the initiation and formation of Martian polar gullies. Geophysical Research Letters, 38(21).

Chiar, J.E., 1997. The Nature and Evolution of Interstellar Ices. Planetary and Interstellar Processes Relevant to the Origins of Life. Springer, Dordrecht.

Choukroun, M., Keihm, S., Schloerb, F.P., Gulkis, S., Lellouch, E., Leyrat, C., von Allmen, P., Biver, N., Bockelée-Morvan, D., Crovisier, J., Encrenaz, P., Hartogh, P., Hofstadter, M., Ip, W.H., Jarchow, C., Janssen, M., Lee, S., Rezac, L., Beaudin, G., Gaskell, B., Jorda, L., Keller, H.U. and Sierks, H., 2015. Dark side of comet 67P/Churyumov-Gerasimenko in Aug.–Oct. 2014. Astronomy & Astrophysics, 583: A28.

Ciesla, F. and Cuzzi, J., 2006. The evolution of the water distribution in a viscous protoplanetary disk. Icarus, 181(1): 178-204.

Clancy, R., Montmessin, F., Benson, J., Daerden, F., Colaprete, A. and Wolff, M., 2017. Mars Clouds. In: R. Haberle, R. Clancy, F. Forget, M. Smith and R. Zurek (Editors), The Atmosphere and Climate of Mars. Cambridge University Press, Cambridge, pp. 76-105.

Clancy, R.T., Lee, S.W., Gladstone, G.R., McMillan, W.W. and Rousch, T., 1995. A new model for Mars atmospheric dust based upon analysis of ultraviolet through infrared observations from Mariner 9, Viking, and Phobos. Journal of Geophysical Research, 100(E3): 5251-5263.

Clark, R.N., Fanale, F.P. and Zent, A.P., 1983. Frost Grain Size Metamorphism: Implications for Remote Sensing of Planetary Surfaces. Icarus, 56: 233-245.

Clow, G.D., 1987. Generation of Liquid Water through the Melting of a Dusty Snowpack. Icarus, 72: 95-127.

Cockell, C.S. and Raven, J.A., 2004. Zones of photosynthetic potential on Mars and the early Earth. Icarus, 169(2): 300-310.

Colaprete, A., 2002. Carbon dioxide snow storms during the polar night on Mars. Journal of Geophysical Research, 107(E7).

Costard, F., Forget, F., Mangold, N. and Peulvast, J.P., 2002. Formation of Recent Martian Debris Flows by Melting of Near-Surface Ground Ice at High Obliquity. Science, 295: 110-113.

Cull, S., Arvidson, R.E., Morris, R.V., Wolff, M., Mellon, M.T. and Lemmon, M.T., 2010. Seasonal ice cycle at the Mars Phoenix landing site: 2. Postlanding CRISM and ground observations. Journal of Geophysical Research, 115.

Dalton, J.B., Cruikshank, D.P., Stephan, K., McCord, T.B., Coustenis, A., Carlson, R.W. and Coradini, A., 2010. Chemical Composition of Icy Satellite Surfaces. Space Science Reviews, 153(1-4): 113-154.

Datt, P., Gusain, H.S. and Das, R.K., 2015. Measurements of Net Subsurface Heat Flux in Snow and Ice Media in Dronning Maud Land, Antartica. Journal Geological Society of India, 86: 613-619.

De Sanctis, M.C., Capria, M.T. and Coradini, A., 2006. 67P/Churyumov–Gerasimenko nucleus model: Portrayal of the Rosetta target. Advances in Space Research, 38(9): 1906-1910.

de Villiers, S., Nermoen, A., Jamtveit, B., Mathiesen, J., Meakin, P. and Werner, S.C., 2012. Formation of Martian araneiforms by gas-driven erosion of granular material. Geophysical Research Letters, 39(13): n/a-n/a.

Devore, J.L., 2004. Probability and Statistics for Engineering and the Sciences. Brooks/Cole - Thomson Learning, Canada.

Dickson, J.L., Head, J.W. and Kreslavsky, M., 2007. Martian gullies in the southern mid-latitudes of Mars: Evidence for climate-controlled formation of young fluvial features based upon local and global topography. Icarus, 188(2): 315-323.

Diniega, S., Hansen, C.J., McElwaine, J.N., Hugenholtz, C.H., Dundas, C.M., McEwen, A.S. and Bourke, M.C., 2013. A new dry hypothesis for the formation of martian linear gullies. Icarus, 225(1): 526-537.

Ditteon, R. and Kieffer, H., H., 1979. Optical properties of solid CO_2: Application to Mars. Journal of Geophysical Research, 84(B14): 8294.

Domine, F., Albert, M., Huthwelker, T., Jacobi, H.-W., Kokhanovsky, A.A., Lehning, M., Picard, G. and Simpson, W.R., 2008. Snow Physics as relevant to Snow Photochemistry. Atmospheric Chemistry and Physics, European Geosciences Union, 8(2): 171-208.

Dundas, C.M., Diniega, S. and McEwen, A.S., 2015. Long-term monitoring of martian gully formation and evolution with MRO/HiRISE. Icarus, 251: 244-263.

Dundas, C.M., McEwen, A.S., Diniega, S., Byrne, S. and Martinez-Alonso, S., 2010. New and recent gully activity on Mars as seen by HiRISE. Geophysical Research Letters, 37(7): n/a-n/a.

Dundas, C.M., McEwen, A.S., Diniega, S., Hansen, C.J., Byrne, S. and McElwaine, J.N., 2017. The formation of gullies on Mars today. Geological Society, London, Special Publications: SP467.5.

Durham, W.B., Prieto-Ballesteros, O., Goldsby, D.L. and Kargel, J.S., 2010. Rheological and Thermal Properties of Icy Materials. Space Science Reviews, 153(1-4): 273-298.

Egan, W., G. and Spagnolo, F.A., 1969. Complex Index of Refraction of Bulk Solid Carbon Dioxide. Applied Optics, 8(11): 2359-2360.

Eluszkiewicz, J., 1991. On the Microphysical State of the Surface of Triton. Journal of Geophysical Research, 96(Suppliment): 19217-19229.

Eluszkiewicz, J., 1993. On the Microphysical State of the Martian Seasonal Caps. Icarus, 103: 13-48.

Eluszkiewicz, J., Leliwa-Kopystynski, J. and Kossacki, K.J., 1995. Metamorphism of Solar System Ices. In: B.E. Schmidt, C. De Bergh and M. Festou (Editors), Solar System Ices. Based on reviews presented at the International Symposium “Solar System Ices”, held in Toulouse, France 27-30th March 1995. Springer-Science+Business Media, B. V.

Eluszkiewicz, J., Moncet, J.-L., Titus, T.N. and Hansen, G.B., 2005. A microphysically-based approach to modeling emissivity and albedo of the martian seasonal caps. Icarus, 174(2): 524-534.

Feldman, W.C., 2003. CO_2 frost cap thickness on Mars during northern winter and spring. Journal of Geophysical Research, 108(E9).

Feldman, W.C., Pathare, A., Maurice, S., Prettyman, T.H., Lawrence, D.J., Milliken, R.E. and Travis, B.J., 2011. Mars Odyssey neutron data: 2. Search for buried excess water ice deposits at nonpolar latitudes on Mars. Journal of Geophysical Research, 116(E11).

Filacchione, G., Raponi, A., Capaccioni, F., Ciarniello, M., Tosi, F., Capria, M.T., De Sanctis, M.C., Migliorini, A., Piccioni, G., Cerroni, P., Barucci, M.A., Fornasier, S., Schmitt, B., Quirico, E., Erard, S., Bockelee-Morvan, D., Leyrat, C., Arnold, G., Mennella, V., Ammannito, E., Bellucci, G., Benkhoff, J., Bibring, J.P., Blanco, A., Blecka, M.I., R. Carlson, R., Carsenty, U., Colangeli, L., Combes, M., Combi, M., Crovisier, J., Drossart, P., Encrenaz, T., Federico, C., Fink, U., Fonti, S., Fulchignoni, M., Ip, W.-H., Irwin, P., Jaumann, R., Kuehrt, E., Langevin, Y., Magni, G., McCord, T., Moroz, L., Mottola, S., Palomba, E., Schade, U., Stephan, K., Taylor, F., Tiphene, D., Tozzi, G.P., Beck, P., Biver, N., Bonal, L., Combe, J.P., Despan, D., Flamini, E., Formisano, M., Frigeri, A., Grassi, D., Gudipati, M.S., Kappel, D., Longobardo, A., Mancarella, F., Markus, K., Merlin, F., Orosei, R., Rinaldi, G., Cartacci, M., Cicchetti, A., Hello, Y., Henry, F., Jacquinod, S., Reess, J.M., Noschese, R., Politi, R. and Peter, G., 2016. Seasonal exposure of carbon dioxide on the nucleus of comet 67P/Churyumov-Gerasimenko. Science, 354(6319): 1563-1566.

Forget, F., 1998. Mars CO_2 Ice Polar Caps. In: B.E. Schmidt (Editor), Solar System Ices. Springer Science & Business Media, B. V., pp. 477-507.

Forget, F., Hansen, G.B. and Pollack, J.B., 1995. Low brightness temperatures of Martian polar caps: CO_2 clouds or low surface emessivity? Journal of Geophysical Research, 100(E10): 21219-21234.

Forget, F., Hourdin, F., Fournier, R., Hourdin, C., Talagrand, O., Collines, M., Lewis, S.R., Read, P.L. and Huot, J.-P., 1999. Improved general circulation models of the Martian atmosphere from the surface to above 80 km. Journal of Geophysical Research, 104(E10): 24155-24176.

Forget, F., Hourdin, F. and Talagrand, O., 1998. CO_2 Snow Fall on Mars: Simulation with a General Circulation Model. Icarus, 131: 302-316.

Forget, F. and Pollack, J.B., 1996. Thermal infrared observations of the condensing Martian polar caps: CO_2 ice temperatures and radiative budget. Journal of Geophysical Research: Planets, 101(E7): 16865-16879.

Foster, J.L., Chang, A.T.C., Hall, D.K., Wergin, W.P., Erbe, E.F. and Barton, J., 1998. Carbon dioxide crystals: An examination of their size, shape, and scattering properties at 37 GHz and comparisons with water ice (snow) measurements. Journal of Geophysical Research: Planets, 103(E11): 25839-25850.

France, J.L., King, M.D. and MacArthur, A., 2010. A photohabitable zone in the martian snowpack? A laboratory and radiative-transfer study of dusty water–ice snow. Icarus, 207(1): 133-139.

Genova, A., Goossens, S., Lemoine, F.G., Mazarico, E., Neumann, G.A., Smith, D.E. and Zuber, M.T., 2016. Seasonal and static gravity field of Mars from MGS, Mars Odyssey and MRO radio science. Icarus, 272: 228-245.

Gillmann, C., Lognonné, P., Chassefière, E. and Moreira, M., 2009. The present-day atmosphere of Mars: Where does it come from? Earth and Planetary Science Letters, 277(3-4): 384-393.

Greeley, R., Leach, R., White, B., Iversen, J.J. and Pollack, J.B., 1980. Threshold Windspeeds for Sand on Mars: Wind Tunnel Simulations. Geophysical Research Letters, 7(2): 121-124.

Grundy, W.M., Binzel, R.P., Buratti, B.J., Cook, J.C., Cruikshank, D.P., Dalle Ore, C.M., Earle, A.M., Ennico, K., Howett, C.J., Lunsford, A.W., Olkin, C.B., Parker, A.H., Philippe, S., Protopapa, S., Quirico, E., Reuter, D.C., Schmitt, B., Singer, K.N., Verbiscer, A.J., Beyer, R.A., Buie, M.W., Cheng, A.F., Jennings, D.E., Linscott, I.R., Parker, J.W., Schenk, P.M., Spencer, J.R., Stansberry, J.A., Stern, S.A., Throop, H.B., Tsang, C.C., Weaver, H.A., Weigle, G.E., 2nd, Young, L.A. and New Horizons Science, T., 2016. Surface compositions across Pluto and Charon. Science, 351(6279): aad9189.

Gubler, H., 1985. Model for Dry Snow Metamorphism by Interparticle Vapour Flux. Journal of Geophysical Research, 90(D5): 8081-8092.

Haberle, R.M., Clancy, R.T., Forget, F., Smith, M.D. and Zurek, R.W., 2017. The Atmosphere and Climate of Mars. Cambridge University Press, Cambridge.

Hansen, C.J., Byrne, S., Portyankina, G., Bourke, M., Dundas, C., McEwen, A., Mellon, M., Pommerol, A. and Thomas, N., 2013. Observations of the northern seasonal polar cap on Mars: I. Spring sublimation activity and processes. Icarus, 225(2): 881-897.

Hansen, C.J., Thomas, N., Portyankina, G., McEwen, A., Becker, T., Byrne, S., Herkenhoff, K., Kieffer, H. and Mellon, M., 2010. HiRISE observations of gas sublimation-driven activity in Mars' southern polar regions: I. Erosion of the surface. Icarus, 205(1): 283-295.

Hansen, G., B., 1997. The infrared absorption spectrum of carbon dioxide ice from 1.8 to 333 μm. Journal of Geophysical Research: Planets, 102(E9): 21569-21587.

Hansen, G.B., 1999. Control of the radiative behavior of the Martian polar caps by surface CO_2 ice: Evidence from Mars Global Surveyor measurements. Journal of Geophysical Research: Planets, 104(E7): 16471-16486.

Harrison, T.N., Malin, M.C. and Edgett, K.S., 2009. Liquid Water on the Surface of Mars Today: Present Gully Activity Observed by the Mars Reconnaissance Orbiter (MRO) and Mars Global Surveyor (MGS) and Direction for Future Missions, American Geophysical Union, San Francisco, USA.

Hartmann, W., 2003. Martian hillside gullies and icelandic analogs. Icarus, 162(2): 259-277.

Hartmann, W.K., 2001. Martian Seeps And Their Relation To Youthful Geothermal Activity. Space Science Reviews, 96: 405-410.

Hayne, P.O., Paige, D.A. and Heavens, N.G., 2014. The role of snowfall in forming the seasonal ice caps of Mars: Models and constraints from the Mars Climate Sounder. Icarus, 231: 122-130.
Hayne, P.O., Paige, D.A., Schofield, J.T., Kass, D.M., Kleinböhl, A., Heavens, N.G. and McCleese, D.J., 2012. Carbon dioxide snow clouds on Mars: South polar winter observations by the Mars Climate Sounder. Journal of Geophysical Research: Planets, 117(E8): 1-23.
Hecht, M., 2002. Metastability of Liquid Water on Mars. Icarus, 156(2): 373-386.
Heki, K., 2004. Dense GPS array as a new sensor of seasonal changes of surface loads. 150: 177-196.
Heldmann, J.L., 2005. Formation of Martian gullies by the action of liquid water flowing under current Martian environmental conditions. Journal of Geophysical Research, 110(E5).
Heldmann, J.L., Carlsson, E., Johansson, H., Mellon, M.T. and Toon, O.B., 2007. Observations of martian gullies and constraints on potential formation mechanisms. II. The Northern Hemisphere. Icarus, 188(2): 324-344.
Heldmann, J.L. and Mellon, M.T., 2004. Observations of martian gullies and constraints on potential formation mechanisms. Icarus, 168(2): 285-304.
Herkenhoff, K., 2000. Surface Ages and Resurfacing Rates of the Polar Layered Deposits on Mars. Icarus, 144(2): 243-253.
Herr, K.C. and Pimentel, G.C., 1969. Infrared Absorptions near Three Microns Recorded over the Polar Cap of Mars. Science, 166(3904): 496-499.
Hibbitts, C.A., 2003. Carbon dioxide on Ganymede. Journal of Geophysical Research, 108(E5).
Hoffman, N., 2002. Active Polar Gullies on Mars and the Role of Carbon Dioxide. Astrobiology, 2(3): 313-323.
Hudgins, D.M., Sandford, S.A., Allamandola, L.J. and Tielens, A.G.G.M., 1993. Mid- and far-infrared spectroscopy of ices - Optical constants and integrated absorbances. Astrophysical Journal Supplement Series, 86(2): 713-870.
Ingersoll, A.P., Svitek, T. and Murray, B.C., 1992. Stability of Polar Frosts in Spherical Bowl-shaped Craters on Moon, Mercury and Mars. Icarus, 100: 40-47.
Irvine, W.M. and Pollack, J.B., 1967. Infrared Optical properties of water and ice spheres. Icarus, 8: 324-360.
Ishii, T. and Sasaki, S., 2004. Formation of Recent Martian Gullies by Avalanches of CO_2 Frost, Lunar and Planetary Science Conference, League City, Texas, USA.
Jouannic, G., Gargani, J., Costard, F., Ori, G.G., Marmo, C., Schmidt, F. and Lucas, A., 2012. Morphological and mechanical characterization of gullies in a periglacial environment: The case of the Russell crater dune (Mars). Planetary and Space Science, 71(1): 38-54.
Kahre, M., Vines, S., Haberle, R.M., Hollingsworth, J. and Leovy, C.B., 2011. Stabilizing the Early Martian Climate: Effects of Airborne Dust, CO_2 Ice Cap Albedo, and Orbital Obliquity on Atmospheric Collapse. American Geophysical Union, Fall Meeting 2011.
Kahre, M.A., Vines, S.K., Haberle, R.M. and Hollingsworth, J.L., 2013. The early Martian atmosphere: Investigating the role of the dust cycle in the possible maintenance of two stable climate states. Journal of Geophysical Research: Planets, 118(6): 1388-1396.
Kang, S.-J., L., 2005. Sintering: Densification, Grain Growth and Microstructure. Elsevier, Oxford, UK.
Kaufmann, E. and Hagermann, A., 2015. Penetration of solar radiation into pure and Mars-dust contaminated snow. Icarus, 252: 144-149.
Kaufmann, E. and Hagermann, A., 2017. Experimental investigation of insolation-driven dust ejection from Mars' CO_2 ice caps. Icarus, 282: 118-126.
Kaufmann, E., Kömle, N. and Kargl, G., 2006. Laboratory simulation experiments on the solid-state greenhouse effect in planetary ices. Icarus, 185(1): 274-286.
Kieffer, H.H., 2000. Annual Punctuated CO_2 Slab-Ice and Jets on Mars, Mars Polar Science, pp. 4095.
Kieffer, H.H., 2007. Cold jets in the Martian polar caps. Journal of Geophysical Research, 112(E8).
Kieffer, H.H., Christensen, P.R. and Titus, T.N., 2006. CO_2 jets formed by sublimation beneath translucent slab ice in Mars' seasonal south polar ice cap. Nature, 442(7104): 793-6.
Kieffer, H.H., Titus, T.N., Mullins, K.F. and Christensen, P.R., 2000. Mars south polar spring and summer behavior observed by TES: Seasonal cap evolution controlled by frost grain size. Journal of Geophysical Research, 105(E4): 9653.

Knauth, L., 2002. Eutectic Brines on Mars: Origin and Possible Relation to Young Seepage Features. Icarus, 158(1): 267-271.
Kömle, N., Deetleff, G. and Dankert, C., 1990. Thermal Behaviour of Pure and Dusty Ices on Comets and Icy Satalites. Astronomy and Astrophysics, 277: 246-254.
Kossacki, K.J., 2015. Comet 9P/Tempel 1: Evolution of the surface. Icarus, 245: 348-354.
Kossacki, K.J., Kömle, N.I., Leliwa-Kopystynski, J. and Kargl, G., 1997. Laboratory Investigation of the Evolution of Cometary Analogs: Results and Interpretation. Icarus, 128: 127-144.
Kossacki, K.J., Spohn, T., Hagermann, A., Kaufmann, E. and Kührt, E., 2015. Comet 67P/Churyumov–Gerasimenko: Hardening of the sub-surface layer. Icarus, 260: 464-474.
Kuroda, T., Medvedev, A.S., Kasaba, Y. and Hartogh, P., 2013. Carbon dioxide ice clouds, snowfalls, and baroclinic waves in the northern winter polar atmosphere of Mars. Geophysical Research Letters, 40(8): 1484-1488.
Laskar, J., Correia, A.C.M., Gastineau, M., Joutel, F., Levrard, B. and Robutel, P., 2004. Long term evolution and chaotic diffusion of the insolation quantities of Mars. Icarus, 170(2): 343-364.
Lee, P., Cockell, C.S., Marinova, M.M., McKay, C. and Rice Jr., J.W., 2001. Snow and ice melt flow features on Devon Island, Nanabut, Arctic Canada as possible analogs for recent slope flow features on Mars., 32nd Lunar and Planetary Science, Houston, Texas, USA.
Leidenfrost, J.G., 1966. On the Fixation of Water in Diverse Fire. International Journal of Heat and Mass Transfer, 9: 1153-1166.
Leighton, R.B. and Murray, B.C., 1966. Behavior of Carbon Dioxide and Other Volatiles on Mars. Science, 153: 136-144.
Levy, J., Head, J. and Marchant, D., 2009. Thermal contraction crack polygons on Mars: Classification, distribution, and climate implications from HiRISE observations. Journal of Geophysical Research, 114(E1).
Levy, J.S., Marchant, D.R. and Head, J.W., 2010. Thermal contraction crack polygons on Mars: A synthesis from HiRISE, Phoenix, and terrestrial analog studies. Icarus, 206(1): 229-252.
Lewis, J.S., 1972. Metal/Silicate Fractionation in the Solar System. Earth and Planetary Science Letters, 15: 286-290.
Lewis, S.R., Collins, M., Read, P.L., Forget, F., Hourdin, F., Fournier, R., Hourdin, C., Talagrand, O. and Huot, J.-P., 1999. A climate database for Mars. Journal of Geophysical Research: Planets, 104(E10): 24177-24194.
Li, W., Stamnes, K., Chen, B. and Xiong, X., 2001. Snow grain size retrieved from near-infrared radiances at multiple wavelengths. Geophysical Research Letters, 28(9): 1699-1702.
Libois, Q., Picard, G., Dumont, M., Arnaud, L., Sergent, C., Pougatch, E., Sudul, M. and Vial, D., 2014. Experimental determination of the absorption enhancement parameter of snow. Journal of Glaciology, 60(224): 714-724.
Libois, Q., Picard, G., France, J.L., Arnaud, L., Dumont, M., Carmagnola, C.M. and King, M.D., 2013. Influence of grain shape on light penetration in snow. The Cryosphere, 7(6): 1803-1818.
Long, D.A., 2002. Survey of Light Scattering Phenomena, The Raman Effect: A Unified Treatment of the Theory of Raman Scattering by Molecules. John Wiley & Sons, Ltd, Chichester, England.
Maass, O. and Barnes, W.H., 1926. Some Thermal Constants of Solid and Liquid Carbon Dioxide. Proceedings of the Royal Society of London. Series A, Containing Papers of a Mathematical and Physical Character, 111(757): 224-244.
Malin, M. and Edgett, K.S., 2000. Evidence for Recent Groundwater Seepage and Surface Runoff on Mars. Science, 288: 2330-2335.
Malin, M.C., A., C.M. and Davis, S.D., 2001. Observational Evidence for an Active Surface Reservoir of Solid Carbon Dioxide on Mars. Science, 294.
Malin, M.C., Edgett, K.S., Posiolova, L.V., McColley, S.M. and Dobrea, E.Z.N., 2006. Present-Day Impact Cratering Rate and Contemnpory Gully Activity on Mars. Science, 314: 1573-1577.
Malkin, T.L., Murray, B.J., Salzmann, C.G., Molinero, V., Pickering, S.J. and Whale, T.F., 2015. Stacking disorder in ice I. Phys Chem Chem Phys, 17(1): 60-76.
Mangan, T.P., Salzmann, C.G., Plane, J.M.C. and Murray, B.J., 2017. CO_2 ice structure and density under Martian atmospheric conditions. Icarus.

Manzhelii, V.G., Tolkachev, A.M., Bagatskii, M.I. and Voitovich, E.I., 1971. Thermal expansion, heat capacity, and compressibility of solid CO_2. Phys. Status Solidi 44(1): 39-49.

Martínez, G.M., Renno, N.O. and Elliott, H.M., 2012. The evolution of the albedo of dark spots observed on Mars polar region. Icarus, 221(2): 816-830.

Matson, D.L. and Brown, B.H., 1989. Solid-State Greenhouses and Their Implications for Icy Satalites. Icarus, 77: 67-81.

Matsuo, K. and Heki, K., 2009. Seasonal and inter-annual changes of volume density of Martian CO_2 snow from time-variable elevation and gravity. Icarus, 202(1): 90-94.

Mc Keown, L.E., Bourke, M.C. and McElwaine, J.N., 2017. Experiments On Sublimating Carbon Dioxide Ice And Implications For Contemporary Surface Processes On Mars. Sci Rep, 7(1): 14181.

McCord, T.B., Hansen, G.B., Clark, R.N., Martin, P.D., Hibbitts, C.A., Fanale, F.P., Granahan, J.C., Segura, M., Matson, D.L., Johnson, T.V., Carlson, R.W., Smythe, W.D. and Danielson, G.E., 1998. Non-water-ice constituents in the surface material of the icy Galilean satellites from the Galileo near-infrared mapping spectrometer investigation. Journal of Geophysical Research: Planets, 103(E4): 8603-8626.

McEwen, A., Ojha, L., Dundas, C., Mattson, S.S., Byrne, S., Wray, J.J., Cull, S.C., Murchie, S.L., Thomas, N. and Gulick, V.C., 2011. Seasonal Flows on Warm Martian Slopes. Science, 333: 740-743.

McEwen, A.S., Dundas, C.M., Mattson, S.S., Toigo, A.D., Ojha, L., Wray, J.J., Chojnacki, M., Byrne, S., Murchie, S.L. and Thomas, N., 2014. Recurring slope lineae in equatorial regions of Mars. Nature Geoscience, 7(1): 53-58.

Mellon, M.T., 1997. Small-scale polygonal features on Mars: Seasonal thermal contraction cracks in permafrost. Journal of Geophysical Research: Planets, 102(E11): 25617-25628.

Mellon, M.T. and Phillips, R.J., 2001. Recent gullies on Mars and the source of liquid water. Journal of Geophysical Research: Planets, 106(E10): 23165-23179.

Mie, G., 1908. Beiträge zur Optik trüber Medien, speziell kolloidaler Metallösungen. Annalen der Physik, 330(3): 377.

Millour, E., Forget, F., Spiga, A., Vals, M., Zakharov, V., Montabone, L., Lefèvre, F., Montmessin, F., Chaufray, J.-Y., López-Valverde, M.A., Gonzalez-Galindo, F., Lewis, S.R., Desjean, M.-C., Cipriani, F. and team, M.d., 2018. THE MARS CLIMATE DATABASE (VERSION 5.3), From Mars Express to ExoMars, Madrid, Spain.

Mitrofanov, I., Malakhov, A., Bakhtin, B., Golovin, D., Kozyrev, A., Litvak, M., Mokrousov, M., Sanin, A., Tretyakov, V., Vostrukhin, A., Anikin, A., Zelenyi, L.M., Semkova, J., Malchev, S., Tomov, B., Matviichuk, Y., Dimitrov, P., Koleva, R., Dachev, T., Krastev, K., Shvetsov, V., Timoshenko, G., Bobrovnitsky, Y., Tomilina, T., Benghin, V. and Shurshakov, V., 2018. Fine Resolution Epithermal Neutron Detector (FREND) Onboard the ExoMars Trace Gas Orbiter. Space Science Reviews, 214(5).

Möhlmann, D.T.F., 2010. Temporary liquid water in upper snow/ice sub-surfaces on Mars? Icarus, 207(1): 140-148.

Molaro, J.L., Choukroun, M., Phillips, C.B., Phelps, E.S., Hodyss, R., Mitchell, K.L., Lora, J.M. and Meirion-Griffith, G., 2019. The Microstructural Evolution of Water Ice in the Solar System Through Sintering. Journal of Geophysical Research: Planets.

Montmessin, F., Gondet, B., Bibring, J.P., Langevin, Y., Drossart, P., Forget, F. and Fouchet, T., 2007. Hyperspectral imaging of convective CO_2 ice clouds in the equatorial mesosphere of Mars. Journal of Geophysical Research, 112(E11).

Mount, C.P. and Titus, T.N., 2015. Evolution of Mars' northern polar seasonal CO_2 deposits: Variations in surface brightness and bulk density. Journal of Geophysical Research: Planets, 120(7): 1252-1266.

Murray, B.J., Malkin, T.L. and Salzmann, C.G., 2015a. The crystal structure of ice under mesospheric conditions. Journal of Atmospheric and Solar-Terrestrial Physics, 127: 78-82.

Murray, B.J., Salzmann, C.G., Heymsfield, A.J., Dobbie, S., III, R.R.N. and Cox, C.J., 2015b. Trigonal Ice Crystals in Earth's Atmosphere. Bulletin of the American Meteorological Society, 96(9): 1519-1531.

Musselwhite, D.S., Swindle, T.D. and Lunine, J.I., 2001. Liquid CO_2 Breakout and the Formation of Recent Small Gullies on Mars. Geophysical Research Letters, 28(7): 1283-1285.

Nash, C. and Bourke, M., 2015. Southern hemisphere sand furrows: spatial patterning and implications for the cryo-venting process., EGU General Assembly. Copernicus, Vienna, Austria.

Niederdorfer, E., 1933. Messungen des Wärmeumsatzes über schneebedecktem Boden. Meteorol. Z, 50: 201-208.

Pasquon, K., Gargani, J., Massé, M. and Conway, S.J., 2016. Present-day formation and seasonal evolution of linear dune gullies on Mars. Icarus, 274: 195-210.

Perovich, D.K., 1996. The Optical Properties of Sea Ice, Monograph 96-1. Office of Naval Research.

Perovich, D.K., 2007. Light reflection and transmission by a temperate snow cover. Journal of Glaciology, 53(181): 201-210.

Phillips, R.J., Davis, B.J., Tanaka, K.L., Byrne, S., Mellon, M.T., Putzig, N.E., Haberle, R.M., Kahre, M.A., Campbell, B.A., Carter, L.M., Smith, I.B., Holt, J.W., Smrekar, S.E., Nunes, D.C., Plaut, J.J., Egan, A.F., Titus, T.N. and Seu, R., 2011. Massive CO_2 Ice Deposits Sequestered in the South Polar Layered Deposits of Mars. Science, 332: 838-841.

Pilorget, C. and Forget, F., 2016. Formation of Gullies on Mars by Debris Flows Triggered by CO_2 Sublimation. Nature Geoscience, 9(1): 65-69.

Pilorget, C., Forget, F., Edwards, C.S. and Ehlmann, B.L., 2014. Seasonal Evolution of surface CO_2 Ice on Mars: Physical processes and Impacts on surface properties. Eighth International Conference on Mars: 1313.

Pilorget, C., Forget, F., Millour, E., Vincendon, M. and Madeleine, J.B., 2011. Dark spots and cold jets in the polar regions of Mars: New clues from a thermal model of surface CO_2 ice. Icarus, 213(1): 131-149.

Pilorget, C., Vincendon, M. and Poulet, F., 2013. A radiative transfer model to simulate light scattering in a compact granular medium using a Monte-Carlo approach: Validation and first applications. Journal of Geophysical Research: Planets, 118(12): 2488-2501.

Piqueux, S., Byrne, S. and Richardson, M.I., 2003. Sublimation of Mars's southern seasonal CO_2 ice cap and the formation of spiders. Journal of Geophysical Research, 108(E8).

Piqueux, S. and Christensen, P.R., 2008. North and south subice gas flow and venting of the seasonal caps of Mars: A major geomorphological agent. Journal of Geophysical Research, 113(E6).

Piqueux, S., Kleinböhl, A., Hayne, P.O., Heavens, N.G., Kass, D.M., McCleese, D.J., Schofield, J.T. and Shirley, J.H., 2016. Discovery of a widespread low-latitude diurnal CO_2 frost cycle on Mars. Journal of Geophysical Research: Planets, 121.

Pollack, J.B. and Toon, O.B., 1982. Quasi-periodic climate changes on Mars: A review. Icarus, 50: 259-287.

Portyankina, G., Hansen, C.J. and Aye, K.-M., 2017. Present-day erosion of Martian polar terrain by the seasonal CO_2 jets. Icarus, 282: 93-103.

Portyankina, G., Hansen, C.J. and Aye, K.-M., 2019. How Martian araneiforms get their shapes: Morphological analysis and diffusion-limited aggregation model for polar surface erosion. Icarus.

Portyankina, G., Markiewicz, W.J., Thomas, N., Hansen, C.J. and Milazzo, M., 2010. HiRISE observations of gas sublimation-driven activity in Mars' southern polar regions: III. Models of processes involving translucent ice. Icarus, 205(1): 311-320.

Portyankina, G., Merrison, J., Iversen, J., J., Yoldi, Z., Hansen, C.J., Aye, K.-M. and Pommerol, A., 2016. Labratory Investigations of Physical State of CO_2 Ice on Mars, Sixth Mars Polar Science Conference.

Portyankina, G., Merrison, J., Iversen, J.J., Yoldi, Z., Hansen, C.J., Aye, K.M., Pommerol, A. and Thomas, N., 2018. Laboratory investigations of the physical state of CO_2 ice in a simulated Martian environment. Icarus.

Portyankina, G., Pommerol, A., Aye, K.-M., Hansen, C.J. and Thomas, N., 2012. Polygonal cracks in the seasonal semi-translucent CO_2 ice layer in Martian polar areas. Journal of Geophysical Research: Planets, 117(E2): n/a-n/a.

Quirico, E. and Schmitt, B., 1997. Near-Infrared Spectroscopy of Simple Hydrocarbons and Carbon Oxides in Solid N2 and as Pure Ices: Implications for Triton and Pluto. Icarus, 127: 354-378.

Read, P.L. and Lewis, S.R., 2004. The Martian Climate Revisited: Atmosphere and Environment of a Desert Planet. Springer, Berlin.

Röttger, K., Endriss, A., Ihringer, J., Doyle, S. and Kuhs, W.F., 2012. Lattice constants and thermal expansion of H_2O and D_2O ice Ih between 10 and 265 K. Addendum. Acta Crystallogr B, 68(Pt 1): 91.

Rusin, N.P., 1961. Meterological and radiational regime of Antarctica. Israel Program for Scientific Translation, Jerusalem.

Sandford, S.A. and Allamandola, L.J., 1990. The Physical and Infrared Spectral Properties of CO_2 in Astrophysical Ice Analogues. The Astrophysical Journal, 355: 357-372.

Schaible, M.J., Johnson, R.E., Zhigilei, L.V. and Piqueux, S., 2017. High energy electron sintering of icy regoliths: Formation of the PacMan thermal anomalies on the icy Saturnian moons. Icarus, 285: 211-223.

Schlatter, T.W., 1972. The Local Surface Energy Balance and Subsurface Temperature Regime in Antarctica. Journal of Applied Meterology, 11: 1048-1062.

Schneider, C.A., Rasband, W.S. and Eliceiri, K.W., 2012. NIH Image to ImageJ:25 Years of Image Analysis. Nature methods, 9(7): 671.

Schorghofer, N. and Edgett, K.S., 2006. Seasonal surface frost at low latitudes on Mars. Icarus, 180(2): 321-334.

Schwamb, M.E., Aye, K.-M., Portyankina, G., Hansen, C.J., Allen, C., Allen, S., Calef, F.J., Duca, S., McMaster, A. and Miller, G.R.M., 2018. Planet Four: Terrains – Discovery of araneiforms outside of the South Polar layered deposits. Icarus, 308: 148-187.

Schwerdtfeger, P. and Weller, G.E., 1977. Radiative Heat Trafsfer Processes in Snow and Ice. Antarctic Research Series, 25.

Seiferlin, K., Kömle, N.I., Kargl, G. and Spohn, T., 1996. Line heat-source measurements of the thermal conductivity of porous H_2O ice, CO_2 ice and mineral powders under space conditions. Planetary and Space Science, 44(7): 691-704.

Shinbrot, T., Duong, N.H., Kwan, L. and Alvarez, M.M., 2004. Dry granular flows can generate surface features resembling those seen in Martian gullies. Proc Natl Acad Sci U S A, 101(23): 8542-6.

Smith, D.E., Zuber, M.T. and Neumann, G.A., 2001. Seasonal Variations of Snow Depth on Mars. Science, 294: 2141 - 2146.

Smith, P.H., Tamppari, L.K., Arvidson, R.E., Bass, D., Blaney, D., Boynton, W.V., Carswell, A., Catling, D.C., Clark, B.C., Duck, T., DeJong, E., Fischer, D., Goetz, W., Gunnlaugsson, H.P., Hecht, M.H., Hipkin, V., Hoffman, J., Hviid, S.F., Keller, H.U., Kounaves, S.P., Lange, C.F., Lemmon, M.T., Madsen, M.B., Markiewicz, W.J., Marshall, J., McKay, C.P., Mellon, M., Ming, D.W., Morris, R.V., Pike, W.T., Renno, N.O., Staufer, U., Stoker, C., Taylor, P., Whiteway, J.A. and Zent, A.P., 2009. H_2O at the Phoenix Landing Site. Science, 325: 58-61.

Snyder, C.W., 1979. The planet Mars as seen at the end of the Viking Mission. Journal of Geophysical Research, 84(B14): 8487.

Soderblom, L.A., Kieffer, S.W., Becker, T.L., Brown, R.H., Cook II, A.F., Hansen, C.J., Johnson, T.V., Kirk, R.L. and Shoemaker, E.M., 1990. Triton's Geyser-Like Plumes: Discovery and Basic Characterization. Science, 250(4979): 410-415.

Soto, A., Mischna, M., Schneider, T., Lee, C. and Richardson, M., 2014. Martian atmospheric collapse: Idealized GCM studies. Icarus, 250: 553-569.

Spiga, A., Hinson, D.P., Madeleine, J.-B., Navarro, T., Millour, E., Forget, F. and Montmessin, F., 2017. Snow precipitation on Mars driven by cloud-induced night-time convection. Nature Geoscience, 10(9): 652-657.

Stern, S.A., 2003. The Evolution of Comets in the Oort Could and Kuiper belt. Nature, 424.

Swinkels, F.B. and Ashby, M.F., 1981. A Second Report on Sintering Diagrams. Acta Metallurgica, 29(2): 259-281.

Sylvest, M.E., Conway, S.J., Patel, M.R., Dixon, J.C. and Barnes, A., 2016. Mass wasting triggered by seasonal CO_2 sublimation under Martian atmospheric conditions: Laboratory experiments. Geophysical Research Letters, 43(24): 12,363-12,370.

Sylvest, M.E., Dixon, J.C., Conway, S.J., Patel, M.R., McElwaine, J.N., Hagermann, A. and Barnes, A., 2018. CO_2 sublimation in Martian gullies: laboratory experiments at varied slope angle and regolith grain sizes. Geological Society, London, Special Publications: SP467.11.

Tanaka, K.L., Skinner, J., J. A. , Dohm, J.M., Irwin, I., R. P. , Kolb, E.J., Fortezzo, C.M., Platz, T., Michael, G.G. and Hare, T.M., 2014. Geologic Map of Mars: U.S. Geological Survey Scientific Investigations Map 3292, scale 1:20,000,000, Pamphlet. In: U.S.G. Survey (Editor), https://pubs.usgs.gov/sim/3292/pdf/sim3292_pamphlet.pdf, Reston, VA.

Thomas, N., Hansen, C.J., Portyankina, G. and Russell, P.S., 2010. HiRISE observations of gas sublimation-driven activity in Mars' southern polar regions: II. Surficial deposits and their origins. Icarus, 205: 296-310.

Thomas, N., Portyankina, G., Hansen, C.J. and Pommerol, A., 2011. Sub-surface CO_2 gas flow in Mars' polar regions: Gas transport under constant production rate conditions. Geophysical Research Letters, 38(8): n/a-n/a.

Thomas, P.C., Calvin, W.M., Gierasch, P., Haberle, R., James, P.B. and Sholes, S., 2013. Time scales of erosion and deposition recorded in the residual south polar cap of Mars. Icarus, 225(2): 923-932.

Thomas, P.C., James, P.B., Calvin, W.M., Haberle, R. and Malin, M.C., 2009. Residual south polar cap of Mars: Stratigraphy, history, and implications of recent changes. Icarus, 203(2): 352-375.

Thomas, P.C., Malin, M., Edgett, K.S., Carr, M.H., Hartmann, W.K., Ingersoll, A.P., James, P.B., Soderblom, L.A., Veverka, J. and Sullivan, R., 2000. North-South Geological Differences Between the Residual Polar Caps on Mars. Nature, 404.

Thomas, P.C., Malin, M.C., James, P.B., Cantor, B.A., Williams, R.M.E. and Gierasch, P., 2005. South polar residual cap of Mars: Features, stratigraphy, and changes. Icarus, 174(2): 535-559.

Timco, G.W. and Frederking, R.M.W., 1996. A Review of Sea Ice Density. Cold Regions Science and Technology, 24: 1-6.

Titus, T.N., Kieffer, H.H., Langevin, Y., Murchie, S.L., Seelos, F. and Vincendon, M., 2007. Bright Fans in Mars Cryptic Region Caused by Adiabatic Cooling of CO_2 Gas Jets. AGU Fall Meeting Abstracts(ID P24A-05).

Titus, T.N., Kieffer, H.H., Mullins, K.F. and Christensen, P.R., 2001. TES premapping data: Slab ice and snow flurries in the Martian north polar night. Journal of Geophysical Research: Planets, 106(E10): 23181-23196.

Toon, O.B., Pollack, J.B. and Sagan, C., 1977. Physical Properties of the Particles Composing the Martian Dust Storm of 1971 - 1972. Icarus, 30: 663-696.

Toon, O.B., Pollack, J.B., Ward, W. and Burns, J.A., 1980. The Astronomical Theory of Climatic Change on Mars. Icarus, 44: 552-607.

Treiman, A., H., 2003. Geologic settings of Martian gullies: Implications for their origins. Journal of Geophysical Research: Planets, 108(E4).

Twomey, S. and Bohren, C.F., 1980. Simple Approximations for Calculations of Absorption in Clouds. Journal of the Atmospheric Sciences, 37: 2086-2094.

Vincendon, M., 2015. Identification of Mars gully activity types associated with ice composition. Journal of Geophysical Research: Planets, 120: 1859-1879.

Vincendon, M., Forget, F. and Mustard, J., 2010a. Water ice at low to midlatitudes on Mars. Journal of Geophysical Research, 115(E10).

Vincendon, M., Mustard, J., Forget, F., Kreslavsky, M., Spiga, A., Murchie, S. and Bibring, J.-P., 2010b. Near-tropical subsurface ice on Mars. Geophysical Research Letters, 37(1): n/a-n/a.

Warren, S., G., 1982. Optical Properties of Snow. Reviews of Geophysics and Space Physics, 20(1): 67-89.

Warren, S., G., 1986. Optical Constants of Carbon Dioxide Ice. Applied Optics, 25(16): 2650-2674.

Warren, S., G., Brandt, R., E. and Grenfell, T., C., 2006. Visible and near-ultraviolet absorption spectrum of ice from transmission of solar radiation into snow. Applied Optics, 45(21): 5320-533.

Warren, S.G., 1984. Impurities in Snow: Effects on Albedo and Snowmelt. Annals of Glaciology, 5: 177-179.

Warren, S.G. and Brandt, R.E., 2008. Optical constants of ice from the ultraviolet to the microwave: A revised compilation. Journal of Geophysical Research, 113(D14).

Warren, S.G., Wiscombe, W.J. and Firestone, J.F., 1990. Spectral albedo and emissivity of CO_2 in Martian polar caps: Model results. Journal of Geophysical Research, 95(B9): 14717.

Whiteway, J., Komguem, L., Dickinson, C., Cook, C., Illnicki, M., Popovici, V., Seabrook, J., Daly, M., Carswell, A., Taylor, P., Davy, R., Pathak, J., Lange, C., Fisher, D., Hipkin, V., Tamppari, L., Lemmon, M., Renno, N., Gunnlaugsson, H., Drube, L., Holstein-Rathlou, C. and Smith, P., 2008. Observations of Dust, Ice Water Clouds, and Precipitation in the Atmosphere of Mars, American Geophysical Union, Fall Meeting 2008.

Winther, J.-G., Elvehøy, H., Bøgglid, C.E., Sand, K. and Liston, G., 1996. Melting, runoff and the forrn.ation of frozen lakes in a mixed snow and blue-ice field in Dronning Maud Land, Antarctica. Journal of Glaciology, 42(141): 271-278.

Wiscombe, W.J. and Warren, S.G., 1980. A Model for the Spectral albedo of Snow, I: Pure Snow. Journal of the Atmospheric Sciences, 37: 2712-2733.

Wriedt, T., 2012. Mie Theory: A Review. In: W. Hergert and T. Wriedt (Editors), The Mie Theory. Springer-Verlag, Berlin, pp. 53-71.

Appendix A

Slab Ice Measurements

A1. Carbon Dioxide Slab Ice

Light intensity measurements were made through samples of carbon dioxide slab ice at decreasing ice thicknesses. Measurements were made using a pyranometer (in millivolts), and four readings were taken per ice thickness: measurement 1 is in the centre of the sample, and then measurements 2, 3 and 4 were taken radially around centre, at least 3 cm from the sample edge, and ensuring the outer platform of the pyranometer was kept within the shadow of the sample. More details of the experimental set up can be found in Chapter 3, and the experimental procedure specifically for the slab ice measurements, in Chapter 4. Tables A.1 and A.2 give results for CO_2 ice.

Ice Depth (mm)	Sample I				Sample II			
	1	2	3	4	1	2	3	4
2	75.673	85.684	73.790	89.302	-	-	-	-
3	69.734	83.568	62.699	83.425	-	-	-	-
4	69.784	67.067	44.779	88.401	86.198	82.169	78.688	74.490
5	60.897	88.590	37.551	92.496	-	-	-	-
6	60.142	44.298	52.752	63.681	66.535	62.915	52.144	55.919
7	43.765	46.237	51.175	76.083	64.434	65.440	41.807	42.888
8	47.574	27.885	72.941	66.752	60.079	32.813	42.501	66.124
9	-	-	-	-	47.273	55.519	54.440	49.832
10	43.676	41.958	24.520	64.219	49.916	42.703	57.419	41.976
11	38.156	25.577	46.116	56.149	-	-	-	-
12	35.603	37.949	24.701	42.500	51.952	44.241	37.148	60.182
13	38.676	48.312	22.812	42.447	51.673	30.840	41.002	64.073
14	29.762	25.227	38.209	41.096	47.362	34.013	42.225	53.791
15	-	-	-	-	-	-	-	-

16	27.228	34.421	21.778	34.577	44.276	35.123	45.458	35.361
17	27.505	23.045	33.827	27.661	-	-	-	-
18	27.231	22.878	32.704	28.626	40.638	51.981	35.003	28.971
19	26.538	27.847	31.165	24.738	-	-	-	-
20	-	-	-	-	33.301	37.387	32.955	25.654
21	25.356	26.229	24.772	26.405	-	-	-	-
22	-	-	-	-	-	-	-	-
23	24.122	19.751	27.075	27.466	33.930	26.013	38.679	25.310
24	-	-	-	-	-	-	-	-
25	-	-	-	-	-	-	-	-
26	21.936	25.783	23.086	21.678	32.042	25.186	29.745	26.006
27	-	-	-	-	-	-	-	-
28	-	-	-	-	30.079	24.759	33.068	25.445
29	21.557	21.963	18.032	20.213	-	-	-	-
30	-	-	-	-	-	-	-	-
31	-	-	-	-	26.883	26.184	26.265	23.171
32	18.682	16.419	18.784	17.759	-	-	-	-
33	-	-	-	-	-	-	-	-
34	-	-	-	-	21.910	20.929	21.990	25.631
35	16.133	17.554	16.107	16.319	-	-	-	-
36	-	-	-	-	-	-	-	-
37	-	-	-	-	20.701	23.027	25.426	20.698
38	-	-	-	-	-	-	-	-
39	-	-	-	-	-	-	-	-
40	13.945	13.787	15.789	15.602	-	-	-	-
41	-	-	-	-	20.639	23.557	19.600	18.639
42	-	-	-	-	-	-	-	-
43	-	-	-	-	-	-	-	-
44	12.023	15.672	13.504	12.841	19.150	17.915	17.411	17.975
45	-	-	-	-	-	-	-	-
46	-	-	-	-	-	-	-	-
47	11.357	10.871	10.653	11.986	-	-	-	-
48	-	-	-	-	-	-	-	-
49	-	-	-	-	-	-	-	-
50	10.684	8.652	10.229	11.088	-	-	-	-
51	-	-	-	-	-	-	-	-
52	-	-	-	-	-	-	-	-
53	9.413	10.074	9.828	9.522	-	-	-	-
67	6.472	6.805	6.723	6.601	-	-	-	-
70	6.381	6.413	5.479	6.148	-	-	-	-
73	6.408	6.441	5.776	6.103	-	-	-	-

Table A.1. Raw light intensity measurements through CO_2 slab ice samples 1 and 2.

Ice Depth (mm)	Sample III				Sample IV			
	1	2	3	4	1	2	3	4
5	87.783	78.158	67.913	89.542	116.203	104.112	107.370	118.617
6	74.571	78.460	63.213	85.177	98.219	109.173	111.530	112.802
7	69.127	66.854	76.875	71.532	86.417	107.524	99.708	94.210
8	81.340	70.837	81.418	84.495	106.213	73.277	99.029	85.807
9	97.154	63.356	69.667	74.413	-	-	-	-
10	97.629	77.818	75.718	66.511	80.463	71.576	97.193	105.799
11	-	-	-	-	83.501	83.248	68.751	79.942
12	81.541	53.650	73.993	78.228	-	-	-	-
13	71.402	80.495	76.291	65.090	94.623	84.690	97.700	70.949
14	-	-	-	-	69.762	79.906	74.385	82.554
15	73.743	66.513	48.390	75.493	76.677	60.721	76.128	77.684
16	-	-	-	-	-	-	-	-
17	62.471	48.273	54.218	79.271	68.271	80.887	79.391	77.608
18	75.855	53.453	41.636	66.068	-	-	-	-
19	-	-	-	-	70.444	55.707	72.815	76.401
20	65.698	62.734	58.649	48.735	-	-	-	-
21	-	-	-	-	89.215	70.571	69.180	86.438
22	62.513	49.337	43.728	77.872	-	-	-	-
23	55.907	64.326	71.647	50.965	83.778	74.041	81.161	60.223
24	-	-	-	-	-	-	-	-
25	73.318	61.812	30.260	76.571	-	-	-	-
26	65.651	60.987	40.203	71.471	74.114	54.103	72.720	66.512
27	72.856	65.570	33.806	42.025	-	-	-	-
28	-	-	-	-	48.775	41.366	52.637	81.845
29	-	-	-	-	-	-	-	-
30	68.362	55.000	37.910	47.677	-	-	-	-
31	-	-	-	-	60.142	79.641	39.568	54.872
32	49.072	58.054	32.944	55.099				
33	34.790	60.352	35.049	44.239	69.908	48.761	69.111	46.338
34	-	-	-	-	-	-	-	-
35	50.629	33.981	43.690	42.996	-	-	-	-
36	-	-	-	-	80.509	34.793	56.208	38.610
37	-	-	-	-	-	-	-	-
38	-	-	-	-	-	-	-	-
39	-	-	-	-	40.924	43.944	39.546	43.062
40	-	-	-	-	-	-	-	-
41	-	-	-	-	41.175	67.132	46.646	34.780
42	-	-	-	-	-	-	-	-
43	-	-	-	-	44.555	27.470	41.853	56.062
48	-	-	-	-	46.484	33.624	21.370	61.777

Table A.2. Raw light intensity measurements through CO_2 slab ice samples 3 and 4.

A2. Water Slab Ice

Light intensity measurements were made through samples of water slab ice at decreasing ice thicknesses. Measurements were made using a pyranometer (in millivolts), and five readings were taken per ice thickness: measurement 1 is in the centre of the sample, and then measurements 2, 3, 4 and 5 were taken radially around centre, at least 3 cm from the sample edge, and ensuring the outer platform of the pyranometer was kept within the shadow of the sample. A second set of measurements were made at each ice thickness to improve data fidelity, which was possible for water ice only, as carbon dioxide ice is comparatively less stable under the temperatures in which the experiments were taken. More details of the experimental set up can be found in Chapter 3, and experimental procedure specifically for the slab ice measurements, in Chapter 4. Tables A.3 through to A.13 give the results for water ice.

Ice Depth (mm)	Run 1				
	1	2	3	4	5
16	44.520	87.723	77.710	85.549	83.55
25	23.203	65.480	42.554	68.078	77.908
30	18.376	17.766	33.972	37.305	59.358
	Run 2				
16	36.397	99.116	97.698	79.273	91.071
25	36.244	51.855	73.924	47.289	66.432
30	17.761	53.215	51.438	48.427	37.618

Table A.3. Raw light intensity measurements through water slab ice Sample 1.

Ice Depth (mm)	Run 1				
	1	2	3	4	5
15	30.531	36.157	37.007	91.630	103.271
22	27.904	53.631	36.094	28.052	69.311
	Run 2				
15	44.152	65.009	33.732	81.477	100.935
22	26.446	69.944	52.460	66.357	62.508

Table A.4. Raw light intensity measurements through water slab ice Sample 2.

Ice Depth (mm)	Run 1				
	1	2	3	4	5
10	26.833	94.117	74.481	37.042	98.544
18	35.058	77.22	103.338	98.495	113.091
29	48.707	107.111	70.276	112.068	85.091
44	20.322	65.574	42.387	80.174	52.701
52	24.867	48.807	24.312	64.975	77.367
59	20.258	71.201	31.298	23.181	72.578
71	16.323	13.385	32.99	32.002	26.918
	Run 2				
10	24.758	64.058	66.672	70.847	92.351
18	24.197	87.146	92.313	100.866	66.071
29	25.67	66.542	84.617	61.022	75.034
44	26.898	87.18	61.656	86.273	94.632
52	25.402	32.967	39.523	61.614	58.332
59	29.009	61.107	43.297	45.49	83.721
71	16.054	12.703	30.309	33.941	33.797

Table A.5. Raw light intensity measurements through water slab ice Sample 3.

Ice Depth (mm)	Run 1				
	1	2	3	4	5
17	35.703	50.899	102.764	99.725	42.984
34	38.564	61.248	40.61	32.831	80.885
42	61.034	59.015	23.85	16.895	57.898
54	27.382	53.883	13.409	55.645	79.105
61	27.901	71.653	15.375	27.021	94.031
	Run 2				
17	33.374	106.34	89.494	71.626	115.333
34	38.166	24.983	43.236	62.443	92.502
42	41.296	82.706	25.148	15.029	95.023
54	30.25	26.638	14.087	106.613	47.965
61	26.093	10.469	16.934	60.646	90.073

Table A.6. Raw light intensity measurements through water slab ice Sample 4.

Ice Depth (mm)	Run 1				
	1	2	3	4	5
20	103.168	65.971	66.984	88.793	99.461
27	44.650	40.691	49.572	31.062	60.473
37	17.283	20.466	22.434	30.077	21.735
	Run 2				
20	105.466	86.098	78.046	62.178	117.237
27	37.161	34.608	42.950	43.662	78.540
37	18.071	23.729	18.867	19.582	23.436

Table A.7. Raw light intensity measurements through water slab ice Sample 5.

Ice Depth (mm)	Run 1				
	1	2	3	4	5
17	76.209	111.173	106.529	93.561	115.06
24	26.963	73.182	109.843	76.208	68.053
31	30.480	78.003	71.663	101.437	41.350
45	25.173	101.98	32.084	90.132	38.273
53	20.105	28.056	58.023	22.326	30.080
	Run 2				
17	58.142	90.784	94.785	110.438	95.650
24	30.517	77.583	66.390	87.990	99.412
31	31.902	93.885	112.175	96.968	53.870
45	29.678	88.187	33.367	90.473	28.917
53	24.375	22.508	22.906	20.377	34.331

Table A.8. Raw light intensity measurements through water slab ice Sample 6.

Ice Depth (mm)	Run 1				
	1	2	3	4	5
20	29.409	61.944	44.028	27.284	32.519
27	36.629	30.724	42.005	65.271	42.575
35	17.709	15.858	25.091	42.365	22.071
47	13.535	17.900	14.992	36.139	20.437
60	11.707	31.631	29.878	15.906	12.585
	Run 2				
20	27.63	38.172	50.027	53.931	68.902
27	34.492	34.778	26.532	89.655	23.737
35	20.367	17.475	18.162	52.931	31.98
47	14.248	15.913	26.875	42.03	11.452
60	13.472	19.75	21.076	47.722	35.573

Table A.9. Raw light intensity measurements through water slab ice Sample 7.

Ice Depth (mm)	Run 1				
	1	2	3	4	5
18	104.943	90.438	113.287	104.305	97.055
28	92.608	92.739	92.346	87.178	88.239
40	80.081	46.285	59.471	75.882	53.908
48	26.798	33.511	38.803	61.753	39.712
	Run 2				
18	110.116	75.880	116.771	91.424	109.427
28	95.320	88.720	92.328	104.540	78.416
40	81.742	53.090	72.539	82.815	55.793
48	32.684	38.190	53.735	74.989	71.114

Table A.10. Raw light intensity measurements through water slab ice Sample 8.

Ice Depth (mm)	Run 1				
	1	2	3	4	5
16	19.631	50.155	87.040	113.863	110.208
23	98.135	99.569	71.850	23.603	20.146
31	85.681	93.275	87.639	64.845	37.273
43	64.561	17.666	11.458	16.052	61.088
50	10.807	7.450	25.709	93.301	8.212
16	19.631	50.155	87.040	113.863	110.208
	Run 2				
16	21.612	34.540	86.923	93.736	100.41
23	95.727	102.319	88.461	17.496	34.732
31	26.986	91.262	90.317	24.269	44.371
43	82.149	30.760	12.422	14.602	96.799
50	19.339	13.728	26.222	88.683	13.014
16	21.612	34.540	86.923	93.736	100.41

Table A.11. Raw light intensity measurements through water slab ice Sample 9.

Ice Depth (mm)	Run 1				
	1	2	3	4	5
13	102.496	76.011	66.054	87.706	78.946
25	52.963	45.830	64.951	66.814	56.472
36	41.354	51.021	33.854	50.803	52.289
51	22.947	21.159	41.305	36.364	35.041
62	21.989	31.782	33.458	29.110	26.200
70	18.018	22.827	20.721	23.290	19.707
79	17.231	28.158	22.009	17.166	20.87
88	16.532	24.213	14.775	17.87	17.911
117	4.432	7.276	4.332	10.400	10.207
	Run 2				
13	90.125	88.391	83.477	96.994	86.986
25	39.246	52.477	63.180	63.243	55.707
36	38.205	43.023	30.624	51.093	49.180
51	27.410	34.151	21.378	36.304	34.636
62	20.009	30.472	34.318	28.354	31.868
70	17.809	30.189	31.705	21.280	16.519
79	19.350	22.381	18.632	18.755	22.359
88	16.435	20.096	19.406	18.005	15.496
117	4.540	8.256	4.325	9.183	11.929

Table A.12. Raw light intensity measurements through water slab ice Sample 10.

Ice Depth (mm)	Run 1				
	1	2	3	4	5
18	19.174	44.803	69.92	113.403	69.197
35	44.351	38.655	75.231	23.151	17.405
43	18.448	25.75	16.016	90.593	59.437
47	18.581	22.842	45.106	13.272	18.105
61	20.278	56.774	31.629	15.748	32.34
	Run 2				
18	19.607	64.095	22.804	99.051	59.907
35	40.252	39.109	69.569	17.764	16.048
43	21.142	26.368	20.029	73.872	50.874
47	16.024	17.32	48.164	61.545	16.145
61	24.829	61.144	60.813	15.908	19.186

Table A.13. Raw light intensity measurements through water slab ice Sample 11.

Appendix B

Snow Measurements

B1. Carbon Dioxide Snow

Light intensity measurements were made through samples of carbon dioxide snow at decreasing ice thicknesses. Measurements were made using a pyranometer (in millivolts), and only one measurement was made per snow thickness. This is due to the rapid sintering rate of CO_2 snow, and the accumulation of water frost as a contaminant. Further explanation of this can be found in Chapter 5. In order to compensate for the lack of multiple measurements per sample, many more samples were used than for the other types of ice experiments, in order to gain enough measurements to be statistically significant. Details of the experimental set up can be found in Chapter 3, and the experimental procedure specifically for the snow measurements in Chapter 5. Table B.1 lists the equipment and its mass and Table B.2 gives the results for CO_2 snow light intensity measurements.

Equipment	Mass (g)
20 mm copper ring	83.40
10 mm copper ring	41.73
5 mm copper ring	20.70
Sample base holder	8.28

Table B.1. The equipment which was used to contain the snow samples was weighed in order to determine mass of snow without having to remove the equipment. This reduced the time taken to weigh the samples, meaning that air exposure, and therefore frost deposition and sintering were kept to a minimum. All copper rings were 86 mm in internal diameter.

	Sample Number						
	Practice	**2**	**3**	**4**	**5**	**6**	**7**
Total Mass (g)	517.04	471.21	134.87	313.62	285.01	326.84	308.77
Snow Mass (g)	209.90	164.07	64.14	159.65	131.04	160.04	141.97
Volume (m^{-3})	$3.19x10^{-4}$	$3.19x10^{-4}$	$8.71x10^{-5}$	$2.03x10^{-4}$	$2.03x10^{-4}$	$2.32x10^{-4}$	$2.32x10^{-4}$
Density (kg m^{-3})	657.00	513.55	736.12	785.26	644.54	688.78	611.01
Snow Depth	**Light Intensity (mV)**						
5 mm	10.029	8.416	7.926	8.090	8.568	7.209	8.59
10 mm		4.197	4.191	-	4.95	4.408	4.621
15 mm	1.999	3.278	3.638	3.773	3.446	3.47	4.27
20 mm	-	-	-	3.104	3.117	3.001	3.303
25 mm	-	-	-	2.997	2.958	2.019	3.189
30 mm	-	-	-	2.682	2.652	1.991	2.97
35 mm	0.957	2.145	-	2.189	2.215	1.774	2.765
40 mm	-	-	-	-	-	1.39	2.04
45 mm	-	-	-	-	-	-	-
50 mm	-	-	-	-	-	-	-
55 mm	0.230	1.919	-	-	-	-	-

	8	**9**	**10**	**11**	**12**	**13**	**14**
Total Mass (g)	279.84	153.17	150.03	184.94	188.55	190.23	150.53
Snow Mass (g)	146.96	82.99	79.85	93.26	96.87	98.55	79.82
Volume (m^{-3})	$1.74x10^{-4}$	$8.71x10^{-5}$	$8.71x10^{-5}$	$1.16x10^{-4}$	$1.16x10^{-4}$	$1.16x10^{-4}$	$8.71x10^{-5}$
Density (kg m^{-3})	843.32	952.46	916.42	802.75	833.82	848.28	916.08
Snow Depth	**Light Intensity (mV)**						
5 mm	13.805	12.212	13.025	11.975	13.196	12.251	12.344
10 mm	9.847	8.13	8.001	8.346	8.779	8.047	6.75
15 mm	7.339	5.782	6.617	6.474	6.3	6.249	5.703
20 mm	6.448	-	-	6.209	6.004	5.846	-
25 mm	5.63	-	-	-	-	-	-
30 mm	5.041	-	-	-	-	-	-

	15	**16**	**17**	**18**	**19**	**20**	**21**
Total Mass (g)	155.81	148.34	155.77	149.60	149.94	144.17	179.41
Snow Mass (g)	85.10	77.63	85.06	78.89	79.23	73.46	87.73
Volume (m^{-3})	$8.71x10^{-5}$	$8.71x10^{-5}$	$8.71x10^{-5}$	$8.71x10^{-5}$	$8.71x10^{-5}$	$8.71x10^{-5}$	$1.16x10^{-4}$
Density (kg m^{-3})	**976.68**	**890.95**	**976.22**	**905.41**	**909.31**	**843.09**	**755.15**
Snow Depth	**Light Intensity (mV)**						
5 mm	11.975	11.055	11.531	12.915	9.148	11.504	10.018
10 mm	7.718	7.504	6.871	7.867	6.947	6.332	6.408
15 mm	6.047	5.773	5.728	5.569	5.373	5.802	6.079
20 mm	-	-	-	-	-	-	4.438
25 mm	-	-	-	-	-	-	-
30 mm	-	-	-	-	-	-	-

	Sample Number						
	22	**23**	**24**	**25**	**26**	**27**	**28**
Total Mass (g)	175.01	150.10	140.69	153.81	145.21	145.32	150.88
Snow Mass (g)	83.33	79.39	69.98	83.10	74.50	74.61	80.17
Volume (m^{-3})	$1.16x10^{-4}$	$8.71x10^{-5}$	$8.71x10^{-5}$	$8.71x10^{-5}$	$8.71x10^{-5}$	$8.71x10^{-5}$	$8.71x10^{-5}$
Density (kg m^{-3})	717.27	911.15	803.15	953.72	855.02	856.29	920.10
Snow Depth	**Light Intensity (mV)**						
5 mm	10.465	13.601	16.372	12.652	12.989	13.654	13.298
10 mm	6.7	8.244	9.671	9.025	8.381	8.805	8.77
15 mm	5.562	6.582	5.683	6.613	6.53	6.503	6.417
20 mm	4.121	-	-	-	-	-	-

	29	**30**	**31**	**32**	**Mean**
Total Mass (g)	137.97	140.03	136.08	136.34	188.13
Snow Mass (g)	67.26	69.32	65.37	65.63	92.87
Volume (m^{-3})	$8.71x10^{-5}$	$8.71x10^{-5}$	$8.71x10^{-5}$	$8.71x10^{-5}$	$1.19x10^{-4}$
Density (kg m^{-3})	771.93	795.57	750.24	753.22	820.54
Snow Depth	**Light Intensity (mV)**				
5 mm	15.341	16.604	16.784	17.246	12.089
10 mm	9.064	11.256	10.231	11.666	7.724
15 mm	6.377	7.485	8.048	8.735	5.847
20 mm	-	-	-	-	4.559
25 mm	-	-	-	-	3.359
30 mm	-	-	-	-	3.067
40 mm	-	-	-	-	2.218
45 mm	-	-	-	-	1.715

Table B.2. Raw light intensity measurements for all samples of carbon dioxide snow measured. Sample 1 was used as a practice, which enabled a number of improvements to be made to the experimental chamber and procedure. As a consequence, the measurements made using Sample 1 (Practice Sample) are not included in any of the analysis or calculations of the e-folding scale.

B2. Water Snow

Light intensity measurements were made through samples of water snow at decreasing snow thicknesses. Measurements were made using a pyranometer (in millivolts), and four readings were taken per snow thickness: measurement 1 is in the centre of the sample, and then measurements 2, 3, and 4 were taken radially around centre, at least 20 mm from the sample edge, and ensuring the outer platform of the pyranometer was kept within the shadow of the sample. In addition to this, the water snow samples were sieved to separate out grain size ranges, in an attempt to determine any grain size dependence on the e-folding scale. This was possible with the water snow, but not with carbon dioxide snow because of the comparative stability of water ice under the temperatures within the experimental chamber. As far as could be determined, minimal melting and no sintering occurred. More details of the experimental set up can be found in Chapter 3, and experimental procedure specifically for snow measurements, in Chapter 5. Tables B.3 through to B.12 give the results for water snow light intensity measurements, separated by grain size range. Upon analysis of the data and photographs of the samples, it was decided that only grains smaller than 1.18 mm in diameter could be classified as snow (further details found in Chapter 5). This was due to both the typical particle size of natural snow, as well as the visual appearance of the larger grains, which looked more like translucent ice granules, rather than fluffy white snow particles.

	Grain Size 2.00 – 3.35 mm							
	Sample 1				Sample 2			
Total Mass	162.88 g				164.18 g			
Snow Mass	50.50 g				51.80 g			
Volume	1.45×10^{-4} m^{-3}				1.45×10^{-4} m^{-3}			
Density	347.75 kg m^{-3}				356.70 kg m^{-3}			
Snow Depth	**Light Intensity (mV)**							
	1	**2**	**3**	**4**	**1**	**2**	**3**	**4**
5 mm	19.603	18.029	20.794	17.622	20.716	20.654	21.228	20.965
10 mm	11.229	12.075	12.761	10.529	11.323	11.992	11.046	10.678
15 mm	6.679	8.364	8.299	7.201	8.693	11.802	10.991	7.140
20 mm	5.717	6.342	5.540	6.605	5.674	5.586	4.868	5.721
25 mm	5.658	4.784	3.722	5.653	3.951	3.967	3.709	6.690

	Sample 3				Sample 4			
Total Mass	162.29 g				149.69 g			
Snow Mass	49.91 g				37.31 g			
Volume	1.45×10^{-4} m^{-3}				1.45×10^{-4} m^{-3}			
Density	343.69 kg m^{-3}				256.92 kg m^{-3}			
Snow Depth	**Light Intensity (mV)**							
	1	**2**	**3**	**4**	**1**	**2**	**3**	**4**
5 mm	19.121	19.673	18.709	20.205	26.491	24.263	25.809	24.142
10 mm	10.743	10.885	10.897	11.829	13.375	12.783	11.089	15.989
15 mm	9.158	9.432	8.728	8.072	9.129	9.425	10.773	10.017
20 mm	5.813	6.108	5.153	6.925	7.124	10.683	9.505	8.247
25 mm	4.861	4.669	4.376	6.537	4.926	4.534	6.083	6.099

	Sample 5				Mean
Total Mass	150.27 g				157.86 g
Snow Mass	37.89 g				45.48 g
Volume	1.45×10^{-4} m^{-3}				1.45×10^{-4} m^{-3}
Density	260.91 kg m^{-3}				313.19 kg m^{-3}
Snow Depth	**Light Intensity (mV)**				
	1	**2**	**3**	**4**	**Mean**
5 mm	19.972	19.691	25.374	21.890	21.248
10 mm	13.760	15.289	15.464	13.041	12.339
15 mm	8.708	10.122	9.993	8.869	9.080
20 mm	7.124	7.136	7.272	6.928	6.704
25 mm	5.333	4.521	5.769	5.772	5.081

Table B.3. Raw light intensity measurements through water snow Samples 1 – 5, of grain size range 2.00 – 3.35 mm.

	Grain Size 1.18 – 2.00 mm							
	Sample 1				Sample 2			
Total Mass	161.51 g				158.63 g			
Snow Mass	49.13 g				46.25 g			
Volume	1.45 x10^{-4} m^{-3}				1.45 x10^{-4} m^{-3}			
Density	338.31 kg m^{-3}				318.48 kg m^{-3}			
Snow Depth	**Light Intensity (mV)**							
	1	**2**	**3**	**4**	**1**	**2**	**3**	**4**
5 mm	19.301	16.239	18.209	16.620	15.167	14.672	14.629	15.984
10 mm	9.548	14.876	11.307	9.229	8.127	8.092	8.389	10.304
15 mm	7.582	9.874	11.578	6.807	6.145	2.030	8.263	7.949
20 mm	5.959	5.041	7.650	5.094	5.297	6.493	7.871	6.076
25 mm	3.714	3.394	3.469	5.073	3.834	4.059	3.408	5.016

	Sample 3				Sample 4			
Total Mass	159.53 g				152.51 g			
Snow Mass	47.15 g				40.13 g			
Volume	1.45 x10^{-4} m^{-3}				1.45 x10^{-4} m^{-3}			
Density	324.68 kg m^{-3}				276.34 kg m^{-3}			
Snow Depth	**Light Intensity (mV)**							
	1	**2**	**3**	**4**	**1**	**2**	**3**	**4**
5 mm	15.880	12.792	13.357	13.814	21.099	16.773	19.178	17.915
10 mm	9.605	10.096	11.083	8.910	10.303	12.527	11.547	11.871
15 mm	5.214	7.410	7.406	7.115	7.691	10.667	10.900	8.324
20 mm	4.584	5.112	5.757	5.827	7.199	5.654	7.769	7.866
25 mm	4.221	4.709	4.918	4.485	3.975	3.363	7.805	5.239

	Sample 5				Mean
Total Mass	155.67 g				157.57 g
Snow Mass	43.29 g				45.19 g
Volume	1.45 x10^{-4} m^{-3}				1.45 x10^{-4} m^{-3}
Density	298.10 kg m^{-3}				311.18 kg m^{-3}
Snow Depth	**Light Intensity (mV)**				
	1	**2**	**3**	**4**	**Mean**
5 mm	14.449	16.257	16.824	14.912	16.204
10 mm	9.695	10.428	12.254	10.500	10.435
15 mm	7.306	7.983	10.915	8.407	7.978
20 mm	6.884	5.968	8.796	7.472	6.418
25 mm	5.549	6.273	7.142	5.685	4.767

Table B.4. Raw light intensity measurements through water snow Samples 1 – 5, of grain size range 1.18 – 2.00 mm.

	Grain Size 1.00 – 1.18 mm							
	Sample 1				**Sample 2**			
Total Mass	132.45 g				133.92 g			
Snow Mass	40.77 g				42.24 g			
Volume	1.16 x10^{-4} m^{-3}				1.16 x10^{-4} m^{-3}			
Density	350.93 kg m^{-3}				363.59 kg m^{-3}			
Snow Depth	**Light Intensity (mV)**							
	1	**2**	**3**	**4**	**1**	**2**	**3**	**4**
5 mm	15.096	13.681	16.665	16.574	13.137	13.328	14.132	15.187
10 mm	8.127	9.442	10.491	10.758	8.771	9.545	9.753	9.076
15 mm	4.730	6.877	8.336	7.080	5.399	6.282	7.304	6.551
20 mm	5.733	5.285	7.683	6.622	4.237	6.043	7.189	4.871

	Sample 3				**Sample 4**			
Total Mass	135.19 g				129.80 g			
Snow Mass	43.51 g				38.12 g			
Volume	1.16 x10^{-4} m^{-3}				1.16 x10^{-4} m^{-3}			
Density	374.52 kg m^{-3}				328.12 kg m^{-3}			
Snow Depth	**Light Intensity (mV)**							
	1	**2**	**3**	**4**	**1**	**2**	**3**	**4**
5 mm	13.476	11.654	15.331	15.890	17.021	17.856	17.120	17.209
10 mm	8.815	8.273	9.619	9.375	8.405	10.174	12.631	11.043
15 mm	5.423	6.808	8.549	6.425	7.577	9.008	11.041	6.977
20 mm	4.379	5.658	5.420	7.875	5.714	5.241	7.530	5.816

	Sample 5				**Mean**
Total Mass	136.34 g				133.54 g
Snow Mass	44.66 g				41.86 g
Volume	1.16 x10^{-4} m^{-3}				1.16 x10^{-4} m^{-3}
Density	384.42 kg m^{-3}				360.32 kg m^{-3}
Snow Depth	**Light Intensity (mV)**				
	1	**2**	**3**	**4**	**Mean**
5 mm	16.795	20.314	14.720	14.153	15.467
10 mm	8.578	9.439	10.490	10.891	9.685
15 mm	6.620	6.369	8.497	7.183	7.152
20 mm	4.205	6.891	7.522	8.211	6.106

Table B.5. Raw light intensity measurements through water snow Samples 1 – 5, of grain size range 1.00 - 1.18 mm.

	Grain Size 0.85 – 1.00 mm							
	Sample 1				Sample 2			
Total Mass	108.61 g				109.04 g			
Snow Mass	37.90 g				38.33 g			
Volume	8.71 x10^{-5} m^{-3}				8.71 x10^{-5} m^{-3}			
Density	434.97 kg m^{-3}				439.91 kg m^{-3}			
Snow Depth	**Light Intensity (mV)**							
	1	**2**	**3**	**4**	**1**	**2**	**3**	**4**
5 mm	12.405	12.478	13.082	14.260	14.051	16.887	15.460	16.376
10 mm	6.539	10.286	9.641	7.724	7.443	8.462	8.404	8.021
15 mm	4.392	6.980	7.773	5.455	5.282	5.342	6.597	6.681

	Sample 3				Sample 4			
Total Mass	108.89 g				104.20 g			
Snow Mass	38.18 g				33.49 g			
Volume	8.71 x10^{-5} m^{-3}				8.71 x10^{-5} m^{-3}			
Density	438.19 kg m^{-3}				384.36 kg m^{-3}			
Snow Depth	**Light Intensity (mV)**							
	1	**2**	**3**	**4**	**1**	**2**	**3**	**4**
5 mm	13.145	13.126	15.907	16.242	15.497	14.878	19.621	19.367
10 mm	7.134	8.222	9.836	7.782	7.930	10.243	11.650	11.824
15 mm	5.031	5.067	5.628	5.216	5.828	7.632	8.601	10.766

	Sample 5				Mean
Total Mass	108.91				107.93 g
Snow Mass	38.20				37.22 g
Volume	8.71 x10^{-5} m^{-3}				8.71 x10^{-4} m^{-3}
Density	438.41 kg m^{-3}				427.17 kg m^{-3}
Snow Depth	**Light Intensity (mV)**				
	1	**2**	**3**	**4**	**Mean**
5 mm	17.935	15.627	16.514	15.873	15.437
10 mm	7.220	9.993	11.439	8.342	8.907
15 mm	5.079	7.850	9.167	5.863	6.512

Table B.6. Raw light intensity measurements through water snow Samples 1 – 5, of grain size range 0.85 - 1.00 mm.

	Grain Size 0.71 – 0.85 mm							
	Sample 1				**Sample 2**			
Total Mass	106.04 g				106.77 g			
Snow Mass	35.33 g				36.06 g			
Volume	8.71 x10^{-5} m^{-3}				8.71 x10^{-5} m^{-3}			
Density	405.48 kg m^{-3}				413.85 kg m^{-3}			
Snow Depth	**Light Intensity (mV)**							
	1	**2**	**3**	**4**	**1**	**2**	**3**	**4**
5 mm	11.510	15.250	16.765	16.199	13.851	15.625	13.155	14.253
10 mm	7.510	8.447	10.816	9.637	7.343	9.319	9.171	9.336
15 mm	6.500	7.684	7.479	6.220	6.404	6.517	8.071	8.492

	Sample 3				**Sample 4**			
Total Mass	101.70 g				105.01 g			
Snow Mass	30.99 g				34.30 g			
Volume	8.71 x10^{-5} m^{-3}				8.71 x10^{-5} m^{-3}			
Density	355.67 kg m^{-3}				393.66 kg m^{-3}			
Snow Depth	**Light Intensity (mV)**							
	1	**2**	**3**	**4**	**1**	**2**	**3**	**4**
5 mm	12.634	14.178	14.584	17.506	13.604	15.208	15.313	16.770
10 mm	7.204	10.118	9.807	9.630	8.022	10.288	11.120	10.134
15 mm	6.475	7.371	7.102	7.879	5.086	7.797	8.674	8.605

	Sample 5				**Mean**
Total Mass	107.19 g				105.34 g
Snow Mass	36.48 g				34.63 g
Volume	8.71 x10^{-5} m^{-3}				8.71 x10^{-5} m^{-3}
Density	418.67 kg m^{-3}				397.47 kg m^{-3}
Snow Depth	**Light Intensity (mV)**				
	1	**2**	**3**	**4**	**Mean**
5 mm	19.032	19.786	22.296	19.239	15.84
10 mm	9.268	10.309	10.374	8.736	9.33
15 mm	5.659	5.733	7.650	5.738	7.06

Table B.7. Raw light intensity measurements through water snow Samples 1 – 5, of grain size range 0.71 – 0.85 mm.

	Grain Size 0.60 – 0.71 mm							
	Sample 1				Sample 2			
Total Mass	106.95 g				103.13 g			
Snow Mass	36.24 g				32.42 g			
Volume	8.71 x10^{-5} m^{-3}				8.71 x10^{-5} m^{-3}			
Density	415.92 kg m^{-3}				372.08 kg m^{-3}			
Snow Depth	**Light Intensity (mV)**							
	1	**2**	**3**	**4**	**1**	**2**	**3**	**4**
5 mm	10.026	10.484	14.092	17.371	13.664	16.793	15.381	16.504
10 mm	7.105	9.991	12.934	8.868	8.627	11.305	12.927	10.342
15 mm	5.122	7.671	9.285	7.190	6.734	6.951	6.489	7.622

	Sample 3				Sample 4			
Total Mass	105.54 g				106.49 g			
Snow Mass	34.83 g				35.78 g			
Volume	8.71 x10^{-5} m^{-3}				8.71 x10^{-5} m^{-3}			
Density	399.74 kg m^{-3}				410.64 kg m^{-3}			
Snow Depth	**Light Intensity (mV)**							
	1	**2**	**3**	**4**	**1**	**2**	**3**	**4**
5 mm	11.801	11.718	13.256	13.541	13.850	12.518	13.579	12.888
10 mm	6.136	7.319	12.587	9.165	7.251	8.857	11.299	7.504
15 mm	5.408	8.873	8.792	7.131	5.156	4.305	7.521	6.920

	Sample 5				Mean
Total Mass	104.76 g				105.37 g
Snow Mass	34.05 g				34.66 g
Volume	8.71 x10^{-5} m^{-3}				8.71 x10^{-5} m^{-3}
Density	390.79 kg m^{-3}				397.83 kg m^{-3}
Snow Depth	**Light Intensity (mV)**				
	1	**2**	**3**	**4**	**Mean**
5 mm	13.780	13.023	13.966	14.108	14.005
10 mm	7.779	7.693	9.574	8.518	9.289
15 mm	5.720	5.801	8.127	7.740	6.928

Table B.8. Raw light intensity measurements through water snow Samples 1 – 5, of grain size range 0.60 – 0.71 mm.

	Grain Size 0.50 – 0.60 mm							
	Sample 1				**Sample 2**			
Total Mass	101.99 g				105.22 g			
Snow Mass	31.28 g				34.51 g			
Volume	8.71 x10^{-5} m^{-3}				8.71 x10^{-5} m^{-3}			
Density	359.00 kg m^{-3}				396.07 kg m^{-3}			
Snow Depth	**Light Intensity (mV)**							
	1	**2**	**3**	**4**	**1**	**2**	**3**	**4**
5 mm	13.064	17.073	15.827	16.714	11.017	13.454	14.639	14.137
10 mm	8.951	11.628	8.070	7.998	5.919	9.221	8.075	10.198
15 mm	5.642	7.457	8.148	6.192	4.740	6.609	8.604	8.746

	Sample 3				**Sample 4**			
Total Mass	106.26 g				105.50 g			
Snow Mass	35.55 g				34.79 g			
Volume	8.71 x10^{-5} m^{-3}				8.71 x10^{-5} m^{-3}			
Density	408.00 kg m^{-3}				399.28 kg m^{-3}			
Snow Depth	**Light Intensity (mV)**							
	1	**2**	**3**	**4**	**1**	**2**	**3**	**4**
5 mm	12.657	13.410	16.957	15.692	12.341	14.996	15.128	13.746
10 mm	7.051	10.192	9.657	10.213	6.107	8.575	9.659	10.582
15 mm	4.698	8.776	8.264	8.429	5.927	6.489	6.998	6.153

	Sample 5				**Mean**
Total Mass	104.52 g				104.70 g
Snow Mass	33.81 g				33.99 g
Volume	8.71 x10^{-5} m^{-3}				8.71 x10^{-5} m^{-3}
Density	388.03 kg m^{-3}				390.07 kg m^{-3}
Snow Depth	**Light Intensity (mV)**				
	1	**2**	**3**	**4**	**Mean**
5 mm	12.834	12.009	12.114	12.130	13.997
10 mm	6.921	9.777	10.825	7.366	8.849
15 mm	5.385	7.227	6.986	7.339	6.940

Table B.9. Raw light intensity measurements through water snow Samples 1 – 5, of grain size range 0.50 – 0.60 mm.

	Grain Size 0.355 – 0.500 mm							
	Sample 1				Sample 2			
Total Mass	106.98 g				107.87 g			
Snow Mass	36.27 g				37.16 g			
Volume	8.71 x10^{-5} m^{-3}				8.71 x10^{-5} m^{-3}			
Density	416.26 kg m^{-3}				426.48 kg m^{-3}			
Snow Depth	**Light Intensity (mV)**							
	1	**2**	**3**	**4**	**1**	**2**	**3**	**4**
5 mm	10.460	11.565	10.973	13.102	11.500	12.823	11.606	15.548
10 mm	6.269	10.568	9.897	9.099	6.457	10.905	7.871	9.415
15 mm	4.890	6.892	8.973	7.892	4.124	8.566	7.572	9.541

	Sample 3				Sample 4			
Total Mass	108.53 g				105.63 g			
Snow Mass	37.82 g				34.92 g			
Volume	8.71 x10^{-5} m^{-3}				8.71 x10^{-5} m^{-3}			
Density	434.05 kg m^{-3}				400.77 kg m^{-3}			
Snow Depth	**Light Intensity (mV)**							
	1	**2**	**3**	**4**	**1**	**2**	**3**	**4**
5 mm	13.721	12.147	14.459	14.824	11.185	18.920	13.780	13.149
10 mm	5.695	8.476	10.195	10.914	6.226	9.403	9.167	9.559
15 mm	4.961	6.756	9.643	7.285	4.529	7.967	7.326	7.135

	Sample 5				Mean
Total Mass	105.24 g				106.85 g
Snow Mass	34.53 g				36.14 g
Volume	8.71 x10^{-5} m^{-3}				8.71 x10^{-5} m^{-3}
Density	396.29 kg m^{-3}				414.77 kg m^{-3}
Snow Depth	**Light Intensity (mV)**				
	1	**2**	**3**	**4**	**Mean**
5 mm	10.930	10.382	12.382	11.760	12.761
10 mm	5.934	7.436	9.269	8.964	8.586
15 mm	5.039	7.718	8.762	5.591	7.058

Table B.10. Raw light intensity measurements through water snow Samples 1 – 5, of grain size range 0.355 – 0.500 mm.

	Grain Size 0.212 – 0.355 mm							
	Sample 1				**Sample 2**			
Total Mass	107.53 g				105.45 g			
Snow Mass	36.82 g				34.74 g			
Volume	8.71×10^{-5} m^{-3}				8.71×10^{-5} m^{-3}			
Density	422.58 kg m^{-3}				398.71 kg m^{-3}			
Snow Depth	**Light Intensity (mV)**							
	1	**2**	**3**	**4**	**1**	**2**	**3**	**4**
5 mm	10.837	12.312	13.401	15.938	10.334	15.429	15.657	11.933
10 mm	4.893	10.284	8.471	9.482	5.762	8.661	11.081	8.549
15 mm	4.072	8.812	8.051	6.232	4.763	7.294	9.276	5.850

	Sample 3				**Sample 4**			
Total Mass	108.92 g				107.32 g			
Snow Mass	38.21 g				36.61 g			
Volume	8.71×10^{-5} m^{-3}				8.71×10^{-5} m^{-3}			
Density	438.53 kg m^{-3}				420.17 kg m^{-3}			
Snow Depth	**Light Intensity (mV)**							
	1	**2**	**3**	**4**	**1**	**2**	**3**	**4**
5 mm	14.703	17.049	16.788	15.111	9.751	15.460	17.150	12.405
10 mm	7.647	12.397	10.682	9.191	4.410	8.499	9.386	9.194
15 mm	4.351	6.688	7.137	6.883	4.371	5.294	7.685	8.172

	Sample 5				**Mean**
Total Mass	106.21 g				107.09 g
Snow Mass	35.50 g				36.38 g
Volume	8.71×10^{-5} m^{-3}				8.71×10^{-5} m^{-3}
Density	407.43 kg m^{-3}				417.48 kg m^{-3}
Snow Depth	**Light Intensity (mV)**				
	1	**2**	**3**	**4**	**Mean**
5 mm	10.245	14.358	12.834	11.942	14.126
10 mm	5.333	11.082	9.756	7.582	8.617
15 mm	4.635	8.317	8.541	5.899	6.616

Table B.11. Raw light intensity measurements through water snow Samples 1 – 5, of grain size range 0.212 – 0.355 mm.

	Grain Size <0.212 mm							
	Sample 1				Sample 2			
Total Mass	103.45 g				99.30 g			
Snow Mass	32.74 g				28.59 g			
Volume	8.71 x10^{-5} m^{-3}				8.71 x10^{-5} m^{-3}			
Density	375.75 kg m^{-3}				328.12kg m^{-3}			
Snow Depth	**Light Intensity (mV)**							
	1	**2**	**3**	**4**	**1**	**2**	**3**	**4**
5 mm	8.701	7.347	11.490	12.978	11.457	11.069	10.195	11.587
10 mm	4.857	10.698	6.713	8.547	4.839	6.594	5.274	8.026
15 mm	3.349	4.211	5.563	4.910	3.802	3.655	6.021	5.503

	Sample 3				Sample 4			
Total Mass	107.23 g				101.87 g			
Snow Mass	36.52 g				31.16 g			
Volume	8.71 x10^{-5} m^{-3}				8.71 x10^{-5} m^{-3}			
Density	419.13 kg m^{-3}				357.62 kg m^{-3}			
Snow Depth	**Light Intensity (mV)**							
	1	**2**	**3**	**4**	**1**	**2**	**3**	**4**
5 mm	8.239	9.316	15.548	13.339	7.980	8.435	10.956	9.410
10 mm	3.855	9.381	9.301	9.257	5.170	4.611	8.403	7.648
15 mm	2.934	6.477	6.513	9.038	3.375	4.441	4.919	9.076

	Sample 5				Mean
Total Mass	106.09 g				103.59 g
Snow Mass	35.38 g				32.88 g
Volume	8.71 x10^{-5} m^{-3}				8.71 x10^{-5} m^{-3}
Density	406.05 kg m^{-3}				377.34 kg m^{-3}
Snow Depth	**Light Intensity (mV)**				
	1	**2**	**3**	**4**	**Mean**
5 mm	7.395	9.198	9.531	9.217	10.169
10 mm	3.837	4.695	3.894	5.587	6.559
15 mm	2.590	2.020	3.592	4.174	4.808

Table B.12. Raw light intensity measurements through water snow Samples 1 – 5, of grain size range <0.212 mm.

Appendix C

Granular Ice Measurements

C1. Granular Carbon Dioxide Ice

Light intensity measurements were made through samples of granular carbon dioxide ice, of discreet grain size ranges, at decreasing ice thicknesses. Measurements were made using a pyranometer (in millivolts), and four measurements were made per ice thickness. Details of the experimental set up can be found in Chapter 3, and experimental procedure specifically for the snow measurements, in Chapter 6. Table C.1 lists the equipment and its mass. Table C.2 give results for CO_2 snow.

Equipment	Mass (g)
20 mm copper ring	83.40
10 mm copper ring	41.73
5 mm copper ring	20.70
Sample base holder	8.28

Table C.1. Equipment which was used to contain the ice samples were weighed in order to determine mass of snow without having to remove the equipment. This reduced the time taken to weigh the samples, meaning that air exposure, and therefore frost deposition and sintering was kept to a minimum. All copper rings were 86 mm in internal diameter.

	Grain Size 5.60 – 8.00 mm							
	Sample 1				Sample 2			
Total Mass	335.83 g				338.71 g			
Snow Mass	160.75 g				163.63 g			
Volume	2.03 x10^{-4} m^{-3}				2.03 x10^{-4} m^{-3}			
Density	790.67 kg m^{-3}				804.84 kg m^{-3}			
Ice Depth	**Light Intensity (mV)**							
	1	**2**	**3**	**4**	**1**	**2**	**3**	**4**
5 mm	36.137	34.725	38.051	35.590	36.402	40.165	39.471	47.552
10 mm	25.308	24.515	26.107	26.842	26.026	22.019	24.102	25.746
15 mm	19.706	20.620	22.038	21.059	19.127	18.893	20.927	20.610
20 mm	15.498	16.216	18.408	17.011	16.886	16.091	16.537	16.360
25 mm	12.606	13.534	18.487	13.251	13.173	12.476	12.767	13.465
30 mm	10.239	10.248	11.385	11.430	10.341	10.007	11.919	11.955
35 mm	7.742	7.259	8.099	9.842	8.038	7.662	9.089	9.742

	Sample 3				Mean
Total Mass	335.17 g				336.57 g
Snow Mass	160.09 g				161.49 g
Volume	2.03 x10^{-4} m^{-3}				2.03 x10^{-4} m^{-3}
Density	787.43 kg m^{-3}				794.31 kg m^{-3}
Ice Depth	**Light Intensity (mV)**				
	1	**2**	**3**	**4**	**Mean**
5 mm	30.803	34.571	45.394	36.907	37.981
10 mm	23.323	20.561	22.409	23.376	24.194
15 mm	18.153	17.907	18.918	19.590	19.796
20 mm	14.429	15.116	15.356	14.073	15.998
25 mm	11.809	11.037	11.641	12.516	13.064
30 mm	9.508	10.205	9.729	10.715	10.640
35 mm	7.657	7.001	7.414	8.336	8.157

Table C.2. Raw light intensity measurements through granular carbon dioxide ice Samples 1 – 3, of grain size range 5.60 – 8.00 mm.

	Grain Size 4.00 – 5.60 mm							
	Sample 1				Sample 2			
Total Mass	275.70 g				278.55 g			
Snow Mass	142.29 g				145.14 g			
Volume	1.74 x10^{-4} m^{-3}				1.74 x10^{-4} m^{-3}			
Density	816.52 kg m^{-3}				832.87 kg m^{-3}			
Ice Depth	**Light Intensity (mV)**							
	1	**2**	**3**	**4**	**1**	**2**	**3**	**4**
5 mm	30.819	28.661	31.209	30.500	33.187	35.609	35.714	31.536
10 mm	21.139	21.438	22.702	21.290	24.175	24.797	24.923	23.740
15 mm	16.976	17.511	19.235	16.819	18.316	20.031	19.844	18.148
20 mm	13.220	14.487	13.798	13.322	15.734	16.549	17.011	16.093
25 mm	10.231	13.002	10.670	11.558	12.209	14.535	14.290	13.723
30 mm	8.022	8.060	9.313	8.948	9.622	11.068	10.640	11.366

	Sample 3				Sample 4			
Total Mass	278.83 g				288.27 g			
Snow Mass	145.42 g				154.86 g			
Volume	1.74 x10^{-4} m^{-3}				1.74 x10^{-4} m^{-3}			
Density	834.48 kg m^{-3}				888.65 kg m^{-3}			
Ice Depth	**Light Intensity (mV)**							
	1	**2**	**3**	**4**	**1**	**2**	**3**	**4**
5 mm	33.179	34.990	36.414	31.382	29.572	31.350	36.899	31.049
10 mm	22.687	26.832	26.293	22.620	19.807	21.178	21.609	21.542
15 mm	19.389	23.042	22.135	17.004	14.977	18.535	18.598	14.892
20 mm	16.593	16.808	14.440	14.851	10.862	13.391	13.763	10.973
25 mm	11.489	15.820	13.962	10.467	8.851	9.930	10.832	9.475
30 mm	9.258	10.552	12.009	9.885	6.386	6.289	7.503	7.690

	Sample 5				Mean
Total Mass	282.07 g				280.68 g
Snow Mass	148.66 g				147.27 g
Volume	1.74 x10^{-4} m^{-3}				1.74 x10^{-4} m^{-3}
Density	853.07 kg m^{-3}				845.12 kg m^{-3}
Ice Depth	**Light Intensity (mV)**				
	1	**2**	**3**	**4**	**Mean**
5 mm	25.615	28.970	27.456	26.171	31.514
10 mm	17.910	17.348	18.725	18.224	21.949
15 mm	15.323	16.068	16.012	14.730	17.879
20 mm	10.869	11.710	12.416	12.147	13.952
25 mm	9.203	11.151	9.914	9.115	11.521
30 mm	6.783	8.974	8.523	7.880	8.939

Table C.3.
Raw light intensity measurements through granular carbon dioxide ice Samples 1 – 5, of grain size range 4.00 – 5.60 mm.

	Grain Size 3.35 – 4.00 mm							
	Sample 1				Sample 2			
Total Mass	276.95 g				276.35 g			
Snow Mass	143.54 g				142.94 g			
Volume	1.74E-04				1.74E-04			
Density	823.69 kg m^{-3}				820.25 kg m^{-3}			
Ice Depth	**Light Intensity (mV)**							
	1	**2**	**3**	**4**	**1**	**2**	**3**	**4**
5 mm	19.446	18.224	18.500	19.295	16.949	18.863	20.606	18.192
10 mm	15.322	15.041	16.136	14.150	12.485	14.749	16.087	14.815
15 mm	11.781	11.218	12.265	13.183	10.401	14.326	12.502	13.496
20 mm	9.241	8.989	11.407	10.081	8.126	9.704	10.734	9.530
25 mm	7.352	7.466	7.710	8.662	6.929	8.763	10.889	8.754
30 mm	19.446	18.224	18.500	19.295	16.949	18.863	20.606	18.192

	Sample 3				Mean
Total Mass	280.91 g				278.07 g
Snow Mass	147.50 g				144.66 g
Volume	1.74 $x10^{-4}$ m^{-3}				1.74 $x10^{-4}$ m^{-3}
Density	846.42 kg m^{-3}				830.12 kg m^{-3}
Ice Depth	**Light Intensity (mV)**				
	1	**2**	**3**	**4**	**Mean**
5 mm	18.183	18.521	18.402	18.204	18.615
10 mm	13.275	14.616	12.827	14.077	14.465
15 mm	10.389	12.930	11.040	11.541	12.089
20 mm	8.036	9.581	8.599	10.848	9.573
25 mm	6.756	8.974	7.203	7.555	8.084
30 mm	18.183	18.521	18.402	18.204	18.615

Table C.4. Raw light intensity measurements through granular carbon dioxide ice Samples 1 – 3, of grain size range 3.35 – 4.00 mm.

	Grain Size 2.00 – 3.35 mm							
	Sample 1				**Sample 2**			
Total Mass	277.64 g				233.40 g			
Snow Mass	144.23 g				121.02 g			
Volume	1.74 x10^{-4} m^{-3}				1.45 x10^{-4} m^{-3}			
Density	827.65 kg m^{-3}				833.36 kg m^{-3}			
Ice Depth	**Light Intensity (mV)**							
	1	**2**	**3**	**4**	**1**	**2**	**3**	**4**
5 mm	30.279	31.750	29.478	28.563	24.908	25.459	27.328	25.981
10 mm	20.855	21.359	19.382	19.707	18.689	17.077	17.634	18.320
15 mm	13.245	14.200	13.814	13.476	12.977	13.560	13.121	13.324
20 mm	12.196	13.171	12.495	11.557	10.267	10.371	10.662	10.710
25 mm	8.731	10.208	9.417	9.189	7.719	8.542	7.801	10.023
30 mm	6.568	6.277	6.441	8.622	-	-	-	-

	Sample 3				**Mean**
Total Mass	239.31 g				250.12 g
Snow Mass	126.93 g				130.73 g
Volume	1.45 x10^{-4} m^{-3}				1.55 x10^{-4} m^{-3}
Density	874.05 kg m^{-3}				845.02 kg m^{-3}
Ice Depth	**Light Intensity (mV)**				
	1	**2**	**3**	**4**	**Mean**
5 mm	25.640	24.432	24.051	26.350	27.018
10 mm	18.887	17.628	17.803	19.475	18.901
15 mm	13.640	12.971	14.805	13.371	13.542
20 mm	10.166	10.280	10.963	10.705	11.129
25 mm	7.745	8.122	9.364	8.780	8.803
30 mm	-	-	-	-	6.977

Table C.5. Raw light intensity measurements through granular carbon dioxide ice Samples 1 – 3, of grain size range 2.00 – 3.35 mm.

	Grain Size 1.18 – 2.00 mm							
	Sample 1				Sample 2			
Total Mass	238.87 g				231.01 g			
Snow Mass	126.49 g				118.63 g			
Volume	1.45 x10^{-4} m^{-3}				1.45 x10^{-4} m^{-3}			
Density	871.02 kg m^{-3}				816.90 kg m^{-3}			
Ice Depth	**Light Intensity (mV)**							
	1	**2**	**3**	**4**	**1**	**2**	**3**	**4**
5 mm	23.779	24.972	25.748	23.693	22.572	21.506	22.186	24.583
10 mm	15.579	15.460	17.123	17.831	13.838	14.601	15.499	15.655
15 mm	10.564	14.158	13.872	11.536	9.550	11.603	13.591	12.136
20 mm	8.239	8.991	11.989	10.263	8.004	10.191	9.839	10.975
25 mm	6.204	7.572	9.070	7.955	6.407	8.028	9.541	9.154

	Sample 3				Mean
Total Mass	235.64 g				235.17 g
Snow Mass	123.26 g				122.79 g
Volume	1.45 x10^{-4} m^{-3}				1.45 x10^{-4} m^{-3}
Density	848.78 kg m^{-3}				845.57 kg m^{-3}
Ice Depth	**Light Intensity (mV)**				
	1	**2**	**3**	**4**	**Mean**
5 mm	21.018	22.004	20.957	22.986	23.000
10 mm	13.114	14.022	16.081	16.150	15.413
15 mm	9.539	10.996	13.890	12.003	11.953
20 mm	7.652	9.225	10.573	10.102	9.670
25 mm	6.228	7.623	8.897	9.066	7.979

Table C.6. Raw light intensity measurements through granular carbon dioxide ice Samples 1 – 3, of grain size range 1.18 – 2.00 mm.

	Grain Size 1.00 – 1.18 mm							
	Sample 1				**Sample 2**			
Total Mass	308.61 g				230.51 g			
Snow Mass	154.50 g				118.13 g			
Volume	2.03 x10^{-4} m^{-3}				1.45 x10^{-4} m^{-3}			
Density	759.93 kg m^{-3}				813.45			
Ice Depth	**Light Intensity (mV)**							
	1	**2**	**3**	**4**	**1**	**2**	**3**	**4**
5 mm	20.051	20.809	25.110	21.993	24.548	24.164	24.082	23.122
10 mm	13.132	15.875	16.043	14.459	15.106	16.145	15.908	14.429
15 mm	10.377	14.711	14.271	12.400	11.445	13.482	13.177	10.736
20 mm	9.089	11.049	11.171	11.136	8.121	10.903	8.685	9.987
25 mm	6.923	10.664	12.554	9.750	6.133	7.057	6.193	7.845
30 mm	6.051	11.299	10.006	6.060	-	-	-	-
35 mm	4.671	7.724	9.816	5.932	-	-	-	-

	Sample 3				**Mean**
Total Mass	235.00 g				258.04 g
Snow Mass	122.62 g				131.75 g
Volume	1.45 x10^{-4} m^{-3}				1.65 x10^{-4} m^{-3}
Density	844.37 kg m^{-3}				805.92
Ice Depth	**Light Intensity (mV)**				
	1	**2**	**3**	**4**	**Mean**
5 mm	20.976	19.708	20.304	20.770	22.136
10 mm	13.916	14.263	14.058	12.955	14.691
15 mm	10.137	11.414	11.655	9.867	11.973
20 mm	9.359	10.931	12.024	8.293	10.062
25 mm	6.152	6.805	7.187	6.015	7.773
30 mm	-	-	-	-	8.354
35 mm	-	-	-	-	7.036

Table C.7. Raw light intensity measurements through granular carbon dioxide ice Samples 1 – 3, of grain size range 1.00 – 1.18 mm.

	Grain Size 0.85 – 1.00 mm							
	Sample 1				Sample 2			
Total Mass	302.72 g				228.01 g			
Snow Mass	148.61 g				115.63 g			
Volume	2.03 x10^{-4} m^{-3}				1.45 x10^{-4} m^{-3}			
Density	730.96 kg m^{-3}				796.24 kg m^{-3}			
Ice Depth	**Light Intensity (mV)**							
	1	**2**	**3**	**4**	**1**	**2**	**3**	**4**
5 mm	18.969	24.781	22.968	18.618	22.178	20.199	20.121	24.072
10 mm	12.410	16.815	20.031	15.805	13.998	13.983	13.414	13.558
15 mm	8.737	16.044	20.183	12.807	12.579	13.082	12.849	11.099
20 mm	7.629	15.762	15.668	9.319	9.931	11.076	9.771	8.045
25 mm	5.862	11.884	8.837	7.337	6.681	8.391	6.287	6.625
30 mm	5.717	5.876	7.515	6.725	-	-	-	-
35 mm	4.407	5.184	6.912	7.530	-	-	-	-

	Sample 3				Mean
Total Mass	228.62 g				253.12 g
Snow Mass	116.24 g				126.83 g
Volume	1.45 x10^{-4} m^{-3}				1.65 x10^{-4} m^{-3}
Density	800.44 kg m^{-3}				775.88 kg m^{-3}
Ice Depth	**Light Intensity (mV)**				
	1	**2**	**3**	**4**	**Mean**
5 mm	25.830	24.897	24.740	24.544	22.660
10 mm	14.202	13.844	13.134	13.962	14.596
15 mm	11.378	12.724	11.296	10.211	12.749
20 mm	8.230	9.705	8.499	7.807	10.120
25 mm	6.028	7.479	6.459	6.837	7.392
30 mm	-	-	-	-	6.458
35 mm	-	-	-	-	6.008

Table C.8. Raw light intensity measurements through granular carbon dioxide ice Samples 1 – 3, of grain size range 0.85 – 1.00 mm.

	Grain Size 0.71 – 0.85 mm							
	Sample 1				Sample 2			
Total Mass	229.00 g				232.61 g			
Snow Mass	116.62 g				120.23 g			
Volume	1.45 x10^{-4} m^{-3}				1.45 x10^{-4} m^{-3}			
Density	803.06 kg m^{-3}				827.92 kg m^{-3}			
Ice Depth	**Light Intensity (mV)**							
	1	**2**	**3**	**4**	**1**	**2**	**3**	**4**
5 mm	21.671	21.546	20.503	20.285	18.595	17.716	19.393	17.140
10 mm	13.146	13.983	12.857	12.452	12.255	12.342	13.870	11.669
15 mm	10.288	12.033	11.316	9.312	8.427	8.058	10.603	8.467
20 mm	7.041	8.556	7.757	7.584	7.041	8.439	8.316	7.034
25 mm	6.329	7.862	6.346	5.567	4.945	4.641	7.976	5.893

	Sample 3				Sample 4			
Total Mass	234.49 g				234.31 g			
Snow Mass	122.11 g				121.93 g			
Volume	1.45 x10^{-4} m^{-3}				1.45 x10^{-4} m^{-3}			
Density	840.86 kg m^{-3}				839.62 kg m^{-3}			
Ice Depth	**Light Intensity (mV)**							
	1	**2**	**3**	**4**	**1**	**2**	**3**	**4**
5 mm	18.075	16.589	17.707	17.327	19.337	19.635	21.374	19.967
10 mm	11.842	11.257	12.918	11.583	12.039	15.459	16.125	13.904
15 mm	9.184	8.091	9.636	8.592	10.157	12.653	13.150	10.378
20 mm	6.538	7.880	7.874	8.999	6.518	11.374	10.103	9.453
25 mm	5.885	6.283	10.473	6.241	5.267	8.512	8.726	7.884

	Mean
Total Mass	233.80 g
Snow Mass	121.42 g
Volume	1.45 x10^{-4} m^{-3}
Density	836.13 kg m^{-3}
Ice Depth	**(mV)**
	Mean
5 mm	19.179
10 mm	12.981
15 mm	10.022
20 mm	8.157
25 mm	6.802

Table C.9. Raw light intensity measurements through granular carbon dioxide ice Samples 1 – 4, of grain size range 0.71 – 0.85 mm.

	Grain Size 0.60 – 0.71 mm							
	Sample 1				Sample 2			
Total Mass	215.32 g				184.62 g			
Snow Mass	102.94 g				72.24 g			
Volume	1.45 x10^{-4} m^{-3}				1.16 x10^{-4} m^{-3}			
Density	708.85 kg m^{-3}				621.81 kg m^{-3}			
Ice Depth	**Light Intensity (mV)**							
	1	**2**	**3**	**4**	**1**	**2**	**3**	**4**
5 mm	22.118	21.175	18.203	19.763	15.809	15.791	17.744	14.988
10 mm	11.377	11.921	11.498	13.244	10.626	10.740	11.732	11.215
15 mm	8.955	11.136	11.085	9.070	7.265	8.433	10.814	7.703
20 mm	7.522	8.868	8.524	6.750	6.713	7.238	8.157	8.677
25 mm	6.274	7.851	5.927	6.291	-	-	-	-

	Sample 3				Mean
Total Mass	189.71 g				196.55 g
Snow Mass	77.33 g				84.17 g
Volume	1.16 x10^{-4} m^{-3}				1.26 x10^{-4} m^{-3}
Density	665.63 kg m^{-3}				665.43 kg m^{-3}
Ice Depth	**Light Intensity (mV)**				
	1	**2**	**3**	**4**	**Mean**
5 mm	17.933	18.640	16.631	17.015	17.984
10 mm	10.436	9.762	12.470	10.516	11.295
15 mm	6.803	7.358	8.205	7.026	8.654
20 mm	5.560	6.873	7.071	5.566	7.293
25 mm	-	-	-	-	6.586

Table C.10. Raw light intensity measurements through granular carbon dioxide ice Samples 1 – 3, of grain size range 0.60 – 0.71 mm.

	Grain Size 0.50 – 0.60 mm							
	Sample 1				Sample 2			
Total Mass	171.34 g				186.12 g			
Snow Mass	79.66 g				94.44 g			
Volume	1.16 x10^{-4} m^{-3}				1.16 x10^{-4} m^{-3}			
Density	685.68 kg m^{-3}				812.90 kg m^{-3}			
Ice Depth	**Light Intensity (mV)**							
	1	**2**	**3**	**4**	**1**	**2**	**3**	**4**
5 mm	16.775	16.274	15.325	17.402	13.616	16.667	14.969	15.435
10 mm	11.210	11.771	10.764	10.691	11.023	11.327	12.996	9.789
15 mm	7.136	9.791	8.235	8.533	7.940	10.410	8.403	6.528
20 mm	5.441	7.283	6.438	6.455	6.531	6.910	8.837	5.246

	Sample 3				Sample 4			
Total Mass	170.22 g				180.41 g			
Snow Mass	78.54 g				88.73 g			
Volume	1.16 x10^{-4} m^{-3}				1.16 x10^{-4} m^{-3}			
Density	676.04 kg m^{-3}				763.75 kg m^{-3}			
Ice Depth	**Light Intensity (mV)**							
	1	**2**	**3**	**4**	**1**	**2**	**3**	**4**
5 mm	13.856	21.498	18.220	15.775	17.984	21.492	20.309	18.262
10 mm	8.632	15.955	11.030	8.257	9.756	13.691	12.065	11.396
15 mm	7.543	9.092	11.131	6.144	7.650	10.448	11.359	8.919
20 mm	4.129	8.516	6.051	5.856	5.034	6.792	8.868	7.753

	Mean
Total Mass	178.92 g
Snow Mass	87.24 g
Volume	1.16 x10^{-4} m^{-3}
Density	750.90 kg m^{-3}
Ice Depth	**(mV)**
	Mean
5 mm	17.116
10 mm	11.272
15 mm	8.704
20 mm	6.634

Table C.11. Raw light intensity measurements through granular carbon dioxide ice Samples 1 – 4, of grain size range 0.50 – 0.60 mm.

	Grain Size 0.355 – 0.500 mm							
	Sample 1				**Sample 2**			
Total Mass	169.30 g				180.02 g			
Snow Mass	77.62 g				88.34 g			
Volume	1.16 x10^{-4} m^{-3}				1.16 x10^{-4} m^{-3}			
Density	668.12 kg m^{-3}				760.40 kg m^{-3}			
Ice Depth	**Light Intensity (mV)**							
	1	**2**	**3**	**4**	**1**	**2**	**3**	**4**
5 mm	15.823	16.909	16.872	16.233	13.815	14.446	15.524	12.667
10 mm	7.705	10.603	9.688	8.111	8.884	11.039	9.195	8.810
15 mm	5.951	7.392	8.863	7.807	5.751	7.754	8.010	6.783
20 mm	3.844	5.499	6.332	4.497	4.915	4.330	5.713	6.015

	Sample 3				**Sample 4**			
Total Mass	178.09 g				172.04 g			
Snow Mass	86.41 g				80.36 g			
Volume	1.16 x10^{-4} m^{-3}				1.16 x10^{-4} m^{-3}			
Density	743.78 kg m^{-3}				691.71 kg m^{-3}			
Ice Depth	**Light Intensity (mV)**							
	1	**2**	**3**	**4**	**1**	**2**	**3**	**4**
5 mm	14.237	15.973	17.891	14.395	14.375	16.678	18.716	15.944
10 mm	8.219	9.922	11.005	7.887	9.020	12.801	12.693	10.009
15 mm	5.504	6.577	9.856	6.872	6.571	10.083	10.374	8.370
20 mm	4.087	4.929	6.625	4.801	5.423	7.471	7.506	7.397

	Mean
Total Mass	176.72 g
Snow Mass	85.04 g
Volume	1.16 x10^{-4} m^{-3}
Density	731.96 kg m^{-3}
Ice Depth	**(mV)**
	Mean
5 mm	15.656
10 mm	9.724
15 mm	7.657
20 mm	5.587

Table C.12. Raw light intensity measurements through granular carbon dioxide ice Samples 1 – 4, of grain size range 0.355 – 0.500 mm.

C2. Granular Water Ice

Light intensity measurements were made through samples of granular water ice, of discreet grain size ranges, at decreasing ice thicknesses. Measurements were made using a pyranometer (in millivolts), and four readings were taken per snow thickness: measurement 1 is in the centre of the sample, and then measurements 2, 3, and 4 were taken radially around centre, at least 20 mm from the sample edge, and ensuring the outer platform of the pyranometer was kept within the shadow of the sample As far as could be determined, minimal melting and no sintering occurred. More details of the experimental set up can be found in Chapter 3, and experimental procedure specifically for snow measurements, in Chapter 5. Tables C.13 through to C.24 give the results for granular water ice, separated by grain size range.

	Grain Size 5.60 – 8.00 mm							
	Sample 1				**Sample 2**			
Total Mass	301.19 g				268.97 g			
Snow Mass	126.11 g				114.86 g			
Volume	2.32 x10^{-4} m^{-3}				2.03 x10^{-4} m^{-3}			
Density	542.75 kg m^{-3}				564.96 kg m^{-3}			
Ice Depth	**Light Intensity (mV)**							
	1	**2**	**3**	**4**	**1**	**2**	**3**	**4**
5 mm	36.780	47.270	42.765	34.567	43.151	31.924	41.334	52.908
10 mm	19.425	19.554	22.898	18.409	27.334	23.078	28.421	29.531
15 mm	15.569	13.298	16.032	14.113	17.398	15.305	16.948	16.997
20 mm	12.178	10.956	13.298	10.273	13.342	14.467	12.914	10.716
25 mm	10.117	8.734	10.680	8.849	9.521	8.619	9.477	8.240
30 mm	7.958	7.369	7.936	7.541	7.831	7.506	6.870	7.583
35 mm	6.411	5.567	6.412	6.269	5.750	4.458	5.531	5.219
40 mm	4.558	4.205	4.412	4.701	-	-	-	-

	Sample 3	**Sample 4**
Total Mass	276.07 g	270.38 g
Snow Mass	121.96 g	116.27 g
Volume	2.03 x10^{-4} m^{-3}	2.03 x10^{-4} m^{-3}
Density	599.88 kg m^{-3}	571.89 kg m^{-3}

Ice Depth	Light Intensity (mV)							
	1	2	3	4	1	2	3	4
5 mm	45.473	45.231	49.826	48.594	35.119	31.471	44.086	30.003
10 mm	27.838	29.993	25.222	30.134	18.509	20.046	19.684	20.742
15 mm	19.756	15.550	17.609	22.291	12.115	14.376	14.409	14.701
20 mm	14.311	13.692	12.302	14.361	11.772	12.761	10.795	16.657
25 mm	11.759	9.076	10.040	11.952	8.668	13.664	10.571	9.165
30 mm	9.221	8.489	7.703	10.384	6.872	8.940	8.434	6.951
35 mm	6.852	5.315	6.471	8.018	5.302	5.141	6.139	9.923
40 mm	-	-	-	-	-	-	-	-

	Sample 5	Sample 6
Total Mass	272.31 g	271.84 g
Snow Mass	118.20 g	117.73 g
Volume	2.03 x10^{-4} m^{-3}	2.03 x10^{-4} m^{-3}
Density	581.38 kg m^{-3}	579.07 kg m^{-3}

Ice Depth	Light Intensity (mV)							
	1	2	3	4	1	2	3	4
5 mm	54.404	51.451	37.087	47.123	44.521	42.053	55.012	43.679
10 mm	30.091	23.854	22.836	29.146	32.546	31.365	28.511	27.398
15 mm	16.102	16.069	17.674	16.940	20.337	20.305	22.401	19.033
20 mm	15.507	13.314	13.471	13.534	14.976	12.007	13.644	13.883
25 mm	10.979	9.304	9.838	9.572	12.517	12.569	12.102	10.850
30 mm	9.163	8.277	8.664	8.265	10.402	11.479	11.103	9.158
35 mm	5.701	5.582	6.160	6.439	6.039	6.233	6.918	6.546
40 mm	-	-	-	-	-	-	-	-

	Mean
Total Mass	276.79 g
Snow Mass	119.19 g
Volume	2.08 x10^{-4} m^{-3}
Density	573.32 kg m^{-3}
Ice Depth	(mV)
	Mean
5 mm	44.747
10 mm	26.310
15 mm	17.387
20 mm	13.136
25 mm	10.189
30 mm	8.598
35 mm	6.125
40 mm	4.469

Table C.13. Raw light intensity measurements through granular water ice Samples 1 – 6, of grain size range 5.60 – 8.00 mm.

	Grain Size 4.00 – 5.56 mm							
	Sample 1				Sample 2			
Total Mass	230.35 g				230.07 g			
Snow Mass	96.94 g				96.66 g			
Volume	1.74 x10^{-4} m^{-3}				1.74 x10^{-4} m^{-3}			
Density	556.28 kg m^{-3}				554.68 kg m^{-3}			
Ice Depth	**Light Intensity (mV)**							
	1	**2**	**3**	**4**	**1**	**2**	**3**	**4**
5 mm	44.827	43.739	45.021	48.032	46.229	44.807	45.956	39.736
10 mm	21.332	19.016	20.597	24.626	21.745	20.164	21.198	24.473
15 mm	15.198	14.189	15.478	16.452	16.086	13.431	15.545	16.732
20 mm	12.608	12.564	11.061	13.669	11.303	11.380	9.705	13.204
25 mm	10.037	10.340	8.351	12.024	8.926	7.989	7.288	10.132

	Sample 3				Sample 4			
Total Mass	224.96 g				228.83 g			
Snow Mass	91.55 g				95.42 g			
Volume	1.74 x10^{-4} m^{-3}				1.74 x10^{-4} m^{-3}			
Density	525.35 kg m^{-3}				547.56 kg m^{-3}			
Ice Depth	**Light Intensity (mV)**							
	1	**2**	**3**	**4**	**1**	**2**	**3**	**4**
5 mm	44.245	37.833	49.293	63.256	39.854	40.066	35.758	35.081
10 mm	23.009	22.795	24.962	30.360	24.543	24.595	22.980	22.811
15 mm	15.073	16.748	14.683	17.062	18.431	21.392	20.357	16.639
20 mm	12.931	12.959	11.108	14.409	13.946	15.067	13.799	12.670
25 mm	9.687	8.886	8.360	10.807	9.587	10.448	8.556	9.814

	Sample 5				Mean
Total Mass	225.85 g				228.01 g
Snow Mass	92.44 g				94.60 g
Volume	1.74 x10^{-4} m^{-3}				1.74 x10^{-4} m^{-3}
Density	530.46 kg m^{-3}				542.87 kg m^{-3}
Ice Depth	**Light Intensity (mV)**				
	1	**2**	**3**	**4**	**Mean**
5 mm	48.362	31.457	53.061	45.870	44.124
10 mm	22.050	21.968	21.370	24.933	22.976
15 mm	18.412	19.279	17.955	16.662	16.790
20 mm	14.021	13.830	13.984	12.409	12.831
25 mm	11.076	10.155	11.815	8.769	9.652

Table C.14. Raw light intensity measurements through granular water ice Samples 1 – 5, of grain size range 4.00 – 5.56 mm.

	Grain Size 3.35 – 4.00 mm							
	Sample 1				Sample 2			
Total Mass	227.29 g				222.91 g			
Snow Mass	93.88 g				89.50 g			
Volume	1.74 x10^{-4} m^{-3}				1.74 x10^{-4} m^{-3}			
Density	538.72 kg m^{-3}				513.59 kg m^{-3}			
Ice Depth	**Light Intensity (mV)**							
	1	**2**	**3**	**4**	**1**	**2**	**3**	**4**
5 mm	29.369	26.266	30.008	43.532	26.955	28.190	27.173	26.957
10 mm	17.489	16.926	15.227	20.629	16.706	18.328	15.620	17.819
15 mm	13.656	15.031	16.697	15.038	12.605	12.258	14.395	14.193
20 mm	10.506	9.474	9.327	11.876	10.467	16.355	13.521	10.020
25 mm	8.649	7.753	7.868	10.736	7.365	8.893	7.930	9.867
30 mm	5.459	4.930	7.168	8.167	5.182	9.745	6.447	8.786

	Sample 3				Sample 4			
Total Mass	225.07 g				222.85 g			
Snow Mass	91.66 g				89.44 g			
Volume	1.74 x10^{-4} m^{-3}				1.74 x10^{-4} m^{-3}			
Density	525.98 kg m^{-3}				513.24 kg m^{-3}			
Ice Depth	**Light Intensity (mV)**							
	1	**2**	**3**	**4**	**1**	**2**	**3**	**4**
5 mm	28.439	34.605	27.694	25.529	38.153	38.604	40.852	32.040
10 mm	18.992	20.097	19.189	19.282	22.377	24.978	28.697	23.699
15 mm	13.611	13.875	18.751	14.203	15.562	19.234	18.761	15.744
20 mm	9.315	10.079	11.973	12.412	12.271	14.980	13.073	11.664
25 mm	8.273	9.195	9.466	10.013	8.306	10.178	8.591	8.806
30 mm	5.175	6.475	7.588	8.174	6.993	7.107	6.998	7.631

	Sample 5				Mean
Total Mass	224.09 g				224.44 g
Snow Mass	90.68 g				91.03 g
Volume	1.74 x10^{-4} m^{-3}				1.74 x10^{-4} m^{-3}
Density	520.36 kg m^{-3}				522.38 kg m^{-3}
Ice Depth	**Light Intensity (mV)**				
	1	**2**	**3**	**4**	**Mean**
5 mm	36.553	33.948	35.271	40.165	31.523
10 mm	22.005	22.547	22.894	25.872	19.753
15 mm	18.293	15.637	20.120	16.632	15.226
20 mm	13.182	12.432	16.120	12.285	11.707
25 mm	9.372	10.966	10.728	7.636	8.868
30 mm	5.734	7.251	7.291	6.450	7.002

Table C.15. Raw light intensity measurements through granular water ice Samples 1 – 5, of grain size range 3.35 – 4.00 mm.

	Grain Size 2.00 – 3.35 mm							
	Sample 1				Sample 2			
Total Mass	222.27 g				224.01 g			
Snow Mass	88.86 g				90.60 g			
Volume	1.74 x10^{-4} m^{-3}				1.74 x10^{-4} m^{-3}			
Density	509.92 kg m^{-3}				519.90 kg m^{-3}			
Ice Depth	**Light Intensity (mV)**							
	1	**2**	**3**	**4**	**1**	**2**	**3**	**4**
5 mm	18.885	24.859	19.527	21.864	24.780	17.402	20.466	26.445
10 mm	10.749	15.945	15.688	12.361	11.341	12.132	11.667	15.540
15 mm	9.577	14.290	14.995	9.156	8.281	16.134	8.687	9.152
20 mm	7.647	10.172	10.164	8.635	7.864	10.236	12.073	7.162
25 mm	6.056	9.122	9.296	8.751	5.129	10.905	9.622	6.611
30 mm	3.496	4.457	5.645	5.906	3.342	4.204	6.971	7.489

	Sample 3				Sample 4			
Total Mass	225.64 g				221.51 g			
Snow Mass	92.23 g				88.10 g			
Volume	1.74 x10^{-4} m^{-3}				1.74 x10^{-4} m^{-3}			
Density	529.25 kg m^{-3}				505.55 kg m^{-3}			
Ice Depth	**Light Intensity (mV)**							
	1	**2**	**3**	**4**	**1**	**2**	**3**	**4**
5 mm	21.796	22.219	24.981	26.015	34.417	35.179	32.735	29.979
10 mm	16.602	17.800	16.296	18.157	18.639	19.891	21.293	18.198
15 mm	11.854	13.356	12.054	11.971	13.970	16.946	18.132	13.045
20 mm	9.437	10.119	11.764	11.838	11.136	13.429	12.478	10.521
25 mm	8.207	11.043	12.297	10.359	9.594	9.792	11.481	8.536
30 mm	4.486	6.837	4.608	7.093	5.166	5.880	4.876	6.535

	Sample 5				Mean
Total Mass	231.85 g				225.06 g
Snow Mass	98.44 g				91.65 g
Volume	1.74 x10^{-4} m^{-3}				1.74 x10^{-4} m^{-3}
Density	564.89 kg m^{-3}				525.90 kg m^{-3}
Ice Depth	**Light Intensity (mV)**				
	1	**2**	**3**	**4**	**Mean**
5 mm	31.260	32.831	31.058	27.264	26.198
10 mm	20.139	26.055	21.447	18.673	16.931
15 mm	16.575	19.029	17.504	11.959	13.333
20 mm	12.085	11.849	14.135	9.730	10.624
25 mm	8.543	7.974	8.019	6.611	8.897
30 mm	4.780	5.911	6.252	5.936	5.494

Table C.16. Raw light intensity measurements through granular water ice Samples 1 – 5, of grain size range 2.00 – 3.35 mm.

	Grain Size 1.18 – 2.00 mm							
	Sample 1				Sample 2			
Total Mass	185.28 g				185.84 g			
Snow Mass	72.90 g				73.46 g			
Volume	1.45 x10^{-4} m^{-3}				1.45 x10^{-4} m^{-3}			
Density	502.00 kg m^{-3}				505.85 kg m^{-3}			
Ice Depth	**Light Intensity (mV)**							
	1	**2**	**3**	**4**	**1**	**2**	**3**	**4**
5 mm	21.895	27.075	19.472	26.167	18.676	20.771	23.182	20.347
10 mm	12.317	11.725	13.696	14.557	10.703	10.871	12.402	13.364
15 mm	9.712	11.805	8.947	12.470	8.004	7.996	10.527	11.059
20 mm	6.681	8.845	9.307	9.589	7.316	10.871	8.447	8.127
25 mm	5.294	8.592	8.854	8.915	4.281	8.129	7.396	8.206

	Sample 3				Sample 4			
Total Mass	182.54 g				185.27 g			
Snow Mass	70.16 g				72.89 g			
Volume	1.45 x10^{-4} m^{-3}				1.45 x10^{-4} m^{-3}			
Density	483.13 kg m^{-3}				501.93 kg m^{-3}			
Ice Depth	**Light Intensity (mV)**							
	1	**2**	**3**	**4**	**1**	**2**	**3**	**4**
5 mm	18.275	22.635	16.601	20.717	25.468	36.758	30.666	27.038
10 mm	10.583	13.149	10.079	13.885	17.041	20.914	26.603	18.261
15 mm	7.559	10.680	8.374	10.986	11.971	18.162	17.936	11.899
20 mm	6.032	9.923	7.489	9.787	7.752	11.166	12.301	9.469
25 mm	4.971	8.996	9.894	8.117	5.614	6.902	8.237	7.205

	Sample 5				Mean
Total Mass	192.89 g				186.36 g
Snow Mass	80.51 g				73.98 g
Volume	1.45 x10^{-4} m^{-3}				1.45 x10^{-4} m^{-3}
Density	554.40 kg m^{-3}				509.46 kg m^{-3}
Ice Depth	**Light Intensity (mV)**				
	1	**2**	**3**	**4**	**Mean**
5 mm	26.408	29.449	26.032	28.587	24.311
10 mm	16.870	16.057	17.306	14.554	14.747
15 mm	11.402	14.573	15.641	11.987	11.585
20 mm	8.491	10.217	9.828	8.745	9.019
25 mm	4.279	5.353	6.174	6.520	7.096

Table C.17. Raw light intensity measurements through granular water ice Samples 1 – 5, of grain size range 1.18 - 2.00 mm.

	Grain Size 1.00 – 1.18 mm							
	Sample 1				Sample 2			
Total Mass	188.04 g				147.68 g			
Snow Mass	75.66 g				56.00 g			
Volume	1.45 x10^{-4} m^{-3}				1.16 x10^{-4} m^{-3}			
Density	521.00 kg m^{-3}				482.03 kg m^{-3}			
Ice Depth	**Light Intensity (mV)**							
	1	**2**	**3**	**4**	**1**	**2**	**3**	**4**
5 mm	20.042	19.760	21.046	22.675	19.338	22.939	20.810	21.842
10 mm	13.946	15.201	14.759	15.081	14.027	14.036	16.470	13.789
15 mm	8.733	8.816	7.954	11.609	9.847	15.404	12.625	9.376
20 mm	6.555	9.132	10.006	10.075	7.380	8.643	9.515	9.816
25 mm	5.271	4.375	5.530	8.356	-	-	-	-

	Sample 3				Sample 4			
Total Mass	144.46 g				152.03 g			
Snow Mass	52.78 g				60.35 g			
Volume	1.16 x10^{-4} m^{-3}				1.16 x10^{-4} m^{-3}			
Density	454.31 kg m^{-3}				519.47 kg m^{-3}			
Ice Depth	**Light Intensity (mV)**							
	1	**2**	**3**	**4**	**1**	**2**	**3**	**4**
5 mm	16.086	14.879	15.090	15.267	19.282	23.841	20.546	21.567
10 mm	8.634	9.737	8.679	9.962	11.994	16.789	16.645	12.524
15 mm	5.569	7.208	6.639	4.760	7.563	12.242	14.889	8.487
20 mm	4.671	6.650	5.177	6.652	5.608	9.054	9.576	7.089
25 mm	-	-	-	-	-	-	-	-

	Sample 5				Mean
Total Mass	151.67 g				156.78 g
Snow Mass	59.99 g				60.96 g
Volume	1.16 x10^{-4} m^{-3}				1.22 x10^{-4} m^{-3}
Density	516.37 kg m^{-3}				498.64 kg m^{-3}
Ice Depth	**Light Intensity (mV)**				
	1	**2**	**3**	**4**	**Mean**
5 mm	19.023	19.949	20.104	19.430	19.676
10 mm	11.602	14.435	12.366	10.670	13.067
15 mm	7.607	8.516	10.028	7.259	9.257
20 mm	5.525	5.804	7.721	5.214	7.493
25 mm	-	-	-	-	5.883

Table C.18. Raw light intensity measurements through granular water ice Samples 1 – 5, of grain size range 1.00 – 1.18 mm.

	Grain Size 0.85 – 1.00 mm							
	Sample 1				Sample 2			
Total Mass	148.44 g				142.70 g			
Snow Mass	56.76 g				51.02 g			
Volume	1.16 x10^{-4} m^{-3}				1.16 x10^{-4} m^{-3}			
Density	488.57 kg m^{-3}				439.16 kg m^{-3}			
Ice Depth	**Light Intensity (mV)**							
	1	**2**	**3**	**4**	**1**	**2**	**3**	**4**
5 mm	22.264	30.363	21.460	20.810	18.737	19.950	23.288	22.593
10 mm	11.508	19.672	15.375	12.623	11.028	14.850	13.513	12.769
15 mm	8.864	10.670	15.893	9.516	6.869	7.015	9.011	9.072
20 mm	7.732	10.230	12.153	8.587	5.924	7.966	9.505	7.519

	Sample 3				Sample 4			
Total Mass	142.35 g				146.26 g			
Snow Mass	50.67 g				54.58 g			
Volume	1.16 x10^{-4} m^{-3}				1.16 x10^{-4} m^{-3}			
Density	436.15 kg m^{-3}				469.80 kg m^{-3}			
Ice Depth	**Light Intensity (mV)**							
	1	**2**	**3**	**4**	**1**	**2**	**3**	**4**
5 mm	12.246	11.950	12.181	13.340	21.107	23.598	23.888	23.579
10 mm	6.443	5.896	7.925	6.997	11.709	13.662	19.509	15.254
15 mm	3.920	4.361	4.932	5.273	12.093	15.319	13.633	10.752
20 mm	3.238	2.431	3.663	4.984	5.666	9.837	8.142	5.804

	Sample 5				Mean
Total Mass	149.45 g				145.84 g
Snow Mass	57.77 g				54.16 g
Volume	1.16 x10^{-4} m^{-3}				1.16 x10^{-4} m^{-3}
Density	497.26 kg m^{-3}				466.19 kg m^{-3}
Ice Depth	**Light Intensity (mV)**				
	1	**2**	**3**	**4**	**Mean**
5 mm	18.571	20.816	23.549	20.081	20.085
10 mm	11.296	14.650	15.455	13.271	12.421
15 mm	7.044	10.097	11.361	8.018	9.200
20 mm	7.369	8.505	9.624	5.971	7.086

Table C.19. Raw light intensity measurements through granular water ice Samples 1 – 5, of grain size range 0.85 – 1.00 mm.

	Grain Size 0.71 – 0.85 mm							
	Sample 1				Sample 2			
Total Mass	142.70 g				142.79 g			
Snow Mass	51.02 g				51.11 g			
Volume	1.16 x10^{-4} m^{-3}				1.16 x10^{-4} m^{-3}			
Density	439.16 kg m^{-3}				439.94 kg m^{-3}			
Ice Depth	**Light Intensity (mV)**							
	1	**2**	**3**	**4**	**1**	**2**	**3**	**4**
5 mm	17.659	19.596	23.213	18.875	18.469	15.543	17.392	20.740
10 mm	8.194	14.588	11.486	13.443	9.082	15.901	11.260	10.362
15 mm	6.105	8.207	10.474	8.293	6.612	8.355	7.836	6.258
20 mm	5.445	7.881	8.679	8.066	4.862	7.929	8.117	6.525

	Sample 3				Sample 4			
Total Mass	139.38 g				140.95 g			
Snow Mass	47.70 g				49.27 g			
Volume	1.16 x10^{-4} m^{-3}				1.16 x10^{-4} m^{-3}			
Density	410.58 kg m^{-3}				424.10 kg m^{-3}			
Ice Depth	**Light Intensity (mV)**							
	1	**2**	**3**	**4**	**1**	**2**	**3**	**4**
5 mm	16.977	14.687	15.198	17.637	15.607	14.904	17.566	16.378
10 mm	8.348	10.332	8.693	10.138	10.303	11.038	8.427	12.523
15 mm	5.159	5.931	5.446	7.498	7.221	11.027	9.211	10.823
20 mm	3.960	3.625	4.821	5.613	3.789	5.537	8.020	5.037

	Sample 5				Mean
Total Mass	142.45 g				141.65 g
Snow Mass	50.77 g				49.97 g
Volume	1.16 x10^{-4} m^{-3}				1.16 x10^{-4} m^{-3}
Density	437.01 kg m^{-3}				430.16 kg m^{-3}
Ice Depth	**Light Intensity (mV)**				
	1	**2**	**3**	**4**	**Mean**
5 mm	15.615	19.476	19.842	19.306	17.528
10 mm	8.848	15.186	14.548	11.261	10.882
15 mm	5.868	9.376	11.034	7.423	7.779
20 mm	5.309	10.385	8.807	6.528	6.119

Table C.20. Raw light intensity measurements through granular water ice Samples 1 – 5, of grain size range 0.71 – 0.85 mm.

	Grain Size 0.60 – 0.71 mm							
	Sample 1				Sample 2			
Total Mass	140.37 g				108.03 g			
Snow Mass	48.69 g				37.32 g			
Volume	1.16 x10^{-4} m^{-3}				8.71 x10^{-5} m^{-3}			
Density	419.11 kg m^{-3}				428.32 kg m^{-3}			
Ice Depth	**Light Intensity (mV)**							
	1	**2**	**3**	**4**	**1**	**2**	**3**	**4**
5 mm	10.782	9.968	10.105	12.456	11.357	11.161	10.795	12.426
10 mm	5.932	5.859	5.204	7.025	5.637	5.558	5.642	6.023
15 mm	3.529	4.073	3.826	4.979	2.604	3.339	3.680	4.457
20 mm	2.749	4.750	2.515	4.442	-	-	-	-

	Sample 3				Sample 4			
Total Mass	112.86 g				117.06 g			
Snow Mass	42.15 g				46.35 g			
Volume	8.71 x10^{-5} m^{-3}				8.71 x10^{-5} m^{-3}			
Density	483.75 kg m^{-3}				531.95 kg m^{-3}			
Ice Depth	**Light Intensity (mV)**							
	1	**2**	**3**	**4**	**1**	**2**	**3**	**4**
5 mm	16.140	13.497	15.942	16.978	14.423	13.208	15.575	15.751
10 mm	5.637	5.558	5.642	6.023	7.300	9.576	10.017	10.520
15 mm	3.612	3.059	2.810	4.477	4.425	7.309	8.116	8.908
20 mm	-	-	-	-	-	-	-	-

	Sample 5				Mean
Total Mass	111.75 g				118.01 g
Snow Mass	41.04 g				43.11 g
Volume	8.71 x10^{-5} m^{-3}				9.29 x10^{-5} m^{-3}
Density	471.01 kg m^{-3}				466.83 kg m^{-3}
Ice Depth	**Light Intensity (mV)**				
	1	**2**	**3**	**4**	**Mean**
5 mm	15.713	14.420	14.619	14.261	13.479
10 mm	7.372	10.058	11.671	8.338	7.230
15 mm	6.074	6.963	10.309	5.276	5.091
20 mm	-	-	-	-	3.614

Table C.21. Raw light intensity measurements through granular water ice Samples 1 – 5, of grain size range 0.60 – 0.71 mm.

	Grain Size 0.50 – 0.60 mm							
	Sample 1				Sample 2			
Total Mass	112.08 g				110.21 g			
Snow Mass	41.37 g				39.50 g			
Volume	8.71 x10^{-5} m^{-3}				8.71 x10^{-5} m^{-3}			
Density	474.80 kg m^{-3}				453.33 kg m^{-3}			
Ice Depth	**Light Intensity (mV)**							
	1	**2**	**3**	**4**	**1**	**2**	**3**	**4**
5 mm	11.994	10.460	11.322	12.649	11.983	11.577	11.457	12.654
10 mm	5.934	8.083	7.980	7.942	6.484	7.967	6.825	7.353
15 mm	3.378	3.381	3.408	5.071	3.090	3.984	3.847	4.915

	Sample 3				Sample 4			
Total Mass	112.64 g				104.18 g			
Snow Mass	41.93 g				33.47 g			
Volume	8.71 x10^{-5} m^{-3}				8.71 x10^{-5} m^{-3}			
Density	481.22 kg m^{-3}				384.13 kg m^{-3}			
Ice Depth	**Light Intensity (mV)**							
	1	**2**	**3**	**4**	**1**	**2**	**3**	**4**
5 mm	12.630	10.792	11.710	12.796	12.099	11.636	10.278	13.638
10 mm	5.287	8.050	6.881	7.476	5.589	6.408	7.407	8.512
15 mm	3.519	2.718	3.625	4.838	3.278	3.107	5.694	4.895

	Sample 5				Mean
Total Mass	102.67 g				108.36 g
Snow Mass	31.96 g				37.65 g
Volume	8.71 x10^{-5} m^{-3}				8.71 x10^{-5} m^{-3}
Density	366.80 kg m^{-3}				432.06 kg m^{-3}
Ice Depth	**Light Intensity (mV)**				
	1	**2**	**3**	**4**	**Mean**
5 mm	10.497	14.303	12.409	11.081	11.898
10 mm	5.765	6.009	8.471	6.728	7.058
15 mm	2.946	3.482	6.203	4.618	4.000

Table C.22. Raw light intensity measurements through granular water ice Samples 1 – 5, of grain size range 0.50 – 0.60 mm.

	Grain Size 0.355 – 0.500 mm							
	Sample 1				Sample 2			
Total Mass	106.95 g				107.91 g			
Snow Mass	36.24 g				37.20 g			
Volume	8.71 x10^{-5} m^{-3}				8.71 x10^{-5} m^{-3}			
Density	415.92 kg m^{-3}				426.94 kg m^{-3}			
Ice Depth	**Light Intensity (mV)**							
	1	**2**	**3**	**4**	**1**	**2**	**3**	**4**
5 mm	12.292	9.740	11.963	14.467	12.275	11.098	11.456	12.218
10 mm	5.732	5.814	5.853	6.737	4.880	5.258	5.755	6.243
15 mm	3.730	3.206	2.131	4.262	2.517	3.046	3.286	3.020

	Sample 3				Sample 4			
Total Mass	110.87 g				103.06 g			
Snow Mass	40.16 g				32.35 g			
Volume	8.71 x10^{-5} m^{-3}				8.71 x10^{-5} m^{-3}			
Density	460.91 kg m^{-3}				371.28			
Ice Depth	**Light Intensity (mV)**							
	1	**2**	**3**	**4**	**1**	**2**	**3**	**4**
5 mm	9.866	9.863	13.659	11.430	11.874	16.981	18.446	10.339
10 mm	4.198	5.024	6.717	8.090	5.466	9.374	8.819	6.250
15 mm	2.502	2.411	3.438	5.273	2.050	5.793	4.487	3.988

	Sample 5				Mean
Total Mass	103.90 g				106.54 g
Snow Mass	33.19 g				35.83 g
Volume	8.71 x10^{-5} m^{-3}				8.71 x10^{-5} m^{-3}
Density	380.92 kg m^{-3}				411.19 kg m^{-3}
Ice Depth	**Light Intensity (mV)**				
	1	**2**	**3**	**4**	**Mean**
5 mm	13.104	17.888	13.817	11.731	12.725
10 mm	6.143	8.374	7.908	6.839	6.474
15 mm	3.083	4.441	6.701	3.528	3.645

Table C.23. Raw light intensity measurements through granular water ice Samples 1 – 5, of grain size range 0.355 – 0.500 mm.

Appendix D

Dusty Snow Measurements

D1. Mars Dust Contaminated Carbon Dioxide Snow

Light intensity measurements were made through samples of carbon dioxide snow, mixed with varying amounts of Mars regolith simulant Mars JSC-1A (of particle diameter <20 µm), at decreasing ice thicknesses. Measurements were made using a pyranometer (in millivolts), and four measurements were made per ice thickness. Details of the general experimental set up can be found in Chapter 3, and experimental procedure specifically for the contaminated snow measurements in Chapter 8. Each batch of snow was made, then weighed, and the required amount of regolith simulant calculated and mixed in. Individual samples made for each percentage dust content were portioned out from one batch of snow mixture, ensuring consistency in dust content. Individual samples were not weighted prior to light intensity measurements, as working as swiftly as possible was paramount to obtaining measurements with the least amount of sintering occurring. This is because the presence of the (thermally absorbing) dust significantly increased the rate of sintering. The same equipment was used for these experiments as used for the snow and granular ice measurements. Tables D.1 to D.5 give the results for Mars dust contaminated CO_2 snow, at increasing dust proportions.

	0.02 % Mars Simulant							
	Sample 1 (mV)				Sample 2 (mV)			
Ice Depth	**1**	**2**	**3**	**4**	**1**	**2**	**3**	**4**
5 mm	3.760	4.691	5.804	3.211	3.475	4.928	6.159	6.851
10 mm	2.258	3.106	3.024	2.261	2.937	4.990	3.280	4.073
15 mm	1.908	1.981	1.829	2.954	1.250	2.369	4.211	2.587

	Sample 3 (mV)				Sample 4 (mV)			
Ice Depth	**1**	**2**	**3**	**4**	**1**	**2**	**3**	**4**
5 mm	7.204	6.251	5.002	5.706	4.968	6.886	5.703	7.871
10 mm	2.503	5.379	4.806	3.458	3.135	3.648	4.537	5.930
15 mm	1.283	4.205	2.817	3.630	2.807	4.464	5.076	4.234

	Sample 5 (mV)				Sample 6 (mV)			
Ice Depth	**1**	**2**	**3**	**4**	**1**	**2**	**3**	**4**
5 mm	4.888	6.294	6.047	7.023	4.921	5.134	7.275	6.723
10 mm	3.725	4.483	5.106	4.900	3.742	4.549	3.175	5.053
15 mm	1.972	2.984	3.502	4.871	2.533	4.415	3.561	3.920

	Sample 7 (mV)				Sample 8 (mV)			
Ice Depth	**1**	**2**	**3**	**4**	**1**	**2**	**3**	**4**
5 mm	4.131	6.925	6.767	7.284	4.449	5.970	7.895	6.902
10 mm	2.992	4.916	5.918	4.447	3.134	5.332	4.570	5.361
15 mm	2.950	3.034	4.171	4.534	3.723	2.707	3.405	4.521

Ice Depth	**Mean**
5 mm	5.847
10 mm	4.085
15 mm	3.263

Table D.1. Raw light intensity measurements through carbon dioxide ice snow mixed with 0.02% (by weight) regolith simulant dust, for Samples 1 – 8.

	0.06 % Mars Simulant							
	Sample 1 (mV)				Sample 2 (mV)			
Ice Depth	**1**	**2**	**3**	**4**	**1**	**2**	**3**	**4**
5 mm	2.890	2.837	6.006	4.079	3.981	4.287	5.992	7.287
10 mm	1.957	1.904	2.130	3.332	1.691	2.910	2.594	3.864
15 mm	2.243	1.469	1.464	1.620	1.766	2.203	3.021	2.320

	Sample 3 (mV)				Sample 4 (mV)			
Ice Depth	**1**	**2**	**3**	**4**	**1**	**2**	**3**	**4**
5 mm	4.209	5.874	3.562	4.140	5.238	4.803	6.402	8.560
10 mm	2.248	3.311	3.307	3.523	2.824	3.849	2.345	5.070
15 mm	2.221	2.570	2.920	3.453	2.186	2.020	1.673	3.100

	Sample 5 (mV)				Sample 6 (mV)			
Ice Depth	**1**	**2**	**3**	**4**	**1**	**2**	**3**	**4**
5 mm	5.501	5.882	5.175	6.471	4.506	4.808	6.672	7.946
10 mm	3.475	2.947	3.964	6.463	2.441	2.853	3.231	4.917
15 mm	2.957	2.283	1.866	3.480	1.349	2.091	3.508	2.092

Ice Depth	Mean
5 mm	5.296
10 mm	3.215
15 mm	2.328

Table D.2 Raw light intensity measurements through carbon dioxide ice snow mixed with 0.06% (by weight) regolith simulant dust, for Samples 1 – 6.

	0.10 % Mars Simulant							
	Sample 1 (mV)				Sample 2 (mV)			
Ice Depth	**1**	**2**	**3**	**4**	**1**	**2**	**3**	**4**
5 mm	5.062	7.836	10.147	10.056	5.709	7.571	10.352	9.332
10 mm	2.043	4.483	3.594	6.776	2.713	5.807	4.322	6.932
15 mm	1.670	2.813	3.217	4.514	1.445	4.708	4.531	3.931

	Sample 3 (mV)				Sample 4 (mV)			
Ice Depth	**1**	**2**	**3**	**4**	**1**	**2**	**3**	**4**
5 mm	4.278	10.945	8.101	10.852	4.875	7.868	8.474	13.879
10 mm	2.575	6.853	7.023	5.460	3.980	5.469	7.647	5.908
15 mm	1.650	4.182	5.189	3.225	2.605	3.264	3.958	5.403

	Sample 5 (mV)				Sample 6 (mV)			
Ice Depth	**1**	**2**	**3**	**4**	**1**	**2**	**3**	**4**
5 mm	4.695	8.823	11.884	9.945	4.603	8.431	7.555	9.074
10 mm	2.808	5.205	6.783	6.901	1.931	3.075	4.661	6.100
15 mm	1.661	4.016	2.987	3.233	1.673	3.166	3.712	4.099

Ice Depth	**Mean**
5 mm	8.348
10 mm	4.960
15 mm	3.369

Table D.3. Raw light intensity measurements through carbon dioxide ice snow mixed with 0.10% (by weight) regolith simulant dust, for Samples 1 – 6.

	0.50 % Mars Simulant							
	Sample 1 (mV)				Sample 2 (mV)			
Ice Depth	**1**	**2**	**3**	**4**	**1**	**2**	**3**	**4**
5 mm	2.198	2.036	5.705	3.647	2.119	4.297	4.834	3.595
10 mm	2.053	2.335	1.758	3.645	2.279	2.751	4.327	3.787
15 mm	1.832	1.655	3.201	2.309	1.884	1.895	3.319	2.881

	Sample 3 (mV)				Sample 4 (mV)			
Ice Depth	**1**	**2**	**3**	**4**	**1**	**2**	**3**	**4**
5 mm	3.014	3.952	4.073	5.294	2.770	3.565	3.893	4.551
10 mm	2.197	3.814	4.731	3.870	2.034	3.788	4.906	2.801
15 mm	2.052	3.527	3.101	3.444	1.644	2.776	2.580	3.992

	Sample 5 (mV)				Sample 6 (mV)			
Ice Depth	**1**	**2**	**3**	**4**	**1**	**2**	**3**	**4**
5 mm	3.214	4.293	6.099	4.788	2.030	6.172	5.419	3.921
10 mm	2.383	3.846	5.783	3.994	3.478	4.570	4.870	3.902
15 mm	2.986	3.401	3.793	4.457	1.904	3.207	2.880	3.430

	Sample 7 (mV)				Sample 8 (mV)			
Ice Depth	**1**	**2**	**3**	**4**	**1**	**2**	**3**	**4**
5 mm	3.190	3.975	5.375	5.015	3.393	5.192	5.223	5.026
10 mm	2.326	2.941	4.205	3.754	2.258	3.166	3.941	4.712
15 mm	2.007	2.403	3.792	3.182	2.576	2.579	3.073	2.903

Ice Depth	**Mean**
5 mm	4.121
10 mm	3.475
15 mm	2.833

Table D.4. Raw light intensity measurements through carbon dioxide ice snow mixed with 0.50% (by weight) regolith simulant dust, for Samples 1 – 8.

	1.00 % Mars Simulant							
	Sample 1 (mV)				Sample 2 (mV)			
Ice Depth	**1**	**2**	**3**	**4**	**1**	**2**	**3**	**4**
5 mm	2.419	3.879	2.438	2.312	2.370	3.329	2.842	2.651
10 mm	1.312	1.455	2.284	2.731	1.690	2.975	2.129	1.578
15 mm	1.156	1.430	1.361	1.453	1.383	2.023	1.774	1.454

	Sample 3 (mV)				Sample 4 (mV)			
Ice Depth	**1**	**2**	**3**	**4**	**1**	**2**	**3**	**4**
5 mm	3.472	4.980	3.850	4.375	3.480	4.052	4.321	3.251
10 mm	2.002	3.263	3.411	2.928	2.943	2.916	2.869	3.760
15 mm	1.670	1.871	1.787	1.800	2.137	2.200	3.102	3.681

	Sample 5 (mV)				Sample 6 (mV)			
Ice Depth	**1**	**2**	**3**	**4**	**1**	**2**	**3**	**4**
5 mm	4.284	3.154	4.165	5.032	4.461	3.708	3.282	3.405
10 mm	4.607	3.277	3.212	2.281	2.414	2.642	3.695	1.828
15 mm	2.810	2.982	1.973	2.598	1.834	1.821	2.135	2.678

Ice Depth	**Mean**
5 mm	3.563
10 mm	2.675
15 mm	2.046

Table D.5. Raw light intensity measurements through carbon dioxide ice snow mixed with 1.00% (by weight) regolith simulant dust, for Samples 1 – 6.